



# Instabilités thermoconvectives de fluides complexes

Christel Metivier

## ► To cite this version:

Christel Metivier. Instabilités thermoconvectives de fluides complexes. Mécanique des fluides [physics.class-ph]. Université de Lorraine, 2018. tel-02432694

HAL Id: tel-02432694

<https://hal.science/tel-02432694>

Submitted on 8 Jan 2020

**HAL** is a multi-disciplinary open access archive for the deposit and dissemination of scientific research documents, whether they are published or not. The documents may come from teaching and research institutions in France or abroad, or from public or private research centers.

L'archive ouverte pluridisciplinaire **HAL**, est destinée au dépôt et à la diffusion de documents scientifiques de niveau recherche, publiés ou non, émanant des établissements d'enseignement et de recherche français ou étrangers, des laboratoires publics ou privés.



Université de Lorraine - CNRS  
LEMTA - UMR 7563

## Habilitation à Diriger des Recherches de l'Université de Lorraine

### Instabilités thermoconvectives de fluides complexes

Christel Métivier

#### Rapporteurs :

Anne Davaille, Directrice de Recherche CNRS, FAST

Sandra Lerouge, Professeure des Universités, Laboratoire Matière et Système Complexe

Guillaume Ovarlez, Directeur de Recherche CNRS, LOF

#### Membres du jury :

Albert Magnin, Directeur de Recherche CNRS, LRP

Eduardo Weisfred, Directeur de Recherche CNRS, LPMMH

Chérif Nouar, Directeur de Recherche CNRS, LEMTA

Denis Funfschilling, Chargé de Recherche CNRS, ICUBE.

Soutenance prévue le 27 novembre 2018



# Table des matières

<b>Curriculum Vitae</b>	<b>5</b>
Formation et déroulement de carrière . . . . .	6
Publications . . . . .	7
Communications . . . . .	9
Activités d'encadrement . . . . .	10
Enseignements . . . . .	10
Rayonnement . . . . .	11
Responsabilités administratives et collectives . . . . .	12
<b>1 Activités d'enseignement</b>	<b>14</b>
1.1 Description . . . . .	14
1.2 Résumé . . . . .	15
<b>2 Instabilités thermoconvectives dans des fluides non-Newtoniens</b>	<b>18</b>
2.1 Thèse : 2003-2006 . . . . .	18
2.2 Convection naturelle dans les fluides à seuil . . . . .	19
2.2.1 Introduction . . . . .	19
2.2.2 Origine du démarrage de la convection . . . . .	20
2.2.3 Effets des conditions aux limites . . . . .	22
2.3 Convection naturelle dans les fluides rhéofluidifiants . . . . .	23
2.3.1 Introduction . . . . .	23
2.3.2 Approche théorique - Cas des fluides rhéofluidifiants thermodépendants . . . . .	24
2.3.3 Approche expérimentale . . . . .	26
2.4 Conclusions et perspectives . . . . .	31
<b>3 Projets de recherche</b>	<b>33</b>
3.1 Thermométrie par IRM (MRT) . . . . .	33
3.2 Convection de Rayleigh-Bénard dans des Matériaux à Changement de Phase . . . . .	37
3.3 Action de l'insertion de particules magnétiques dans des fluides à seuil . . . . .	41
<b>Bibliographie</b>	<b>49</b>
<b>A Rayleigh-Bénard convection in thermodependent shear-thinning fluids</b>	<b>54</b>
<b>B Articles significatifs publiés</b>	<b>55</b>



# Curriculum Vitae

**Christel Métivier,**

Née le 8 février 1980

Mariée, deux enfants

**Maître de Conférences**

Université de Lorraine

LEMTA - UMR 7563

Faculté des Sciences et Technologie

Christel.Metivier@univ-lorraine.fr

Tel : 00 33 3.72.74.42.79

---

## FORMATION ET DÉROULEMENT DE CARRIÈRE

---

Sept 2015- Juillet 2016 : Congé maternité (et arrêts maladie)

Avril 2013 - Décembre 2013 : Congé maternité (et arrêts maladie)

Depuis février 2012 : Mutation en tant que Maître de Conférences à l'Université de Lorraine, FST\* - LEMTA†.

septembre 2007 - février 2012 : Maître de Conférences à Polytech' Grenoble, Université Joseph Fourier.

2006 - 2007 : ATER à l'Ecole Supérieure des Sciences et Technologies de l'Ingénieur de Nancy (ESSTIN), Université Henri Poincaré.

2003 - 2006 :

**Doctorat** de l'Université de Nancy à l'école doctorale 'Energie Mécanique Matériaux' en Mécanique des Fluides - Bourse MENRT - LEMTA (C.N.R.S UMR 7563). **Directeur de thèse** : Chérif NOUAR - Directeur de Recherche CNRS.

**Monitorat** à l'ENSMN‡, I.N.P.L\*.

2003 :

**DEA de Mécanique**, option Mécanique des Fluides de l'école doctorale de mécanique à l'université Pierre et Marie Curie (Paris 6). **Mention : Bien**

**Diplôme d'ingénieur** de l'Ecole Nationale Supérieure des Arts et Métiers (ENSAM) - Centre de Paris.

**Stage de D.E.A. / projet de fin d'études réalisé au LIMSI§.**

2000-2003 : Formation d'ingénieur à Arts et Métiers ParisTech (ex-ENSAM).

1997-2000 : Classes préparatoires filière Physique Technologie au Lycée Saint Joseph - Laxou (54).

Juin 1997 : Baccalauréat dans la série générale Scientifique.

---

## PRIX ET DISTINCTIONS

---

\*. Faculté des Sciences et Technologies

†. Laboratoire d'Energétique et de Mécanique Théorique et Appliquée

‡. Ecole Nationale Supérieure des Mines de Nancy

§. Laboratoire d'Informatique pour la Mécanique et les Sciences de l'Ingénieur

**Prix de thèse** 2007 de l'AUM/AFM (Activités Universitaires de Mécanique/Association Française de Mécanique),

**Prix de thèse** 2007 de l'Institut National Polytechnique de Lorraine.

2016-2020 : Obtention de la **PEDR** (Prime d'Encadrement Doctoral et de Recherche).

---

## RECHERCHE

---

### Thématiques :

Dynamique des fluides, thermique, rhéologie, fluides complexes, fluides à seuil, stabilités hydrodynamiques, vélocimétrie et thermométrie par IRM.

### Objectifs :

Etablir l'influence des propriétés physiques (seuil de contrainte, rhéofluidification) des matériaux sur le déclenchement et l'évolution des instabilités.

Comprendre l'interaction entre la (micro)structure du matériau et le comportement macroscopique des écoulements étudiés.

Etude du couplage hydrodynamique et thermique en convection de Rayleigh-Bénard pour des fluides non-Newtoniens.

### Méthodologies :

Analyses de stabilité : analyses linéaire et non linéaire, approches énergétiques.

Approches expérimentales : Mesures de vitesse et de température par IRM, ombroscopie, PIV.

---

## PUBLICATIONS

---

### Articles dans des revues de rang A :

1. **C. Métivier**, M. Darbouli, F. Brochard, A. Magnin, “*Oscillatory Rayleigh-Bénard convection in elastoviscoplastic Carbopol gels*”, **à soumettre**
2. M.S. Aghighi, **C. Métivier**, A. Ammar, “*Natural convection in a square enclosure filled with a Casson fluid - Comparison with a Bingham fluid*”, **à soumettre** à Journal of Thermal Science and Engineering Applications (ASME)
3. S. Leclerc & **C. Métivier**, “*MRI Temperature and velocity measurements in a fluid layer with heat transfer*”, Exp. Fluids 59(2) (2018)

4. S. Aghighi, A. Ammar, **C. Métivier**, M. Gharagozlu, “Rayleigh-Bénard convection of Casson fluids”, Int. J. Thermal Sci. 127 (2018)
5. T. Varé, C. Nouar, **C. Métivier**, “Instabilities of convection patterns in a shear-thinning fluid between plates of finite conductivity”, Phys. Rev. E, 96, 043109 (2017)
6. **C. Métivier**, C. Li, A. Magnin, “Origin of the onset of Rayleigh-Bénard convection in a concentrated suspension of microgels with a yield stress behavior”, Phys. Fluids, 29, 104102 (2017)
7. C. Li, A. Magnin, **C. Métivier**, “Natural convection in shear-thinning yield stress fluids in a square enclosure”, AIChE Journal, 62(4), 1347-1355 (2016)
8. M. Darbouli, **C. Métivier**, S. Leclerc, C. Nouar, D. Stemmelen, M. Bouteraa, “Natural convection in shear-thinning fluids : Experimental investigations by MRI”, Int. J. Heat Mass Transfer, 95, 742-754 (2016)
9. M. Bouteraa, C. Nouar, E. Plaut, **C. Métivier**, A. Kalck, “Weakly nonlinear analysis of Rayleigh-Bénard convection in shear-thinning fluids : nature of the bifurcation and pattern selection”, J. Fluid Mech., 767, 696-734 (2015)
10. M.S. Aghighi, A. Ammar, **C. Métivier**, F. Chinesta, “Parametric solution of the Rayleigh-Bénard convection model by using the PGD - Application to nanofluids”, Int. J. Numer. Methods Heat Fluid Flow, 25 (6) (2015)
11. M. Darbouli, **C. Métivier**, A. Magnin, J.-M. Piau, A. Abdelali, “The onset of the Rayleigh-Bénard instability for viscoplastic fluids”, Phys. Fluids 25, 023101, (2013).
12. M.S. Aghighi, A. Ammar, **C. Métivier**, M. Normandin, F. Chinesta, “Non-incremental transient solution of the Rayleigh-Bénard convection model by using the PGD”, J. Non-Newtonian Fluid Mech., 200, 65-78 (2013)
13. **C. Métivier**, Y. Rharbi, A. Magnin, A. Bou Abboud, “Stick-slip control of the Carbopol gels on transparent smooth walls”, Soft Matter, 8, 7365 (2012).
14. **C. Métivier** et C. Nouar, “Stability of a Rayleigh-Bénard Poiseuille flow for yield stress fluids - Comparison between Bingham and regularised models”, Int. J. Non-linear Mech., 46 (9), 1205-1212 (2011).
15. **C. Métivier** et A. Magnin, “The effect of the boundary stick-slip on the stability of the Rayleigh-Bénard Poiseuille flow for viscoplastic fluids”, J. Non-Newtonian Fluid Mech., 166, 839-846 (2011).

16. **C. Métivier**, C. Nouar et J.-P. Bracher, “*Weakly non-linear dynamics of thermoconvective instability involving viscoplastic fluids*”, J. Fluid Mech., 660, 316-353 (2010)
  17. **C. Métivier** et C. Nouar, “*Linear stability of the Rayleigh-Bénard Poiseuille flow for thermodependent viscoplastic fluids*”, J. Non-Newtonian Fluid Mech., 163, 1-8 (2009)
  18. **C. Métivier**, I. A. Frigaard et C. Nouar, “*Nonlinear stability of the Bingham Rayleigh-Bénard Poiseuille flow*”, J. Non-Newtonian Fluid Mech., 158, 127-131 (2009).
  19. **C. Métivier** et C. Nouar, “*On linear stability of Rayleigh-Bénard Poiseuille flow of viscoplastic fluids*”, Phys. Fluids 20 104101, (2008).
  20. **C. Métivier**, C. Nouar et J.-P. Bracher, “*Linear stability involving the Bingham model when the yield stress approaches zero*”, Phys. Fluids 17 (10) (2005).
- 

## COMMUNICATIONS

---

Colloques internationaux avec comité de lecture et publication d'abstract :

**C. Métivier**, M. Darbouli, S. Leclerc, C. Nouar, T. Varé D. Stemmelen, Communication orale, Annual European Rheology Conference, Avril 2018.

**C. Métivier**, C. Li, A. Magnin, Communication orale, EMI International Conference, 2016.

M. Darbouli, **C. Métivier**, S. Leclerc, C. Nouar, D. Stemmelen, M. Bouteraa, Poster, 10th Annual European Rheology Conference, Avril 2015.

**Métivier C.**, Rharbi Y., Magnin A. (2013), Communication orale, 8th Annual European Rheology Conference, Avril 2013.

Darbouli M., **Métivier C.**, Magnin A., Piau J.-M. (2012), Communication orale, XVIth International Congress on Rheology - ICR, Août 2012.

**Métivier C.**, Nouar C. et Brancher J.-P. (2007), Communication orale, 4th Annual European Rheology Conference - AERC, Avril 2007.

**Métivier C.**, Nouar C. et Brancher J.-P. (2006), Communication orale, 6th Euromech Fluid Mechanics Conference, Juin 2006.

Colloques nationaux avec comité de lecture et publication d'actes :

Participation régulière sous forme de communications orales et articles de 6 pages au Congrès Français de la Mécanique en 2005, 2007, 2011, 2015.

Mémoires :

“*Instabilités thermoconvectives pour des fluides viscoplastiques*”, Thèse de doctorat - Institut National Polytechnique de Lorraine, réalisée au LEMTA, Décembre 2006 (175 pages).

Mémoire de DEA - Ecole doctorale de l'ENSA - Université Pierre et Marie Curie, réalisé au LIMSI, Juin 2003 (60 pages).

Workshops internationaux :

“*Visco-plastic Fluids, from theory to application*”, Communications orales, Chypre, Novembre 2009 ; Monte Verita, Octobre 2007 ; Banff, Octobre 2005 .

“*15th International Couette-Taylor Workshop*”, Communication orale, LMPG, Le Havre, France, Juillet 2007.

---

## ACTIVITES D'ENCADREMENT

---

Co-encadrement de thèses :

- Mohamed Darbouli, inscrit à l'**Université de Grenoble**, thèse financée par le gouvernement syrien. Début : Novembre 2009, soutenance : 16 avril 2013. Co-encadrement à 50%.
- Chong Li, inscrit à l'**Université de Grenoble**, thèse financée par un projet blanc de l'ANR (THIM). Début : Janvier 2012, Soutenance : 13/10/2015. Co-encadrement à 50%.
- Mondher Bouteraa, inscrit à l'**Université de Lorraine**, thèse financée par un projet blanc de l'ANR (THIM). Début : mi-septembre 2012 - Soutenance : 7/03/2016. Co-encadrement à 50%.
- Thomas Varé, inscrit à l'**Université de Lorraine**, thèse ministérielle. Début : 01/10/2015. Co-encadrement à 50%.

Encadrements de stages réguliers niveau M1. Encadrement de stage de Master M2 :

- Février 2017 à Juillet 2017 : Dinmukhambet Baimbetov.

---

## ENSEIGNEMENTS

---

Depuis février 2012 : (FST, Université de Lorraine)

- Cours, Travaux Dirigés de **Mécanique du solide**, L2 MI Nancy,

---

¶. Ecole Nationale Supérieure d'Electricité et de Mécanique

- Travaux Dirigés de **Résistance des Matériaux**, L3 Mécanique,
- Travaux Dirigés de **Mécanique des fluides**, L3 Mécanique,
- Cours, Travaux Dirigés de **Compléments de Mécanique - Ecoulements potentiels, turbomachines, méthodes asymptotiques**, L3 Mécanique,
- Cours, Travaux Dirigés de **Compléments de Mécanique des Fluides : Rhéologie**, M1 Mécanique Energétique,
- Cours, Travaux Dirigés de **Compléments de Mécanique des Fluides : Ecoulements compressibles**, M1 Mécanique Energétique,
- Cours, Travaux Dirigés de **Mécanique des Fluides : Turbulence**, M1 Mécanique Energétique,
- Cours, Travaux Dirigés de **Mécanique des Fluides avancée : Instabilités hydrodynamiques**, M2 Mécanique Energétique,

Septembre 2007-fevrier 2012 : (Polytech Grenoble, Université Joseph Fourier)

- Cours, Travaux Dirigés, Travaux Pratiques de **Mécanique des Milieux Continus**, filières Géotechnique et Matériaux (1ère année d'école, niveau L3) ,
- Cours, Travaux Dirigés, Travaux Pratiques de **Résistance des Matériaux**, filière Matériaux (2ème année d'école, niveau M1) ,

2003-2007 :

Enseignements effectués à l'ENSEM<sup>¶</sup>, à l'ENSMN<sup>†</sup> (monitorat) et l'ESSTIN (ATER) dans les matières suivantes : Thermodynamique (TD, niveaux L3 et M1), Mécaniques des Milieux Continus (TD, L3), Mécanique du Point (TD, L1), Mécanique des Fluides (TD et TP, L3), Thermique (TP, M1).

## RAYONNEMENT

- Membre de **quatre comités de sélection** pour des postes de MCF depuis 2012 : poste 1890, Université Toulouse 3 Paul Sabatier (2012) ; poste 677, Université Joseph Fourier Grenoble 1 (2013) ; poste 0614, Université de Lorraine (2015) ; poste MCF à l'Université de Poitiers (2018).
- Membre des jurys de thèse de Amhed Abdelali (soutenance en février 2011 à l'Université de Grenoble), de Mohammad Saeid AGHIGHI (soutenance en mars 2014 à Arts et Métiers Paris Tech - Angers).
- Expertises régulières pour “Journal of Non-Newtonian Fluid Mechanics” depuis 2008, expertises pour “Compte-rendu de mécanique” en 2011 et 2018, expertise pour “Computers and Fluids” en 2018, expertise pour “Physics of Fluids” en 2018.
- Deux expertises d'article pour le Congrès Français de Mécanique 2011,
- Présidente de deux séances au Congrès Français de Mécanique 2011,
- Deux expertises d'article pour le Congrès de la Société Française de Thermique 2013.

**Collaborations :**

- Collaboration sur la thématique “Instabilités thermoconvectives pour des fluides microstructurés” entre le **LEMTA**, le **LTN** et le **Laboratoire de Rhéologie** dans le cadre du projet blanc “THIM” financé par l’ANR 2011-2015,
- Collaboration internationale avec Saeid Aghighi, Enseignant Chercheur, Department of Mechanical Engineering, Bu-Ali Sina University, Iran. **3 publications communes + 1 soumise.**
- Collaboration nationale avec Amine Ammar, Professeur, Arts et Métiers ParisTech, ENSAM Angers. **3 publications communes.**
- Collaboration nationale avec Albert Magnin, Directeur de Recherche CNRS, Laboratoire de Rhéologie et Procédés, Université Grenoble Alpes. **4 publications communes.**
- Collaboration internationale avec Mohamed Darbouli, Enseignant Chercheur, Syrie. **Publication à venir.**

#### **Contrats de recherche :**

- Dépôt d’un pré-projet européen - Interreg Rhin Supérieur Offensive Science, porteur : Denis Funf-schilling (ICube, Strasbourg) - Projet à **1M€** (190k€ pour le LEMTA dont je suis responsable scientifique).
- 2017-2018 : Responsable d’un Projet Exploratoire (PE) de la cellule énergie du CNRS “Développement d’une technique innovante de mesures de température : Thermométrie par IRM”, financé par le CNRS et TOTAL - **17 k€.**
- 2015-2016 : Responsable d’un projet PEPS “Action de l’insertion de particules magnétiques sur la mise en écoulement d’un fluide à seuil” financé par le CNRS **15k€.** Collaboration avec l’IJL (Institut Jean Lamour, Université de Lorraine).
- 2011-2015 : Rédaction d’un projet ANR blanc et responsable scientifique pour le Laboratoire de Rhéologie et Procédés (LRP) - **500k€** (180k€ pour le LRP).
- 2013-2014 : Responsable d’un projet région - Université de Lorraine **40k€.**

#### **RESPONSABILITES ADMINISTRATIVES ET COLLECTIVES**

- Depuis Octobre 2015 : Membre élu du CNU - Section 60
- Depuis Janvier 2018 : Membre élu du Conseil de Laboratoire
- Juillet 2014 - Juillet 2018 : Membre élu du conseil de la FST (Faculté des Sciences et Technologies)
- Octobre 2013 - Octobre 2015 : Secrétaire du GTT-AUM (Groupe Transverse de Travail - Activités Universitaires de Mécanique) de la société savante de mécanique AFM. Membre élu depuis janvier 2011.
- Depuis 2013 : Responsable de la plateforme de Travaux Pratiques de rhéologie à la FST.
- Octobre 2013 - Octobre 2014 : Responsable scientifique d’un projet co-financé par la Région Lorraine et l’Université de Lorraine. Obtention d’une bourse post-doctorale attribuée à M. Darbouli.
- Janvier 2011 - Février 2012 : Responsable scientifique pour le Laboratoire de Rhéologie du projet “Instabilités thermoconvectives pour des fluides microstructurés” (THIM), financé par l’ANR.
- Septembre 2009 - septembre 2011 : Responsable des stages de première année Polytech’Grenoble, filière Matériaux. Obtention de la **Prime de Responsabilité Pédagogique** pour cette période.

- Septembre 2007 - février 2012 : Responsable de l'acquisition, de la mise en place et du fonctionnement des TP de mécanique et d'hydraulique à Polytech' Grenoble, filières Géotechnique et Matériaux.

# Chapitre 1

## Activités d'enseignement

### 1.1 Description

Mes activités d'enseignement ont débuté dès le début de mon doctorat avec l'obtention d'un **monitorat** à l'Ecole Nationale Supérieure des Mines (ENSM) de Nancy. Entre 2003 et 2006, j'y ai enseigné la **thermodynamique** (TD : 23h) ainsi que la **mécanique des milieux continus** (TD : 43h) en première année (niveau L3).

A l'issue de mon doctorat, j'ai été recrutée en octobre 2006 sur un poste d'**Attaché Temporaire d'Enseignement et de Recherche** à l'ESSTIN (Ecole Supérieure de Sciences et Technologie de l'Ingénieur de Nancy, actuellement Polytech' Nancy). Mes enseignements ont consisté en des TD et TP de **mécanique du point** (TD : 24h), de **mécanique des fluides** (TD : 16h, TP : 38h) et des TP de **thermique** (18h).

En septembre 2007, j'ai été nommé **Maître de Conférences** à l'**Université Joseph Fourier**, Grenoble. Mon affectation pédagogique était à Polytech Grenoble. J'ai pris la **responsabilité des modules** de **mécanique des milieux continus** et de **résistance des matériaux** en première année (niveau L3) des départements 'Géotechnique' (environ 50-60 étudiants) et 'Matériaux' (30-40 étudiants). La totalité de mon service s'est réalisée sur les enseignements de Cours Magistraux, de Travaux Dirigés et de Travaux Pratiques. Par ailleurs, le développement de ces modules s'est accompagné de l'acquisition et de la mise en place des TP de mécanique et d'hydraulique, **responsabilité qui m'a été confiée entre septembre 2007 et février 2012**.

Pour des raisons familiales, j'ai obtenu une mutation sur un poste de Maître de Conférences à l'**Université de Lorraine** (Nancy) en février 2012. Depuis cette date, mes enseignements s'effectuent à la Faculté des Sciences et Technologie (FST) de Nancy. Les premières années, j'ai eu l'opportunité d'enseigner la **mécanique du solide** (CM et TD en L2), la **résistance des matériaux** (TD en L3), ainsi que des modules associés à la **mécanique des fluides**, niveaux L3 et M1. Ce n'est que récemment que je me suis concentrée uniquement sur des enseignements dans le domaine de la **mécanique des fluides**, domaine qui se rapproche de mes activités de recherche. Ainsi, **depuis 2014**, je suis **responsable des modules suivants :**

- **compléments de mécanique des fluides** en L3 (module optionnel - CM, TD),
- **compléments de mécanique des fluides : Rhéologie et Fluides compressibles** en M1 (CM, TD, TP),

– **mécanique des fluides avancée** : Instabilités hydrodynamiques en M2 (CM, TD, projets). Par ailleurs, j'interviens également en L3 en **mécanique des milieux continus - partie fluide** (CM et TD) et en TD de **mécanique des fluides** (L2 et L3).

Depuis 2018, je suis aussi responsable d'un module de mécanique des fluides (L3).

En termes de **supports d'enseignement**, pour la plupart de mes modules dont j'ai la responsabilité, je propose des polycopiés de cours, de TD et de TP que j'ai rédigés. Lors des CM, je travaille sur tableau pour les démonstrations de cours et je propose des transparents aux étudiants pour présenter les notions (essentielles) du cours. Lorsque cela est adapté, je propose aux étudiants de travailler par petits groupes (4 à 5 étudiants) en séances de TD.

**Depuis 2013**, suite à la demande d'un financement région qui nous a permis d'acquérir plusieurs viscosimètres et rhéomètres, je suis **responsable de la plateforme de TP** de rhéologie (module compléments de mécanique des fluides de M1).

## 1.2 Résumé

**2003 – 2007** : Monitorat et ATER à l'Université de Lorraine

Année	Auditoire	Matière - Type	Volume horaire
<b>2003 -</b>	ENSEM	Mécanique des milieux continus - TD	12h
<b>2004</b>	ENSEM	Thermodynamique - TD	12h
	ENSM	Thermodynamique - TD	43h
<b>2004 -</b>		Mécanique des milieux continus - TD	43h
	ENSM	Thermodynamique - TD	23h
		Encadrement de projet	6h
<b>2005 -</b>		Mécanique des milieux continus - TD	43h
	ENSM	Mécanique des fluides - TP	23h
		Encadrement de projets	16h
<b>2006 -</b>		Mécanique du point - TD	24h
	ESSTIN	Mécanique des fluides - TD	16h
		Mécanique des fluides - TP	38h
		Thermique - TP	18h

**2007 – 2012 : Maître de Conférences à l'université Joseph Fourier, Grenoble**

Année	Auditoire	Matière - Type	Volume horaire
<b>2007 - 2012</b> (moyenne)	Polytech Grenoble	Mécanique des milieux continus - CM/TD/TP  Résistance des matériaux - CM/TD  Encadrement de projets  Encadrement de stages	116h  50h 12h 20h

**Depuis 2012 : Maître de conférences à l'Université de Lorraine - Enseignements à la Faculté des Sciences et Technologies FST de Nancy**

Année	Auditoire	Matière - Type	Volume horaire
<b>2012 - 2013</b> FST	L2 CPU M1 L3 L3 L2 M1 Erasmus mundus	Mécanique générale - CM/TD  Compléments de mécanique des fluides - CM/TD  RDM - TD  Compléments de mécanique des fluides - CM/TD  Maple - TP  MMC - TD (en Anglais)	45h  70h  20h  37.5h  16h  20h

<b>Année</b>	<b>Auditoire</b>	<b>Matière - Type</b>	<b>Volume horaire</b>
<b>2013 - 2014</b>	L2 CPU M1 M1 Bébé	Mécanique générale - CM/TD Compléments de mécanique des fluides - CM/TD <b>Congé maternité et arrêts maladies (10 mois)</b>	45h 37.5h décharge 50%
<b>2014 - 2015</b>	M1 M2 L2 FST	Turbulence - CM/TD Mécanique des fluides avancée (instabilités) - CM/TD Mécanique des fluides - CM Méca. Fluides - TD	14h 25h 21h 40h
	M1 L3	Compléments de méca. fluides - CM/TD/TP Compléments de mécanique des fluides - CM/TD	64h 37.5h
<b>2015 - 2016</b>	Bébé	<b>Congé maternité et arrêts maladie (10 mois)</b>	décharge 100%
<b>2016 - 2017</b>	M2 L3 M1 M2	Compléments Méca. fluides - CM/TD/projets Méca. Fluides - TD Rhéologie - CM/TD Projets CRCT	25h 20H 49h 11h décharge 50%

## Chapitre 2

# Instabilités thermoconvectives dans des fluides non-Newtoniens

Jusqu'à récemment, mes activités de recherche se sont principalement concentrées sur la convection dans des fluides non-Newtoniens. L'étude des instabilités thermo-convectives dans une couche de fluide chauffée par le bas a été très largement considérée dans le cas des fluides Newtoniens. Ceci s'explique par le nombre important d'applications physiques ou industrielles qui mettent en jeu des gradients thermiques dans des couches fluides. Aux grandes échelles, la convection thermique peut avoir lieu dans l'atmosphère, les océans ou encore le manteau terrestre. A une échelle moindre, la connaissance des régimes thermiques peut avoir un impact sur les procédés industriels et leur optimisation, puisque la convection thermique améliore les transferts thermiques. A cet égard, l'apparition et l'évolution des instabilités thermo-convectives ainsi que leur dynamique représentent un intérêt majeur. La plupart des fluides rencontrés sont non-Newtoniens, c'est à dire qu'ils présentent une relation non-linéaire entre contrainte et taux de cisaillement. Malgré leur importance notamment dans les secteurs industriels (ex : secteurs cosmétique, pétrolier, agro-alimentaire, pharmaceutique...), ces fluides restent peu étudiés comparativement aux fluides Newtoniens.

### 2.1 Thèse : 2003-2006

Lors de ma thèse, la stabilité de l'écoulement de **Poiseuille Rayleigh-Bénard** pour des **fluides à seuil** a été examinée via des approches théoriques linéaires (modale et énergétique), faiblement non linéaire et non linéaire. Dans cette étude, le comportement rhéologique du fluide est supposé être décrit par le modèle de Bingham. Ce modèle suppose que lorsque la contrainte appliquée au matériau est inférieure à la contrainte seuil  $\tau_y$ , le matériau se comporte comme un solide indéformable. Au-delà de la contrainte seuil, le matériau se comporte comme un fluide visqueux rhéofluidifiant, c'est à dire que la viscosité diminue avec le taux de déformation qui augmente. Cette étude avait pour objet de comprendre l'influence de la contrainte seuil sur les conditions de stabilité de l'écoulement de Poiseuille soumis à un gradient de température vertical tel que le fluide est chauffé par le bas (Rayleigh-Bénard). L'effet de la contrainte se manifeste à travers la modification de l'épaisseur de la zone cisaillée, la stratification de la viscosité dans cette zone ainsi que la modification de la dissipation visqueuse. Une difficulté fondamentale liée à ce problème réside dans le traitement de l'interface séparant les phases "solides" et "liquides".

Dans un premier temps, des analyses linéaires de stabilité avec des approches modale et énergétique ont été menées. Les résultats mettent clairement en évidence l'effet stabilisant de la contrainte seuil (Métivier *et al.* (2005); Métivier & Nouar (2008)). Ensuite une analyse faiblement non linéaire de stabilité

a été conduite afin de déterminer la nature de la bifurcation. Des résultats originaux ont été obtenus montrant un changement de nature de bifurcation lorsque le nombre de Péclet est augmenté (Metivier *et al.* (2010)). En-dessous d'un nombre de Péclet critique  $Pe_c = O(1)$ , nous avons montré que la bifurcation est surcritique. Au-delà, la bifurcation devient sous-critique avec un passage surcritique/sous-critique abrupt.

Ma thèse a donné lieu à 6 publications dans des revues de rang A (Métivier *et al.* (2005); Métivier & Nouar (2008, 2009); Métivier *et al.* (2009); Metivier *et al.* (2010); Métivier & Nouar (2011)).

## 2.2 Convection naturelle dans les fluides à seuil

Lors de mon recrutement en 2007 en tant que maître de conférences au Laboratoire de Rhéologie et Procédés (LRP), j'ai travaillé sur la convection naturelle dans un fluide à seuil initialement au repos, à savoir la configuration de Rayleigh-Bénard. Durant cette étude, j'ai eu l'opportunité de **co-encadrer deux thèses** (Mohamed Darbouli 2009-2013 et Chong Li 2012-2015). Par ailleurs, j'ai rédigé un **projet ANR** jeune chercheur qui a finalement été présenté comme projet blanc étant donné l'ampleur du projet. Ce projet intitulé ‘ThIM’ a été financé par l’ANR de fin 2011 à fin 2015 et porté par Cathy Castelain, LTN. Ce projet avait trait aux instabilités thermoconvectives dans des fluides micro-structurés.

### 2.2.1 Introduction

Dans la configuration de Rayleigh-Bénard, l'origine de l'instabilité convective est due à un gradient vertical de température entre deux plaques horizontales qui induit une force de poussée (poussée d'Archimède). Dans le cas d'un fluide visqueux ne présentant pas de contrainte seuil, l'origine de l'instabilité est gouvernée par le nombre de Rayleigh  $Ra$ , défini par :

$$Ra = \frac{\rho g \beta \Delta T d^3}{\mu \kappa}, \quad (2.1)$$

où  $\rho$  est la masse volumique du fluide,  $g$  la gravité,  $\beta$  le coefficient d'expansion volumique,  $\Delta T$  la différence de température entre les plaques horizontales,  $d$  la distance entre ces deux plaques,  $\mu$  la viscosité du fluide et  $\kappa$  sa diffusivité thermique. L'écoulement de base correspond à un état statique purement conductif. Pour des fluides visqueux, tant que le nombre de Rayleigh est suffisamment petit, les forces de poussée ne peuvent pas vaincre les effets stabilisants de la diffusion visqueuse et thermique. A partir d'une valeur critique  $Ra_c$ , l'équilibre est rompu et des rouleaux thermo-convectifs apparaissent. Dans le cas des fluides à seuil, un effet stabilisant supplémentaire doit être pris en compte, celui lié à la contrainte seuil  $\tau_y$ . Ainsi, le déclenchement des instabilités n'est possible que si la force de poussée est suffisamment importante pour vaincre à la fois la contrainte seuil et les effets conjugués de dissipation thermique et visqueuse.

Des études théoriques de stabilité linéaire (Zhang *et al.* (2006); Vikhansky (2009)) ont considéré le cas d'un fluide à seuil inélastique (modèle de Bingham) dans la configuration de Rayleigh-Bénard. Ces études ont montré que pour une valeur de contrainte seuil finie, le régime conductif est linéairement stable pour toutes valeurs de  $Ra$  et est conditionnellement stable sinon. Cela signifie que vis à vis de petites perturbations, la Convection de Rayleigh-Bénard (RBC) ne peut pas se développer dans des fluides de Bingham (ou Herschel-Bulkley). Ces conclusions sont en contradiction avec des résultats expérimentaux récents (Darbouli *et al.* (2013); Davaille *et al.* (2013); Kebiche *et al.* (2014); Métivier *et al.* (2017)) qui

ont observé le développement de l'instabilité convective dans des gels de Carbopol. Cette contradiction est en partie liée au fait que les gels présentent un comportement élastique en-dessous de la contrainte seuil et non pas un comportement de type “solide indéformable” comme cela est modélisé dans le cas d'un fluide de Bingham. L'origine du démarrage de l'écoulement, ou encore la transition du comportement solide à fluide, au sein des fluides à seuil reste un sujet de recherche actif.

### 2.2.2 Origine du démarrage de la convection

Dans les travaux de Darbouli *et al.* (2013) et Métivier *et al.* (2017), nous avons montré que le démarrage de l'instabilité était gouverné par le nombre seuil  $Y$  qui représente le rapport entre la contrainte seuil  $\tau_y$  et la contrainte liée à la flottabilité, il est défini comme suit :

$$Y = \frac{\tau_y}{\rho g \beta \Delta T d}. \quad (2.2)$$

Nous avons montré que la valeur critique  $Y_c$  lors du démarrage de la convection est telle que  $1/Y_c^g \approx 40-60$  dans le cas de surfaces glissantes (plaques en verre et plaques en cuivre pour les plaques horizontales respectivement supérieure et inférieure) et que  $1/Y_c^a \approx 80$  dans le cas où le gel adhère aux parois.

Par ailleurs, nous avons proposé et exploré trois scenarios possibles à l'origine du démarrage de la RBC dans des gels de Carbopol :

(i) Le premier scenario consiste à considérer les gels de Carbopol comme des matériaux élastoviscoplastiques. A ce titre, on peut introduire une échelle de viscosité basée sur des mesures viscoélastiques linéaires (SAOS). Dans le domaine élastique, les contraintes au sein du gel peuvent s'écrire  $\sigma = G'\gamma$ . Proche de la transition solide-fluide, l'échelle caractéristique de contrainte est la contrainte seuil  $\tau_y$ , ainsi  $\tau_y = G'\gamma_c$ ,  $\gamma_c$  étant la déformation critique obtenue à la valeur de la contrainte seuil (croisement des courbes  $G'$  et  $G''$  respectivement les modules élastique et visqueux). A partir des mesures SAOS, nous introduisons une viscosité  $\mu^*$  définie par  $\mu^* = \frac{\sqrt{G'^2 + G''^2}}{\omega}$ , où  $\omega$  est la fréquence angulaire de l'oscillation en (rad/s). En prenant le temps de diffusion thermique  $\kappa/d^2$  comme échelle de temps, nous pouvons déduire de ce qui précède, une échelle de viscosité :  $\mu = \frac{\tau_y d^2}{\kappa}$ . En introduisant cette échelle de viscosité dans le nombre de Rayleigh (2.1), on trouve  $Ra = 1/Y$  comme paramètre de contrôle.

(ii) Des études rhéométriques récentes (Møller *et al.* (2009); Dimitriou *et al.* (2013); Lidon *et al.* (2017)) ont montré qu'en-dessous de la contrainte seuil, une viscosité instantanée  $\mu^+$  peut être mesurée lors d'essais de fluage. Cette viscosité  $\mu^+$  est définie comme le rapport entre la valeur de la contrainte imposée et la valeur du taux de cisaillement  $\dot{\gamma}$  mesurée. Ces études ont montré que  $\mu^+$  dépend du temps  $\mu^+ \approx t^m$ . Cela signifie qu'en dessous de la contrainte seuil, une valeur constante de la viscosité pour un temps donné peut être définie dans les gels de Carbopol. A ce titre, nous avons réalisé des essais de fluage sur des gels de Carbopol afin de déterminer  $\mu^+$  dans nos systèmes. Dans Métivier *et al.* (2017), nous avons retrouvé la dépendance temporelle  $\mu^+ \approx t^m$  et nous avons déterminé  $m \approx 1$ , dans le cas de nos gels de Carbopol. De la même manière que précédemment, en considérant des échelles caractéristiques pour  $\mu^+$ , nous avons montré que  $1/Y$  est bien le paramètre de contrôle. En réalité,  $\mu^+$  ne représente pas une viscosité réelle mais représente plutôt une traduction macroscopique d'un réarrangement des microgels lorsque le matériau est soumis à une contrainte  $\tau \lesssim \tau_y$  sur des temps longs (Coussot (2018)).

(iii) Le troisième scenario consiste à considérer les gels de Carbopol d'un point de vue microscopique

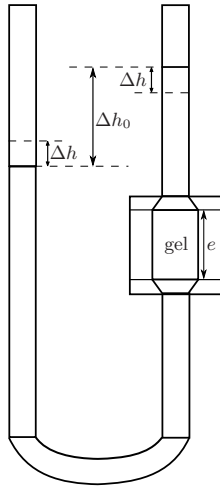


FIGURE 2.1 – Schéma du dispositif de mesure de perméabilité

comme un milieu poreux. En effet, les gels de Carbopol sont des suspensions concentrées, percolées et désordonnées de microgels (taille de l'ordre de  $10 \mu\text{m}$  d'après notamment Oppong *et al.* (2006); Piau (2007)). Schématiquement, les microgels peuvent être considérés comme des éponges élastiques. Les forces colloïdales de surface ne semblent pas dominer leurs comportements en écoulement. Les gels aqueux de Carbopol ont donc une structure de verre mou, c'est à dire une structure désorganisée, amorphe. Dans ce scenario, les microgels seraient la phase solide et le solvant (eau) serait la phase liquide. En effet, Oppong *et al.* (2006); Piau (2007) ont montré que la diffusion brownienne de l'eau est restreinte aux interstices dus à la présence des microgels de Carbopol qui se comportent comme des obstacles. Le mouvement convectif pourrait apparaître en premier dans le bain de solvant imposant alors une contrainte aux microgels qui se transmettrait dans le volume.

Pour explorer ce scenario, nous avons proposé pour la première fois des mesures de perméabilité  $k$  dans des gels de Carbopol (Métivier *et al.* (2017)). La perméabilité est mesurée via l'utilisation de deux tubes capillaires verticaux connectés à la partie haute et basse de l'échantillon de Carbopol (voir Fig. 2.2.2). Ces tubes sont remplis d'eau. La différence de hauteur initiale  $\Delta h_0$  induit une variation de pression  $\Delta P$  et permet ainsi l'écoulement de l'eau à travers le gel considéré comme le milieu poreux dans ce cas. En régime permanent, la perméabilité est donnée par la loi de Darcy :

$$k = \frac{Q\mu e}{S\Delta P} \quad (2.3)$$

où  $Q$  est le débit d'eau qui traverse le milieu poreux,  $\mu$  est la viscosité du solvant (eau) et  $S$  correspond à la section de l'écoulement. Le débit est obtenu en mesurant la variation de hauteur  $\Delta h(t)$  de l'eau dans un tube. La variation de la pression est évaluée comme suit :

$$\Delta P = \rho g(\Delta h_0 - 2\Delta h(t)). \quad (2.4)$$

Nos résultats montrent que  $k = O(10^{-14}) \text{ m}^2$  et  $k \propto \tau_y^{0.2}$  dans les gels de Carbopol associées à un gradient de pression de volume (loi de Darcy). En première approximation, nous avons comparé notre système au problème de Rayleigh-Bénard Newtonien dans un milieu poreux indéformable, configuration de Horton, Rogers & Lapwood (HRL). Dans ce cas, le paramètre de contrôle est le nombre de Rayleigh-Darcy défini par  $Ra_p = (k\rho_l g \beta_l \Delta T d) / (\kappa_l \mu_l)$ , où l'indice 'l' est utilisé pour se référer à la phase 'liquide'. Dans la confi-

guration HRL, le nombre de Rayleigh-Darcy critique obtenu est  $Ra_p = 27.1$ . Nos résultats expérimentaux dans les gels de Carbopol conduisent à  $Ra_p = O(10^{-4})$ , montrant que la comparaison avec la configuration HRL n'est pas adaptée dans le cas des gels. La différence est principalement associée au fait que le milieu poreux constitué de microgels n'est pas indéformable contrairement au problème HRL. Une autre explication serait que les microgels ainsi que la solution sont ionisés et peuvent alors induire des effets supplémentaires tels que effets osmotiques, voire électro-osmotiques. Ces effets peuvent introduire des perméabilité additionnelles à la perméabilité de Darcy. Une étude plus poussée des gels de Carbopol considérés comme un milieu poreux est laissée en perspective.

### 2.2.3 Effets des conditions aux limites

Dans le cas où les parois de la cellule expérimentale présentent du glissement, nous observons expérimentalement qu'une convection oscillatoire a lieu au sein du gel, en-dessous de la valeur critique  $1/Y_c$ . Ce mouvement oscillatoire n'est observé que lorsque les parois de la cavité sont glissantes. Cette étude est décrite à travers le brouillon d'article ci-après. “Oscillatory Rayleigh-Bénard Convection in elastoviscoplastic Carbopol gels” by C. Métivier, M. Darbouli, F. Brochard and A. Magnin.

# Oscillatory Rayleigh-Bénard Convection in elasto-viscoplastic Carbopol gels

C. Métivier,<sup>a)</sup> M. Darbouli,<sup>b)</sup> F. Brochard,<sup>c)</sup> and A. Magnin<sup>b)</sup>

(Dated: 17 December 2018)

Rayleigh-Bénard convection is studied in an elasto-viscoplastic gel, the widespread used and studied Carbopol gel. The transition from conductive to convective regime is determined by the Schmidt-Milverton principle which leads to a critical value of the inverse of the Yield number  $1/Y_c$ . However, an oscillatory motion in the gel is observed below  $1/Y_c \approx 60$  in the only case of slip walls. Particles within the gel describe periodically loops close to their initial positions for  $16.5 < 1/Y < 25$ . For larger values of  $1/Y \approx 50 < 1/Y_c$ , loops are still obtained but particles move away progressively from their initial position. The oscillations take the form of periodic traveling waves (TW). We demonstrate that elastic effects play the major role in the occurrence of oscillations.

PACS numbers:

Keywords: Elasto-viscoplastic fluids, Carbopol gels, Oscillatory Rayleigh-Bénard convection, slip at walls.

In a review of Rayleigh-Bénard convection in viscoelastic fluids in the 1990's, Larson<sup>1</sup> wrote "*viscoelastic effects are unimportant in the linear stability of Rayleigh-Bénard flow, except perhaps under extraordinary conditions*". He would be certainly right because linear stability analyses<sup>2-4</sup> of a viscoelastic fluid layer heated from below show that in most cases a stationary convection is obtained beyond a critical Rayleigh number  $Ra_c$  which value is similar to that of a Newtonian fluid. However, under some specific conditions, an overstable mode can develop, leading to an oscillatory convection below  $Ra_c$ . For a Maxwell fluid, it is shown that the occurrence of such a mode implies high Prandtl number  $Pr$  and a Deborah number, ratio between the relaxation time and the thermal diffusivity time of the fluid, such as  $De \geq 0.03$ . Larson explained that the fluid must have a long relaxation time, the fluid layer height  $d$  must be of several cm and the temperature difference between the two horizontal plates should be around  $\Delta T = 50 K$ . In the unlikely case where oscillations occurred, their frequency would be  $\omega_c < 10^{-3} \text{ Hz}$ . To our knowledge, only one experimental study reported by Kolodner<sup>5</sup> highlights an oscillatory convection in a viscoelastic fluid, a DNA suspension. However, it is not sure that the oscillatory convection is only due to elastic effects. In his study, Kolodner claims that oscillations could also be due to the migration of the DNA polymer in the solution, i.e. that the Soret effect could play an important role. It renewed the interest for the oscillatory convection in (binary) viscoelastic fluids till now.

Elasto-viscoplastic gels can also present significant elastic effects. In addition to viscoelastic effects, they also present an important feature, namely the yield stress  $\tau_y$  below which the gel has a solid-like behavior and above

which it flows with a shear-thinning behavior usually described by the Herschel-Bulkley law  $\tau = \tau_y + K\dot{\gamma}^n$ , where  $\tau$  is the stress,  $\dot{\gamma}$  the shear rate and  $K, n < 1$  are respectively the consistency and the shear-thinning exponent. The yield stress materials, especially concentrated suspensions, promote slip at solid surfaces rather than deformation or shear flow<sup>6,7</sup>. Slip at walls of microgel suspensions has been the subject of extensive experimental and theoretical studies in rheometric flows<sup>8-11</sup>.

The Rayleigh-Bénard convection in viscoplastic fluids has been widely studied<sup>12-17</sup> in the beginning of this century, however theoretical studies never consider elastic yield stress fluids. This is probably because yield stress fluids are usually modeled by inelastic models such as the Bingham and the Herschel-Bulkley ones. Furthermore, it was not clear that elasticity had a major effect on the onset of convection regarding the yield stress effect. In previous experimental studies<sup>15-17</sup>, it is shown that the governing parameter is the ratio between buoyancy and yield stress effects, i.e. the inverse of the Yield number  $1/Y = (\rho g \beta \Delta T d)/\tau_y$ , with  $\rho$  the fluid density,  $g$  the gravitational acceleration,  $\beta$  the thermal expansion coefficient. It is also shown that steady convection in Carbopol gels occurs above the threshold value  $1/Y_c \approx 80$  for no-slip boundaries and that  $1/Y_c$  is smaller for slip boundaries, for instance<sup>15</sup> when  $\tau_y = 0.03 \text{ Pa}$  we get  $1/Y_c \approx 60$ . These studies focus on the determination of  $1/Y_c$  and the characterization of the steady convection. There is no mention to any oscillatory motion below  $1/Y_c$ . In the present paper, we focus on the subcritical conditions and highlight the occurrence of an oscillatory convection in the only case of slip at walls.

We study one Carbopol gel (Carbopol 940 at a weight concentration of 0.047% in distilled water). The rheological features have been presented in a previous paper<sup>15</sup> for no-slip and slip conditions (see Figures 2 and 3 in Darbouli et al.<sup>15</sup>). From a steady state rheometry, we find  $K = 0.26 \text{ Pa.s}^n$ ,  $n = 0.46$  and from SAOS (Small Amplitude Oscillatory Shear) rheometry we obtain an elastic modulus  $G' = 0.77 \text{ Pa}$  and a loss modulus

<sup>a)</sup>Christel.Metivier@univ-lorraine.fr; Laboratoire d'Energétique et de Mécanique Théorique et Appliquée (Université de Lorraine, CNRS), France

<sup>b)</sup>Laboratoire Rhéologie et Procédés - Université (Grenoble Alpes, CNRS), France

<sup>c)</sup>Institut Jean Lamour (Université de Lorraine, CNRS), France

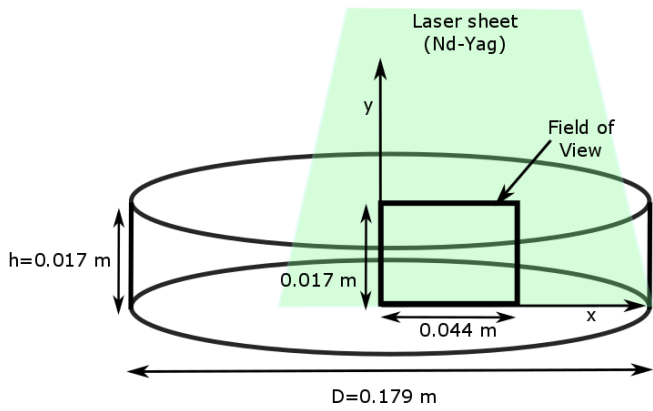


FIG. 1. Scheme of the experimental device

$G'' = 0.23$  Pa. The bulk yield stress has been measured by steady state and SAOS rheometry, in both cases it led to  $\tau_y \approx 0.03 \pm 0.001$  Pa.

As verified by our rheological measurements, the Carbopol gel used in this study is considered as a simple yield stress fluid, in the sense that it does not involve any thixotropic behavior or significant shear-banding<sup>19–21</sup>.

The experimental device, depicted in Fig. 1, is the same as that of our previous studies<sup>15,17</sup>, it consists in a cylindrical cavity which aspect ratio is  $A = D/d = 0.179/0.017 = 10.5$ . The fluid layer is heated from below via a heat flux and cooled from above via a cold water flow, the lateral wall is considered as adiabatic. In addition to previously reported experiments, hollow silver spheres supplied by Dantec<sup>7</sup> (mean radius  $r = 8 \mu\text{m}$ ) have been mixed in the Carbopol gel in order to probe the flow. They are enlightened by a vertical laser sheet (Nd-Yag, with a wavelength of 1064 nm and a thickness of 1mm). It enables us to observe the particles in a vertical plane defined in Fig. 1 by the field of view, it includes the vertical cylinder axis  $y$  (center of the cavity) and the horizontal plates along a radial direction  $x$ .

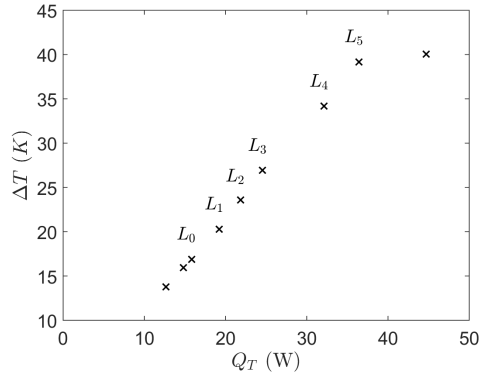


FIG. 2.  $\Delta T$  vs.  $Q_t$  for the Carbopol gel  $\tau_y = 0.03$  Pa - slip boundaries. L0:  $1/Y = 16.5$ , L1:  $1/Y = 17$ , L2:  $1/Y = 23$ , L3:  $1/Y = 25$ , L4:  $1/Y = 41$ , L5:  $1/Y = 55$ , L6:  $1/Y = 61.5$ .

A first way to determine the onset of convection is to use the Schmidt-Milverton principle<sup>23</sup>. It consists in considering  $\Delta T$  vs.  $Q_t$ , the heat flux at the lower plate, as done in Fig. 2 in the case of slip boundaries. The threshold value  $\Delta T_c$  is characterized by a change in the curve slope corresponding to the transition from conductive to convective regime. The Nusselt number  $Nu = Q_t \times d/(S\lambda_c\Delta T)$ , with  $S = \pi D^2/4$  and  $\lambda_c$  the thermal conductivity of the fluid, is also evaluated. For  $\Delta T < \Delta T_c$ , we find that  $Nu \approx 1$  which should confirm that the regime is conductive. In the case of no-slip boundaries obtained by treating every surfaces in the cavity<sup>22</sup>, we have not observed any motion within the gel below the threshold temperature difference  $\Delta T_c$ . However, when walls are untreated (slip walls), the tracking of probe particles in the gel highlights a motion in the gel (see videos in supplementary materials for L0 and L5).

The video data have been processed with the TRACK software<sup>18</sup> from APREX, a PTV software capable of efficiently analyzing data with low Signal-to-Noise ratio. In our case, the best results have been obtained by combining the detection method based on auto-adaptative thresholding techniques with the predictive tracking based on Bayesian methods. As a result, several tens of particles are correctly tracked over the entire videos, making it possible to carry out detailed analysis. The TRACK software provides at each time, the position  $x, y$  and the velocity vector  $v_x, v_y$  of tracked particles. Some trajectories are displayed in Fig. 3. We can observe that trajectories consist in periodic loops with amplitude of displacement of the order of few mm. The particles displacement increases with  $1/Y$ . For small values of  $1/Y$  ( $1/Y < 25$ ), each particle remains close to its initial position and nearly goes back to its initial position after one period. For larger values of  $1/Y$  and still below the critical value, loops are still obtained but a continuous drift is observed, i.e. particles move away progressively from their initial position. The spatial average velocity magnitude denotes amplitudes of the order

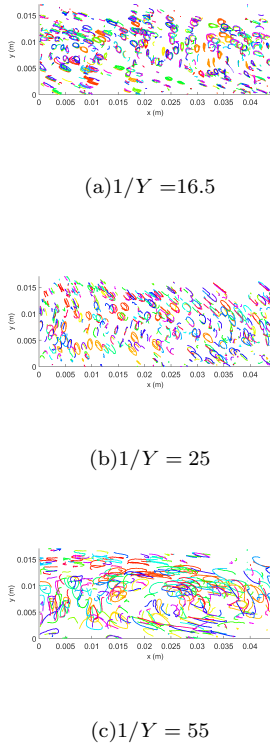


FIG. 3. Trajectories obtained in the gel ( $\tau_y = 0.03$  Pa) for (a)  $1/Y = 16.5$ , (b)  $1/Y = 25$  and (c)  $1/Y = 55$ . One color corresponds to one tracked particle. For a sake of clarity, all tracked particles trajectories are not represented.

of  $10^{-5}$  m/s and an oscillation phenomenon as depicted in Fig. 4. Due to the weak motion, we could expect that the material behaves as a solid (elastic solid or elasto-plastic solid as described by Coussot<sup>24</sup>). However, the evaluation of the angle  $\alpha(\vec{e}_x, \vec{e}_y) = C_{xy}/\sqrt{C_{xx}C_{yy}}$  where  $C_{ij}$  is the right Cauchy-Green tensor components, leads to very large values of deformation of elements which were initially parallel to  $x$  and  $y$  directions. The maximal values of  $\alpha(\vec{e}_x, \vec{e}_y)$  tend to  $\pi/2$ , leading to very large values of strain  $\gamma$  since  $\gamma = \tan \alpha$ . It means that the gel is sheared, i.e. fluidized (liquid-like), rather than only subject to small strain (solid-like). This is confirmed by the evaluation of the strain rate tensor components  $\dot{\gamma}_{ij}$ : the maximal values of the second invariant  $\dot{\gamma}$  is the order of  $10^{-2}$  s<sup>-1</sup> for all values of  $1/Y$  while it increases slightly with  $1/Y$ .

The oscillations observed in Figs. 3 and 4, can be characterized by a spatial average period  $P$  corresponding to the time for a mean particle to describe one loop. As depicted in Fig. 5,  $P$  increases with the increase in  $1/Y$ , with a law  $P \propto 5/Y$ , meaning that one particle takes more time to describe a loop when the buoyancy is increased. This feature is associated to an increase in the distance covered by a mean particle, i.e. around 4-5

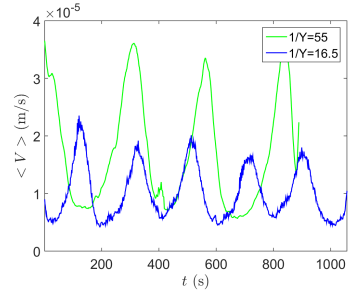


FIG. 4. Spatial average velocity magnitude  $\langle V \rangle$  vs. time for  $1/Y = 16.5$  and  $1/Y = 55$

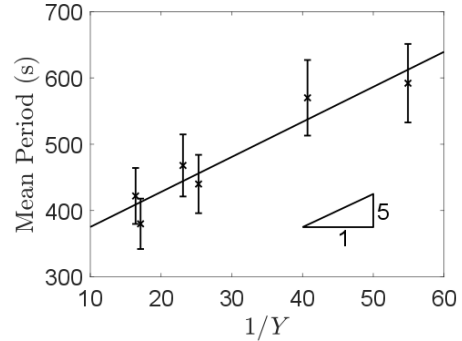


FIG. 5. Spatial average period  $P$  as a function of  $1/Y$

millimeters per period for  $1/Y < 25$  to the order of a centimeter per period for  $1/Y = 55$ . It leads to a space-time averaged particle velocity around  $10^{-5}$  m/s for  $1/Y < 25$  and around  $2.10^{-5}$  m/s for  $1/Y = 55$ .

It is worth noting that the oscillatory regime is characterized by long oscillations period  $P$  and weak velocity amplitude. This motion occurs in a state which would be expected for time-independent conduction. The time-averaged Nusselt number  $Nu$  is consistent with the value that one would expect for steady-state conduction since one obtains  $Nu \simeq 1$  and the fluctuations in  $Nu$  are of the order of few percents. It means that the oscillatory motion within the gel has not a sufficient amplitude to induce a change in heat transfer. A Fourier transform of the time variations of  $Nu$  leads to a frequency of the order of  $10^{-3}$  Hz. This is in agreement with frequencies obtained from the particles velocity fluctuations  $\omega = 1/P$ .

Considering the structure of the flow via the velocity vectors at different time (Fig. 6), we observe the onset of counter-rotative large convective cells. These cells are traveling with time as underlined by the motion of their boundaries (blue or red dashed lines) in Fig. 6. The traveling waves (TW) are also highlighted in Fig. 7 which displays space time diagrams of the vertical velocity  $v_y$  at the horizontal mid-plane of the cavity for different values of  $1/Y$ . The TW periods are similar to the mean period  $P$  which corresponds to the time needed for a particle to describe one loop. These phenomena are clearly correlated. During half a period, a particle can describe

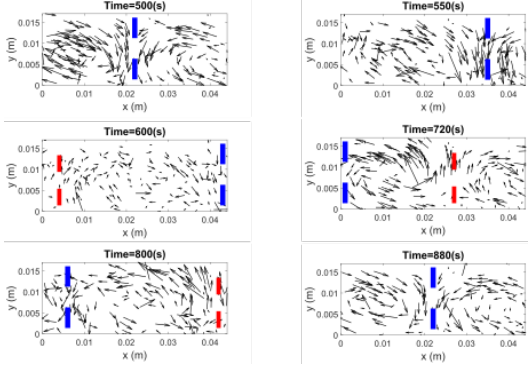


FIG. 6. Velocity vectors during a period for  $1/Y = 16.5$  - Dashed lines: approximate boundaries between two counter-rotative cells, Blue for the lower flow and Red for the upper flow. Oscillations take the form of traveling waves (TW) moving from left to right in this case ( $v_p > 0$ )

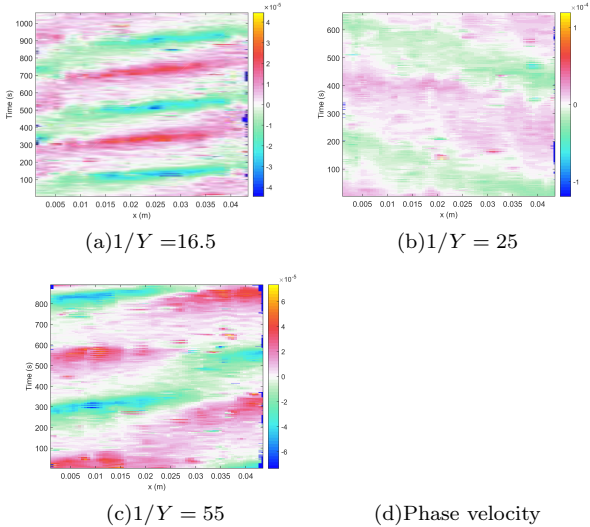


FIG. 7. Space-time diagrams (a)-(c) showing the evolution of the midplane vertical velocity  $v_y$  as a function of location  $x$  obtained in the gel ( $\tau_y = 0.03$  Pa) for (a)  $1/Y = 16.5$ , (b)  $1/Y = 25$  and (c)  $1/Y = 55$ . Phase velocity  $v_p$  (m/s) vs.  $1/Y$  of the TW deduced from space-time diagrams.

half a loop, e.g. in the upward direction, then the direction reverses and the particle goes downward and reaches nearly its initial position at one period. This is in agreement with the directions of the velocity vectors in Fig. 6 during one period. However, the TW cover larger distances during one period, meaning that the waves should propagate faster than mean particles. This is confirmed by their phase velocity which is found quasi-constant of the order of  $10^{-4}$  m/s as displayed in Fig. 7(d), for all values of  $1/Y$ .

It is worth noting that when  $\Delta T$  (or  $1/Y$ ) is modified, the direction of propagation of the TW reverses, i.e. the pattern corresponds indifferently to left- ( $v_p < 0$ )

or right- ( $v_p > 0$ ) going waves. This has been already observed in DNA suspensions<sup>5</sup>.

The slip boundaries play a key role in the oscillatory convection since such a motion has not been observed with no-slip boundaries. We can assume that the oscillatory motion may be initiated by slippage at walls, especially at horizontal walls where the driven force (or stress) due to buoyancy is maximal. The slippage leads to “*an extreme realization of strain localization where most of the deformation occurs near the confining walls whereas the bulk of the material behaves more or less like a solid body or exhibits negligible deformation*” after Cloître and Bonnecaze<sup>7</sup>. Wall slip favors the oscillation. However, the slippage is not the major effect at play because our results show that the gel is sheared in the volume and not in localized bands.

Oscillations would rather be due to elastic effects. While the Carbopol gels behavior is quite different from a Maxwellian fluid, we can only discuss the magnitude orders of the governing parameters which lead to oscillatory convection in viscoelastic fluids. The relaxation time  $\lambda$  defined in the Maxwell model corresponds in the linear regime to the ratio between the viscosity  $\mu$  of the fluid and the elastic modulus  $G'$ . Close to the solid-like to liquid-like transition, we consider that the viscosity of Carbopol gels can be scaled<sup>17</sup> by  $\mu = \tau_y \times P$ , since  $P$  is the characteristic time of the observed phenomenon. In this case, we get that  $\lambda = O(10)$  s (for  $P = 500$  s and  $\tau_y = 0.03$  Pa, we find  $\mu \approx 15$  Pa.s and  $\lambda \approx 20$  s). The Deborah number  $De = \lambda \kappa / d^2$  is then  $De = O(10^{-2})$ . Similarly, we obtain that  $Pr = \mu / (\rho \kappa) = O(10^5)$ , which is a very large value. These values orders can correspond to the “extraordinary” conditions determined theoretically in Maxwell fluids<sup>1-4</sup> for slip boundaries. Furthermore, the frequencies of oscillations measured in our experiments are also close to the values evaluated by Larson<sup>1</sup>  $\omega < 10^{-3}$  Hz.

Finally, the analogy to the oscillation convection in Maxwell fluid is valid and tends to demonstrate that elastic effects play the major role in concentrated suspension of microgels subject to heat transfer. Obviously, considering an elasto-viscoplastic model will be the key to describe mechanisms at play. That could answer the question whether the yield stress plays also a role in the occurrence of oscillatory convection in Carbopol gels.

## ACKNOWLEDGMENTS

The authors are really thankful to Laurent Farge and Julien Boisse for their help in the evaluation of the strain and deviation angle. The LRP is part of the LabEx Tec 21 (grant agreement ANR-11-LABX-0030) and of the PolyNat Carnot Institut (grant agreement ANR-11-CARN-030-01).

<sup>1</sup>R.G. LARSON, Rheol. Acta **31**, 213 (1992).

<sup>2</sup>T. GREEN, Phys. Fluids **11**, 1410 (1968).

<sup>3</sup>C.M. VEST, AND V.S. ARPACI, J. Fluid Mech. **36**, 613 (1969).

- <sup>4</sup>M. SOKOLOV, AND R.I. TANNER, Phys. Fluids **15**, 534 (1972).
- <sup>5</sup>P. KOLODNER, J. Non-Newtonian Fluid Mech. **75**, 167 (1998).
- <sup>6</sup>H.A. BARNES, J. Non-Newtonian Fluid Mech. **36**, 85 (1995).
- <sup>7</sup>M. Cloître, and R.T. Bonnecaze, Rheol. Acta **56** (2017).
- <sup>8</sup>S.P. Meeker, R.T. Bonnecaze and M. Cloître, Phys. Rev. Lett **92** 198302 (2004).
- <sup>9</sup>J. Seth, M. Cloître and R.T. Bonnecaze , J. Rheol. **52** 1241 (2008).
- <sup>10</sup>J. Seth, L. Mohan, C. Locatelli-Champagne, M. Cloître and R.T. Bonnecaze , Nat. Mater. **10** 838 (2011).
- <sup>11</sup>A.L Vayssade, C. Lee, E. Terriac, F. Monti, M. Cloître and P. Tabeling, Phys. Rev. E **89** 052309 (2014).
- <sup>12</sup>J. ZHANG, D. VOLA AND I.A. FRIGAARD, J. Fluid Mech. **566**, 389 (2006).
- <sup>13</sup>A. VIKHANSKY Phys. Fluids **21** 103103 (2009).
- <sup>14</sup>C. LI, A. MAGNIN AND C. MÉTIVIER Aiche J. **62**(4) 1347 (2016).
- <sup>15</sup>M. DARBOULI, C. MÉTIVIER, J.-M. PIAU, A. MAGNIN, AND A. ABDELALI Phys. Fluids **25** 023101 (2013).
- <sup>16</sup>Z. KEBICHE, C. CASTELAIN, AND T. BURGELEA, J. Non-Newtonian Fluid Mech. **203**, 9 (2014).
- <sup>17</sup>C. MÉTIVIER, C. LI AND A. MAGNIN Phys. Fluids **25** 023101 (2017).
- <sup>18</sup>R. Baude and M. Desecures, "TRACK software".  
<http://www.aprex-solutions.com>.
- <sup>19</sup>T. DIVOUX, D. TAMARII, C. BARENTIN, AND S. MANNEVILLE, Phys. Rev. L **104**, 208301 (2010).
- <sup>20</sup>G. OVARLEZ , S. COHEN-ADDA, K. KRISHAN, J. GOYON, AND P. COUSSOT, J.Non-Newtonian Fluid Mech. **193** (2013).
- <sup>21</sup>M. DRINKGREVE , M. FAZILATI, M.M. DENN, AND D. BONN, J. Rheol. **62**(2) (2018).
- <sup>22</sup>C. MÉTIVIER, Y. RHARBI, A. MAGNIN AND A. BOU ABBOU, Soft Matter, **8**, 7365 (2012).
- <sup>23</sup>R.J. SCHMIDT, AND S.W. MILVERTON, Proc. Roy. Soc. (London)A. **152**, (1935).
- <sup>24</sup>P. Coussot, Rheol. Acta **57** (2018).

## 2.3 Convection naturelle dans les fluides rhéofluidifiants

Ma mutation au LEMTA en février 2012 s'est faite de manière naturelle dans la mesure où le LEMTA était partenaire du projet ThIM (ANR) et avait pour rôle de traiter d'un point de vue théorique la RBC dans des fluides rhéofluidifiants. Je me suis donc associée à ces travaux en co-encadrant notamment deux thèses (Mondher Bouteraa et Thomas Varé) avec Chérif Nouar.

J'ai par ailleurs développé une activité expérimentale sur le sujet avec utilisation de l'IRM (Imagerie par Résonance Magnétique) en collaboration avec l'équipe transverse du LEMTA "IRM pour l'ingénierie", en particulier avec Sébastien Leclerc. Dans ce cadre, j'ai été responsable d'une étude post-doctorale entre 2013 et 2014 (M. Darbouli).

### 2.3.1 Introduction

L'effet de la rhéofluidification sur les conditions d'instabilités et leur évolution a été peu examiné malgré un intérêt grandissant pour les fluides non-Newtoniens. Les premières études qui concernent la convection de Rayleigh-Bénard dans des fluides rhéofluidifiants ont été proposées par Pierre & Tien (1963) et Tsuei & Tien (1973). Il s'agissait d'études expérimentales dans lesquelles des corrélations entre le nombre de Nusselt  $Nu$  et les paramètres de contrôle tels que le nombre de Rayleigh  $Ra$ , le nombre de Prandtl  $Pr$  et les propriétés rhéologiques ont été proposées sur une large gamme de valeurs de  $Ra$ , à savoir  $10^3 < Ra < 10^6$ . Le comportement rhéologique des fluides utilisés dans ces études étaient ajustées par des lois puissance. Ce type de modèle présente une singularité lorsque le taux de cisaillement  $\gamma$  tend vers zero, ce qui ne rend pas possible les analyses de stabilité classiques Chi *et al.* (1969).

Lorsque le fluide présente un plateau Newtonien à faibles valeurs de taux de cisaillement tel que le fluide de Carreau, les études expérimentales Liang & Acrivos (1970); Ozoe (1973); Darbouli *et al.* (2016) et théoriques Balmforth & Rust (2009); Albaalbaki & Khayat (2011); Bouteraa *et al.* (2015) notamment indiquent que le nombre de Rayleigh critique est similaire à celui obtenu pour un fluide Newtonien. Au-delà du démarrage de l'instabilité, ces études montrent l'augmentation des transferts thermiques avec l'augmentation du caractère rhéofluidifiant. Une analyse faiblement non linéaire a été développée dans les travaux de Balmforth & Rust (2009); Albaalbaki & Khayat (2011); Bouteraa *et al.* (2015). Dans ces articles, il est montré que pour un faible degré de rhéofluidification caractérisé par  $\alpha = |d\mu/d\Gamma|_{\Gamma=0}$  où  $\Gamma$  représente le deuxième invariant du tenseur des taux de déformations, la bifurcation est surcritique. L'augmentation de la valeur de  $\alpha$  a pour effet de changer la nature de la bifurcation : à partir d'une valeur critique  $\alpha_c$ , la transition devient sous-critique. Dans le cas de conditions limites d'adhérence aux parois, on obtient  $\alpha_c = 2.15 \times 10^{-4}$  et dans le cas de conditions de glissement parfait  $\alpha_c = 24/(601\pi^4)$ .

En outre, l'étude de la sélection des structures thermoconvectives, réalisée par Bouteraa *et al.* (2015), nous a permis de montrer que les rouleaux sont les structures les plus stables en comparaison avec les carrés et les hexagones.

Ces études théoriques ont été réalisées dans le cas de fluide de Carreau dont les propriétés physiques (thermodynamiques et rhéologiques) ne dépendent pas de la température excepté la masse volumique dans le terme de flottabilité (approximation de Boussinesq). Cependant, les fluides non-Newtoniens étant généralement très visqueux, le démarrage de la convection n'est possible que si les différences de température entre les deux plaques horizontales sont importantes. À ce titre, les effets non-Boussinesq ne sont plus négligeables. Pour rendre compte de ces effets, nous avons étendu les travaux de Bouteraa *et al.* (2015) au cas de fluide rhéofluidifiant thermodépendant (thèses de M. Bouteraa et T. Varé). Dans un premier temps, nous ne prenons en compte que la thermodépendance de la viscosité dans l'approche

théorique présentée dans la section 2.3.2. L'étude expérimentale est présentée dans la section 2.3.3.

### 2.3.2 Approche théorique - Cas des fluides rhéofluidifiants thermodépendants

Afin de prendre en compte la thermodépendance des propriétés physiques des fluides rhéofluidifiants au voisinage des conditions critiques, une étude de stabilité faiblement non linéaire, à l'ordre cubique en amplitude, a été réalisée dans le cadre de la thèse de Thomas Varé.

Dans cette partie, on ne considère que la compétition rouleaux-hexagones. L'étude de la compétition rouleaux-carrés montre que dans les rouleaux sont les structures préférées lorsque le rapport des viscosités entre les plaques froide et chaude  $r = \mu_{max}/\mu_{min}$  est tel que  $r < 3$  dans le cas Newtonien et  $r \leq 4$  dans le cas d'un fluide de Carreau. Au-delà de cette valeur de  $r$ , les carrés peuvent être stables. On considère un rapport d'aspect infini. L'approximation de Boussinesq pour la masse volumique est considérée, ceci signifie que la masse volumique ne varie avec la température que dans le terme de flottabilité. Les propriétés rhéologiques du fluide sont décrites par le modèle de Carreau :

$$\mu = \mu_0 [1 + (\lambda \dot{\gamma})^2]^{(n-1)/2} \quad (2.5)$$

où  $\lambda$  correspond au temps de relaxation du fluide,  $n < 1$  est l'indice de rhéofluidification et  $\mu_0$  est la viscosité lorsque le taux de cisaillement est nul  $\dot{\gamma} = 0$  (plateau Newtonien). Le degré de rhéofluidification est défini par :

$$\alpha = |d\mu/d\Gamma|_{\Gamma=0} = \frac{1-n}{2} \frac{\lambda^2 \kappa^2}{d^4}. \quad (2.6)$$

Les variations de viscosité avec la température sont décrites par la relation suivante :

$$\mu_0(T) = \mu_0(T_{ref}) \exp(-K(T - T_{ref})) \quad (2.7)$$

où  $T_{ref}$  est une température de référence prise comme étant la moyenne de température entre les deux plaques horizontales.

La méthode ainsi que les résultats associés à la nature de la bifurcation, la sélection des structures et la gamme des nombres d'onde stables sont détaillés dans une ébauche d'article (voir Annexe A). Dans cet article, une analyse faiblement non linéaire basée sur une approche multiéchelle est développée afin d'aboutir à l'équation d'amplitude de Ginzburg-Landau. Cette dernière équation permet de décrire l'évolution spatio-temporelle de l'amplitude de la perturbation. De manière générale, il s'agit de perturber légèrement le système dans son état purement diffusif stationnaire (régime conductif). Pour celà, une petite perturbation de vitesse, température, pression est ajoutée au système en régime conductif stationnaire. Les différents paramètres du problème (vitesse, température) sont développés en puissance de  $\sqrt{\epsilon}$ , où  $\epsilon = (Ra - Ra_c)/Ra_c$  est l'écart relatif au seuil. Les expressions obtenues sont injectées dans les équations aux perturbations. Un système d'équations différentielles ordinaires est déduit pour chaque ordre. A chaque puissance de  $\epsilon$ , une solution du système est déterminée sous forme d'une série de Fourier. Dans le cas des rouleaux, à l'ordre  $\sqrt{\epsilon}$ , on retrouve le problème linéaire qui permet de déterminer les conditions critiques ainsi que le mode fondamental de la perturbation. L'interaction du fondamental avec lui-même (premier harmonique) et avec son complexe conjugué (première modification de l'état conductif) est donnée à l'ordre  $\epsilon$ . Dans le cas des hexagones, il faut noter que des termes supplémentaires sont obtenus. Cela vient du fait qu'un hexagone est formé par la superposition de trois rouleaux dont les vecteurs d'onde sont décalés d'un angle de  $2\pi/3$ .

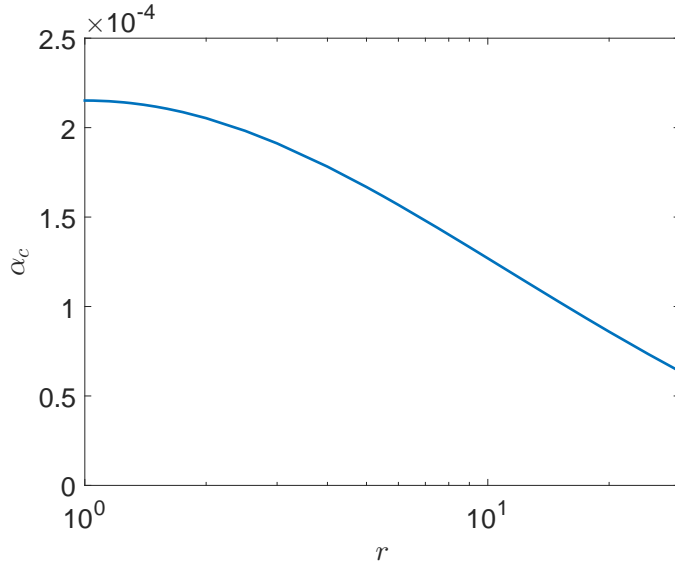


FIGURE 2.2 – Variations de  $\alpha_c$  avec  $r$  dans le cas des rouleaux.

L'équation de Ginzburg-Landau est déduite par application de la condition de solvabilité (alternative de Fredholm) à l'ordre  $\epsilon^{3/2}$ . Si on ne tient pas compte de la modulation spatiale de l'amplitude, on retrouve l'équation de Landau. En particulier, cette équation permet d'étudier la nature de la bifurcation ainsi que la sélection des structures au voisinage des conditions critiques. Des explications plus détaillées sur le principe et l'obtention de l'équation d'amplitude peuvent être trouvées dans les ouvrages de Hoyle (2006); Misbah (2011) ainsi que dans l'ébauche d'article en Annexe A.

### Nature de la bifurcation

Comme indiqué précédemment, dans le cas des rouleaux, la nature de la bifurcation est soit surcritique lorsque  $\alpha < \alpha_c$ , soit sous-critique au-delà de  $\alpha_c$ . Dans le cas où le fluide est thermodépendant,  $\alpha_c$  n'est plus constant mais dépend de  $r$  comme indiqué sur la Figure 2.2. On remarque que pour  $1 < r < 2$ , la variation de  $\alpha_c$  reste faible.

Pour ce qui concerne les hexagones, la thermodépendance a pour effet de briser la symétrie par rapport au plan médian (horizontal), induisant une bifurcation transcritique. Outre cet aspect, la bifurcation du régime conductif au régime convectif pour les hexagones est sous-critique.

### Sélection des structures

Le diagramme de bifurcation concernant les rouleaux et hexagones est indiqué sur la Fig. 2.3 en fonction de l'écart au seuil  $\epsilon$ . On constate que les hexagones sont les structures stables pour  $\epsilon_a < \epsilon < \epsilon_h$ ; pour  $\epsilon_h < \epsilon < \epsilon_r$  les rouleaux et hexagones peuvent co-exister puis lorsque  $\epsilon > \epsilon_r$ , seuls les rouleaux sont stables. Les variations de  $\epsilon_a$ ,  $\epsilon_h$ ,  $\epsilon_r$  en fonction de  $r$  sont données pour différentes valeurs de  $\alpha$  sur la Fig. 2.4. On remarque que la thermodépendance favorise la convection sous forme d'hexagone dans la mesure où le domaine de stabilité des hexagones augmente avec l'augmentation de  $r$  et diminue avec l'augmentation de  $\alpha$ . Ceci peut s'expliquer par un effet de résonance entre les vecteurs d'onde d'une structure hexagonale générée par les termes non linéaires quadratiques. L'interaction du fondamental avec lui-même induit des modes de même longueur d'onde dans le cas des hexagones. A l'inverse, les effets rhéofluidifiants, via l'augmentation de  $\alpha$  ont tendance à favoriser les rouleaux, comme cela avait

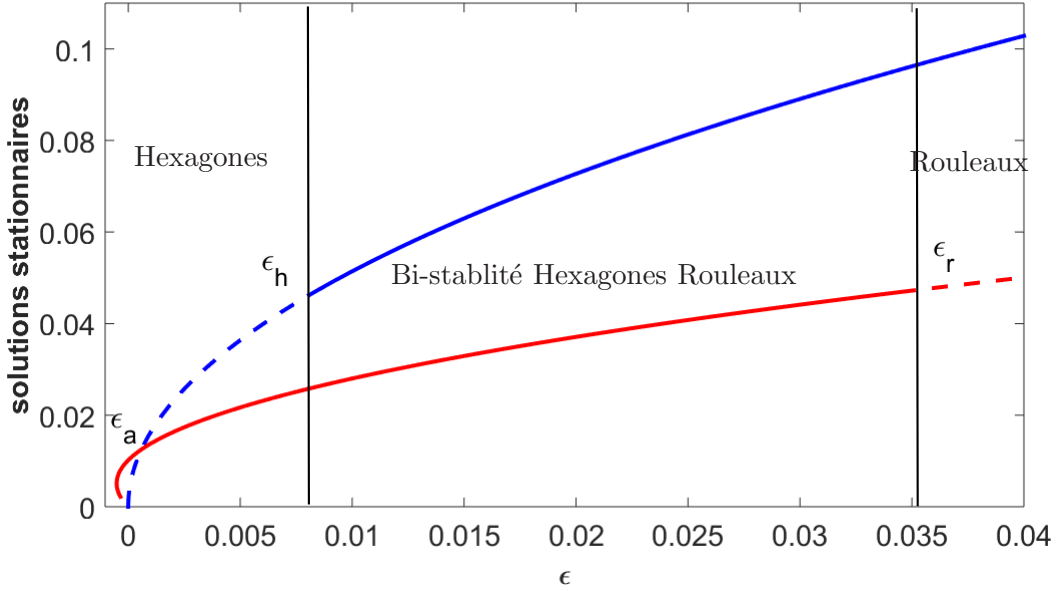


FIGURE 2.3 – Diagramme de stabilité des solutions Hexagones (rouge) et Rouleaux (bleu) obtenu pour  $r = 1.5$  et  $\alpha = 1.5 \times 10^{-4}$ .

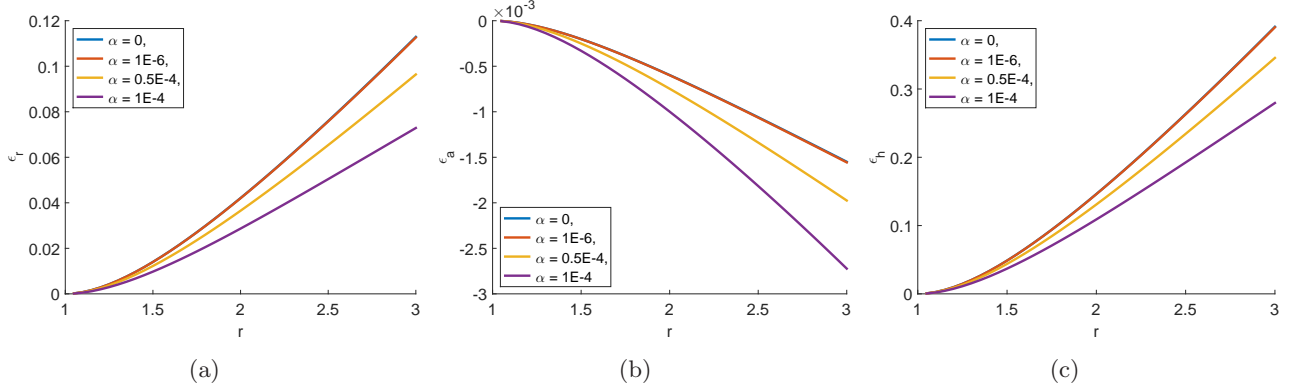


FIGURE 2.4 – Variations de (a)  $\epsilon_r$ , (b)  $\epsilon_a$ , (c)  $\epsilon_h$  en fonction du rapport  $r$ .

déjà été montré par Bouteraa *et al.* (2015). Par ailleurs, le domaine de bi-stabilité est respectivement diminué avec  $\alpha$  qui augmente et augmenté avec  $r$  qui augmente.

### 2.3.3 Approche expérimentale

Cette partie a fait l'objet d'un article Darbouli *et al.* (2016) dans lequel de plus amples détails peuvent être trouvés.

### Matériaux et méthodes

Le fluide utilisé correspond à des solutions aqueuses de xanthane à différentes concentrations massiques de xanthane comprises entre 0.1 et 0.2%. Leurs propriétés rhéologiques, représentées sur la Fig. 2.3.3 sont ajustées par un modèle de Carreau donné par l'Eq. (2.5). Le Tableau 2.1 résume les paramètres obtenus pour les différentes solutions de xanthane étudiées. Les valeurs du degré de rhéofluidification  $\alpha$  sont évaluées, elles sont de l'ordre de  $10^{-7}$  sur la gamme de concentration utilisée. Ces valeurs de  $\alpha$  correspondent à des bifurcations surcritiques dans le cas des rouleaux, d'après Bouteraa *et al.* (2015).

C %	n	$\lambda$ ( $s^{-1}$ )	$\mu_0$ (Pa.s)	$\alpha$	$K$ ( $^{\circ}C$ ) $^{-1}$	$r(\Delta T_c)$
0.1	0.59	4	0.27	$3.7 \cdot 10^{-7}$	0.058	1.25
0.15	0.50	4.2	0.51	$4.96 \cdot 10^{-7}$	0.048	1.37
0.18	0.46	5.4	0.85	$8.8 \cdot 10^{-7}$	0.025	1.31
0.2	0.44	11.4	1.77	$4.3 \cdot 10^{-7}$	0.023	1.65

TABLE 2.1 – Paramètres rhéologiques obtenus pour différentes concentrations de gomme de Xanthane en solution aqueuse.

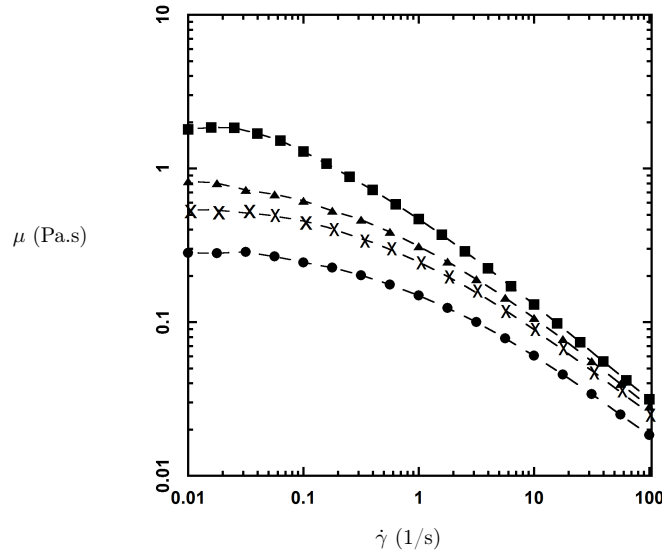


FIGURE 2.5 – Flow curves of the Xanthan gum solutions at  $T = 24^{\circ}C$ . The dashed lines correspond to the Carreau model. ● : 0.1 % Xanthan gum concentration, ✕ : Xanthan 0.15 %, ▲ : Xanthan 0.18 %, ■ : 0.2 % - Figure empruntée à Darbouli *et al.* (2016)

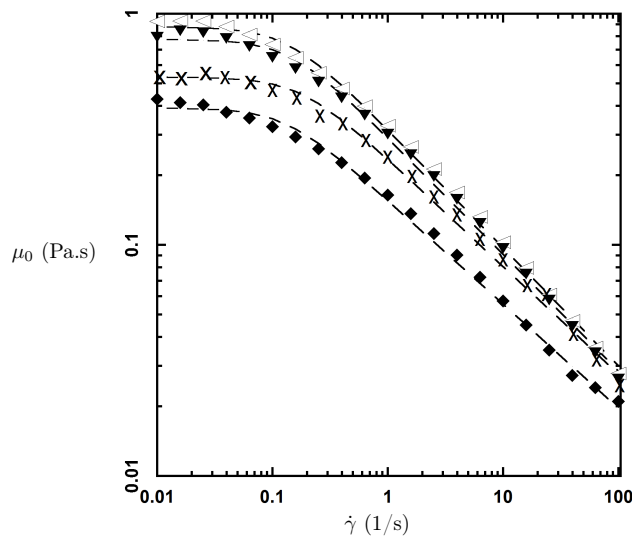


FIGURE 2.6 – Flow curves of the 0.15 % Xanthan solution at different temperatures. ◇ :  $T = 10^{\circ}C$ , ▼ :  $T = 15^{\circ}C$ , ✕ :  $T = 24^{\circ}C$ , ◆ :  $T = 30^{\circ}C$ . The dashed lines correspond to the Carreau model - Figure empruntée à Darbouli *et al.* (2016)

Les variations de la viscosité avec la température sont présentées sur la Fig. 2.6. Ces variations sont principalement gouvernées par la thermodépendance de  $\mu_0$  dont les variations avec la température sont bien décrites par le modèle (2.7). Dans le cadre de nos expérimentations, nous obtenons que le rapport de viscosité évalué au démarrage de la convection est tel que  $r = \mu_{max}/\mu_{min} \leq 2$ , ce qui correspond à la gamme de valeurs de  $r$  déterminée théoriquement où seuls les rouleaux et les hexagones sont stables.

Concernant le dispositif expérimental, la cavité de Rayleigh-Bénard est cylindrique de rapport d'aspect  $A = D/d = 6$  avec  $D = 120$  mm (le diamètre) et  $d = 20$  mm (la hauteur). Les mesures de vitesse ont été réalisées par IRM (Imagerie par Résonance Magnétique).

La technique IRM constitue une méthode non intrusive qui permet d'obtenir rapidement des résultats 2D dans des plans sélectionnés et bien définis mais aussi des résultats 3D. En outre, elle permet d'obtenir des résultats dans des milieux transparents ou opaques, ce qui est un avantage certain sur les techniques classiques.

L'IRM repose sur le principe de Résonance Magnétique Nucléaire (RMN) qui utilise les propriétés quantiques des noyaux atomiques pour la spectroscopie. L'IRM nécessite un champ magnétique  $B_0$  important et homogène produit par un aimant. Cet aimant crée une aimantation  $M$  par alignement des moments magnétiques de spin. Sous l'effet d'une perturbation appropriée, sous la forme d'une onde électromagnétique radiofréquence, l'aimantation  $M$  est écartée de sa position d'équilibre et est animée d'un mouvement de précession autour de la direction  $B_0$  à la fréquence de Larmor  $\nu_0$ , proportionnelle à  $B_0$ . Lorsque  $M$  est basculée dans le plan perpendiculaire à  $B_0$  par un champ magnétique alternatif  $B_1$ , perpendiculaire à  $B_0$ , un signal électrique d'amplitude maximale et de fréquence  $\nu_0$  est détectable aux bornes de la bobine ayant induit  $B_1$ . C'est ce signal qui est mesuré en RMN et IRM au moyen d'une antenne réceptrice.

Dans nos expériences, la vitesse est mesurée par expérience d'imagerie par écho de spin avec encodage de la phase par gradient bipolaire. Le principe d'encodage de la phase est lié au comportement de la phase de l'aimantation transversale (perpendiculaire à  $B_0$ ) en présence de gradients de champs magnétiques. Un gradient de champ a pour effet de modifier la fréquence de rotation des spins en fonction de leur position. Par exemple, les spins localisés à la position  $z(t)$  et soumis à un gradient de champ magnétique  $g_z(t)$  précessent à la fréquence de Larmor  $\nu = \gamma[B_0 + g_z(t)z(t)]$ , où  $\gamma$  correspond au rapport gyromagnétique et est égal à  $26.75 \cdot 10^7$  rad.T $^{-1}$ . s $^{-1}$  pour l'hydrogène. Ceci crée un déphasage  $\Phi$  entre les spins situés à des positions différentes et qui voient un champ magnétique différent lors de l'application du gradient. L'utilisation d'un gradient de forme spécifique dit gradient bipolaire permet d'encoder la vitesse suivant la relation :

$$\Phi = \gamma M_1(t)v(t), \quad (2.8)$$

où  $M_1$  correspond au moment de gradient de champ magnétique et  $v(t)$  est la vitesse.

De plus amples détails concernant le principe de mesure de la vitesse par IRM peuvent être trouvés dans Stapf & Song-I (2006), Rigal (2012).

Les expérimentations sont réalisées avec un imageur Bruker Biospec 24/40 qui possède un aimant supraconducteur horizontal et qui génère un champ magnétique statique de  $B_0 = 2.34$  T, soit une fréquence de résonance du proton de 100 MHz. Son diamètre d'ouverture effectif est de 20 cm. L'antenne dans laquelle le dispositif expérimental est positionné a un diamètre de 16 cm.

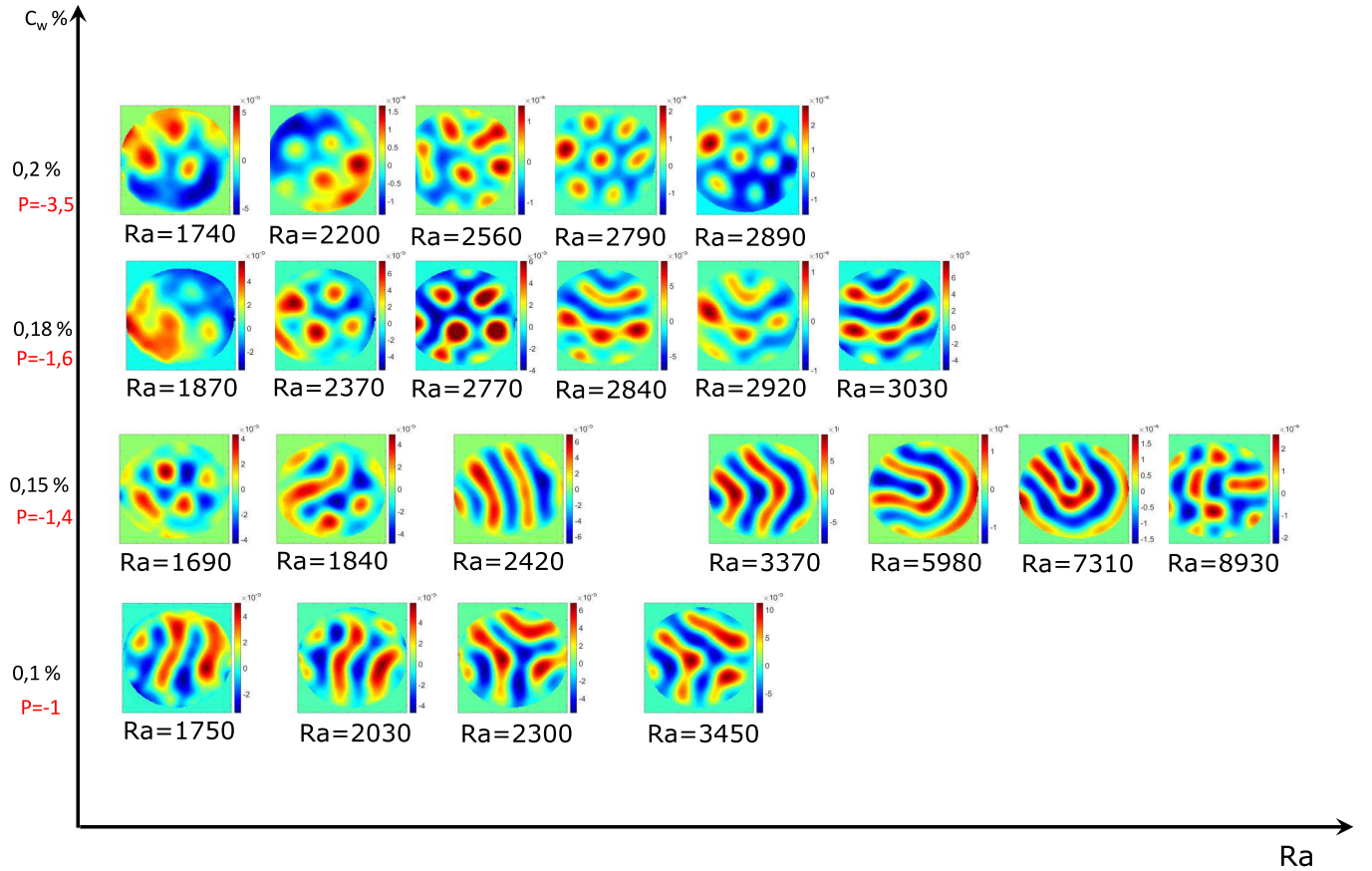


FIGURE 2.7 – Evolution des structures avec le nombre de Rayleigh pour différentes concentrations de Xanthane en solution. Chaque image correspond à la vitesse verticale  $V_z$  représentée dans le plan horizontal médian de la cavité.

## Résultats

Les résultats sont résumés sur la Fig. 2.7 où chaque image correspond aux champs de vitesse vertical  $V_z$  représentés dans le plan horizontal médian de la cavité en fonction du nombre de Rayleigh. Le nombre de Rayleigh est défini avec la viscosité  $\mu_0$  obtenue à taux de cisaillement nul. Le nombre de Rayleigh critique, pour les différentes solutions de xanthane, est bien le même que dans le cas Newtonien ( $Ra_c \approx 1725$  dans le cas d'un rapport d'aspect de 6, d'après Pampaloni *et al.* (1992)), l'erreur maximale obtenue pour les différentes concentrations étant inférieure à 10%. Les structures convectives obtenues sont soit des rouleaux, soit des hexagones. Leur taille est telle que le nombre d'onde  $k$  pour les rouleaux et les hexagones est  $k = 3 \pm 0.3$ , pour toutes les concentrations de xanthane. Cette valeur correspond à la valeur théorique obtenue par une analyse linéaire de stabilité ( $k_c = 3.1$ ) dans le cas des rouleaux et des hexagones. Nous observons que pour de faibles valeurs de concentration de xanthane (0.1 %), les structures qui apparaissent lors du démarrage de l'instabilité sont sous forme de rouleaux. A cette concentration, les rouleaux restent stables lorsque  $Ra$  augmente. Lorsque la concentration en xanthane augmente, nous observons que les structures thermoconvectives qui apparaissent sont des hexagones. On observe que le domaine de stabilité, en termes de valeurs de  $Ra$ , des hexagones augmente avec la concentration. Au-delà de ce domaine de stabilité, nous observons un domaine de bi-stabilité où les hexagones et les rouleaux coexistent puis avec l'augmentation de  $Ra$ , les hexagones disparaissent laissant les rouleaux comme uniques structures. Un résumé, reprenant tous les résultats expérimentaux obtenus, est donné avec la Fig. 2.8 dans le plan  $(\mu_0, \epsilon)$ .

Lorsque la concentration de xanthane augmente, les hexagones sont les structures stables qui appa-

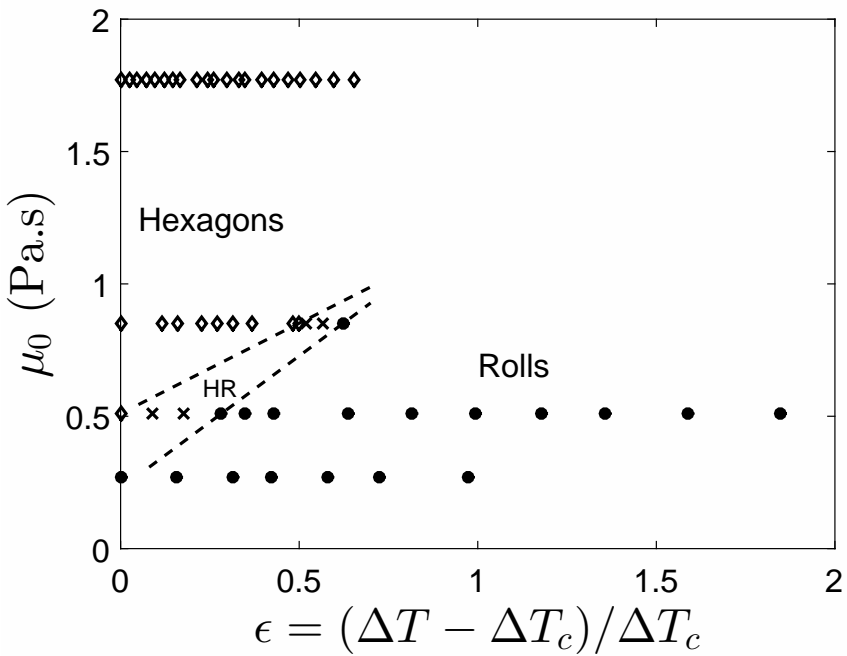


FIGURE 2.8 – Domaines d’existence des structures thermoconvectives (rouleaux et hexagones) dans le plan  $(\mu_0, \epsilon)$  - Résultats expérimentaux obtenus dans le cas de solutions de xanthane.

raissent lors du démarrage de la RBC. Ceci est en accord avec les résultats théoriques dans la mesure où l’augmentation de la concentration implique une augmentation des effets de thermodépendance via  $r$ . Néanmoins, les faibles variations de  $\alpha$  et de  $r$  avec l’augmentation de la concentration (voir tableau 2.1) ne sont pas suffisantes pour expliquer l’augmentation du domaine de stabilité des hexagones. Dans l’article Darbouli *et al.* (2016), nous expliquons que l’apparition des hexagones et l’augmentation de leur domaine de stabilité sont liées aux effets non Oberbeck-Boussinesq (non-OB). En effet, la viscosité  $\mu_0$  augmentant avec la concentration, les différences de température critiques  $\Delta T_c$  augmentent. L’augmentation du caractère non-OB favorise l’apparition des hexagones lors du démarrage de la convection. Ces observations ont aussi été reportées dans le cas de fluides Newtoniens par Busse (1967); Dubois *et al.* (1978); Bodenschatz *et al.* (1991).

Le caractère non-OB peut être évalué via le paramètre  $P$  introduit par Busse (1967) et défini par :

$$P = \sum_{i=0}^4 \delta_i P_i \quad (2.9)$$

où  $\delta_0 = -\Delta\rho/\rho_m$ ,  $\delta_1 = \Delta(\beta\rho)/(2\beta_m\rho_m)$ ,  $\delta_2 = \Delta\mu/\mu_m$ ,  $\delta_3 = \Delta\lambda/\lambda_m$  et  $\delta_4 = \Delta C_p/(C_p)_m$ , l’indice  $m$  désigne la valeur prise à la température  $T_{ref} = 24^\circ\text{C}$ , moyenne de température entre les deux plaques horizontales. Les valeurs  $P_i$  ont été déterminées par Tschammer (1997) en fonction de  $Pr$  dans le cas Newtonien :

$$P_0 = 2.676 - 0.361/Pr, \quad (2.10)$$

$$P_1 = -6.631 - 0.772/Pr, \quad (2.11)$$

$$P_2 = 2.765, \quad (2.12)$$

$$P_3 = 9.540, \quad (2.13)$$

$$P_4 = -6.225 + 0.386/Pr. \quad (2.14)$$

C %	$P$	$\delta_0 P_0$	$\delta_1 P_1$	$\delta_2 P_2$	$\delta_3 P_3$	$\delta_4 P_4$
0.1	-1	0.003	-0.468	-0.643	0.106	0.003
0.15	-1.4	0.004	-0.734	-0.826	0.1625	0.0045
0.18	-1.6	0.008	-1.211	-0.693	0.27	0.006
0.2	-3.5	0.013	-2.71	-1.401	0.627	0.018

TABLE 2.2 – Paramètre de Busse  $P$  et les différentes contributions  $\delta_i P_i$  pour les différentes concentrations de xanthane.

Pour des valeurs de  $P$  négatives (cas des liquides), l'écoulement est ascendant au centre des structures hexagonales Graham (1934); Busse (1967). La valeur de  $P$  calculée aux conditions critiques, ainsi que la contribution des différents termes  $\delta_i P_i$  sont reportées dans le tableau 2.2 pour chaque concentration de xanthane. On remarque bien que  $P$  diminue avec la concentration qui augmente, ce qui traduit une augmentation du caractère non-OB du système. Les deux termes qui contribuent le plus aux effets non-OB sont les termes  $\delta_1 P_1$  et  $\delta_2 P_2$ . Ces termes correspondent respectivement aux variations du coefficient d'expansion thermique  $\beta$  et de la viscosité  $\mu_0$ . On remarque que pour les faibles concentrations de xanthane, c'est à dire en dessous de 0.15%, la contribution principale est liée aux variations de viscosité avec la température. Lorsque les concentrations en xanthane augmentent, les effets non-OB sont plutôt liés aux variations de  $\beta$  avec la température.

## 2.4 Conclusions et perspectives

Les différentes études réalisées sur la convection de Rayleigh-Bénard dans des fluides à seuil et dans des fluides rhéofluidifiants ont permis d'avancer dans la compréhension des mécanismes mis en jeu dans le démarrage de la convection, dans la sélection des structures, l'évolution des perturbations.

Dans les gels de Carbopol, nous avons montré que l'origine du démarrage de la convection était liée au comportement des gels autour de la contrainte seuil. Le paramètre de contrôle peut être construit à partir du nombre de Rayleigh classique dans lequel l'échelle de la viscosité est reliée à la contrainte seuil, que ce soit en considérant le gel comme un matériau élastoviscoplastique (scenario (i)) ou que ce soit en considérant une viscosité instantanée  $\mu^+$  mesurée par fluage en-dessous de la contrainte seuil (scenario (ii)). Le scenario consistant à considérer les gels de Carbopol comme un milieu poreux nécessite de plus amples investigations (scenario (iii)). En réalité, ce scenario représente une approche microscopique plus complexe qu'un milieu poreux indéformable. Pour être mené à bien, il nécessite une compréhension plus fine des phénomènes mis en jeu à cette échelle. Cet aspect représente une perspective.

L'effet des conditions limites a pu être mis en évidence à travers l'observation d'un mouvement oscillatoire en-dessous de la valeur critique  $1/Y_c$  déterminée par le principe de Schmidt-Milverton. Nous avons montré que ce mouvement était principalement lié aux effets élastiques des gels. De plus amples investigations expérimentales sont nécessaires pour mieux comprendre ce phénomène. Nous nous proposons aussi de réaliser une étude numérique considérant la convection de Rayleigh-Bénard dans un fluide élastoviscoplastique pour des parois glissantes mais aussi adhérentes. Cette étude pourra nous permettre d'investiguer l'effet des différentes propriétés rhéologiques (élasticité, contrainte seuil, rhéofluidification) sur le déclenchement des oscillations et/ou le déclenchement de la convection stationnaire.

Dans le cas des fluides rhéofluidifiants, des études théoriques sont menées au voisinage des conditions

critiques. Nous avons considéré des fluides non-thermodépendants dans un premier temps. La prise en compte de la thermodépendance a été réalisée dans une étude faiblement linéaire de stabilité afin de permettre une meilleure comparaison avec nos études expérimentales. Néanmoins, la comparaison demeure encore délicate dans la mesure où des différences fondamentales apparaissent entre nos études théoriques et expérimentales. Il s'agit notamment de l'effet du confinement qui n'est pas pris en compte dans la théorie, ou encore des effets non-OB qui deviennent importants dans nos expérimentations, notamment à travers les variations avec la température du coefficient d'expansion thermique. Une perspective pour permettre une meilleure comparaison avec nos résultats expérimentaux est de réaliser des simulations numériques directes. Cet aspect est en projet actuellement au LEMTA où un code CFD "LS-STAG" est en développement et peut permettre de considérer des fluides incompressibles non-Newtoniens dans des géométries 3D complexes. Des premiers tests ont été réalisés dans le cas de la convection de Rayleigh-Bénard dans un fluide Newtonien.

Dans le cadre d'une analyse faiblement non linéaire, outre la thermodépendance de la viscosité, nous souhaitons prendre en compte les variations du coefficient d'expansion thermique afin d'étudier leurs effets sur la sélection des structures au voisinage des conditions critiques. Pour permettre d'aller bien au-delà des conditions critiques, une approche fortement non linéaire est en cours de réalisation.

Finalement, d'un point de vue expérimental, l'influence du degré de rhéofluidification  $\alpha$  a été peu étudié. Une perspective à ce travail est de considérer des fluides présentant une plus large gamme de valeurs de  $\alpha$ , afin d'observer notamment la transition d'une bifurcation surcritique à une bifurcation sous-critique.

# Chapitre 3

## Projets de recherche

### 3.1 Thermométrie par IRM (MRT)

Lors des premières expérimentations de convection de Rayleigh-Bénard dans des fluides rhéofluidifiants réalisées (Darbouli *et al.* (2016)), seuls les champs de vecteurs vitesse ont été mesurés par IRM. Nous avons cherché à obtenir les champs de température par MRT (Magnetic Resonance Thermometry), technique non développée jusqu'alors au LEMTA. Il s'agit d'une technique qui émerge depuis peu et qui consiste à mesurer la température dans des fluides par IRM (Imagerie par Résonance Magnétique). La technique MRT est assez répandue dans le domaine médical (voir les articles de revue Quesson *et al.* (2000); Rieke & Butts Pauly (2008); Turner & Streicher (2012)). Dans ce domaine, la MRT se fait principalement *in vivo* sur des systèmes au repos (sans écoulement), elle est notamment utilisée pour la thérapie thermique qui induit de grandes variations de température très localisées ne nécessitant pas de grandes résolutions sur les valeurs de température et permettant de réaliser des mesures sur des temps très courts. Malgré les avantages exceptionnels qu'offrent les techniques IRM, la technique MRT n'est quasiment pas développée dans les sciences de l'ingénieur où les problématiques et les systèmes étudiés sont très éloignés du domaine médical. A notre connaissance, il existe très peu d'études Weber & Kimmich (2002); Buchenberg *et al.* (2016); Williams *et al.* (2016); Leclerc & Métivier (2018) dans lesquelles des mesures de température ont été réalisées par IRM. L'étude Weber & Kimmich (2002) présente des résultats qualitatifs sur les écoulements et transferts de chaleur dans une couche d'huile de silicone ou d'éthylène glycol soumise à un gradient thermique vertical pour des grandes variations de température (et grandes valeurs de Rayleigh). Les études Buchenberg *et al.* (2016); Williams *et al.* (2016) traitent l'écoulement d'un mélange eau-agent de contraste dans, respectivement un échangeur thermique et un mélangeur.

Les difficultés liées à la mesure de température par IRM sont que cette dernière est indirecte et dépend essentiellement du système (fluide) étudié. En effet, la mesure de température se fait via la thermodépendance de paramètres physiques du fluide mesurables par RMN (Résonance Magnétique Nucléaire). Trois techniques RMN se distinguent pour évaluer la thermodépendance d'un fluide :

- (i) La sensibilité à la température d'un matériau peut être évaluée à partir de la fréquence de résonance du proton (PRF). Les champs de température peuvent être obtenus en mesurant le changement de phase résultant de la variation de la fréquence de résonance, cette variation étant due à la température (Hindman (1966); Ishihara *et al.* (1995); Poorter *et al.* (1995); Shapiro *et al.* (2002)). Cette technique nécessite une référence de phase obtenue à une valeur de température connue. Cette technique est la plus couramment utilisée dans le domaine médical Quesson *et al.* (2000); Rieke & Butts Pauly (2008); Turner & Streicher (2012).
- (ii) Le coefficient de diffusion moléculaire présente une variation linéaire connue avec la température,

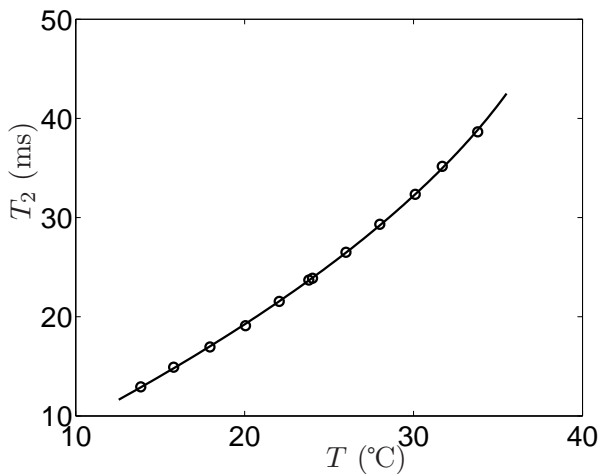


FIGURE 3.1 – Transverse relaxation time  $T_2$  as function of temperature in isothermal conditions. Continuous line : second order polynomial fit.

comme proposée par l'équation d'Einstein :  $D = (k_b T)/(6\pi r \mu)$ , où  $k_b$  représente la constante de Boltzmann,  $T$  est la température absolue,  $r$  correspond au rayon des particules fluides soumises au mouvement brownien et  $\mu$  la viscosité du fluide. Cette mesure peut être réalisée par IRM (Delannoy *et al.* (1991)) dans un système au repos. En présence d'écoulement, ce qui est mesuré n'est plus un coefficient de diffusion mais un coefficient de dispersion qui combine les effets d'advection et de diffusion moléculaire. Par conséquent, cette méthode n'est pas indiquée dans le cas d'écoulement.

(iii) La dernière technique consiste à mesurer le temps de relaxation longitudinale  $T_1$  ou le temps de relaxation transversale  $T_2$  (Bloembergen *et al.* (1948); Parker (1984)). La relaxation en Résonance Magnétique Nucléaire (RMN) est le processus par lequel l'aimantation au sein du fluide retourne à son état d'équilibre après avoir été perturbé. Les mesures de temps de relaxation conduisent à des valeurs de température absolue à condition de connaître a priori la corrélation entre temps de relaxation et température. Cette technique n'est pas couramment utilisée dans des applications médicales car la corrélation n'est généralement pas connue dans le cas de tissus biologiques Rieke & Butts Pauly (2008).

En fonction de la méthode choisie, la mesure de température est soit absolue, soit relative nécessitant la comparaison avec une référence obtenue dans des conditions expérimentales identiques et à des instants suffisamment proches Buchenberg *et al.* (2016); Williams *et al.* (2016).

Récemment, nous avons réalisé des mesures de champs de température dans un fluide newtonien, du glycérol en utilisant la méthode (iii), c'est à dire en mesurant le temps de relaxation transversal  $T_2$  au sein du glycérol. La relation temps de relaxation - température n'étant a priori pas connue, une calibration doit être réalisée au préalable, elle est représentée sur la Figure 3.1. Cette étude est décrite en détail dans l'article Leclerc & Métivier (2018). Dans cet article, nous montrons que dans le régime conductif, les mesures de température sont en très bon accord avec la théorie. Dans le régime convectif, les champs de température et de vitesse obtenus par IRM sont en accord en termes de structure d'écoulement, comme on peut le constater sur la Figure 3.2. Pour tous nos résultats, nous obtenons des incertitudes sur la température inférieures à 1 °C.

Par la suite, nous avons réalisé des essais expérimentaux afin d'étendre la mesure de température par IRM au cas des solutions de xanthane. Ces solutions étant principalement aqueuses, les temps de relaxation sont bien plus grands que dans le cas du glycérol. La conséquence est que les temps nécessaires

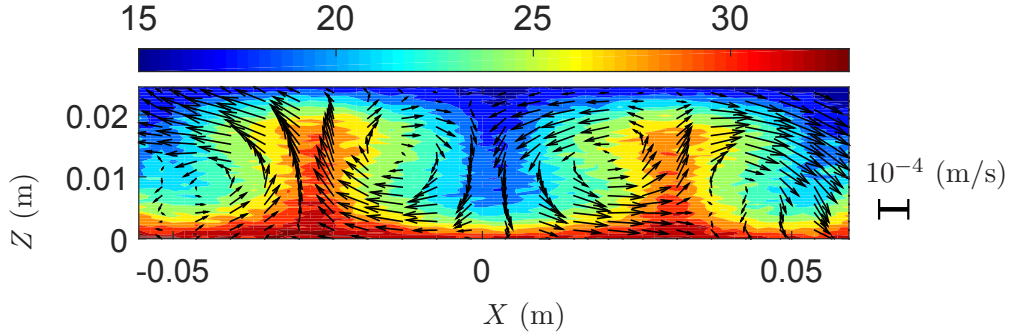


FIGURE 3.2 – Superposition des vecteurs vitesses sur le champ de température (en couleur) dans le cas du glycérol,  $\Delta T = 13.7$ ,  $Ra = 7795$ .

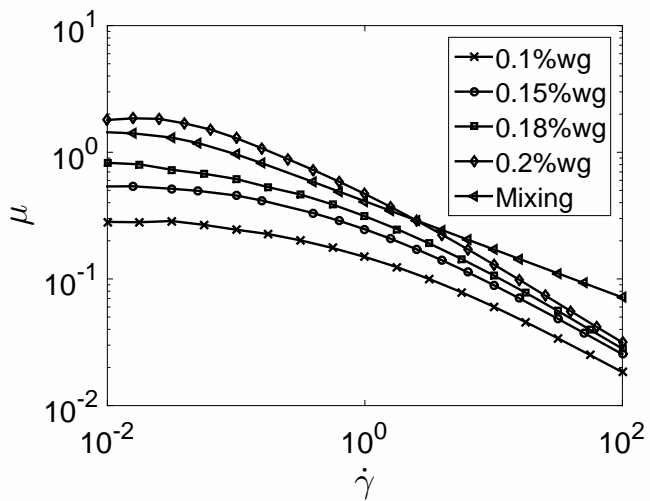


FIGURE 3.3 – Viscosité vs. taux de cisaillement de différentes solutions de xanthane et du mélange xanthane - glycérol ('mixing')

à la mesure de  $T_1$  ou  $T_2$  sont augmentés. La durée de la mesure augmentée combinée au mouvement des particules ont pour effet de réduire la précision de mesure. Généralement, pour pallier à ce genre de difficulté, un agent de contraste tel que le sulfate de cuivre est ajouté au fluide. Néanmoins, dans notre cas, l'ajout d'un agent de contraste modifie très significativement les propriétés rhéologiques des solutions de xanthane. La solution envisagée a été de faire un mélange entre une solution de xanthane (40% en masse) et du glycérol (60 %). La solution de xanthane a été réalisée préalablement, elle correspondait à une concentration de xanthane de 0.2% dans l'eau. Les propriétés rhéologiques de ce mélange sont modifiées par rapport à une solution de xanthane à 0.2 % sans glycérol. Néanmoins, le mélange présente toujours un caractère rhéofluidifiant marqué comme le montre la Figure 3.3. Dans le cas du mélange, la rhéométrie conduit à  $\mu_0 = 1.46$  Pa.s,  $n = 0.62$ ,  $\lambda = 11.4$ ,  $\alpha = 1.2 \cdot 10^{-5}$  et  $K = 0.046 (\text{°C})^{-1}$ .

Les champs de température ont été obtenus via la mesure du temps de relaxation longitudinale  $T_1$ . Bien que la sensibilité soit moins bonne que dans le cas du glycérol pur, des résultats prometteurs ont été obtenus en convection naturelle. Par exemple, la Figure 3.4 représente une comparaison entre champ de température et de vitesse verticale  $V_z$  dans le plan horizontal médian de la cavité. De même, la Figure 3.5 représente la superposition des vecteurs vitesse sur le champ de température (en couleur). Dans le cas de ce mélange, nous trouvons  $P = -0.8$  pour le paramètre de Busse (Eq. (2.9)), ce qui dénote des effets

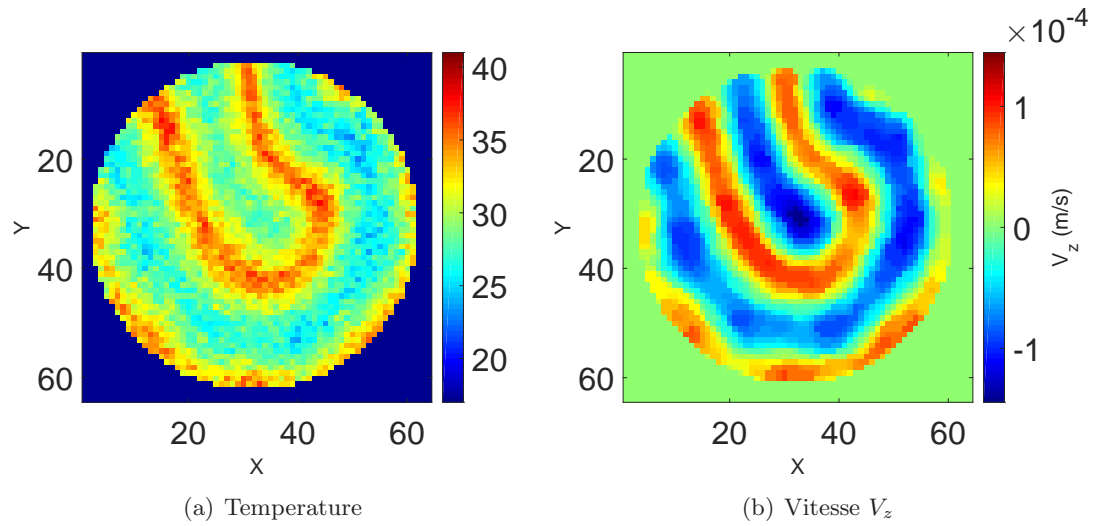


FIGURE 3.4 – Champs de (a) température et de (b) vitesse verticale  $V_z$  dans le plan horizontal médian. Convection dans un mélange solution de xanthane - glycérol,  $\Delta T = 17.5$  et  $Ra = 5090$

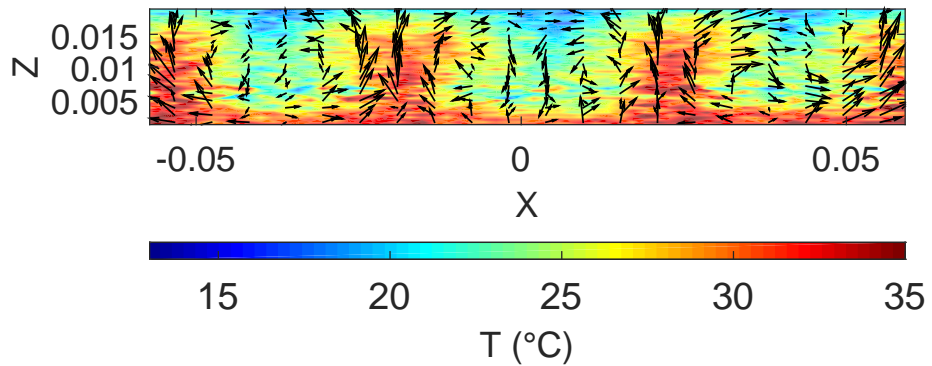


FIGURE 3.5 – Superposition des vecteurs vitesse sur le champ de température (en couleur). Convection dans un mélange solution de xanthane - glycérol,  $\Delta T = 17.5$  et  $Ra = 5090$

non-OB moins importants que dans les cas des solutions de xanthane discutées au chapitre précédent. Des hexagones sont observés au démarrage de la convection ( $Ra = 1660$ ). Lorsque le nombre de Rayleigh est augmenté, à partir de  $Ra = 1805$ , les structures sont sous forme de rouleaux.

Au-delà de l'étude des structures et de leur évolution, nous cherchons aussi à évaluer les transferts thermiques via notamment le nombre de Nusselt défini par :

$$Nu = \int_{\text{plaque}} \frac{\lambda_c (\frac{\partial T}{\partial z})}{\lambda_c (\frac{\partial T_c}{\partial z})} dx dy, \quad (3.1)$$

où  $T_c$  correspond à la solution obtenue en régime conductif,  $\lambda_c$  est la conductivité thermique du fluide, l'intégration est réalisée sur une plaque horizontale (inférieure ou supérieure). La difficulté d'obtenir les transferts thermiques réside dans l'évaluation de la dérivée de la température au niveau de la plaque, où la résolution expérimentale est la plus faible. Nous travaillons actuellement sur ce point.

Le potentiel exceptionnel qu'offre la MRT nous permet d'envisager des mesures simultanées de température et de vitesse dans des systèmes semi-transparents ou opaques. Un système que nous souhaitons explorer, en collaboration avec le Laboratoire de Rhéologie et Procédés (LRP) de Grenoble, concerne des suspensions de billes en solution à différentes concentrations, allant de particules isolées jusqu'à un empilement compact de particules. Cette dernière configuration permettrait notamment d'étudier la convection de Rayleigh-Bénard dans un milieu poreux.

Dans le cadre d'un autre projet, nous souhaitons considérer le cas de matériaux à changement de phase qui est détaillé dans la section suivante. Cette étude fera l'objet d'une collaboration avec le laboratoire ICube de Strasbourg. Elle a fait l'objet d'une réponse à un appel à projet européen.

## 3.2 Convection de Rayleigh-Bénard dans des Matériaux à Changement de Phase

### Objectifs

Un enjeu majeur du 21ème siècle est le stockage de l'énergie du fait de la non-coïncidence de la demande et la production/disponibilité d'énergie thermique (Castell *et al.* (2008); Martinelli (2016)). Cette tendance ne va que s'accentuer avec le développement des énergies renouvelables, aussi bien pour l'énergie solaire que l'énergie éolienne qui sont par nature même extrêmement variables dans le temps. Un réel intérêt s'est porté sur les Matériaux à Changement de Phase (MCP) ces dernières décennies car ces matériaux ont l'avantage de fournir une grande quantité d'énergie pour une faible variation de température, par utilisation de la chaleur latente de changement de phase. Le stockage de l'énergie via l'utilisation des MCP repose sur un principe physique simple : le changement d'état solide-liquide est endothermique, i.e. le matériau absorbe l'énergie, réciproquement le matériau restitue cette énergie lorsque la température de l'environnement est inférieure à sa température de fusion. Les domaines d'application associés aux MCP sont nombreux : ils concernent notamment les capteurs solaires, les réseaux de chaleur, le bâtiment, la régulation thermique corporelle via l'intégration de ces matériaux aux textiles, la climatisation ou le refroidissement... L'utilisation de la chaleur latente (transition de phase liquide/gaz ou solide/liquide dans notre cas) d'un Matériaux à Changement de Phase (MCP), plus que l'énergie sensible (capacité calorifique due à l'augmentation de la température d'un matériau) est une solution intéressante pour le stockage temporaire d'énergie thermique du fait de l'importante énergie échangée lors d'un chan-

gement de phase. Les matériaux de changement de phases se partagent entre (Sharma *et al.* (2009)) : (i) les matériaux organiques de type paraffine. Elles ont le désavantage d'avoir une faible conductivité, mais l'avantage d'avoir une large gamme de température de fusion qui sont fonction des longueurs de chaînes, (ii) les matériaux organiques à bas point de fusion comme certains alcools, glycols ou acides gras, (iii) les matériaux inorganiques comme les sels hydratés. Ceux-ci ont l'avantage d'une importante chaleur latente volumique et une conductivité relativement importante, (iv) les matériaux métalliques. Bien que de nombreuses études se soient concentrées sur les propriétés physiques et l'utilisation des MCP, des verrous demeurent quant à leur utilisation optimale. Actuellement le principal frein au développement de l'utilisation des MCP réside dans la difficulté à extraire/stocker rapidement l'énergie, d'où les nombreux travaux récents sur les échangeurs de chaleur pour les MCP (Martinelli *et al.* (2016); Caron-Soupart *et al.* (2016); Castell *et al.* (2008)). Lors de la fusion ou solidification des MCP, trois zones apparaissent : une zone solide, une zone liquide, et intermédiairement, une zone appelée « *Mushy Zone* » où les deux phases solide/liquide sont en présence. La zone solide peut être particulièrement longue à faire fondre lors de la fusion. Par ailleurs, ces matériaux présentent généralement de relativement faibles valeurs de conductivité thermique, ce qui ne permet pas d'obtenir des transferts thermiques optimaux, lors du processus de déstockage. Une manière d'améliorer les dynamiques de changement de phase et des transferts thermiques est de réaliser le changement de phase en régime convectif.

Le but de ce projet est de comprendre la convection naturelle dans un MCP lors de sa fusion/solidification dans le but de pouvoir l'optimiser. La convection naturelle n'a été que peu étudiée dans les MCP, même si elle constitue l'un des facteurs clés du transfert de chaleur d'après de nombreux auteurs (Martinelli *et al.* 2016, Caron-soupart *et al.* 2016, Castell *et al.* 2007). Cela est certainement lié à la complexité de traiter les couplages entre dynamique, thermique et les différentes phases en présence, notamment expérimentalement. En effet, les MCP peuvent être opaques ou peuvent présenter une variation d'indice de réfraction telle que les techniques optiques classiques sont complexes à utiliser. A ce titre, nous proposons d'**étudier expérimentalement par IRM les transferts de chaleur induits dans des MCP en convection naturelle, dans la configuration de Rayleigh-Bénard**. Nous souhaitons comprendre finement les couplages entre champs de vitesse et de température ainsi que l'évolution spatiale des zones solides et liquides. En particulier, les techniques IRM de mesures simultanées de champs de vitesse et de température développées précédemment seront adaptées au cas des MCP (Darbouli *et al.* (2016); Leclerc & Métivier (2018)). En outre, les phases solides n'étant pas directement visibles par IRM, il sera possible de visualiser leurs contours par différence avec les phases liquides.

Par ailleurs, le couplage hydrodynamique et thermique dépend fortement de la rhéologie du matériau. A ce titre, une étude systématique de la rhéologie des MCP utilisés dans notre étude sera réalisée à différentes températures incluant les températures où le MCP est solide, liquide et proche de la température de fusion (*mushy zone*). Leurs propriétés thermodynamiques seront aussi déterminées dans cette étude.

## Premiers résultats

Des premiers essais ont été effectués avec du stéarate de butyl fourni par Sigma Aldrich (formule linéaire  $CH_3(CH_2)_{16}COO(CH_2)_3CH_3$ ), la température de fusion/solidification indiquée par le fournisseur est  $T_f = 17 - 22^\circ\text{C}$ . La calibration des temps de relaxation avec la température, nous a permis de constater que pour des valeurs de température telles que  $19^\circ\text{C} < T \leq 21^\circ\text{C}$ , des zones solides et liquides sont présentes et que pour  $T < 19^\circ\text{C}$ , le matériau est solide dans tout le volume, ceci nous laisse à penser

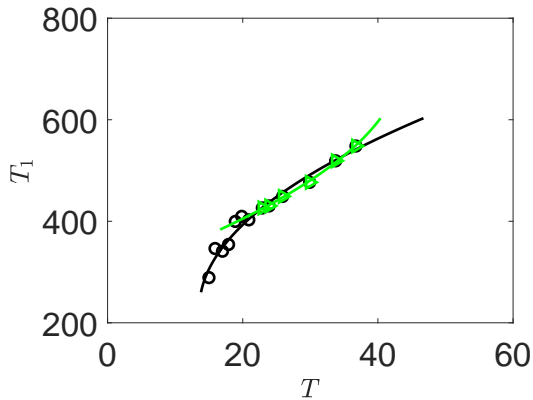


FIGURE 3.6 – Calibration du temps de relaxation  $T_1$  pour différentes valeurs de température. Les courbes correspondent aux modèles ajustés pour  $15^\circ\text{C} < T < 36.8^\circ\text{C}$  (courbe noire), pour les températures  $T > 21^\circ\text{C}$  (courbe verte)

qu'il s'agit d'un mélange de plusieurs corps purs où le changement de température conduit à une variation de la proportion de solide par rapport à celle de liquide. Le choix de la gamme de température pour la calibration des temps de relaxation par IRM est alors essentielle pour la suite. En première approche, nous avons choisi d'ajuster nos données avec une loi polynomiale pour des temps de relaxation obtenus pour  $T > 22^\circ\text{C}$ , soit dans la gamme de température où le matériau est totalement liquide (courbe verte sur la Figure 3.6).

Nous avons réalisé des mesures de masse volumique à différentes températures avec un densimètre DMA™ 4500 d'Anton Paar précis à  $0.00005\text{g/cm}^3$ . Les résultats obtenus sont représentés sur la Figure ???. On remarque que sur la gamme de températures comprises entre  $22$  et  $45$   $^\circ\text{C}$ , les variations de  $\rho$  sont linéaires. Les mesures sont réalisées uniquement en phase liquide, elles nous permettent d'évaluer le coefficient d'expansion thermique  $\beta$  du matériau grâce à la formule suivante :

$$\beta = -\frac{1}{\rho_0} \frac{\partial \rho}{\partial T}, \quad (3.2)$$

où  $\rho_0$  est la masse volumique évaluée à une température de référence  $T_{\text{ref}} = 22^\circ\text{C}$ . Dans notre cas, la dérivée étant constante, on obtient  $\beta \approx 8.3 \cdot 10^{-4} \cdot \text{C}^{-1}$

A ce stade, toutes les propriétés thermodynamiques du stéarate de butyl n'ont pas été mesurées.

Des mesures rhéologiques ont été réalisées avec un rhéomètre AR200 TA Instruments, à des températures telles que le stéarate de butyl est sous forme liquide. Le comportement obtenu est Newtonien, les valeurs de viscosité sont présentées sur la Figure 3.8.

Nous avons réalisé des mesures de temps de relaxation et de vitesse par IRM en convection naturelle. La température moyenne entre les deux plaques horizontales est fixée à  $20.5^\circ\text{C}$  afin de tester la possibilité d'obtenir des résultats lorsque phases solide et liquide sont simultanément présentes.

Les résultats obtenus pour la température sont représentés sur la Figure 3.9 où les zones blanches correspondent aux régions où  $T < 22^\circ\text{C}$ . Nous pouvons constater que les mesures ne nous permettent pas

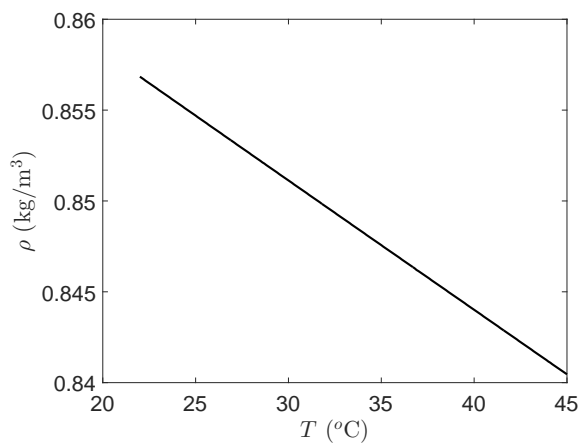


FIGURE 3.7 – Variations de la masse volumique  $\rho$  avec la température - cas du stearate de butyl.

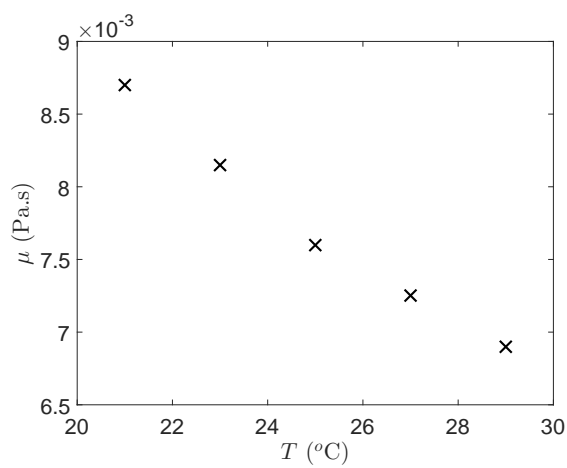


FIGURE 3.8 – Variations de la viscosité  $\mu$  du stéarate de butyl avec la température.

de déterminer de manière réaliste le champ de température dans la phase liquide. En effet, les valeurs maximales de température obtenues dans les zones liquides (zones où  $T > 22^\circ\text{C}$ ) dépassent fortement les valeurs de la température de la plaque chaude. Ces valeurs importantes de température se concentrent principalement à l'interface des phases liquide-solide. Par ailleurs, les champs de température obtenus via  $T_1$  ne nous permettent pas d'identifier des régions de fluide ascendantes (resp. descendantes) comme on peut le constater sur la Figure 3.9, alors que les champs de vitesse montrent clairement des mouvements de convection (Figure 3.10). De nouveaux essais sont nécessaires et seront effectués ultérieurement afin de dépasser ces difficultés lors de la mesure des temps de relaxation.

Comme indiqué précédemment, les mesures de vitesse permettent d'obtenir des résultats plus réalistes. Le traitement des phases est plus aisé dans la mesure où les zones solides sont déterminées là où le signal mesuré est faible (de l'ordre du bruit). Dans ces régions, nous imposons que les composantes de la vitesse soient fixées à la valeur 0. Les zones intermédiaires (mushy zones) pourront être observées en fonction de l'amplitude du signal obtenu, c'est à dire en fonction de la proportion entre phases solide et liquide. Les phases liquides peuvent être déterminées là où le signal est le plus important. La Figure 3.10 montre des champs de vitesse verticale  $V_z$  et horizontale  $V_x$  pour différentes valeurs de  $\Delta T$ . Les résultats montrent que des mouvements de convection sont observés dans une région proche de la paroi inférieure pour  $\Delta T \geq 1.7^\circ\text{C}$ . À travers nos résultats, il est possible de distinguer principalement deux régions : une région présentant des mouvements de convection (proche de la paroi inférieure) et une région, proche de la paroi supérieure, où la vitesse est nulle (en blanc sur la Figure 3.10), où la phase est solide.

Ces premiers essais nous permettent de mettre en évidence de nouveaux aspects à améliorer pour aboutir à nos objectifs. Une première difficulté liée aux mesures de température pourra être contournée en choisissant un matériau présentant une viscosité plus importante lorsque le matériau est liquide afin de travailler à des valeurs de température telles que  $\Delta T \geq 5^\circ\text{C}$  en régime convectif afin de minimiser les intervalles d'erreur sur nos mesures.

Les efforts seront redoublés sur la détermination des champs de température à partir des temps de relaxation. Une calibration plus précise sera effectuée, le régime conductif ( $\Delta T < 0$ ) sera largement étudié.

### 3.3 Action de l'insertion de particules magnétiques dans des fluides à seuil

Un deuxième projet que je souhaite explorer concerne l'action de l'insertion de particules magnétiques en suspension dans un fluide à seuil et soumises à un champ magnétique. La motivation principale provient du fait que la mise en écoulement d'un fluide à seuil n'est pas entièrement résolue. On pourra notamment prendre l'exemple de la mise en écoulement du pétrole initialement au repos lors de son extraction des puits de forage. Les valeurs de contrainte seuil associées au pétrole peuvent être importantes et ainsi nécessitent des puissances mécaniques importantes (pompes) pour permettre l'écoulement du matériau. Cette problématique est généralisable à tout procédé (industriel) nécessitant d'améliorer l'écoulement ou de mettre en écoulement un fluide à seuil pour permettre de l'extraire, de le transporter, de le mélanger, le filtrer etc... La mise en écoulement d'un fluide au repos peut être réalisée en imposant un gradient de pression (pompe par exemple), en poussant, cisaillant le fluide (piston, plaque mobile) ou en **imposant des forces volumiques supplémentaires**. C'est cette dernière solution que nous souhaitons exploiter dans le projet proposé par ajout de particules magnétiques dans un fluide à seuil. Plus précisément,

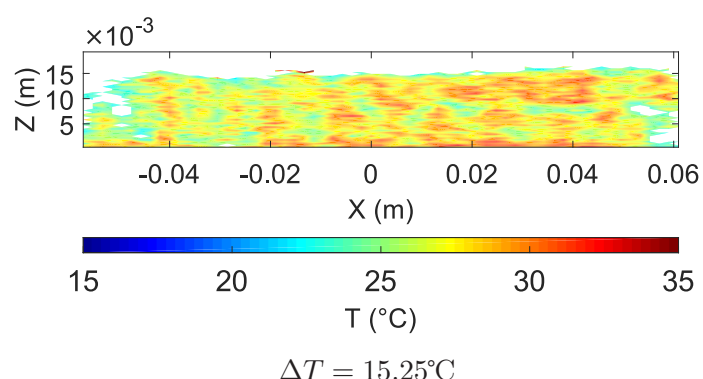
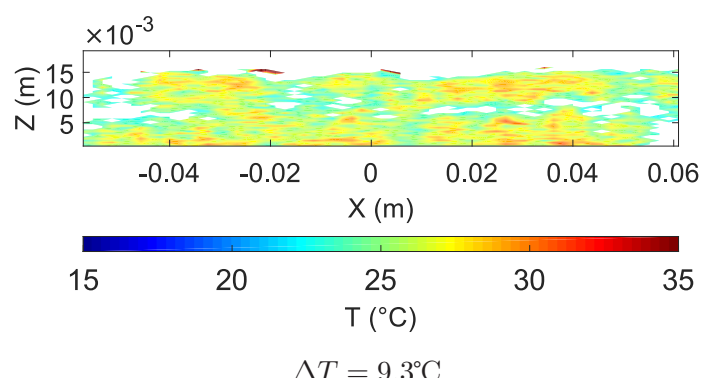
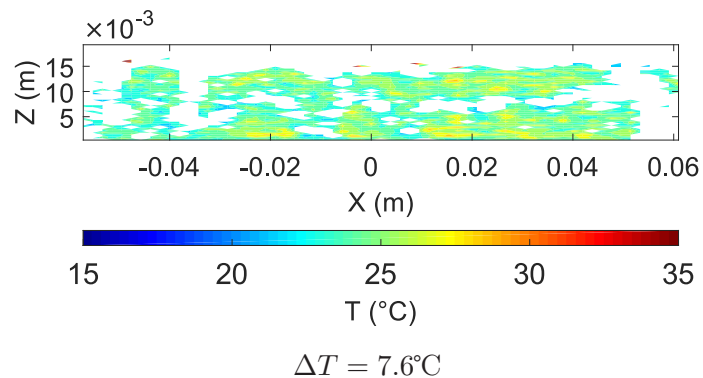
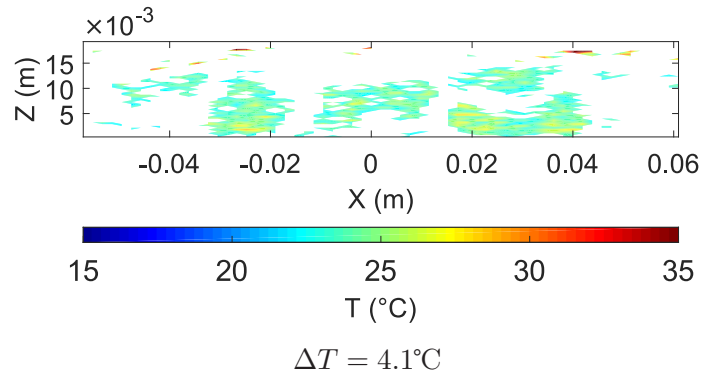


FIGURE 3.9 – Champs de températures pour différentes valeurs de  $\Delta T$  ( de haut en bas  $\Delta T = 4.1 ; 7.6 ; 9.3 ; 15.25 ^{\circ}\text{C}$ ). Les zones blanches sont telles que  $T < 22^{\circ}\text{C}$

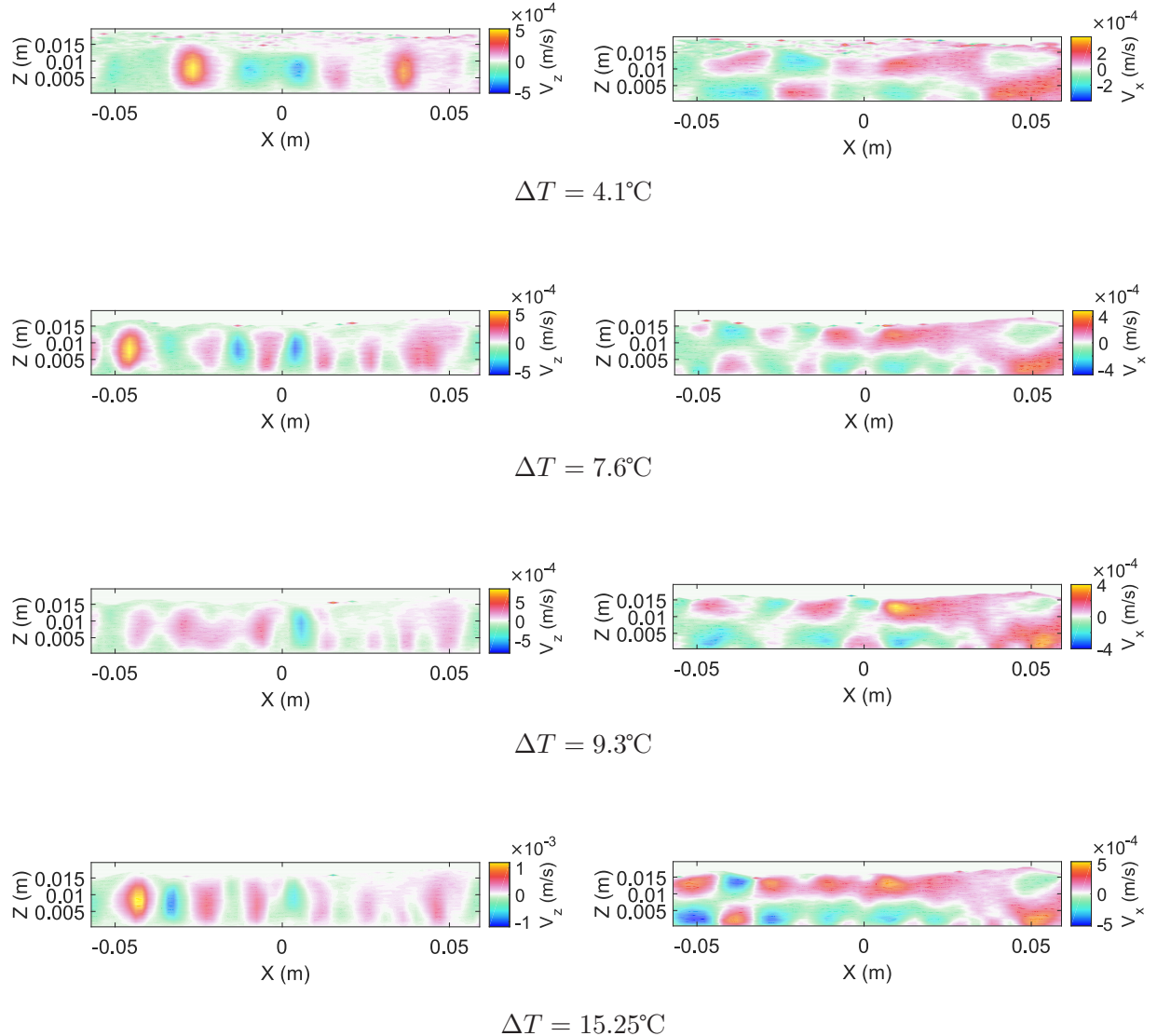
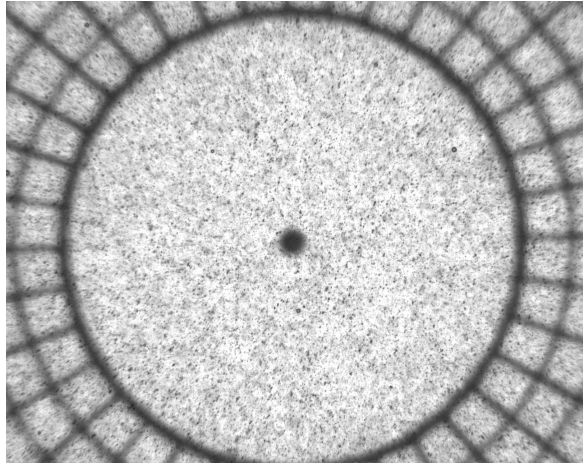
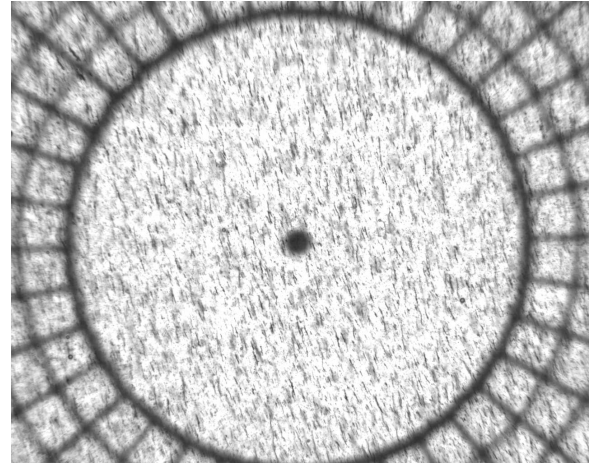


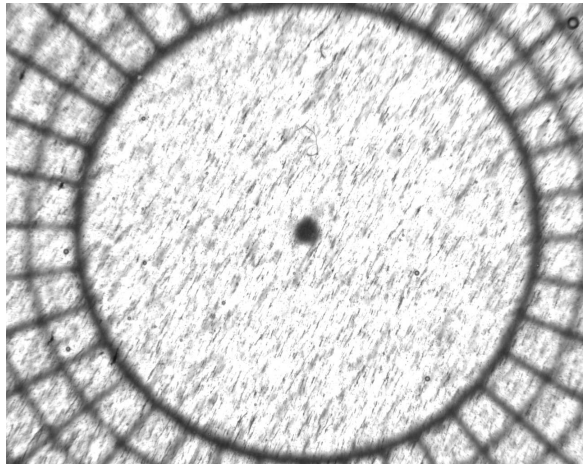
FIGURE 3.10 – Champs de vitesses verticale  $V_z$  (gauche) et horizontale  $V_x$  (droite) à différentes valeurs de  $\Delta T$ .



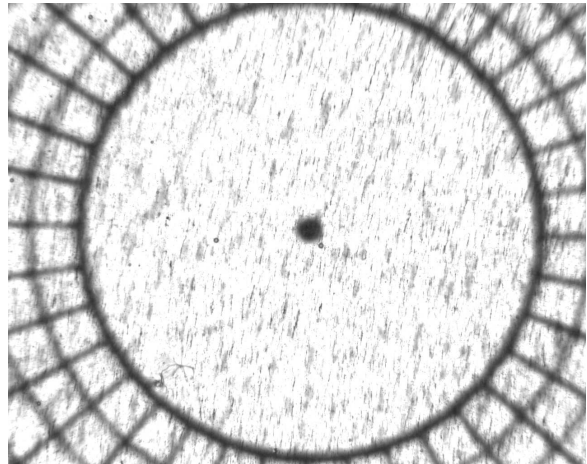
(a)  $B = 0.0075$  T ( $U=1.5$  V)



(b)  $B = 0.0275$  T ( $U=5.5$  V)



(c)  $B=0.04$  T ( $U=8$  V)



(d)  $B = 0.05$  T ( $U=10$  V)

FIGURE 3.11 – Particules magnétiques A en suspension dans du glycérol (concentration massique de 0.06%) et soumises à un champ magnétique tournant à la fréquence  $f = 0.5$  Hz. Un papier (transparent) millimétré circulaire est inséré sous le dispositif.

nous souhaitons exploiter le contrôle du mouvement des particules magnétiques pour **faciliter la mise en écoulement de fluides à seuil** et pour **moduler leurs propriétés rhéologiques**. Le principe consiste à placer des particules magnétiques, i.e. susceptibles d'acquérir une aimantation induite sous l'action d'un champ magnétique extérieur, en suspension dans le gel à des concentrations suffisamment importantes. Soumises à l'action d'un champ magnétique extérieur uniforme, les particules magnétiques en suspension dans un fluide se groupent en chaînes orientées dans la direction du champ magnétique comme représentées sur la Fig. 3.11. Si la direction du champ magnétique change au cours du temps, l'orientation des chaînes suit ce changement de direction et tourne à la même vitesse que la vitesse de rotation du champ.

Le projet consiste en une étude expérimentale et sera complétée par une modélisation numérique magnéto-hydrodynamique multi-échelle prenant en compte l'échelle microscopique (particules magnétiques) et l'échelle mésoscopique (écoulement du fluide). Le dispositif expérimental consiste en une cavité cylindrique de diamètre 35 mm, remplie de fluide dans lequel des particules magnétiques et des particules passives en suspension sont préalablement introduites. Cette cavité est placée dans un stator de moteur électrique cylindrique et opaque. Les bobinages du moteur sont tels que le champ magnétique généré est uniforme. L'alimentation électrique triphasée du stator a été développée au LEMTA ; sa particularité est de fonctionner à des fréquences non standards pour un moteur électrique mais qui conviennent aux be-

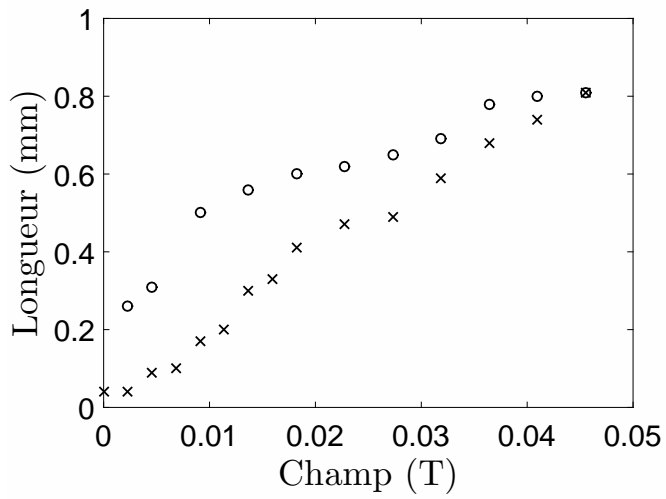


FIGURE 3.12 – Taille des chaînes en fonction de l’intensité du champ magnétique  $B$  lorsque  $B$  augmente ( $\times$ ) et diminue ( $\circ$ ).

soins de l’expérimentation (de l’ordre du Hz). Un fluide modèle transparent est considéré pour permettre l’observation des particules. Les chaînes de particules magnétiques sont donc mises en mouvement par le champ magnétique tournant dont l’intensité du champ ainsi que sa fréquence de rotation peuvent être réglées. L’intensité du champ peut varier de 0 à  $4.55 \cdot 10^{-2}$  T. L’évolution de la dynamique ainsi que l’état des contraintes locales au sein du gel pourront être obtenus via le suivi de particules passives (PTV, PIV). L’état des contraintes locales sera déduit à partir de la corrélation contrainte - déformation (ou taux de cisaillement) obtenue à partir d’une étude rhéométrique en volume.

Ce projet exploratoire nécessite plusieurs compétences telles que la mécanique des fluides, la rhéologie ainsi que l’électromagnétisme. A ce titre, ce projet implique la participation de plusieurs personnes du LEMTA au sein de l’Opération Scientifique “Hydrodynamique et Rhéophysique”, notamment Gérard Vinsard, Stéphane Dufour et Nicolas Louvet. Ma contribution est principalement liée à la mécanique des fluides et la rhéologie que ce soit pour les expérimentations et la modélisation. Par ailleurs, le traitement des images sera réalisé avec l’Institut Jean Lamour et la startup APREX qui ont développé le logiciel TRACK de détection et de suivi automatisé de particules. Ce logiciel est capable de discriminer les particules en fonction de nombreux paramètres, notamment leur taille ou leur intensité lumineuse. TRACK a été développé pour permettre la détection de petites particules (à partir de  $20\mu\text{m}$  environ pour une observation à une distance de 1 mètre) dans des configurations présentant de mauvaises conditions d’illuminations, ou ne permettant pas l’ajout d’un éclairage extérieur. L’utilisation de particules magnétiques de taille ou coloration différentes de celles des particules passives permettra à TRACK de les différencier.

Des résultats préliminaires ont été obtenus dans un fluide Newtonien, le glycérol. Des particules magnétiques, de la ferrite sous forme de poudre, ont été introduites à une concentration massique de 0.06% et 0.03%. La taille d’une particule est inférieure à 0.1 mm, elle n’a pas été mesurée précisément. Par la suite ces particules seront dénommées particules A. Nous constatons sur les Figures 3.11 et 3.12 que la longueur des chaînes formées augmente avec l’intensité du champ  $B$  qui augmente. La longueur moyenne des chaînes est de 0.8 mm pour  $B = 4.55 \cdot 10^{-2}$  T. La décroissance du champ a pour effet de diminuer la taille des chaînes, néanmoins un hystérésis est visible sur la longueur des chaînes comme représenté sur la Fig. 3.12. En effet, les résultats, obtenus en augmentant le champ et en le diminuant, ne se superposent pas à intensité de champ égale.

	Gel à cheveux	Gel hydro-alcoolique
Contrainte seuil $\tau_y$ (Pa)	48.4	2.7
Consistance $K$ (Pa.s $^{-n}$ )	77.9	4.2
$n$	0.4	0.48

TABLE 3.1 – Paramètres rhéologiques des gels étudiés.

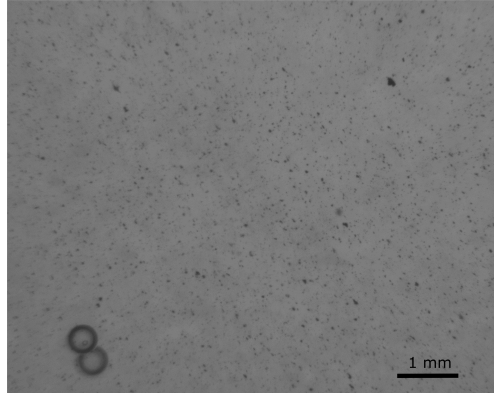


FIGURE 3.13 – Particules A en suspension dans le gel hydro-alcoolique soumises à un champ magnétique d'intensité  $B = 4.55 \cdot 10^{-2}$  T et de fréquence de rotation 0.2 Hz.

Des essais ont aussi été réalisés sur deux gels : un gel hydro-alcoolique (Sanytol) et un gel à cheveux (Freshea Men Wet Look) du commerce. La rhéométrie à température ambiante ( $23.7^\circ\text{C}$ ) montre que les gels se comportent comme un fluide d'Herschel-Bulkley au-dessus de la contrainte seuil. Les paramètres rhéologiques obtenus sont indiqués dans le tableau 3.1.

Deux types de particules de dimensions différentes sont utilisées : les particules A présentées précédemment ainsi que les particules B dont la taille moyenne est d'environ 0.5 mm. Ces particules ont été mélangées aux différents gels à des concentrations en masse de 0.03% pour les particules A et 1% pour les particules B. La fréquence de rotation du champ magnétique est fixée à 0.5 Hz.

Concernant les particules A et B dans le gel hydro-alcoolique, des mouvements oscillatoires des particules ont été observés pour une intensité de champ magnétique de  $4.55 \cdot 10^{-3}$  T. Au-delà de ce champ, la formation de chaînes en rotation ou d'amas de particules a été observée. Les chaînes de particules A obtenues dans le gel hydro-alcoolique ont des tailles moindres que dans le cas du glycérol, comme on peut le constater dans la Figure 3.13.

Dans le cas des particules B, l'augmentation de l'intensité du champ magnétique a pour effet de réduire le nombre de chaînes au sein du fluide mais d'augmenter leur taille. Les chaînes de particules ont une fréquence de rotation proche de celle du champ magnétique. Cette rotation entraîne le cisaillement du gel. Parce que la masse volumique des particules est supérieure à celle du fluide, une fois les chaînes formées et en rotation, nous observons une sédimentation des chaînes de particules au niveau de la paroi inférieure de la cavité. Pour une intensité de  $4.55 \cdot 10^{-2}$  T, une unique chaîne de la taille du diamètre de la cavité est observée comme représentée sur la Figure 3.14. Nous avons parfois observé la fragmentation puis la re-formation de certaines chaînes. Lorsque l'intensité du champ magnétique est diminuée, la chaîne se divise progressivement en deux à trois chaînes. En dessous d'une intensité de champ magnétique de  $2.28 \cdot 10^{-2}$  T, nous observons deux amas de particules comme représentés sur la Figure 3.15. En dessous d'une intensité de champ de  $1.8 \cdot 10^{-2}$  T, ces deux amas sont statiques et restent ainsi formés jusqu'à une intensité de champ nulle.

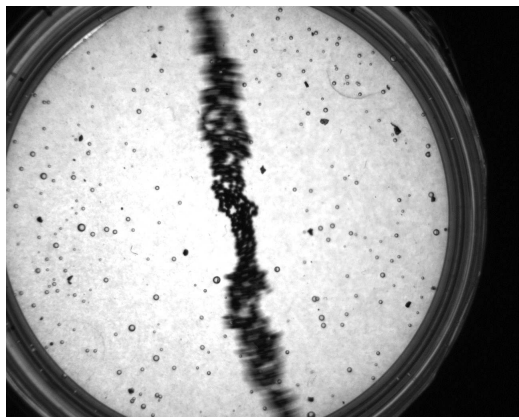


FIGURE 3.14 – Particules B dans le gel hydro-alcoolique soumis à un champ magnétique d'intensité  $4.55 \times 10^{-2}$  T et tournant à une fréquence de 0.5 Hz.

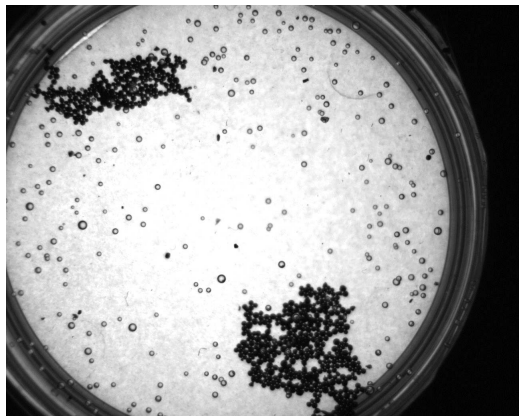


FIGURE 3.15 – Particules B dans le gel hydro-alcoolique soumis à un champ magnétique d'intensité  $2.28 \times 10^{-2}$  T après diminution de l'intensité du champ magnétique, fréquence de rotation du champ fixée à 0.5 Hz.

$H_0$ (T)	$Mn$ (Gel à cheveux)	$Mn$ (Gel hydro-alcoolique)	$Mn$ (glycérol)
$4.55 \cdot 10^{-3}$	1.47	$8.2 \cdot 10^{-2}$	0.1
$9.1 \cdot 10^{-3}$	$3.67 \cdot 10^{-1}$	$2 \cdot 10^{-2}$	$2.5 \cdot 10^{-2}$
$1.1 \cdot 10^{-2}$	$1.63 \cdot 10^{-1}$	$9 \cdot 10^{-3}$	$1.1 \cdot 10^{-2}$
$1.8 \cdot 10^{-2}$	$9.2 \cdot 10^{-2}$	$5 \cdot 10^{-3}$	$6.4 \cdot 10^{-3}$
$2.3 \cdot 10^{-2}$	$5.9 \cdot 10^{-2}$	$3 \cdot 10^{-3}$	$4 \cdot 10^{-3}$
$2.7 \cdot 10^{-2}$	$4.1 \cdot 10^{-2}$	$2 \cdot 10^{-3}$	$2.8 \cdot 10^{-3}$
$3.2 \cdot 10^{-2}$	$3 \cdot 10^{-2}$	$1.7 \cdot 10^{-3}$	$2.1 \cdot 10^{-3}$
$3.6 \cdot 10^{-2}$	$2.3 \cdot 10^{-2}$	$1.3 \cdot 10^{-3}$	$1.6 \cdot 10^{-3}$
$4.1 \cdot 10^{-2}$	$1.8 \cdot 10^{-2}$	$10^{-3}$	$1.3 \cdot 10^{-3}$
$4.55 \cdot 10^{-2}$	$1.5 \cdot 10^{-2}$	$8 \cdot 10^{-4}$	$10^{-3}$

TABLE 3.2 – Nombre de Mason  $Mn$  évalué pour les différents fluides testés.

Lorsque la contrainte seuil est augmentée (cas du gel à cheveux), un mouvement oscillatoire des particules B est observé jusqu'à une intensité de champ magnétique de  $2.28 \cdot 10^{-3}$  T. Au-delà, la rotation des particules est stationnaire. De manière générale, les particules restent isolées, certaines forment des chaînes de deux particules.

Aucun mouvement des particules A n'a été observé dans le gel à cheveux.

Dans le cas des fluides Newtoniens, il a été montré par Melle & Martin (2003); Kang *et al.* (2007); Erb *et al.* (2016), notamment, que sous l'effet d'un champ tournant, des particules magnétiques présentes dans un fluide sont soumises à des forces dipolaires magnétiques permettant la formation de chaînes et à des forces visqueuses ayant pour effet de limiter la formation de chaînes. Le nombre de Mason  $Mn$  traduit la compétition de ces forces, il est défini par :

$$Mn = \frac{\mu\omega}{2\mu_0\mu_l\beta_{lp}^2 H_0^2}, \quad (3.3)$$

où  $\mu$  est la viscosité du fluide,  $\omega = 2\pi f$  est la vitesse de rotation angulaire du champ,  $H_0 = B/\mu_0$ ,  $\mu_0 = 4\pi \cdot 10^{-7}$  Tm/A est la perméabilité du vide,  $\mu_l$  est la perméabilité du liquide (fluide),  $\beta_{lp} = (\mu_p - \mu_c)/(\mu_p + 2\mu_c)$  est le facteur de contraste de perméabilité et  $\mu_p$  la perméabilité de la particule. Melle & Martin (2003); Kang *et al.* (2007) ont montré que les chaînes se forment si  $Mn \ll 1$ . Plus précisément, ils ont montré qu'une chaîne reste stable et ne se déforme quasiment pas pour  $Mn = 0.0005$ , la déformation d'une chaîne stable a lieu pour  $Mn = 0.001$ , pour  $Mn > 0.002$  la chaîne se fragmente puis se rassemble. Finalement, lorsque  $Mn > 0.5$ , la chaîne est immobile et n'est plus affectée par le champ magnétique tournant.

Nous avons évalué  $Mn$  dans le cas de nos expérimentations, les valeurs sont reportées dans le tableau 3.2. Pour les gels, l'échelle de viscosité a été prise comme étant  $\mu = \tau_y/\omega$  où l'échelle de temps est prise comme l'inverse de la vitesse de rotation angulaire du champ et de celle des chaînes. Pour tous les fluides utilisés, nous avons pris  $\mu_l = 1$  Tm/A et  $\beta_{lp} = 1$  ( $\mu_p \rightarrow \infty$  pour des particules de fer).

Nous constatons que :

- Dans le cas des particules A en suspension dans du glycérol, les chaînes se forment pour  $Mn \leq 2.5 \cdot 10^{-2}$ . Les chaînes de particules sont réparties dans tout le volume.
- Dans le cas des particules A et B en suspension dans du gel hydro-alcoolique, un mouvement oscillatoire est observé pour  $Mn = 8.2 \cdot 10^{-2}$ , puis les chaînes se forment et se mettent en rotation pour  $Mn < 2 \cdot 10^{-2}$ . Les particules A forment des chaînes plus petites que dans le cas du glycérol. Dans le cas des particules B, la fragmentation-assemblage de chaîne de particules est aussi observée

pour  $Mn < 2 \cdot 10^{-2}$ .

- Dans le cas des particules B en suspension dans du gel à cheveux, un mouvement oscillatoire est observé pour  $1.47 > Mn > 5.9 \cdot 10^{-2}$ , puis une rotation stationnaire des particules est observée pour  $1.5 \cdot 10^{-2} < Mn < 4.1 \cdot 10^{-2}$ .

Il semble que la valeur de  $Mn$  à partir de laquelle les particules forment des chaînes est de l'ordre de  $Mn = 2 \cdot 10^{-2}$  dans le cas du glycérol et du gel hydro-alcoolique. Dans le cas du gel à cheveux, on observe l'effet de la contrainte seuil qui stabilise le système en limitant la formation de chaînes. En effet, la formation de chaînes de particules n'est pas clairement visible pour des valeurs telles que  $Mn < 1.4 \cdot 10^{-2}$ , alors que dans le cas du gel hydro-alcoolique, des chaînes se forment pour ces valeurs de  $Mn$ .

Ces premiers résultats sont à confirmer dans la mesure où quelques difficultés expérimentales ont été rencontrées, notamment la sédimentation des particules dès lors que des chaînes se forment et cisaillent le gel du fait de leur rotation. Il s'agit notamment de trouver des particules magnétiques sub-millimétriques qui présenteraient une densité proche, voire similaire à celle des fluides utilisés pour éviter la sédimentation comme cela a été observé avec les particules B. Nous souhaiterions aussi améliorer le dispositif produisant le champ source afin d'augmenter l'intensité du champ magnétique au-delà de la valeur maximale actuelle ( $4.55 \cdot 10^{-2}$  T). Par ailleurs, nous n'avons pas trouvé à ce jour de particules passives (traceurs) qui nous permettraient de décrire l'écoulement au sein du fluide. Les particules généralement utilisées pour la PIV ne peuvent pas être utilisées dans cette expérimentation car il n'est pas possible d'éclairer un plan horizontal grâce à une nappe laser.

## Bibliographie

- ALBAALBAKI, BASHAR & KHAYAT, ROGER E 2011 Pattern selection in the thermal convection of non-newtonian fluids. *Journal of Fluid Mechanics* **668**, 500–550.
- BALMFORTH, NEIL J & RUST, ALISON C 2009 Weakly nonlinear viscoplastic convection. *Journal of Non-Newtonian Fluid Mechanics* **158** (1-3), 36–45.
- BLOEMBERGEN, NICOLAAS, PURCELL, EDWARD MILLS & POUND, ROBERT V 1948 Relaxation effects in nuclear magnetic resonance absorption. *Physical review* **73** (7), 679.
- BODENSCHATZ, EBERHARD, DE BRUYN, JOHN R, AHLERS, GUENTER & CANNELL, DAVID S 1991 Transitions between patterns in thermal convection. *Physical review letters* **67** (22), 3078.
- BOUTERA, MONDHER, NOUAR, CHÉRIF, PLAUT, EMMANUEL, MÉTIVIER, CHRISTEL & KALCK, AURÉLIE 2015 Weakly nonlinear analysis of rayleigh–bénard convection in shear-thinning fluids : nature of the bifurcation and pattern selection. *Journal of Fluid Mechanics* **767**, 696–734.
- BUCHENBERG, WALTRAUD B, WASSERMANN, FLORIAN, GRUNDMANN, SVEN, JUNG, BERND & SIMPSON, ROBIN 2016 Acquisition of 3d temperature distributions in fluid flow using proton resonance frequency thermometry. *Magnetic resonance in medicine* **76** (1), 145–155.
- BUSSE, FH 1967 The stability of finite amplitude cellular convection and its relation to an extremum principle. *Journal of Fluid Mechanics* **30** (4), 625–649.

- CARON-SOUPART, ADÈLE, FOURMIGUÉ, JEAN-FRANÇOIS, MARTY, PHILIPPE & COUTURIER, RAPHAËL 2016 Performance analysis of thermal energy storage systems using phase change material. *Applied Thermal Engineering* **98**, 1286–1296.
- CASTELL, ALBERT, SOLÉ, CRISTIAN, MEDRANO, MARC, ROCA, JOAN, CABEZA, LUISA F & GARCÍA, DANIEL 2008 Natural convection heat transfer coefficients in phase change material (pcm) modules with external vertical fins. *Applied Thermal Engineering* **28** (13), 1676–1686.
- CHI, TIEN, TSUEI, HUH SHENG *et al.* 1969 Thermal instability of a horizontal layer of non-newtonian fluid heated from below. *International Journal of Heat and Mass Transfer* **12** (9), 1173–1178.
- COUSSOT, P 2018 Slow flows of yield stress fluids : yielding liquids or flowing solids ? *Rheologica Acta* pp. 1–14.
- DARBOULI, MOHAMED, MÉTIVIER, CHRISTEL, LECLERC, SÉBASTIEN, NOUAR, CHÉRIF, BOUTEERA, MONDHER & STEMMELÉN, DIDIER 2016 Natural convection in shear-thinning fluids : Experimental investigations by mri. *International Journal of Heat and Mass Transfer* **95**, 742–754.
- DARBOULI, MOHAMED, MÉTIVIER, CHRISTEL, PIAU, JEAN-MICHEL, MAGNIN, ALBERT & ABDELALI, AHMED 2013 Rayleigh-bénard convection for viscoplastic fluids. *Physics of Fluids* **25** (2), 023101.
- DAVAILLE, ANNE, GUESLIN, BLANDINE, MASSMEYER, ANNA & DI GIUSEPPE, ERIKA 2013 Thermal instabilities in a yield stress fluid : existence and morphology. *Journal of Non-Newtonian Fluid Mechanics* **193**, 144–153.
- DELANNOY, JOSÉ, CHEN, CHING-NIEN, TURNER, ROBERT, LEVIN, RL & LE BIHAN, DENIS 1991 Noninvasive temperature imaging using diffusion mri. *Magnetic resonance in medicine* **19** (2), 333–339.
- DIMITRIOU, CHRISTOPHER J, EWOLDT, RANDY H & MCKINLEY, GARETH H 2013 Describing and prescribing the constitutive response of yield stress fluids using large amplitude oscillatory shear stress (laostress). *Journal of Rheology* **57** (1), 27–70.
- DUBOIS, M, BERGE, P & WESFREID, J 1978 Non boussinesq convective structures in water near 4° c. *Journal de Physique* **39** (12), 1253–1257.
- ERB, RANDALL M, MARTIN, JOSHUA J, SOHEILIAN, RASAM, PAN, CHUNZHOU & BARBER, JABULANI R 2016 Actuating soft matter with magnetic torque. *Advanced Functional Materials* **26** (22), 3859–3880.
- GRAHAM, A 1934 Shear patterns in an unstable layer of air. *Philosophical Transactions of the Royal Society of London. Series A, Containing Papers of a Mathematical or Physical Character* **232**, 285–296.
- HINDMAN, JC 1966 Proton resonance shift of water in the gas and liquid states. *The Journal of Chemical Physics* **44** (12), 4582–4592.
- HOYLE, REBECCA 2006 *Pattern formation. An introduction methods..* Cambridge University Press.
- ISHIHARA, YASUTOSHI, CALDERON, ARTURO, WATANABE, HIDEHIRO, OKAMOTO, KAZUYA, SUZUKI, YOSHINORI, KURODA, KAGAYAKI & SUZUKI, YUTAKA 1995 A precise and fast temperature mapping using water proton chemical shift. *Magnetic resonance in medicine* **34** (6), 814–823.

KANG, TAE GON, HULSEN, MARTIEN A, ANDERSON, PATRICK D, DEN TOONDER, JAAP MJ & MEIJER, HAN EH 2007 Chaotic mixing induced by a magnetic chain in a rotating magnetic field. *Physical Review E* **76** (6), 066303.

KEBICHE, ZINEDDINE, CASTELAIN, CATHY & BURGHELEA, TEODOR 2014 Experimental investigation of the rayleigh–bénard convection in a yield stress fluid. *Journal of Non-Newtonian Fluid Mechanics* **203**, 9–23.

LECLERC, S & MÉTIVIER, C 2018 MRI temperature and velocity measurements in a fluid layer with heat transfer. *Experiments in Fluids* **59** (2), 34.

LIANG, SF & ACRIVOS, A 1970 Experiments on buoyancy driven convection in non-newtonian fluid. *Rheologica Acta* **9** (3), 447–455.

LIDON, PIERRE, VILLA, LOUIS & MANNEVILLE, SÉBASTIEN 2017 Power-law creep and residual stresses in a carbopol gel. *Rheologica Acta* **56** (3), 307–323.

MARTINELLI, MATTHIEU 2016 Stockage d'énergie thermique par changement de phase—application aux réseaux de chaleur. PhD thesis, Université Grenoble Alpes.

MARTINELLI, MATTHIEU, BENTIVOGLIO, FABRICE, CARON-SOUPART, ADÈLE, COUTURIER, RAPHAËL, FOURMIGUE, JEAN-FRANÇOIS & MARTY, PHILIPPE 2016 Experimental study of a phase change thermal energy storage with copper foam. *Applied Thermal Engineering* **101**, 247–261.

MELLE, SONIA & MARTIN, JAMES E 2003 Chain model of a magnetorheological suspension in a rotating field. *The Journal of chemical physics* **118** (21), 9875–9881.

MÉTIVIER, CHRISTEL, FRIGAARD, IAN A & NOUAR, CHÉRIF 2009 Nonlinear stability of the bingham rayleigh–bénard poiseuille flow. *Journal of Non-Newtonian Fluid Mechanics* **158** (1-3), 127–131.

MÉTIVIER, CHRISTEL, LI, C & MAGNIN, A 2017 Origin of the onset of rayleigh-bénard convection in a concentrated suspension of microgels with a yield stress behavior. *Physics of Fluids* **29** (10), 104102.

MÉTIVIER, CHRISTEL & NOUAR, CHÉRIF 2008 On linear stability of rayleigh–bénard poiseuille flow of viscoplastic fluids. *Physics of Fluids* **20** (10), 104101.

MÉTIVIER, CHRISTEL & NOUAR, CHÉRIF 2009 Linear stability of the rayleigh–bénard poiseuille flow for thermodependent viscoplastic fluids. *Journal of Non-Newtonian Fluid Mechanics* **163** (1-3), 1–8.

MÉTIVIER, CHRISTEL & NOUAR, CHÉRIF 2011 Stability of a rayleigh–bénard poiseuille flow for yield stress fluids—comparison between bingham and regularized models. *International Journal of Non-Linear Mechanics* **46** (9), 1205–1212.

MÉTIVIER, CHRISTEL, NOUAR, CHÉRIF & BRANCHER, J-P 2005 Linear stability involving the bingham model when the yield stress approaches zero. *Physics of fluids* **17** (10), 104106.

METIVIER, CHRISTEL, NOUAR, CHÉRIF & BRANCHER, J-P 2010 Weakly nonlinear dynamics of thermoconvective instability involving viscoplastic fluids. *Journal of Fluid Mechanics* **660**, 316–353.

MISBAH, CHAOUIQI 2011 *Dynamiques complexes et morphogenèse - Introduction aux sciences non linéaires*. Springer-Verlag France.

- MØLLER, PCF, FALL, A & BONN, D 2009 Origin of apparent viscosity in yield stress fluids below yielding. *EPL (Europhysics Letters)* **87** (3), 38004.
- OPPONG, FELIX K, RUBATAT, LAURENT, FRISKEN, BARBARA J, BAILEY, ARTHUR E & DE BRUYN, JOHN R 2006 Microrheology and structure of a yield-stress polymer gel. *Physical Review E* **73** (4), 041405.
- OZOE, H 1973 Hydrodynamic stability and natural convection in newtonian and non-newtonian fluids heated from below. In *AICHE Symposium Series Heat Transfer*, , vol. 69, pp. 126–133.
- PAMPALONI, E, PEREZ-GARCIA, C, ALBAVETTI, L & CILIBERTO, S 1992 Transition from hexagons to rolls in convection in fluids under non-boussinesq conditions. *Journal of Fluid Mechanics* **234**, 393–416.
- PARKER, DENNIS L 1984 Applications of nmr imaging in hyperthermia : an evaluation of the potential for localized tissue heating and noninvasive temperature monitoring. *IEEE transactions on biomedical engineering* (1), 161–167.
- PIAU, JM 2007 Carbopol gels : Elastoviscoplastic and slippery glasses made of individual swollen sponges : Meso-and macroscopic properties, constitutive equations and scaling laws. *Journal of non-newtonian fluid mechanics* **144** (1), 1–29.
- PIERRE, CARL ST & TIEN, CHI 1963 Experimental investigation of natural convection heat transfer in confined space for non-newtonian fluid. *The Canadian Journal of Chemical Engineering* **41** (3), 122–127.
- POORTER, JOHN DE, WAGTER, CARLOS DE, DEENE, YVES DE, THOMSEN, CARSTEN, STÅHLBERG, FREDDY & ACHTEN, ERIC 1995 Noninvasive mri thermometry with the proton resonance frequency (prf) method : in vivo results in human muscle. *Magnetic resonance in medicine* **33** (1), 74–81.
- QUESSON, BRUNO, DE ZWART, JACCO A & MOONEN, CHRIT TW 2000 Magnetic resonance temperature imaging for guidance of thermotherapy. *Journal of Magnetic Resonance Imaging* **12** (4), 525–533.
- RIEKE, VIOLA & BUTTS PAULY, KIM 2008 Mr thermometry. *Journal of magnetic resonance imaging* **27** (2), 376–390.
- RIGAL, CLAIRE 2012 Comportement de fluides complexes sous écoulement : approche expérimentale par résonance magnétique nucléaire et techniques optiques et simulations numériques. PhD thesis, Université de Lorraine.
- SHAPIRO, ERIK M, BORTHAKUR, ARIJITT, SHAPIRO, MICHAEL J, REDDY, RAVINDER & LEIGH, JOHN S 2002 Fast mri of rf heating via phase difference mapping. *Magnetic resonance in medicine* **47** (3), 492–498.
- SHARMA, ATUL, TYAGI, V VEER, CHEN, CR & BUDDHI, DHARAM 2009 Review on thermal energy storage with phase change materials and applications. *Renewable and Sustainable energy reviews* **13** (2), 318–345.
- STAPF, SIEGFRED & SONG-I, HAN 2006 *NRM Imaginf in chemical engineering*. Willey-VCH Verlag GmcH & Co., Weinheim.
- TSCHAMMER, A. 1997 Nichtlineare aspekte der rayleigh-bénard konvektion in isotropen und anisotropen fluiden. PhD thesis, Univ. Bayreuth, Germany.

TSUEI, HUH-SHENG & TIEN, CHI 1973 Free convection heat transfer in a horizontal layer of non-newtonian fluid. *The Canadian Journal of Chemical Engineering* **51** (2), 249–251.

TURNER, ROBERT & STREICHER, MARKUS 2012 Measuring temperature using mri : a powerful and versatile technique.

VIKHANSKY, A 2009 Thermal convection of a viscoplastic liquid with high rayleigh and bingham numbers. *Physics of Fluids* **21** (10), 103103.

WEBER, MARKUS & KIMMICH, RAINER 2002 Rayleigh-bénard percolation transition of thermal convection in porous media : Computational fluid dynamics, nmr velocity mapping, nmr temperature mapping. *Physical Review E* **66** (5), 056301.

WILLIAMS, ELLIOTT T, SPIRNAK, JONATHAN R, SAMLAND, MARC C, TREMONT, BRANT G, MCQUIRTER, ALFRED L, VERHULST, CLAIRE M, VAN POPPEL, BRETT P, BENSON, MICHAEL J, ELKINS, CHRISTOPHER J, BURTON, LAUREN S *et al.* 2016 Magnetic resonance thermometry experimental setup : A portable heat transfer experiment. In *ASME 2016 International Mechanical Engineering Congress and Exposition*, pp. V008T10A094–V008T10A094. American Society of Mechanical Engineers.

ZHANG, J, VOLA, D & FRIGAARD, IA 2006 Yield stress effects on rayleigh–bénard convection. *Journal of Fluid Mechanics* **566**, 389–419.

## Annexe A

# Rayleigh-Bénard convection in thermodependent shear-thinning fluids

Ci-après une ébauche d'article qui concerne l'étude de la convection de Rayleigh-Bénard dans un fluide rhéofluidifiant dont la viscosité  $\mu_0$  dépend de la température par une approche faiblement non linéaire à l'ordre 3.

# Rayleigh-Bénard convection in thermodependent shear-thinning fluids

LEMTA, UMR 7563 CNRS-Université de Lorraine, 2 Avenue de la Forêt de Haye, TSA 60604,  
54518 Vandoeuvre lès Nancy cedex, France

(Received 2 October 2018)

## 1. Introduction

Rayleigh-Bénard convection in a fluid layer which viscosity depends on temperature is an important problem, because of its interest in many industrial and natural systems such as the convection in the Earth mantle and in magma chambers. The viscosity,  $\mu$ , is much lower near the heated lower plate than near the cold upper plate. This spatially varying viscosity modifies the onset of convection. Furthermore, the variation of  $\mu$  with the temperature,  $T$ , causes an additional nonlinear coupling between the velocity and the temperature fields and breaks the up-down reflection symmetry with respect to the midplane of the fluid layer. These features will affect the onset of convection and the selection of the pattern convection.

The effect of a temperature dependent viscosity on the onset of convection was first studied by Palm (1960). Assuming stress-free boundary conditions with a cosine law for the function  $\mu(T)$ , analytical expressions of the critical Rayleigh number,  $Ra_c$ , and wavenumber  $k_c$  are derived. In these expressions,  $Ra_c$  and  $k_c$  differ by  $O(\Delta\mu/\mu_0)^2$  from that obtained with constant viscosity. The Rayleigh number is defined with the viscosity  $\mu_0$  evaluated at the mean of the temperature boundaries, and  $\Delta\mu$  is the viscosity variation between the top and bottom boundaries. It is shown that  $Ra_c$  and  $k_c$  decrease with

increasing the ratio,  $r$ , of the viscosities at the top and bottom plates. Busse & Frick (1985) assumed, for numerical convenience, a linear dependence of the viscosity on temperature. The onset of convection is determined in the case of rigid boundary conditions. The variation of  $Ra_c$  and  $k_c$  as a function of the viscosity ratio  $r$  is quite similar to that obtained by Palm (1960) using cosine law for  $\mu(T)$ . As pointed out by Busse & Frick (1985), for cosine and linear functions  $\mu(T)$ , the viscosity at the midplane equals to the average viscosity of the static layer, this is why  $Ra_c$  decreases with increasing  $r$ . Stengel *et al.* (1982) adopted a more realistic law for  $\mu(t)$ : exponential or superexponential. In this case, the average viscosity exceeds the value used in the definition of  $Ra_c$ . The critical Rayleigh number  $Ra_c$  for fluids with exponential and super-exponential viscosity variation is nearly constant at low values of the viscosity ratio,  $r$ ; increases at moderate values of  $r$ , reaching a maximum at a ratio of about 3000, and then decreases. This behavior is explained by a simple physical argument based on the idea that convection begins first in the sublayer with maximum Rayleigh-number. Whereas, for cosine and linear laws  $\mu(t)$ , the convection occurs throughout the entire fluid layer. The variation of  $Ra_c$  with  $r$ , was checked by Stengel *et al.* (1982) and White (1988) using glycerol and golden syrup respectively as a fluid test. The onset of two-dimensional convection with strongly temperature dependent viscosity has been also considered by Bottaro & Metzener (1992), assuming Arrhenius law. In this case, the viscosity ratio depends on the temperature difference across the fluid layer and on the temperature level, while for exponential law, the viscosity ratio depends only on the temperature difference.

According to Solomatov (1995), when the viscosity ratio exceeds 3000, a stagnant lid regime occurs, where a thick cold boundary layer develops at the top plate. Such regime was observed for  $Ra$  up to  $10^8$  by Davaille & Jaupart (1993).

The effect of weakly temperature-dependent viscosity on the planform near the critical

conditions, has been studied by Palm (1960), Palm *et al.* (1967), Busse (1967). They found that near the onset, the convection occurs in the form of hexagons, when  $r$  is small. The occurrence of hexagonal pattern can be explained by the triadic wavevector interactions enabled by the quadratic term in the amplitude equation. If the Rayleigh number is increased slightly, hexagons become unstable to rolls solution. A formula for the range of Rayleigh numbers where the hexagons are stable was proposed by Palm *et al.* (1967). It is shown that the extent of the interval where the hexagons are stable is proportional to the inverse of the fluid depth to the sixth power. Experimental planform studies performed by Hoard *et al.* (1970) and Stengel *et al.* (1982) confirm qualitatively the results of the weakly nonlinear theory at low values of  $r$ . The quantitative disagreement may be due partly to the influence of the lateral walls and also to the fact that the Rayleigh numbers considered are probably outside the domain of validity of the theory. Besides rolls and hexagons, a new planform in the form of squares was observed when the viscosity contrast between upper and lower boundaries exceed a value of order ten, Stengel *et al.* (1982) and White (1988). The planform selection problem between rolls and squares was analyzed by Busse & Frick (1985) with the assumption that the viscosity varies linearly with temperature. They found that near the critical conditions, rolls are preferred for low values of  $r$ , but squares are preferred for large values of  $r$ . The change from rolls to squares occurs at  $r \approx 2$ . Jenkins (1987) used a weakly nonlinear method to investigate the stability of squares. In the case of a linear variation of the viscosity with temperature, he found that the transition from rolls to squares occurs at  $r \approx 3.2$ . The disagreement with Busse & Frick (1985) was not clarified in the literature. For exponential fluids, Jenkins (1987) found that the transition occurs at  $r \approx 3$ .

To our knowledge, the influence of nonlinear rheology on the pattern selection in the Rayleigh-Bénard convection problem, taking into account the variation of the rheologi-

cal parameters with the temperature, has not been considered in the literature. Shear-thinning fluids are the most kind of non-Newtonian fluids and are characterized by a decreasing viscosity with increasing shear rate. Furthermore, their viscosity may vary strongly with temperature. The decrease of the viscosity with temperature modifies the flow structure. The shear rate is higher near the heated wall. This leads to a further decrease of the viscosity near the heated wall because of the shear-thinning behavior of the fluid. Hence, the degree of asymmetry with respect to the midplane becomes more significant.

The objective of the present paper is to investigate the influence of shear-thinning effects on the nature of the primary bifurcation, the pattern selection and the flow structure, taking into account the dependence of the viscosity on temperature. In this paper, we only consider values of  $r$  sufficiently small that the convective patterns are rolls or hexagons.

This paper is organized as follows. We start with the governing equations in Sec. 2. The linear stability analysis is presented in Sec. 3. In Sec. 4, the weakly nonlinear method is briefly presented, then the nature of the bifurcation, pattern selection and flow structure are described. The Section 5 deals with the wavenumber selection. The results are summarized in Sec.6.

## 2. Basic equations

Hereafter, quantities with hats are dimensional quantities. We consider a layer of shear-thinning fluid of depth  $\hat{d}$  confined between two impermeable horizontal plates, infinite in extent, which are perfect heat conductors. The bottom and top plates are kept at constant temperatures, respectively  $\hat{T}_0 + \delta\hat{T}/2$  and  $\hat{T}_0 - \delta\hat{T}/2$ , with  $\delta\hat{T} > 0$ . The fluid has density  $\hat{\rho}$ , thermal diffusivity  $\hat{\kappa}$ , thermal expansion coefficient  $\hat{\beta}$  and viscosity  $\hat{\mu}_0$  at

zero shear-rate. In the absence of convection, the heat conducting state is described by

$$\hat{\mathbf{u}} = 0 \quad \text{and} \quad \hat{T}_{cond} - \hat{T}_0 = \frac{\delta\hat{T}}{2} \left( 1 - \frac{2\hat{z}}{\hat{d}} \right), \quad (2.1)$$

where  $\hat{\mathbf{u}}$  is the fluid velocity and  $\hat{T}_0$  the mean of the boundary temperatures. The  $z$ -axis is directed upwards, with its origin located at the bottom plate. The stability of the hydrostatic solution is considered by introducing temperature and pressure perturbation as well as a fluid motion. Using the units  $\hat{d}^2/\hat{\kappa}$ ,  $\hat{d}$ ,  $\hat{\kappa}/\hat{d}$  and  $\Delta\hat{T}$  for time, length, velocity and temperature, the dimensionless perturbation equations are:

$$\nabla \cdot \mathbf{u} = 0, \quad (2.2)$$

$$\frac{1}{Pr} \left[ \frac{\partial \mathbf{u}}{\partial t} + (\mathbf{u} \cdot \nabla) \mathbf{u} \right] = -\nabla p + Ra \theta \mathbf{e}_z + \nabla \cdot \boldsymbol{\tau}, \quad (2.3)$$

$$\frac{\partial \theta}{\partial t} + \mathbf{u} \cdot \nabla \theta = \mathbf{u} \cdot \mathbf{e}_z + \nabla^2 \theta. \quad (2.4)$$

Here,  $\mathbf{e}_z$  denotes the unit vector in the vertical direction,  $p(\mathbf{x}, t)$  and  $\theta(\mathbf{x}, t)$  represent the pressure and temperature deviations from their values in the conductive state. The Boussinesq approximations are taken into account, i.e., the variation of the density is neglected except in the buoyancy term. Denote  $(x, y, z)$  the components of the position vector  $\mathbf{x}$ , and  $(u, v, w)$  the components of the velocity vector  $\mathbf{u}$ . The Rayleigh number  $Ra$  and the Prandtl number  $Pr$  are

$$Ra = \frac{\hat{\rho}_0 \hat{g} \hat{\beta} \delta\hat{T} \hat{d}^3}{\hat{\kappa} \hat{\mu}_0} ; \quad Pr = \frac{\hat{\mu}_0}{\hat{\rho}_0 \hat{\kappa}}. \quad (2.5)$$

The reference viscosity,  $\hat{\mu}_0$ , is the zero-shear rate viscosity evaluated at  $\hat{T}_0$ , i.e. the mean of the boundary temperatures.

### 2.1. Rheological model and parameters

The fluid is assumed to be purely viscous and shear-thinning. The viscous stress-tensor

$$\boldsymbol{\tau} = \mu(\Gamma) \dot{\gamma} \quad \text{with} \quad \dot{\gamma} = \nabla \mathbf{u} + (\nabla \mathbf{u})^T \quad (2.6)$$

with  $\dot{\gamma}$  the rate-of-strain tensor and its second invariant  $\Gamma$  writes:

$$\Gamma = \frac{1}{2} \dot{\gamma}_{ij} \dot{\gamma}_{ij}. \quad (2.7)$$

We assume a Carreau-law fluid where the viscosity depends exponentially on temperature,

$$\frac{\mu - \mu_\infty}{\mu_0 - \mu_\infty} = \exp \left[ -\hat{b} \left( \hat{T} - \hat{T}_0 \right) \right] \left( 1 + \hat{\lambda}^2 \hat{\Gamma} \right)^{\frac{n_c - 1}{2}}, \quad (2.8)$$

with  $\mu_0 = \hat{\mu}_0 / \hat{\mu}_0$  and  $\mu_\infty = \hat{\mu}_\infty / \hat{\mu}_0$  the viscosities at low and high shear rate,  $\hat{b}$  the thermodependency coefficient which measures the sensitivity of viscosity to variation in temperature,  $n_c < 1$  the shear-thinning index,  $\hat{\lambda}$  the characteristic time of the fluid. The characteristic shear rate for the onset of shear-thinning is determined by  $1/\hat{\lambda}$ . The infinite shear viscosity,  $\hat{\mu}_\infty$ , is generally significantly smaller ( $10^3$  to  $10^4$  times smaller) than  $\hat{\mu}_0$ , Bird *et al.* (1987); Tanner (2000). The ratio  $\hat{\mu}_\infty / \hat{\mu}_0$  will be thus neglected in the following. The dimensionless effective viscosity is then

$$\mu = \frac{\hat{\mu}}{\hat{\mu}_0} = \mu_b(z) \exp(-c\theta) \left( 1 + \lambda^2 \Gamma \right)^{\frac{n_c - 1}{2}}, \quad (2.9)$$

where,  $\mu_b(z)$  is the viscosity profile at quiescent state and  $c = \hat{b} \delta \hat{T}$  is a measure of the viscosity contrast. The Newtonian behavior,  $\hat{\mu} = \hat{\mu}_0$ , is obtained by setting  $n_c = 1$  or  $\hat{\lambda} = 0$ . The viscosity ratio across the fluid layer,

$$\ln(r) = \hat{b} \delta \hat{T}, \quad (2.10)$$

depends on  $\hat{b}$  and on  $\delta \hat{T}$ , but not on the temperature level. For a small amplitude disturbance, the viscosity can be expanded about the hydrostatic solution,

$$\mu = \mu_b [1 - c\theta + \dots] \left[ 1 + \left( \frac{n_c - 1}{2} \right) \lambda^2 \Gamma + \dots \right] \quad (2.11)$$

At the second order Taylor expansion of  $(1 + \lambda^2 \Gamma)^{\frac{n_c - 1}{2}}$ , a relevant rheological parameter,

i.e., the ‘degree of shear-thinning’ appears:

$$\alpha = \left| \frac{d\mu}{d\Gamma} \right|_{\Gamma=0} = \frac{1-n_c}{2} \lambda^2. \quad (2.12)$$

## 2.2. Boundary conditions

For the velocity field, no-slip boundary conditions (NSBC) are considered. For the temperature deviation, the thermal conductivity of the boundaries is assumed much larger than that of the fluid, so that their temperature remains ‘fixed’. The boundary conditions are:

$$\theta = u = v = w = 0 \quad \text{on} \quad z = 0, 1. \quad (2.13)$$

## 2.3. Reduction: elimination of the pressure

Applying twice the ***curl*** to momentum equations (2.3) and using the continuity equation, we get the following evolution equations for the velocity components  $w$ ,  $u$  and  $v$ :

$$\begin{aligned} \frac{1}{Pr} \frac{\partial}{\partial t} \Delta w &= \frac{1}{Pr} \left[ \frac{\partial^2}{\partial y \partial z} \mathcal{N}(v) + \frac{\partial^2}{\partial x \partial z} \mathcal{N}(u) - \Delta_H \mathcal{N}(w) \right] + Ra \Delta_H \theta + \\ &\quad \mu_b \Delta^2 w + 2 \left( \frac{d\mu_b}{dz} \right) \Delta \left( \frac{\partial w}{\partial z} \right) + \frac{d^2 \mu_b}{dz^2} \left( \frac{\partial^2 w}{\partial z^2} - \Delta_H w \right) + \\ &\quad \left[ \Delta_H \mathcal{N} V_z - \frac{\partial^2}{\partial x \partial z} \mathcal{N} V_x - \frac{\partial^2}{\partial y \partial z} \mathcal{N} V_y \right], \end{aligned} \quad (2.14)$$

$$\begin{aligned} \frac{1}{Pr} \frac{\partial}{\partial t} \left[ \Delta_H u + \frac{\partial^2 w}{\partial x \partial z} \right] &= \frac{1}{Pr} \left[ \frac{\partial^2}{\partial x \partial y} \mathcal{N}(v) - \frac{\partial^2}{\partial y^2} \mathcal{N}(u) \right] + \mu_b \Delta \left[ \Delta_H u + \frac{\partial^2 w}{\partial x \partial z} \right] + \\ &\quad \frac{d\mu_b}{dz} \frac{\partial}{\partial z} \left[ \Delta_H u + \frac{\partial^2 w}{\partial x \partial z} \right] - \frac{\partial}{\partial y} \mathcal{N} V_z \end{aligned} \quad (2.15)$$

$$\begin{aligned} \frac{1}{Pr} \frac{\partial}{\partial t} \left[ \Delta_H v + \frac{\partial^2 w}{\partial y \partial z} \right] &= \frac{1}{Pr} \left[ \frac{\partial^2}{\partial x \partial y} \mathcal{N}(u) - \frac{\partial^2}{\partial x^2} \mathcal{N}(v) \right] + \mu_b \Delta \left[ \Delta_H v + \frac{\partial^2 w}{\partial y \partial z} \right] + \\ &\quad \frac{d\mu_b}{dz} \frac{\partial}{\partial z} \left[ \Delta_H v + \frac{\partial^2 w}{\partial y \partial z} \right] + \frac{\partial}{\partial x} \mathcal{N} V_z, \end{aligned} \quad (2.16)$$

where the ‘horizontal Laplacian’

$$\Delta_H = \frac{\partial^2}{\partial x^2} + \frac{\partial^2}{\partial y^2}.$$

The nonlinear inertial terms  $\mathcal{N}(\cdot)$  and nonlinear viscous terms  $\mathcal{NV}_x$  are defined by

$$\mathcal{N}(\cdot) = (\mathbf{u} \cdot \nabla)(\cdot); \quad \mathcal{NV}_x = [\nabla \cdot ((\mu - \mu_b) \dot{\gamma})] \cdot \mathbf{e}_x, \quad (2.17)$$

similarly for  $\mathcal{NV}_y$  and  $\mathcal{NV}_z$ . The boundary conditions are

$$\theta = w = \frac{\partial w}{\partial z} = u = v = 0 \quad \text{at} \quad z = 0, 1 \quad (2.18)$$

$$(2.19)$$

In a matrix notation, the above system can be written formally as

$$\mathbf{M} \frac{\partial \Psi}{\partial t} = \mathbf{L}\Psi + \mathbf{NI} + \mathbf{NV}, \quad (2.20)$$

where  $\Psi = (w, u, v, \theta)^T$ , the operators  $\mathbf{M}$ ,  $\mathbf{L}$ ,  $\mathbf{NI}$  and  $\mathbf{NV}$  represent the weight matrix, the linear operator, the nonlinear inertial operator and the nonlinear viscous operator respectively. The nonlinear operators can also be decomposed as

$$\mathbf{NI} = [NI_w, NI_u, NI_v, NI_\theta]^t \quad \text{and} \quad \mathbf{NV} = [NV_w, NV_u, NV_v, 0]^t. \quad (2.21)$$

### 3. Linear stability analysis

#### 3.1. Onset of convection: direct eigenvalue problem

In the linear theory,  $\mathbf{u}$  and  $\theta$  are assumed infinitesimal. By neglecting the nonlinear terms in (2.14)- (2.16) and (2.4), one obtains the linear problem:

$$\frac{1}{Pr} \frac{\partial}{\partial t} \Delta w = \mu_b \Delta^2 w + 2 \frac{d\mu_b}{dz} \Delta \left( \frac{\partial w}{\partial z} \right) + \frac{d^2 \mu_b}{dz^2} \left( \frac{\partial^2 w}{\partial z^2} - \Delta_H w \right) + Ra \Delta_H \theta, \quad (3.1)$$

$$\frac{1}{Pr} \frac{\partial}{\partial t} \left[ \Delta_H u + \frac{\partial^2 w}{\partial x \partial z} \right] = \mu_b \Delta \left[ \Delta_H u + \frac{\partial^2 w}{\partial x \partial z} \right] + \frac{d\mu_b}{dz} \frac{\partial}{\partial z} \left[ \Delta_H u + \frac{\partial^2 w}{\partial x \partial z} \right] \quad (3.2)$$

$$\frac{1}{Pr} \frac{\partial}{\partial t} \left[ \Delta_H v + \frac{\partial^2 w}{\partial y \partial z} \right] = \mu_b \Delta \left[ \Delta_H v + \frac{\partial^2 w}{\partial y \partial z} \right] + \frac{d\mu_b}{dz} \frac{\partial}{\partial z} \left[ \Delta_H v + \frac{\partial^2 w}{\partial y \partial z} \right] \quad (3.3)$$

$$\frac{\partial \theta}{\partial t} = w + \Delta \theta. \quad (3.4)$$

At this order, no non-Newtonian effects enter the problem and the thermodependency appears through the viscosity profile of the base state  $\mu_b(z)$ . The disturbance quantities

$w, u, v, \theta$  are assumed periodic and of the form:

$$(w, u, v, \theta) = (F_{11}(z), U_{11}, V_{11}(z), G_{11}(z)) f(x, y) \exp(st) \quad (3.5)$$

with  $f(x, y) = \exp(ik_x x + ik_y y)$ ,  $\mathbf{k} = (k_x, k_y, 0)$  the horizontal wavenumber and  $s = s_r + is_i$  a complex number. This leads to the differential equations

$$\begin{aligned} s Pr^{-1} (D^2 - k^2) F_{11} &= \mu_b (D^2 - k^2)^2 F_{11} + 2D\mu_b (D^2 - k^2) DF_{11} + \\ &\quad D^2 \mu_b (D^2 + k^2) F_{11} - k^2 Ra G_{11}, \end{aligned} \quad (3.6)$$

$$\begin{aligned} s Pr^{-1} (-k^2 U_{11} + ik_x DF_{11}) &= \mu_b (D^2 - k^2) (-k^2 U_{11} + ik_x DF_{11}) + \\ &\quad \frac{d\mu_b}{dz} (-k^2 U_{11} + ik_x DF_{11}) \\ s Pr^{-1} (-k^2 V_{11} + ik_y DF_{11}) &= \mu_b (D^2 - k^2) (-k^2 V_{11} + ik_y DF_{11}) + \\ &\quad \frac{d\mu_b}{dz} (-k^2 V_{11} + ik_y DF_{11}) \\ s G_{11} &= F_{11} + (D^2 - k^2) G_{11}, \end{aligned} \quad (3.7) \quad (3.8) \quad (3.9)$$

with  $D$  the derivative with respect to  $z$  and  $k$  the norm of the vector  $\mathbf{k}$ . The boundary conditions are

$$F_{11} = DF_{11} = U_{11} = V_{11} = G_{11} = 0 \quad \text{at} \quad z = 0, 1. \quad (3.10)$$

The solutions to equations (3.6)-(3.9) can be divided into two eigenmode classes. The first one corresponds to the set of eigenmodes of (3.6), (3.9) with a particular solution of (3.7), (3.8). The second class represents the set of eigenmodes of (3.7), (3.8) with  $F_{11} = 0$ . For this class of eigenmodes, it can be shown straightforwardly that

$$s_i = 0 \quad \text{and} \quad s_r = -\frac{k^2 \langle \mu_b (|U_{11}|^2 + |V_{11}|^2) \rangle + \langle \mu_b (|DU_{11}|^2 + |DV_{11}|^2) \rangle}{\langle |U_{11}|^2 + |V_{11}|^2 \rangle} < 0. \quad (3.11)$$

The second class of eigenmodes are thus always damped. The first class of eigenmodes corresponds to the eigenvalue problem (3.6), (3.9) where  $s$  is the eigenvalue and  $\mathbf{X}_{11} =$

$(F_{11}, G_{11})$  the eigenvector. It can be written

$$s \tilde{\mathbf{M}} \cdot \mathbf{X}_{11} = \tilde{\mathbf{L}} \cdot \mathbf{X}_{11}. \quad (3.12)$$

It is easy to show that the principle of exchange of stability still holds, i.e.  $s_i = 0$ , when the viscosity profile is not uniform. Since any multiple of the eigenvector  $\mathbf{X}_{11}$  is also a solution of (3.12), and for symmetry reasons,  $\mathbf{X}_{11}$  can be normalized such that

$$G_{11}(z = 1/2) = 1. \quad (3.13)$$

A spectral Chebyshev method is used to determine the critical Rayleigh number and the critical wave number Bouteraa *et al.* (2015). The marginal stability curve  $Ra(k)$  is obtained by the condition  $s(Ra, k) = 0$ . Using 20 Chebyshev polynomials, the first eigenvalue, i.e. that for which the real part is the largest, is calculated with an accuracy of  $10^{-4}$ . The minimum of the marginal stability curves gives the critical Rayleigh number  $Ra_c$  and critical wave number  $k_c$ . In the case of exponential fluids, figure 1 displays the variation of the critical Rayleigh number for the onset of convection,  $Ra_c$ , as well as the critical wave number,  $k_c$ , as a function of the viscosity ratio  $r$  for no-slip boundary conditions (NSBC) and stress-free boundary conditions (SFBC). This later was added only as a validation test. Our results are in very quantitative agreement with those obtained by Stengel *et al.* (1982). As indicated by these authors, three different ranges of the viscosity ratio can be distinguished: (i) At low viscosity ratio,  $0 \leq r \leq 1.5$ ,  $Ra_c$  and  $k_c$  are almost constant; (ii) at moderate viscosity ratio,  $1.5 \leq r \leq 8$ ,  $Ra_c$  increases with increasing  $r$  and  $k_c$  is nearly constant or decreases slightly for SFBC. The viscosity variation in the moderate viscosity ratio stabilizes the onset of convection; (iii) for large viscosity ratio,  $Ra_c$  decreases with increasing  $r$  and  $k_c$  increases rapidly. In this regime, the convection is governed by a sublayer that is more unstable than the full layer Stengel *et al.* (1982). The results of Busse & Frick (1985) can be reproduced by a linear approximation of the

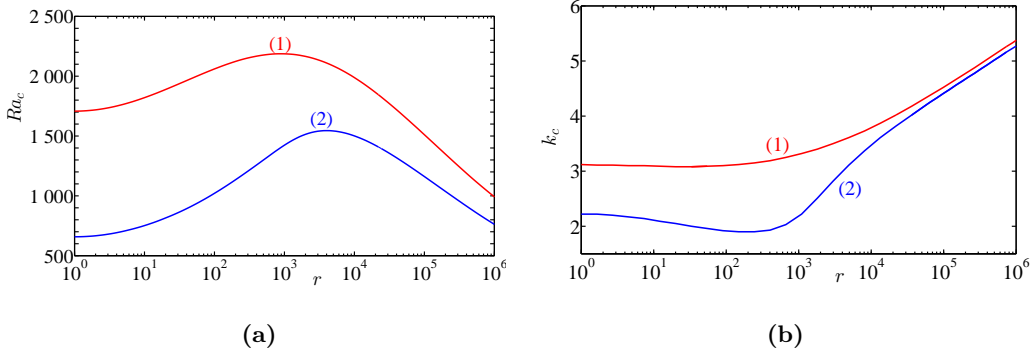


FIGURE 1. Exponential fluid. Critical Rayleigh number (a) and critical wavenumber (b) as function of the viscosity ratio. (1) NSBC, (2) SFBC.

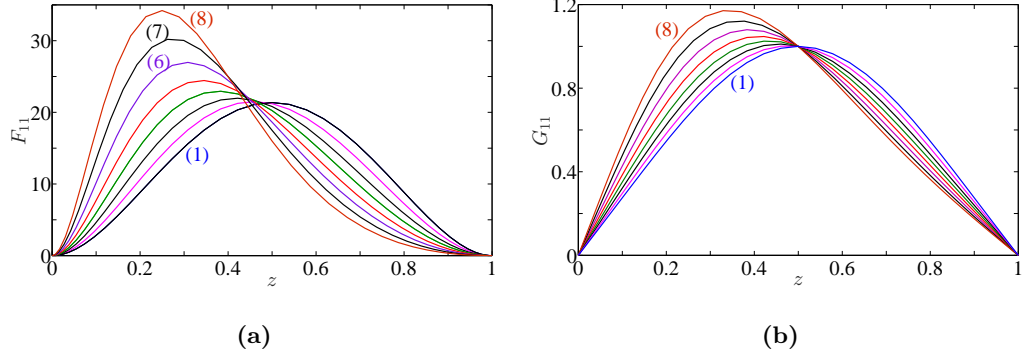


FIGURE 2. Exponential fluid. (a) Vertical velocity eigenfunction and (b) temperature perturbation at the first order as function of the depth  $z$  for different values of the thermodependency coefficient  $c$ . (1)  $c = 0$ ; (2)  $c = 1$ ; (3)  $c = 2$ ; (4)  $c = 3$ ...increasing  $c$  by step 1 until curve (8)  $c = 7$ .

exponential law (2.9). Figure 2 displays the profiles of the vertical velocity eigenfunction and the temperature perturbation at the first order for different values of the thermodependency coefficient. With increasing  $c$ , the maximum of  $F_{11}(z)$  takes place near the bottom plate where the fluid is less viscous, i.e., the center of the convection rolls is shifted towards the bottom plate, and the fluid motion is significantly reduced near the top wall. The shear rate increases near the lower boundary and decreases near the upper. The viscosity contrast between the top and the lower boundaries will be reinforced by the shear-thinning effects. The temperature perturbation becomes more confined near the

heated wall. Of course, when  $c = 0$ , the eigenfunctions,  $F_{11}(z)$  and  $G_{11}(z)$ , are symmetric with respect to the midplane of the fluid layer.

### 3.2. Adjoint eigenvalue problem: Adjoint mode

In the analysis developed in the next section, it will be necessary to eliminate secular terms in non homogeneous differential equations, i.e. the solvability condition must be applied. It is therefore necessary to determine the linear adjoint of the direct problem at the critical conditions. For vector fields  $\mathbf{f}$  and  $\mathbf{g}$ , one defines a scalar product by

$$\langle \mathbf{f}, \mathbf{g} \rangle = \int_0^1 \mathbf{f} \cdot \mathbf{g} dz. \quad (3.14)$$

To the direct eigenvalue problem (3.12) corresponds the adjoint problem

$$s \tilde{\mathbf{M}}^+ \cdot \mathbf{X}_{ad} = \tilde{\mathbf{L}}^+ \cdot \mathbf{X}_{ad} \quad \text{with} \quad \mathbf{X}_{ad} = (F_{ad}, G_{ad}), \quad (3.15)$$

where the adjoint operators  $\tilde{\mathbf{M}}^+$  and  $\tilde{\mathbf{L}}^+$  are defined by

$$\langle \mathbf{X}_{ad}, \tilde{\mathbf{M}} \cdot \mathbf{X}_{11} \rangle = \langle \tilde{\mathbf{M}}^+ \cdot \mathbf{X}_{ad}, \mathbf{X}_{11} \rangle, \quad \langle \mathbf{X}_{ad}, \tilde{\mathbf{L}} \cdot \mathbf{X}_{11} \rangle = \langle \tilde{\mathbf{L}}^+ \cdot \mathbf{X}_{ad}, \mathbf{X}_{11} \rangle \quad (3.16)$$

where  $\mathbf{X}_{11}$  fulfills the ‘linear’ boundary conditions (3.10). By integrating by part we get the linear adjoint problem and the corresponding boundary conditions

$$\begin{aligned} s Pr^{-1} (D^2 - k^2) F_{ad} &= \mu_b (D^2 - k^2)^2 F_{ad} + 2D\mu_b (D^2 - k^2) DF_{ad} + \\ &\quad D^2 \mu_b (D^2 + k^2) F_{ad} + G_{ad}, \end{aligned} \quad (3.17)$$

$$s G_{ad} = -k^2 Ra F_{ad} + (D^2 - k^2) G_{ad}, \quad (3.18)$$

with

$$F_{ad} = 0, \quad DF_{ad} = 0, \quad G_{ad} = 0 \quad \text{at} \quad z = 0, \quad (3.19a)$$

$$F_{ad} = 0, \quad DF_{ad} = 0, \quad G_{ad} = 0 \quad \text{at} \quad z = 1. \quad (3.19b)$$

The solution of these equations is obtained using the same method as for the direct problem. Similarly, the normalization adopted for the adjoint mode is

$$G_{ad}(z = 1/2) = 1. \quad (3.20)$$

At  $Ra = Ra_c$ , the so-called adjoint critical mode does not depend on the Prandtl number.

#### 4. Weakly nonlinear stability analysis

The critical Rayleigh number for the onset of convection determined from the linear stability analysis depends only on the norm  $k_c$  of the wavevector. Because of the isotropy of the extended horizontal plane, the direction of the wavevector is arbitrary. In addition any linear combination of modes  $A_p \exp(i\mathbf{k}_p \cdot \mathbf{r}) (F_{11}(z), G_{11}(z))$ , where  $\mathbf{r} = (x, y)$ ,  $\mathbf{k}_p = (k_{px}, k_{py})$ ,  $|\mathbf{k}_p| = k_c$  and  $A_p$ 's are constant coefficients, is a solution of the linear problem, i.e. there is also a pattern degeneracy. We consider the case where the wavevectors lie on a hexagonal lattice

$$(w, \theta) = \sum_{p=1}^3 A_p (F_{11}, G_{11}) \exp(i\mathbf{k}_p \cdot \mathbf{r}) + c.c. + \text{h.o.t.}, \quad (4.1)$$

where, as before “c.c.” denotes the complex conjugate of the prior expression and “h.o.t.” means “higher order terms”. The hexagon patterns are made of three pairs of wavevectors at  $2\pi/3$  angles apart:  $\mathbf{k}_1 = k_c \mathbf{e}_x$ ,  $\mathbf{k}_2 = k_c \left(-\mathbf{e}_x/2 + (\sqrt{3}/2) \mathbf{e}_y\right)$  and  $\mathbf{k}_3 = k_c \left(-\mathbf{e}_x/2 - (\sqrt{3}/2) \mathbf{e}_y\right)$ . The objective is to determine the spatio-temporal evolution of the amplitude  $A_p$ , above threshold, due to different nonlinearities of the problem.

##### 4.1. Multiple scales method

As the Rayleigh number is increased above the onset  $Ra_c$ , the growth-rate of the perturbation is positive for any wavenumber within a band  $\sqrt{\epsilon}$ , with  $\epsilon = (Ra - Ra_c)/Ra_c$ , around the critical wavenumber. Actually, Taylor expansion of the dispersion curve near its maximum shows that  $s \propto \epsilon$ ,  $k - k_c \propto \sqrt{\epsilon}$ . For  $\epsilon > 0$ , emergent patterns are described

by an infinite sum of unstable modes (in a continuous band) of the form  $e^{\frac{\epsilon t}{\tau_0}} e^{ik_c x} e^{i\frac{\sqrt{\epsilon}x}{\xi_0}}$ .

For small  $\epsilon$ , we can separate the dynamics into fast eigen-modes and slow modulation of the form  $e^{\frac{\epsilon t}{\tau_0}} e^{\frac{i\sqrt{\epsilon}x}{\xi_0}}$ . A similar reasoning can be done for the  $y$ -direction.

Let us denote  $\delta = \sqrt{\epsilon}$ . The multiple-scales approach is used to obtain the amplitude equation, which describes the slow temporal and spatial variation of the field variables.

The slow scales

$$X = \delta x , \quad Y = \delta y \quad \text{and} \quad T = \delta^2 t \quad (4.2)$$

are treated as independent of the fast scales  $x$ ,  $y$  and  $t$ . The derivatives with respect to the new variables are

$$\frac{\partial}{\partial t} \longrightarrow \frac{\partial}{\partial t} + \delta^2 \frac{\partial}{\partial T}, \quad \frac{\partial}{\partial x} \longrightarrow \frac{\partial}{\partial x} + \delta \frac{\partial}{\partial X}, \quad \frac{\partial}{\partial y} \longrightarrow \frac{\partial}{\partial y} + \delta \frac{\partial}{\partial Y}, \quad \frac{\partial}{\partial z} \longrightarrow \frac{\partial}{\partial z}. \quad (4.3)$$

The fast spatial variables vary on the order of a typical wavelength. The slow variables describe, the temporal and the spatial modulations of these fast variables. Furthermore, as the marginal mode is stationary, then

$$\frac{\partial}{\partial t} \longrightarrow \delta^2 \frac{\partial}{\partial T}. \quad (4.4)$$

The solution of the nonlinear problem in the neighbourhood of the critical conditions, corresponding to the onset of convection is developed with respect to the parameter  $\delta$  by

$$\Psi = \delta \Psi^{(1)} + \delta^2 \Psi^{(2)} + \delta^3 \Psi^{(3)} + O(\delta^4), \quad (4.5)$$

$$Ra = Ra_c + \delta Ra^{(1)} + \delta^2 Ra^{(2)} + O(\delta^3). \quad (4.6)$$

The Taylor expansion is also applied to the operators

$$\mathbf{M} = \mathbf{M}^{(0)} + \delta \mathbf{M}^{(1)} + O(\delta^2), \quad (4.7)$$

$$\mathbf{L} = \mathbf{L}^{(0)} + \delta \mathbf{L}^{(1)} + \delta^2 \mathbf{L}^{(2)} + O(\delta^3), \quad (4.8)$$

$$\mathbf{NI} = \delta^2 \mathbf{NI}^{(2)} + \delta^3 \mathbf{NI}^{(3)} + O(\delta^3), \quad (4.9)$$

$$\mathbf{NV} = \delta^2 \mathbf{NV}^{(2)} + \delta^3 \mathbf{NV}^{(3)} + O(\delta^3). \quad (4.10)$$

The explicit expressions of  $\mathbf{M}$ ,  $\mathbf{L}$ ,  $\mathbf{NI}$  and their sub-scales are given in Appendix A. The expressions of  $\mathbf{NV}$  and its sub-scales are too lengthy, and thus are not shown.

#### 4.2. Derivation of the Ginzburg-Landau equation

Taking (4.3), (4.4) into account, the expansion of variables (4.5), (4.6) and operators (4.7)-(4.10) are substituted formally into the nonlinear system of equations (2.4), (2.14)-(2.16). After ordering according to the power of  $\delta$ , a sequence of systems of equations is obtained. In the following, the first three orders are determined.

##### 4.2.1. Solution at order $\delta$

At the first order of  $\delta$ , the linearized problem is obtained

$$\mathbf{L}^{(0)} \Psi^{(1)} = 0. \quad (4.11)$$

The system (4.11) corresponds to the linear problem discussed in Sec.3. However, now  $\Psi^{(1)}$  is also a function of the slow variables  $X$ ,  $Y$  and  $T$ . These variables do not appear in the linear stability analysis section. For hexagon patterns, the first order solution  $\Psi^{(1)} = [w^{(1)}, u^{(1)}, v^{(1)}, \theta^{(1)}]^t$  is

$$w^{(1)} = F_{11}(z) [A_1 \exp(i\mathbf{k}_1 \cdot \mathbf{r}) + A_2 \exp(i\mathbf{k}_2 \cdot \mathbf{r}) + A_3 \exp(i\mathbf{k}_3 \cdot \mathbf{r})] + c.c., \quad (4.12)$$

$$\theta^{(1)} = G_{11}(z) [A_1 \exp(i\mathbf{k}_1 \cdot \mathbf{r}) + A_2 \exp(i\mathbf{k}_2 \cdot \mathbf{r}) + A_3 \exp(i\mathbf{k}_3 \cdot \mathbf{r})] + c.c., \quad (4.13)$$

$$\mathbf{u}_H^{(1)} = \frac{DF_{11}}{k^2} \nabla_{Hx} [A_1 \exp(i\mathbf{k}_1 \cdot \mathbf{r}) + A_2 \exp(i\mathbf{k}_2 \cdot \mathbf{r}) + A_3 \exp(i\mathbf{k}_3 \cdot \mathbf{r})] + c.c. \quad (4.14)$$

where  $\nabla_{Hx}$  denotes the horizontal gradient for the fast variables,  $\mathbf{u}_H = (u, v)$  the horizontal velocity components, and  $A_p$  the amplitude of the perturbation:

$$A_p = A_p(X, Y, T) \quad p = 1, 2, 3. \quad (4.15)$$

#### 4.2.2. Solution at order $\delta^2$

At the next order  $\delta^2$ , we have

$$\mathbf{L}^{(0)}\Psi^{(2)} = -\mathbf{L}^{(1)}\Psi^{(1)} - \mathbf{NI}^{(2)} - \mathbf{NV}^{(2)}. \quad (4.16)$$

The forcing terms in the right-hand side of equation (4.16) are computed by introducing the first order solution (4.12)-(4.14). This forcing is composed of four components: (1) Terms proportional to  $|A_p|^2$  ( $p = 1, 2, 3$ ), with the wavenumber modulus  $|k| = 0$ , due to the interaction of the eigenmode with its complex conjugate. (2) Terms proportional to  $A_p^2 \exp(2i\mathbf{k}_p \cdot \mathbf{r})$ ,  $|\mathbf{k}| = 2k_c$ , due to the interaction of the eigenmode with itself, (3) terms proportional to  $A_p A_q^* \exp(i(\mathbf{k}_p - \mathbf{k}_q) \cdot \mathbf{r})$ ,  $|\mathbf{k}| = \sqrt{3}k_c$  and (4) resonant forcings with wavevector  $\mathbf{k}_\ell$  ( $\ell = 1, 2, 3$  and  $|\mathbf{k}_\ell| = k_c$ ). Four separate sets of non homogeneous differential equations are then derived for each component. They are given in Appendix B. For the fourth component, the right-hand side of the non-homogeneous differential contains secular terms. A solvability condition, known as the Fredholm alternative should then be applied for a solution to exist, i.e. the left hand side of equation (4.16) has to be

orthogonal to the null-space of the adjoint adjoint operator. We obtain

$$\begin{aligned}
& A_2^* A_3^* \int_0^1 G_{ad} (2F_{11} D G_{11} + G_{11} D F_{11}) dz + \\
& A_2^* A_3^* \frac{1}{Pr} \int_0^1 F_{ad} (2DF_{11} D^2 F_{11} + F_{11} D^3 F_{11} - 3k_c^2 F_{11} DF_{11} dz) - \\
& A_2^* A_3^* \int_0^1 F_{ad} [\mathbf{N} \mathbf{V}_w]_{A_2^* A_3^*}^{(2)} dz - \\
& 2i(\mathbf{k}_1 \cdot \nabla_{HX}) A_1 \left[ 2 \int_0^1 \mu_b (D^2 F_{11} - k_c^2 F_{11}) F_{ad} dz + 2 \int_0^1 \frac{d\mu_b}{dz} \frac{dF_{11}}{dz} F_{ad} dz \right] - \\
& 2i(\mathbf{k}_1 \cdot \nabla_{HX}) A_1 \left[ - \int_0^1 \frac{d^2 \mu_b}{dz^2} F_{11} F_{ad} dz + Ra_c \int_0^1 G_{11} F_{ad} dz \right] - \\
& k_c^2 Ra_1 A_1 \int_0^1 G_{11} F_{ad} dz = 0.
\end{aligned} \tag{4.17}$$

Two other similar relations are obtained by circular permutation of the indices. The integrals in (4.17) are evaluated numerically by means of the Clenshaw and Curtis method. The calculation leads to a result of the form

$$Ra_1 A_1 + b A_2^* A_3^* = 0. \tag{4.18}$$

Again, two other similar relations are obtained by circular permutation. These expressions allow to determine the solution at the second order.

### 4.3. Solution at order $\delta^3$

At this order, we obtain the equation for the evaluation of  $\Psi^{(3)}$ :

$$\mathbf{L}^{(0)} \Psi^{(3)} = \mathbf{M}^{(0)} \frac{\partial \Psi^{(1)}}{\partial T} - \mathbf{L}^{(1)} \Psi^{(2)} - \mathbf{L}^{(2)} \Psi^{(1)} - \mathbf{N} \mathbf{I}^{(3)} - \mathbf{N} \mathbf{V}^{(3)} \tag{4.19}$$

The solvability condition at this order, yields an equation for  $Ra_2$ . To obtain the amplitude equations at cubic order, we use equation (4.6), combined with  $\epsilon = (Ra - Ra_c)/Ra_c$ , the departure from the linear threshold. We have

$$\epsilon A_1 = \frac{\delta}{Ra_c} Ra^{(1)} + \frac{\delta^2}{Ra_c} Ra^{(2)} A_1. \tag{4.20}$$

We substitute in (4.20),  $Ra^{(1)}$  and  $Ra^{(2)}$  by their expressions derived from the solvability

conditions at orders  $\delta^2$  and  $\delta^3$ . Finally, returning to the fast variable  $\delta A_j(X, Y, T) = A'_j(x, y, t)$ ,  
 $\frac{\partial}{\partial X} = \frac{1}{\delta} \frac{\partial}{\partial x}$ , ..., we obtain

$$\begin{aligned} \frac{\partial A_1}{\partial t} = & \epsilon \alpha_l A_1 + \alpha_d (\mathbf{k}_1 \cdot \nabla_{Hx})^2 A_1 + \gamma A_2^* A_3^* - \\ & g_1 |A_1|^2 A_1 - g_2 (|A_2|^2 + |A_3|^2) A_1 + \\ & i \beta_1 [A_2^* (\mathbf{k}_3 \cdot \nabla_{Hx}) A_3^* + A_3^* (\mathbf{k}_2 \cdot \nabla_{Hx}) A_2^*] + \\ & i \beta_2 [A_2^* (\mathbf{k}_2 \cdot \nabla) A_3^* + A_3^* (\mathbf{k}_3 \cdot \nabla_{Hx}) A_2^*]. \end{aligned} \quad (4.21)$$

Companion equations for  $A_2$  and  $A_3$  are obtained by subindex permutation. The coefficient  $\gamma$  arises from non Oberbeck-Boussinesq effects. It increases with increasing the viscosity ratio and the Prandtl number as it is shown in figure 3. However, from  $Pr \approx 50$ , there is no significant effect of  $Pr$ . The coefficient  $g_1$  refers to the self-saturation coefficient and  $g_2$  the cross-saturation coefficient. It can be shown straightforwardly that  $g_1$  and  $g_2$  can be written as the sum of two contributions. The first one ( $g_1^N, g_2^N$ ) similar to that obtained for a Newtonian fluid arises from the nonlinear inertial terms and the thermodependency of the viscosity. The second contribution arises ( $g_1^V, g_2^V$ ) arises from the nonlinear viscous terms:

$$g_1 = g_1^I + g_1^V \quad \text{with} \quad g_1^V = -\alpha g_1^{NN} \quad (4.22)$$

Following Echebarría & Pérez-García (1998), it is useful to express the derivatives in equation (4.21) in terms of unitary vectors of the corresponding mode. One obtains (Echebarría & Pérez-García 1998)

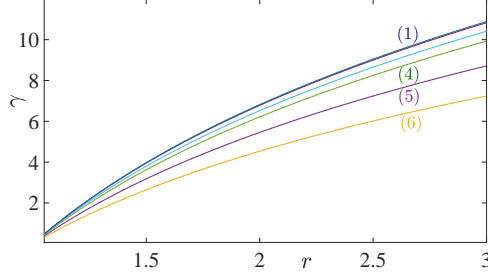


FIGURE 3. Variation of  $\gamma$  with  $r$  and Prandtl number. (1)  $Pr = 100$ ; (2)  $Pr = 50$ ; (3)  $Pr = 10$ ; (4)  $Pr = 5$ ; (5)  $Pr = 2$ ; (6)  $Pr = 1$ .

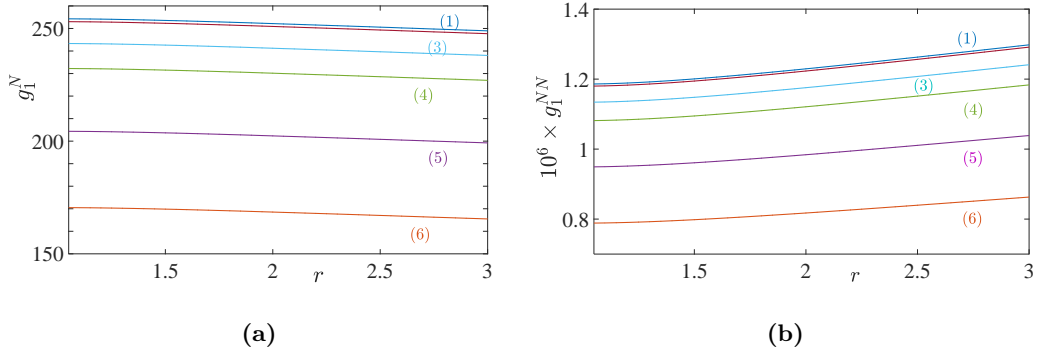


FIGURE 4. (a) ‘Newtonian’ and (b) non-Newtonian contribution to the first Landau coefficient as a function of  $r$  for different values of  $Pr$ . (1)  $Pr = 100$ ; (2)  $Pr = 50$ ; (3)  $Pr = 10$ ; (4)  $Pr = 5$ ; (5)  $Pr = 2$ ; (6)  $Pr = 1$ .

$$\begin{aligned}
 \frac{\partial A_1}{\partial t} = & \frac{\epsilon}{\tau_0} A_1 + \frac{\xi^2}{\tau_0} (\mathbf{n}_1 \cdot \nabla_{Hx})^2 A_1 + \gamma A_2^* A_3^* - \\
 & g_1 |A_1|^2 A_1 - g_2 (|A_2|^2 + |A_3|^2) A_1 + \\
 & i\alpha_1 [A_2^* (\mathbf{n}_3 \cdot \nabla_{Hx}) A_3^* + A_3^* (\mathbf{n}_2 \cdot \nabla_{Hx}) A_2^*] + \\
 & i\alpha_2 [A_2^* (\boldsymbol{\tau}_3 \cdot \nabla) A_3^* + A_3^* (\boldsymbol{\tau}_2 \cdot \nabla_{Hx}) A_2^*] , \tag{4.23}
 \end{aligned}$$

where  $\mathbf{n}_i$  is the unitary vector in the direction of  $\mathbf{k}_i$  and  $\boldsymbol{\tau}_i$  orthogonal to  $\mathbf{n}_i$ ,  $\alpha_1$  and  $\alpha_2$  are real coefficients. The term with the coefficient  $\alpha_1$  accounts for distortions in the directions of rolls and it therefore corresponds to dilatations of hexagons, while the terms with  $\alpha_2$  account for distortions in the hexagonal form.

#### 4.4. Pattern selection

In this section, we investigate the competition between rolls and hexagons near the critical conditions. First, the stationary solutions of the amplitude equations are determined, then their linear stability is considered.

By considering uniform patterns, i.e. without spatial modulations, the amplitude equations 4.23 reduce to:

$$\begin{aligned}\frac{\partial A_1}{\partial t} &= \frac{\epsilon}{\tau_0} A_1 + \gamma A_2^* A_3^* - g_1 |A_1|^2 A_1 - g_2 |A_2|^2 A_1 \\ \frac{\partial A_2}{\partial t} &= \frac{\epsilon}{\tau_0} A_2 + \gamma A_2^* A_3^* - g_1 |A_2|^2 A_2 - g_2 |A_1|^2 A_2.\end{aligned}\quad (4.24)$$

The steady solutions of (4.24) are determined and their linear stability is investigated (Hoyle 2006).

- (i) Conduction state,  $A_1 = A_2 = A_3 = 0$ , is stable for  $\epsilon < 0$  and unstable for  $\epsilon > 0$ .
- (ii) Roll solution given by  $A_1 = \sqrt{s/g_1}$ ,  $A_2 = A_3 = 0$  and any circular permutation is linearly stable if  $\delta_1 > g_1$  and  $\epsilon > \epsilon_r$ , where

$$\epsilon_r = \frac{\tau_0 \gamma^2 g_1}{(g_1 - \delta_1)^2}, \quad (4.25)$$

- (iii) Hexagon solutions (three sets of rolls of equal amplitude) given by

$$A_1 = A_2 = A_3 = \frac{\gamma + \sqrt{\gamma^2 + 4s(g_1 + 2\delta_1)}}{2(g_1 + 2\delta_1)}, \quad (4.26)$$

called up-hexagons, that correspond to up flow in the centre, and

$$A_1 = A_2 = A_3 = \frac{-\gamma + \sqrt{\gamma^2 + 4s(g_1 + 2\delta_1)}}{2(g_1 + 2\delta_1)}, \quad (4.27)$$

called down hexagons, that correspond to down flow motion in the center. Solutions called *up-hexagons*, exist for

$$\epsilon > \epsilon_a = -\frac{\gamma^2 \tau_0}{4(g_1 + 2\delta_1)}, \quad (4.28)$$

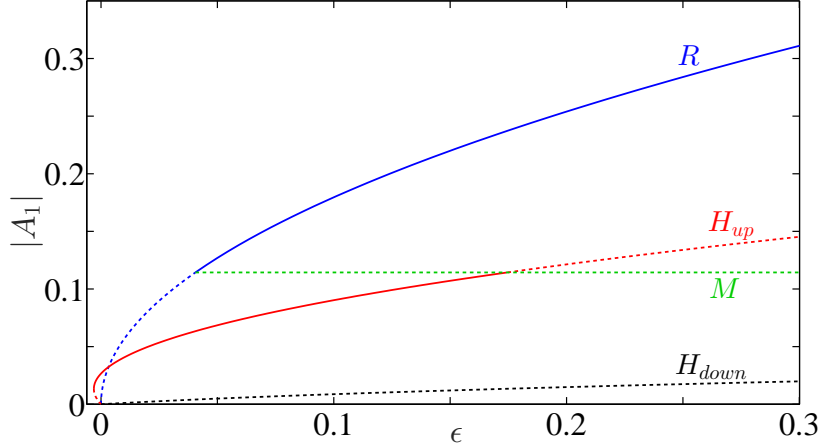


FIGURE 5. Bifurcation diagram for hexagons in the case ( $\delta_1 > g_1$ ),  $r = 2.5$  and  $\alpha = 1.5 \cdot 10^{-4}$ . The amplitude  $|A_1|$  is plotted against the distance to the threshold  $\epsilon$ , for the roll-solution branch (labelled  $R$ ), for the mixed mode branch (labelled  $M$ ) and for the two hexagon-solution branches, up-hexagons  $\text{Arg}(A_1 A_2 A_3) = 0$  and down-hexagons  $\text{Arg}(A_1 A_2 A_3) = \pi$ . Solid lines indicate stable solutions and dashed lines represent unstable solutions.

and are linearly stable for  $\epsilon_a < \epsilon < \epsilon_h$ , with

$$\epsilon_h = \frac{\tau_0 \gamma^2 (2g_1 + \delta_1)}{(g_1 - \delta_1)^2} \quad (4.29)$$

Solutions called *down hexagons*, exist for  $\epsilon > 0$  and are linearly unstable.

(iv) The "mixed states" given by

$$A_1 = \frac{\gamma}{\delta_1 - g_1}, \quad A_2 = A_3 = \sqrt{\frac{s - g_1 A_1^2}{g_1 + \delta_1}} \quad (4.30)$$

and any circulation permutation exist for  $\epsilon > 0$  and are linearly unstable.

The bifurcation diagram is shown in Fig. 5. Hexagons bifurcate transcritically from the conductive state. Both hexagons and the conductive state are stable in the range  $\epsilon_a \leq \epsilon \leq 0$  and both hexagons and rolls are stable in the range  $\epsilon_r \leq \epsilon \leq \epsilon_h$ . In this range, rolls and hexagons are linked via a branch of mixed modes which are always unstable.

Variations of  $\epsilon_a$ ,  $\epsilon_r$ ,  $\epsilon_h$  and  $(\epsilon_h - \epsilon_r)$  as a function of the viscosities ratio,  $r$  for different values of the shear-thinning degree are depicted in Fig. 6. Overall, the thermodependency

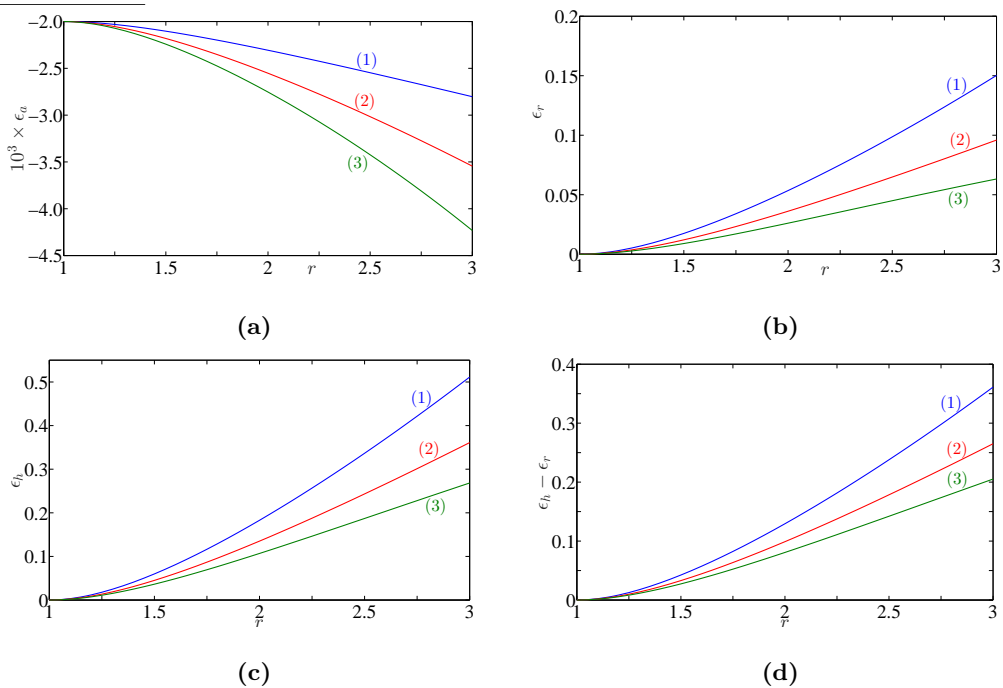


FIGURE 6. Variations of  $\epsilon_a$ ,  $\epsilon_r$ ,  $\epsilon_h$  and  $(\epsilon_h - \epsilon_r)$  versus  $r$  for three values of the shear-thinning degree  $\alpha$ : (1) Newtonian fluid,  $\alpha = 0$ ; (2) Carreau fluid with  $\alpha = 1.07 \cdot 10^{-4}$ ; (3) Carreau fluid with  $\alpha = 1.43 \cdot 10^{-4}$ .

of the viscosity favors convection in form of hexagons and their stability whereas shear-thinning effects favor convection in form of rolls and their stability. For instance, in Fig. 6(b), the domain of stability of hexagons increases with increasing  $r$  and decreases with increasing shear-thinning effects. In the same way, the domain of bistability rolls and hexagons shrinks with increasing  $\alpha$ , and increases with increasing the viscosities ratio, i.e. the thermodependency

## 5. Wavenumber selection

For a given Rayleigh number greater than  $Ra_c$ , the conduction state is unstable to all periodic convective patterns whose wavenumber satisfies  $(k - k_c) \leq O(\epsilon^{1/2})$ . This leads to a slow spatial modulation of the convection on a length of order  $O(\epsilon^{-1/2})$ . However,

these periodic solution are then unstable, unless  $k$  falls in a smaller range that it has to be determined. For this, amplitude equations with an additional term, Ginzburg-Landau equations, describing smooth spatial evolution of the amplitude are considered (Newell & Whitehead 1969; Segel 1969). This additional term is easily obtained from the growth rate

$$s(Ra, k^2) = \frac{\epsilon}{\tau_0} - \frac{\xi_0^2}{\tau_0} \frac{(k^2 - k_c^2)^2}{4k_c^2} + O\left([k^2 - k_c^2]^3\right). \quad (5.1)$$

The coherence length  $\xi_0$  is defined as

$$\xi_0^2 = -\frac{1}{2}\tau_0 \left( \frac{\partial^2 s}{\partial k^2} \right)_{Ra_c, k_c} = -\frac{1}{2Ra_c} \left( \frac{\partial^2 Ra}{\partial k^2} \right)_{Ra_c, k_c}. \quad (5.2)$$

It diminishes with increasing  $r$  as it is shown in Fig. 7. Note that  $(k^2 - k_c^2)^2 \approx 4k_c^2 (\mathbf{n} \cdot \mathbf{q})^2$ , where  $\mathbf{q} = (\mathbf{k} - \mathbf{k}_c)$  and  $\mathbf{n}$  a unit vector parallel to the wave vector. Returning from Fourier space to real space via  $\mathbf{q} \rightarrow i\nabla$ , therefore  $4k_c^2 (k^2 - k_c^2)^2$  becomes a linear diffusion term  $(\mathbf{n} \cdot \nabla)^2$  (Echebarria & Perez-Garcia 2001; Hoyle 2006).

### 5.1. Existence and stability of modulated patterns in a hexagonal lattice

The evolution of modulated hexagonal patterns can be described by a set of three coupled Ginzburg-Landau equations (Sushchik & Tsimring 1994; Hoyle 1995). They read

$$\frac{\partial A_i}{\partial t} = \frac{\epsilon}{\tau_0} A_1 + \gamma A_j^* A_k^* - [g_1 |A_i|^2 + \delta_1 (|A_j|^2 + |A_k|^2)] A_i + \frac{\xi_0^2}{\tau_0} \frac{\partial^2 A_i}{\partial x_i^2}, \quad (5.3)$$

where  $i, j, k = 1, 2, 3$  and any circular permutation. Here,  $\partial/\partial x_i = \mathbf{n}_i \cdot \nabla$ , where  $\mathbf{n}_i$  is a unit vector parallel to the wavevector  $\mathbf{k}_i$ . The cartesian coordinates  $x_i$ ,  $i = 1, 2, 3$  are orthogonal to roll axes,

$$x_1 = x \quad , \quad x_2 = \frac{-x + \sqrt{3}y}{2} \quad , \quad x_3 = \frac{-x - \sqrt{3}y}{2}. \quad (5.4)$$

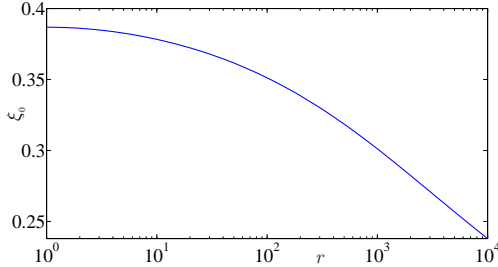


FIGURE 7. Coherence length versus the viscosities ratio.

### 5.1.1. Stationary solutions

Amplitude equations (5.3) possess a continuous family of uniform stationary solutions defined as

$$A_i = \mathcal{A}_i \exp(iqx_i) \quad ; \quad i = \{1, 2, 3\} \quad ; \quad q = k - k_c \quad ; \quad \mathcal{A}_i > 0 \quad (5.5)$$

They are obtained by substituting the above expression into (5.3). These are

- Rolls,  $\mathcal{A}_1 = R$ ,  $\mathcal{A}_2 = \mathcal{A}_3 = 0$ , with  $R = \left[ \left( \frac{\epsilon}{\tau_0} - \frac{\xi_0 q^2}{\tau_0} \right) / g_1 \right]^{1/2}$ .

- Up hexagons,  $\mathcal{A}_1 = \mathcal{A}_2 = \mathcal{A}_3 = H$ , with

$$H = \frac{\gamma + \sqrt{\gamma^2 + 4(g_1 + 2\delta_1) \left( \frac{\epsilon}{\tau_0} - q^2 \frac{\xi_0^2}{\tau_0} \right)}}{2(g_1 + 2\delta_1)}, \quad (5.6)$$

they exist for

$$\epsilon > \epsilon_{am} = \xi_0^2 q^2 - \frac{\tau_0 \gamma^2}{4(g_1 + 2\delta_1)} \quad (5.7)$$

Down hexagons and mixed modes are not considered, because they are linearly unstable.

### 5.1.2. Linear stability analysis of hexagons and rolls

The stability of the solution (5.6) is determined considering perturbation in the form

$$\mathcal{A}_i = (H + r_i) \exp(qx_i + \phi_i), \quad (5.8)$$

where  $|r_i| \ll 1$  and  $|\phi_i| \ll 1$  are the amplitude and phase perturbations, respectively.

Substituting the perturbed amplitudes (5.8) into (5.3) and linearizing with respect to

$r_i$  and  $\phi_i$ , lead to the following set of equations:

$$\frac{\partial r_i}{\partial t} = \gamma R_0(-r_i + r_j + r_k) - 2g_1 R_0^2 r_i - 2\beta R_0^2(r_j + r_k) - 2R_0 q \frac{\xi_0^2}{\tau_0} \frac{\partial \phi_i}{\partial x_i} + \frac{\xi_0^2}{\tau_0} \frac{\partial^2 r_i}{\partial x_i^2} \quad (5.9)$$

$$\frac{\partial \phi_i}{\partial t} = -\gamma R_0(\phi_i + \phi_j + \phi_k) + \frac{2q}{R_0 \tau_0} \frac{\xi_0^2}{\partial x_i} \frac{\partial r_i}{\partial x_i} + \frac{\xi_0^2}{\tau_0} \frac{\partial^2 \phi_i}{\partial x_i^2} \quad (5.10)$$

The spatial pattern may be subject to two possible modes of perturbations. The amplitude mode and the phase mode.

### 5.1.3. Amplitude instabilities

A linear stability analysis with respect to homogeneous perturbations is performed similarly as in the previous section.

- For rolls, the perturbation is in the form:  $\mathcal{A}_1 = R(1 + r_1)$ ,  $\mathcal{A}_{2,3} = r_{2,3}$ . It is found that rolls are stable for

$$\epsilon > \epsilon_r = \dots \quad (5.11)$$

The stability of the solution (5.5), (5.6) to perturbations with the same wavevectors is studied as in the previous section. The hexagons appear through a saddle-node bifurcation at  $\epsilon = \epsilon_{am}$ ,

$$\epsilon_{am} = \xi_0^2 q^2 - \frac{\tau_0 \gamma^2}{4(g_1 + 2\delta_1)} \quad (5.12)$$

and becomes unstable at  $\epsilon = \epsilon_{hm}$ ,

$$\epsilon_{hm} = \xi_0^2 q^2 + \frac{\tau_0 \gamma^2 (2g_1 + \delta_1)}{(g_1 - \delta_1)^2} \quad (5.13)$$

### 5.1.4. Long-wave approximation: Phase equation

The linear stability analysis of the stationary hexagonal solution (5.6) is conducted in a classical way. The amplitudes are perturbed around a hexagonal pattern

$$A_i(x_1, x_2, x_3, t) = (R_0 + r_i(x_1, x_2, x_3, t)) \exp(i(qx_i + \phi_i(x_1, x_2, x_3, t))), \quad (5.14)$$

In the following, we consider the long wavelength limit where spatial derivatives of variables are very small compared to the variables themselves. In this case, it is possible to simplify the problem by using the phase approximation

## 6. Conclusion

### Appendix A. Operators and matrix coefficients

#### A.1. The operator $\mathbf{M}$

$$\mathbf{M} = \begin{pmatrix} M_{11} & 0 & 0 & 0 \\ M_{21} & M_{22} & 0 & 0 \\ M_{31} & 0 & M_{33} & 0 \\ 0 & 0 & 0 & 1 \end{pmatrix} \quad (\text{A } 1)$$

with

$$\begin{aligned} M_{11} &= Pr^{-1}\Delta, & M_{21} &= \frac{\partial^2}{\partial x \partial z}, & M_{22} &= \nabla_{Hx}^2, \\ M_{31} &= \frac{\partial^2}{\partial y \partial z}, & M_{33} &= \nabla_{Hx}^2. \end{aligned} \quad (\text{A } 2)$$

#### A.1.1. The sub-scale $\mathbf{M}^0$

The coefficients of  $\mathbf{M}^0$  in eq. (4.7) are

$$\begin{aligned} M_{11}^{(0)} &= Pr^{-1} \left( \Delta_{Hx} + \frac{\partial^2}{\partial z^2} \right), \\ M_{21}^{(0)} &= \frac{\partial^2}{\partial x \partial z}, & M_{22}^{(0)} &= \Delta_{H0}, \\ M_{31}^{(0)} &= \frac{\partial^2}{\partial y \partial z}, & M_{33}^{(0)} &= \Delta_{H0}, \\ M_{44}^{(0)} &= 1, \end{aligned} \quad (\text{A } 3)$$

The other components of  $M^{(0)}$  are zero.

A.1.2. The sub-scale  $\mathbf{M}^1$ 

The coefficients of  $\mathbf{M}^1$  in eq. (4.7) are

$$M_{11}^{(1)} = 2 Pr^{-1} \nabla_{Hx} \cdot \nabla_{HX}, \quad (\text{A } 4)$$

$$M_{21}^{(1)} = \frac{\partial^2}{\partial X \partial z}, \quad M_{22}^{(1)} = 2 \nabla_{Hx} \cdot \nabla_{HX},$$

$$M_{31}^{(1)} = \frac{\partial^2}{\partial Y \partial z}, \quad M_{33}^{(1)} = 2 \nabla_{Hx} \cdot \nabla_{HX},$$

The other components of  $M^{(1)}$  are zero.

A.2. The operator  $\mathbf{L}$ 

The coefficients of the  $4 \times 4$  matrix  $\mathbf{L}$  in eq. (2.20) are given by

$$L = \begin{pmatrix} L_{11} & 0 & 0 & L_{14} \\ L_{21} & L_{22} & 0 & 0 \\ L_{31} & 0 & L_{33} & 0 \\ 1 & 0 & 0 & \Delta \end{pmatrix} \quad (\text{A } 5)$$

with

$$L_{11} = \mu_b \Delta^2 + 2 \frac{d\mu_b}{dz} \Delta \frac{\partial}{\partial z} + \frac{d^2 \mu_b}{dz^2} \left( \frac{\partial^2}{\partial z^2} - \Delta_H \right), \quad L_{14} = Ra \Delta_H, \quad (\text{A } 6)$$

$$L_{21} = \mu_b \Delta \frac{\partial^2}{\partial x \partial z} + \frac{d\mu_b}{dz} \frac{\partial}{\partial z} \left( \frac{\partial^2}{\partial x \partial z} \right), \quad L_{22} = \mu_b \Delta \Delta_H + \frac{d\mu_b}{dz} \frac{\partial}{\partial z} \Delta_H,$$

$$L_{31} = \mu_b \Delta \frac{\partial^2}{\partial y \partial z} + \frac{d\mu_b}{dz} \frac{\partial}{\partial z} \left( \frac{\partial^2}{\partial y \partial z} \right), \quad L_{33} = \mu_b \Delta \Delta_H + \frac{d\mu_b}{dz} \frac{\partial}{\partial z} \Delta_H.$$

### A.3. sub-scale $\mathbf{L}^{(0)}$

The components of  $\mathbf{L}^{(0)}$  in eq. (4.8) are

$$\begin{aligned}
L_{11}^{(0)} &= \mu_b \left( \nabla_{Hx}^2 + \frac{\partial^2}{\partial z^2} \right)^2 + 2 \frac{d\mu_b}{dz} \left( \nabla_{Hx}^2 + \frac{\partial^2}{\partial z^2} \right) \frac{\partial}{\partial z} + \frac{d^2\mu_b}{dz^2} \left( \frac{\partial^2}{\partial z^2} - \nabla_{Hx}^2 \right), \\
L_{14}^{(0)} &= Ra_c \nabla_{Hx}^2, \\
L_{21}^{(0)} &= \mu_b \left( \nabla_{Hx}^2 + \frac{\partial^2}{\partial z^2} \right) \frac{\partial^2}{\partial x \partial z} + \frac{d\mu_b}{dz} \frac{\partial}{\partial z} \left( \frac{\partial^2}{\partial x \partial z} \right), \\
L_{22}^{(0)} &= \mu_b \left( \nabla_{Hx}^2 + \frac{\partial^2}{\partial z^2} \right) \nabla_{Hx}^2 + \frac{d\mu_b}{dz} \frac{\partial}{\partial z} \nabla_{Hx}^2, \\
L_{31}^{(0)} &= \mu_b \left( \nabla_{Hx}^2 + \frac{\partial^2}{\partial z^2} \right) \frac{\partial^2}{\partial y \partial z} + \frac{d\mu_b}{dz} \frac{\partial}{\partial z} \left( \frac{\partial^2}{\partial y \partial z} \right), \\
L_{33}^{(0)} &= L_{22}^{(0)}, \\
L_{41}^{(0)} &= 1, \quad L_{44}^{(0)} = \left( \nabla_{Hx}^2 + \frac{\partial^2}{\partial z^2} \right).
\end{aligned} \tag{A 7}$$

### A.4. sub-scale $\mathbf{L}^{(1)}$

The components of  $\mathbf{L}^{(1)}$  in eq. (4.8) are

$$\begin{aligned}
L_{11}^{(1)} &= 4 \mu_b \left( \nabla_{Hx}^2 + \frac{\partial^2}{\partial z^2} \right) (\nabla_{Hx} \cdot \nabla_{HX}) + 4 \frac{d\mu_b}{dz} (\nabla_{Hx} \cdot \nabla_{HX}) \frac{\partial}{\partial z} - 2 \frac{d^2\mu_b}{dz^2} (\nabla_{Hx} \cdot \nabla_{HX}) \\
L_{14}^{(1)} &= Ra_1 \nabla_{Hx}^2 + 2Ra_c \nabla_{Hx} \cdot \nabla_{HX}, \\
L_{44}^{(1)} &= 2 \nabla_{Hx} \cdot \nabla_{HX}.
\end{aligned} \tag{A 8}$$

### A.5. sub-scale $\mathbf{L}^{(2)}$

A compléter...

## Appendix B. Second-order solution (hexagons)

### B.1. Solution proportional to $|A_p|^2$ (zero mode)

The first component of the second order solution, proportional to  $|A_p|^2$ , provides a correction of the basic state. Considering the  $w$ -equation, it is shown that the factor of  $|A_1|^2$ ,  $|A_2|^2$  and  $|A_3|^2$  in the non linear inertial  $NI_w^{(2)}$  and viscous  $NV_w^{(2)}$  terms vanishes,

therefore

$$w_1^{(2)} = 0. \quad (\text{B } 1)$$

Here  $w_1^{(2)}$  means the first component of the second order solution. Similarly, for the horizontal velocity, we have

$$u_1^{(2)} = v_1^{(2)} = 0. \quad (\text{B } 2)$$

There is no velocity for the zero mode. The correction of the conductive temperature profile can be written as  $\theta_1^{(2)} = T_1(z) [ |A_1|^2 + |A_2|^2 + |A_3|^2 ]$ , where  $T_1(z)$  satisfies

$$D^2 T_1 = 2 [G_{11}(DF_{11}) + F_{11}(DG_{11})], \quad (\text{B } 3)$$

with

$$T_1 = 0 \quad \text{at} \quad z = 0 \text{ and } z = 1. \quad (\text{B } 4)$$

As for the linear problem, equation (B 3) with the boundary conditions (B 4) is solved numerically using a spectral Chebyshev collocation method.

### B.2. Solution proportional to $A_p^2 \exp(2i\mathbf{k}_p \cdot \mathbf{r})$

The second component of the second order solution, proportional to  $A_p^2 E_p^2$ , where  $E_p = \exp(i\mathbf{k}_p \cdot \mathbf{r})$  represents the first harmonic of the fundamental. We have

$$(w_2^{(2)}, \theta_2^{(2)}) = (W_2(z), T_2(z)) (A_1^2 E_1^2 + A_2^2 E_2^2 + A_3^2 E_3^2) + c.c., \quad (\text{B } 5)$$

with

$$\begin{aligned} & \left[ \mu_b (D^2 - 4k_c^2)^2 + 2 \frac{d\mu_b}{dz} (D^3 - 4k_c^2 D) + \frac{d^2 \mu_b}{dz^2} (D^2 + 4k_c^2) \right] W_2 - 4k_c^2 Ra_c T_2 = \\ & \frac{2}{Pr} (F_{11} D^3 F_{11} - DF_{11} D^2 F_{11}) - [NV_w]_{A_p^2 E_p^2}^{(2)}, \end{aligned} \quad (\text{B } 6)$$

$$W_2 + (D^2 - 4k_c^2) T_2 = F_{11} DG_{11} - G_{11} DF_{11}. \quad (\text{B } 7)$$

The boundary conditions on  $W_2$  and  $T_2$  are identical to those on  $F_{11}$  and  $G_{11}$ , (3.10).

Concerning the horizontal velocity, we have

$$\nabla_{Hx}^2 \mathbf{u}_{H2}^{(2)} + \nabla_{Hx} \frac{\partial w_2^{(2)}}{\partial z} = 0. \quad (\text{B } 8)$$

We obtain,

$$\mathbf{u}_{H2}^{(2)} = \frac{DW_2}{4k_c^2} \nabla_{Hx} [A_1^2 E_1^2 + A_2^2 E_2^2 + A_3^2 E_3^2] + c.c.. \quad (\text{B } 9)$$

### B.3. Solution proportional to $A_p A_q^* E_p E_q^*$

The third component of the second order solution, proportional to  $A_p A_q^* E_p E_q^*$ , reads

$$(w_3^{(2)}, \theta_3^{(2)}) = (W_3(z), T_3(z)) (A_1 A_2^* E_1 E_2^* + A_1 A_3^* E_1 E_3^* + A_2 A_3^* E_2 E_3^*) + c.c., \quad (\text{B } 10)$$

with

$$\left[ \mu_b (D^2 - 3k_c^2)^2 + 2 \frac{d\mu_b}{dz} (D^3 - 3k_c^2 D) + \frac{d^2 \mu_b}{dz^2} (D^2 + 3k_c^2) \right] W_3 - 3k_c^2 R_a c T_3 = \frac{3}{Pr} (F_{11} D^3 F_{11} - k_c^2 F_{11} D F_{11}) - [NV_w]_{E_p E_q^*}^{(2)} \quad (\text{B } 11)$$

$$W_3 + (D^2 - 3k_c^2) T_3 = 2F_{11} D G_{11} - G_{11} D F_{11}. \quad (\text{B } 12)$$

Boundary conditions on  $(W_3, T_3)$  are the same as the ones on  $(F_{11}, G_{11})$ .

The horizontal velocity components satisfy

$$\nabla_{Hx}^2 \mathbf{u}_{H3}^{(2)} + \nabla_{Hx} \frac{\partial w_3^{(2)}}{\partial z} = 0. \quad (\text{B } 13)$$

We obtain

$$\mathbf{u}_{H3}^{(2)} = \frac{DW_3}{3k_c^2} \nabla_{Hx} (A_1 A_2^* E_1 E_2^* + A_1 A_3^* E_1 E_3^* + A_2 A_3^* E_2 E_3^*) + c.c. \quad (\text{B } 14)$$

B.4. Solution proportional to  $\exp(i\mathbf{k}_p \cdot \mathbf{r})$ 

The fourth component of the second order solution is proportional to  $\exp(i\mathbf{k}_p \cdot \mathbf{r})$  (resonant term). The solution is achieved using the solvability condition.

$$(w_4^{(2)}, \theta_4^{(2)}) = (W_{41}, T_{41}) E_1 + (W_{42}, T_{42}) E_2 + (W_{43}, T_{43}) E_3 + c.c., \quad (\text{B } 15)$$

with

$$\begin{aligned} & \left[ \mu_b (D^2 - k_c^2)^2 + 2 \frac{d\mu_b}{dz} (D^3 - k_c^2 D) + \frac{d^2 \mu_b}{dz^2} (D^2 + k_c^2) \right] W_{41} - Ra_c k_c^2 T_{41} = \\ & -4i\mu_b (D^2 F_{11} - k_c^2 F_{11}) (\mathbf{k}_1 \cdot \nabla_{HX}) A_1 + k_c^2 Ra_1 G_{11} A_1 - 2iRa_c (\mathbf{k}_1 \cdot \nabla_{HX}) A_1 + \\ & \frac{1}{Pr} (F_{11} D^3 F_{11} + 2DF_{11} D^2 F_{11} - 3k_c^2 F_{11} DF_{11}) A_2^* A_3^* - \left[ NV_w^{(2)} \right]_{E_1} A_2^* A_3^*, \quad (\text{B } 16) \\ & W_{41} + (D^2 - k_c^2) T_{41} = -2iG_{11} (\mathbf{k}_1 \cdot \nabla_{HX}) A_1 + (2F_{11} DG_{11} + G_{11} DF) A_2^* A_3^*. \end{aligned}$$

(B 17)

Similar equations are obtained for the amplitudes  $A_2$  and  $A_3$ . The boundary conditions on  $W_{41}$  and  $T_{41}$  are the same as the ones on  $(F_{11}, G_{11})$ .

For the horizontal velocity, we have

$$\mathbf{u}_{H4}^{(2)} = \mathbf{U}_{H41} E_1 + \mathbf{U}_{H42} E_2 + \mathbf{U}_{H43} E_3 + c.c., \quad (\text{B } 18)$$

with

$$\begin{aligned} & \mu_b (D^2 - k_c^2) \left( -k_c^2 \mathbf{U}_{H41} + i \nabla_{Hx} (\mathbf{k}_1 \cdot \mathbf{r}) \frac{\partial W_{41}}{\partial z} \right) + \\ & \frac{d\mu_b}{dz} \left( -k_c^2 \mathbf{U}_{H41} + i \nabla_{Hx} (\mathbf{k}_1 \cdot \mathbf{r}) \frac{\partial W_{41}}{\partial z} \right) = 2 \frac{d\mu_b}{dz} D^2 F_{11} \nabla_{HX} A_1 + \\ & \left[ \mu_b (D^3 F_{11} - k_c^2 DF_{11}) + \frac{d\mu_b}{dz} D^2 F_{11} \right] \left[ 2 \frac{\mathbf{k}_1}{k_c^2} \cdot (\mathbf{k}_1 \cdot \nabla_{HX} A_1) - \nabla_{HX} A_1 \right] \end{aligned} \quad (\text{B } 19)$$

- BIRD, R. B., AMSTRONG, R. & HASSAGER, O. 1987 *Dynamics of polymeric liquids*. New York: Wiley-Interscience.
- BOTTARO, A. & METZENER, P. 1992 Onset and two-dimensional patterns of convection with strongly temperature-dependent viscosity. *Phys. Fluids* **4**, 655–663.
- BOUTERAA, M., NOUAR, C., PLAUT, E., MÉTIVIER, C. & KALCK, A. 2015 Weakly nonlinear analysis of Rayleigh-Bénard convection in shear-thinning fluids: nature of the bifurcation and pattern selection. *J. Fluid. Mech.* **767**, 696–734.
- BUSSE, F.H. 1967 The stability of finite amplitude cellular convection and its relation to an extremum principle. *J. Fluid Mech.* **30**, 625–649.
- BUSSE, F. H. & FRICK, H. 1985 Square-pattern convection in fluids with strongly temperature-dependent viscosity. *J. Fluid. Mech.* **150**, 451–465.
- DAVAILLE, A. & JAUPART, P. 1993 Transient high Rayleigh number thermal convection with large viscosity variation. *J. Fluid. Mech.* **253**, 141–166.
- ECHEBARRÍA, BLAS & PÉREZ-GARCÍA, C. 1998 Phase instabilities in hexagonal patterns. *EPL (Europhysics Letters)* **43** (1), 35.
- ECHEBARRIA, B. & PEREZ-GARCIA, C. 2001 Stability of hexagonal pattern in Bénard-marangoni convection. *Phys. Rev. E* **63**, 066307.1–13.
- HOARD, C. Q., ROBERTSON, C. R. & ACRIVOS, A. 1970 Experiments on the cellular structure in bénard convection. *Int. J. Heat. Mass Transfer* **13**, 849–856.
- HOYLE, R. 1995 Nonlinear phase diffusion equations for the long-wave instabilities of hexagons. *Appl. Math. Lett.* **8**, 81–85.
- HOYLE, R. 2006 *Pattern formation. An introduction methods*. Cambridge: Cambridge University Press.
- JENKINS, D. R. 1987 Rolls versus squares in thermal convection of fluids with temperature-dependent viscosity. *J. Fluid. Mech.* **178**, 491–506.
- NEWELL, A.C. & WHITEHEAD, J.A. 1969 Finite bandwidth, finite amplitude convection. *J. Fluid Mech.* **38**, 279–303.
- PALM, E. 1960 On the tendency towards hexagonal cells in steady convection,. *J. Fluid Mech.* **8**, 183–192.

- PALM, E., ELLINGSEN, T. & GJEVIK, B. 1967 On the occurrence of cellular motion in bénard convection,. *J. Fluid Mech.* **30**, 651–661.
- SEGEL, L.A. 1969 Distant side-walls cause slow amplitude modulation of cellular convection. *J. Fluid Mech.* **38**, 203–224.
- SOLOMATOV, V. S. 1995 Scaling of temperature-and-stress-dependent viscosity convection. *Phys. Fluids* **7**, 266–274.
- STENGEL, KARL C., OLIVIER, DEAN S. & BOOKER, JOHN R. 1982 Onset of convection in a variable-viscosity fluid. *J. Fluid. Mech* **120**, 411–431.
- SUSHCHIK, M. M. & TSIMRING, L. S. 1994 The eckhaus instability in hexagonal patterns. *Physica D* **74**, 90–106.
- TANNER, R. 2000 Engineering rheology. Oxford University Press, New York.
- WHITE, D. B. 1988 The planforms and the onset of convection with a temperature dependent-viscosity. *J. Fluid. Mech* **191**, 2247–286.

## **Annexe B**

### **Articles significatifs publiés**

# Origin of the onset of Rayleigh-Bénard convection in a concentrated suspension of microgels with a yield stress behavior

C. Métivier,<sup>1,a)</sup> C. Li,<sup>2</sup> and A. Magnin<sup>2</sup>

<sup>1</sup>Laboratoire d'Energétique et de Mécanique Théorique et Appliquée, UMR 7563, Université de Lorraine, CNRS, Vandoeuvre-lès-Nancy, France

<sup>2</sup>Laboratoire Rhéologie et Procédés (LRP), Grenoble INP Institute of Engineering Université Grenoble Alpes, CNRS, F-38000 Grenoble, France

(Received 13 July 2017; accepted 16 September 2017; published online 5 October 2017)

In this paper, we propose to explore experimentally the origin of the onset of motion in a well-known Carbopol gel, a concentrated suspension of microgels, when submitted to a vertical temperature gradient, namely, the Rayleigh-Bénard Convection (RBC). We consider three possible scenarios: (i) the gel behaves as an elasto-viscoplastic material, (ii) the gel presents a low-stress viscosity  $\mu^+$  below the yield stress  $\tau_y$ , and (iii) the gel can be considered as a two phase system, say the microgels and the solvent, i.e., a porous medium. We propose a complete rheological characterization of Carbopol 940. Creep measurements lead to obtain an instantaneous viscosity plateau  $\mu^+ \sim t^m$  with  $m \approx 1$ . For the first time, we measure and provide permeability values  $k$  in the Carbopol gels. We show that  $k = O(10^{-14}) \text{ m}^2$  and  $k \propto \tau_y^{0.2}$ . Our study focuses on the reference case of the RBC with no-slip conditions at walls, and new results are provided. The results lead to the conclusion that the control parameter is the (inverse) of the yield number  $Y$ , ratio between the yield stress and the buoyancy stress, and they show that the critical value is  $1/Y_c \approx 80$  for no-slip conditions. One shows that both scenarios (i) and (ii) lead to recover  $1/Y$  as the control parameter. By considering the Carbopol gels as porous media [scenario (iii)], one finds that the critical porous Rayleigh-Darcy number is  $Ra_p = O(10^{-4})$ . Published by AIP Publishing. <https://doi.org/10.1063/1.4995699>

## I. INTRODUCTION

Concentrated suspensions of microgels are widely used in a large range of applications.<sup>1</sup> In particular, Carbopol gels are very popular for the last 50 years because they are easy to prepare and use. They are considered as near ideal yield stress fluids in rheology and in the fluid mechanics areas since they present a clear yield stress  $\tau_y$ , below which they behave mainly as an elastic solid, and above  $\tau_y$ , they present a shear thinning behavior, even at low weight concentrations  $C$  of Carbopol. The yield stress is due to the microstructure of the Carbopol gels which is a percolated, amorphous assembly of soft jammed particles, named as microgels.<sup>2–4</sup> These microgels consist in highly cross-linked regions where polymers are bound together leading to dense domains. Carbopol gels have received increased attention this last decade<sup>4–17</sup> in order to understand their structure and their fluidization mechanisms. This understanding is of utmost importance since the solid-liquid transition is responsible for the onset of motion in a lot of viscoplastic fluids. A situation where this transition is involved is the Rayleigh-Bénard convection (RBC). This configuration is of great interest since numerous industrial processes as well as natural settings involve natural convection, e.g., the mantle convection in Earth. The onset of motion in the RBC is driven by the buoyancy involved by a temperature difference  $\Delta T$  between the lower (hot) wall and the upper (cold) wall. In the case of Newtonian fluids,<sup>18–20</sup> convection occurs

when the buoyancy effects overcome the viscous and thermal diffusive effects, leading to the Rayleigh number  $Ra$  as the control parameter,

$$Ra = \frac{\rho g \beta \Delta T d^3}{\mu \kappa}, \quad (1)$$

where  $\rho$  is the density,  $g$  is the gravitational acceleration,  $\beta$  is the thermal volume expansion,  $d$  is the fluid layer,  $\mu$  is the viscosity, and  $\kappa$  is the thermal diffusivity. Few studies have been devoted to the RBC in yield stress fluids. Theoretical studies<sup>21–23</sup> have considered an inelastic yield stress fluid (Bingham model) and show that for a finite yield stress the motionless solution is linearly stable at all  $Ra$  values and is conditionally stable otherwise. These conclusions mean that the RBC cannot occur in viscoplastic fluids regarding small amplitude perturbations. This is in contradiction with recent experimental results<sup>24,25</sup> which have observed the onset of convection in a yield stress fluid without adding any perturbation. The first experimental study<sup>24</sup> shows that the control parameter is the (inverse) of the yield number  $Y$ , the ratio between the buoyancy stress and the yield stress,

$$Y^{-1} = \frac{\rho g \beta \Delta T d}{\tau_y}. \quad (2)$$

Darbouli *et al.*<sup>24</sup> show that criticality depends on the boundary conditions. A recent review on slippage,<sup>26</sup> in the particular case of microgel suspensions, highlights the importance to take into account this phenomenon. Based on an extensive work, Darbouli *et al.* show that for slip conditions “S” in

<sup>a)</sup>Christel.Metivier@univ-lorraine.fr

the Rayleigh-B  nard cavity (use of glass, copper alloy, and PMMA walls), criticality is such as  $1/Y_c^S \approx 40$ . Darbouli *et al.* show that by defining the control parameter  $Y$  with the yield stress at the interface  $\tau_f$  instead of the bulk yield stress  $\tau_y$ , the results converge to  $1/Y_c \approx 80$ . The case of no-slip conditions “NS” was only considered for one experiment,<sup>24</sup> leading to  $1/Y_c^{NS} \approx 80$ .

Further experiments in the case of slip conditions have been proposed by Kebiche *et al.*<sup>25</sup> which confirm that  $1/Y$  is the adequate control parameter. However, the criticality is significantly smaller ( $1/Y_c^S \approx 5$ ) which is certainly due to their boundary conditions: slippage at walls and weak conductivity at the horizontal boundaries. These conditions are all known to decrease significantly critical conditions in Newtonian fluids.<sup>34-36</sup> However it is difficult to compare quantitatively these two studies since Kebiche *et al.*<sup>25</sup> do not evaluate clearly neither the level of the gel’s slippage at walls nor the wall’s conductivity in their experiments.

In the field of natural convection in Carbopol gels, one can also highlight the experimental work of Davaille *et al.*<sup>27</sup> This work investigates the onset of thermal plumes when a viscoplastic fluid layer is submitted to a localized heating. The authors show that convection occurs around the heater above a critical value  $1/Y_{c1} = 120(\pm 15)$  and plumes develop above  $1/Y_{c2} = 260(\pm 20)$ . The value of  $1/Y_{c1}$  is numerically confirmed by Karimfazli *et al.*<sup>28</sup>

In spite of these recent studies,<sup>24,25,27</sup> the origin of the onset of motion in Carbopol gels when heated from below is still not well understood. Darbouli *et al.*<sup>24</sup> proposed three possible scenarios which could be at the origin of the onset of the RBC in Carbopol gels. The first scenario (i) consists in considering the Carbopol gels as elasto-viscoplastic materials, especially below and close to the yield stress. This scenario received a first consideration in the work of Darbouli *et al.*<sup>24</sup> in the RBC case with slip conditions at walls and in the work of Davaille *et al.*<sup>27</sup> in the case of thermal plumes. The second scenario (ii) is a viscous scenario; it consists in considering a finite viscosity at low values of shear rates. This scenario has been numerically investigated by Massmayer *et al.*<sup>29</sup> in the case of thermal plumes and by Li *et al.*<sup>30</sup> in the RBC case. These studies consider regularized models of a Herschel-Bulkley fluid. In the first study,<sup>29</sup> the authors consider the regularization proposed by de Souza Mendes and Dutra,<sup>31</sup> and in the second study,<sup>30</sup> the Papanastasiou regularization is considered. The use of regularized models can provide information; however, they present some problems regarding the regularized parameter;<sup>32,33</sup> furthermore, they are not realistic models. This is all the more true when regarding recent studies<sup>10,14,15</sup> which have provided rheological measurements in Carbopol gels below the yield stress. In these studies, an instantaneous viscosity plateau  $\mu^+$  has been measured below the yield stress. The value of  $\mu^+$  is defined as the ratio between the imposed stress  $\tau$  and the measured shear rate  $\dot{\gamma}$ . It has been shown that  $\mu^+$  depends on the delay time:  $\mu^+ \approx t^m$ . It means that below the yield stress, the Carbopol gels do not lead to a constant (Newtonian) viscosity but to a constant value of viscosity at fixed time. The third proposed scenario (iii) would consist in considering the microstructure of the gels, i.e., a structure composed by percolated elastic microgels and pools of solvent all around. In this

sense, the motion could first occur in these pools of a Newtonian solvent (water) inducing then a sufficient level of stress in the bulk up to yield the whole material. In this scenario, one would consider the Carbopol gels as a particular class of porous media.

While the scenario (i) has to be considered in the case of no-slip conditions, the scenarios (ii) and (iii) have never been investigated.

The present paper aims to investigate the origin of the onset of the RBC in Carbopol gels. For this, we propose to study the different scenarios (i)-(iii) outlined above and especially the scenarios (ii) and (iii). Section II is dedicated to present the structure of our working system as well as its rheometry. In order to explore the scenario (iii) which considers the gels as porous media, one section is dedicated to present permeability measurements in our Carbopol gels. To our best knowledge, this is the first time that the permeability of Carbopol gels is provided. Because the reference case of the RBC in Carbopol gels with no-slip conditions has been understudied (only one experiment has been performed), our study focuses on this case, and new results are provided in Sec. IV. Finally all scenarios are discussed in Sec. V which also includes a conclusion.

## II. MATERIALS AND RHEOMETRY

Carbopol gels are considered as simple yield stress fluids<sup>8,9</sup> by contrast with that ones which present thixotropy. Carbopol is a polymer made of cross-linked polyacrylic acid. When mixed with water, a turbid dispersion is obtained with an acid pH. The yield stress appears when the dispersion is neutralized by adding sodium hydroxide around pH = 7. During this process, the carboxyl group is ionized leading to repulsive forces. Molecules swell in the whole space due to an outward osmotic pressure in the presence of ions.<sup>37</sup> The swollen microgel size is about 2-20  $\mu\text{m}$ <sup>4,7,13</sup>, depending on the pH, the ionic strength, the degree of ionisation, and the concentration.

In the present study, we use Carbopol 940 from BF Goodrich in the range of concentrations  $0.035\% < C < 0.12\%$ . In this concentration domain, the material consists in a weak percolated structure containing pools of solvent and fully swollen microgels. Because the weight concentration of the microgel is sensitive to many parameters, our gels will be referred to their rheological properties, in particular their respective yield stress value  $\tau_y$  ranging from 0.02 Pa to 6 Pa as indicated below. The Carbopol gels present an elasto-viscoplastic behavior. Below the yield stress, a linear viscoelastic regime is observed under small amplitude oscillatory shear (SAOS) measurements, highlighting a solid elastic response regarding small deformation. Figure 1 displays the elastic modulus  $G'$  and the loss (viscous) modulus  $G''$  as a function of the strain  $\gamma$  for two different Carbopol gels. The linear domain is defined for  $\gamma < 1\%$ , where  $G'$  and  $G''$  are constants. In this regime, the Carbopol gels present a dominant elastic behavior since  $G' > G''$ . For larger strain values, the moduli decrease, and they cross at a critical strain value  $\gamma_c$ . For our Carbopol gels, we find  $\gamma_c \approx 10\%$ . The stress measured at this particular value of strain, i.e.,  $\tau_c = G'\gamma_c$ , is a

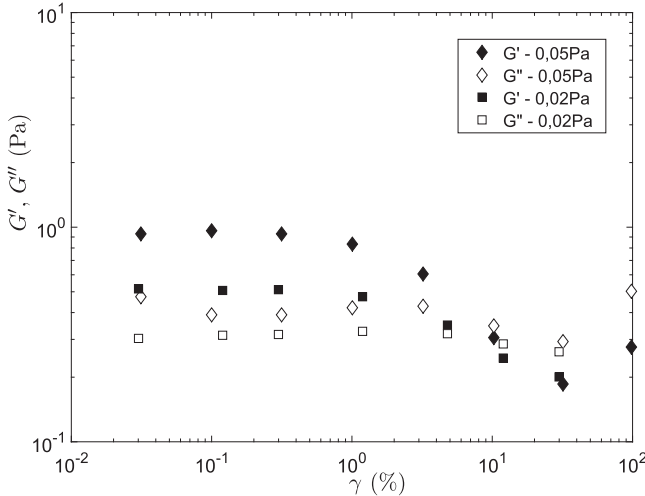


FIG. 1. Elastic modulus (full symbols) and loss modulus (empty symbols) as a function of the strain for two Carbopol gels ( $\phi$ :  $\tau_y = 0.05$  Pa and  $\square$ :  $\tau_y = 0.02$  Pa) at  $\omega = 10$  rad/s.

good estimation of the yield stress  $\tau_y$ . One finds  $\tau_c = 0.047$  Pa (respectively,  $\tau_c = 0.022$  Pa) for the gel characterized by  $\tau_y = 0.05$  Pa (respectively,  $\tau_y = 0.02$  Pa) with steady-state rheometry.

In SAOS rheometry,  $G'$  and  $G''$  are measured by varying the oscillation pulsation  $\omega$  (or frequency) in the linear regime. In this respect, we fix the strain to 0.5% which implies a maximal stress value of 0.01 Pa ( $<\tau_y$ ). As given in Fig. 2, the Carbopol, characterized by  $\tau_y = 0.05$  Pa, displays a dominant elastic modulus for all values of  $\omega$  and  $\gamma = 0.5\%$ . The elastic modulus  $G'$  is found one order larger than the viscous modulus  $G''$ . Similar tendencies are observed for all the Carbopol gels used.

Above the yield stress, the Carbopol flow curves are well fitted by the Herschel-Bulkley (HB) model given by

$$\tau = \tau_y + K\dot{\gamma}^n, \quad (3)$$

where  $\dot{\gamma}$  is the shear rate,  $K$  is the consistency, and  $n = 0.3\text{--}0.6$  is the shear thinning coefficient. Flow curves of the Carbopol

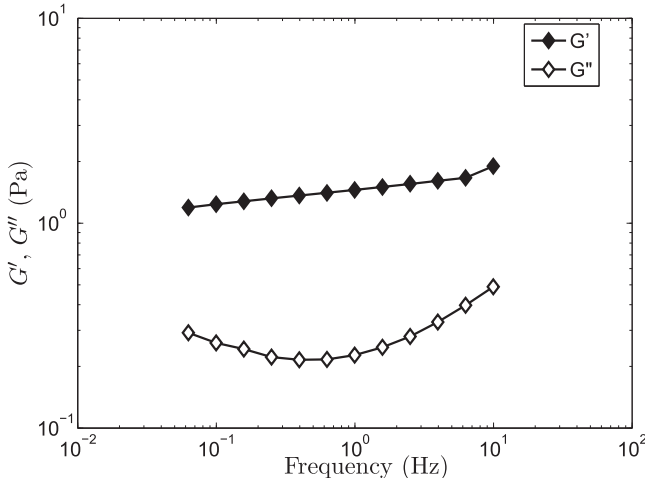


FIG. 2. Elastic and loss moduli for a Carbopol gel ( $\tau_y = 0.05$  Pa) at  $\gamma = 0.5\%$ .

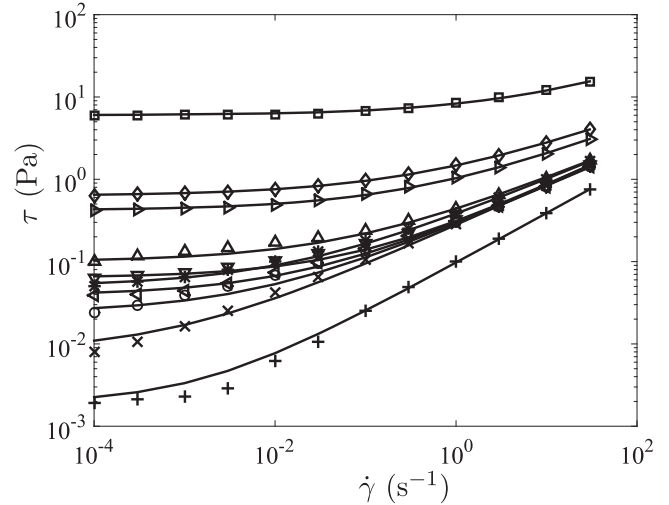


FIG. 3. Steady-state flow curves of different Carbopol gels— $\tau_y = 0.002$  Pa, 0.008 Pa, 0.02 Pa, 0.039 Pa, 0.05 Pa, 0.063 Pa, 0.1 Pa, 0.42 Pa, 0.63 Pa, 6 Pa (from + to  $\square$  symbols), straight lines: the Herschel-Bulkley model.

gels used in our study are obtained by performing steady-state rheometry. Results are shown in Fig. 3. Results are nicely fitted by the Herschel-Bulkley model given by Eq. (3) and represented by straight lines. At low Carbopol concentrations (low yield stress values), one can observe some discrepancies between the Herschel-Bulkley model and the experimental data. These discrepancies are due to the increase in the measurement errors when the yield stress values are weak. In the following, we fix the yield stress value of our Carbopol gels to the value measured at  $\dot{\gamma} = 10^{-4}$  s<sup>-1</sup>, which is also a value fixed in the Herschel-Bulkley fitting procedure.

## A. Fluidization mechanisms

In the last decade, several studies<sup>5,6,10,12</sup> have explored the fluidization mechanisms in Carbopol gels under imposed shear stress. This situation is of great interest to our study since it is involved in the natural convection experiments where buoyancy stresses are increased from a motionless state (conductive regime) to the onset of motion (convection regime). When the imposed shear stress is larger than the residual stresses  $\tau_r$ , these surveys observe three regimes before reaching the steady flow regime modeled by the HB law:

- (1) A first regime corresponds to an elastic response of the material over short times whatever the applied stress is.
- (2) Then, the microgels experience a creep deformation below the yield stress. It is shown that the deformation rate presents a slow decay characterized by a power law  $\dot{\gamma} \propto t^{-p}$ , similar to Andrade's law as observed in solid materials.<sup>39,40</sup> Values of  $p$  vary depending on the literature, i.e.,  $p = 2/3$  in the case of Carbopol ETD 2050 gels,<sup>12,15</sup> while  $p = 1$  in the case of hair gels, Carbopol 940 gels, and composite materials.<sup>5,6,40</sup> Andrade's creep finds its origin in the dynamics of dislocations of soft metals' microstructure. After several studies,<sup>41,42</sup> heterogeneous materials as well as jammed systems (e.g., gels, foams and granular media) exhibit similar mechanisms as the metals such as the primary creep regime.

Furthermore, Moller *et al.*<sup>10</sup> have also measured a creep below the yield stress characterized by a low-stress viscosity plateau  $\mu^+$  which depends on the delay time following a power law  $\mu^+ \propto t^m$ , with  $m = 0.6$  in the case of Carbopol Ultrez U10 gels. This viscosity corresponds to an instantaneous value since no steady-state shear is observed in this regime. By performing large amplitude oscillatory shear stress (LAOSTress), Dimitriou *et al.*<sup>14</sup> found a similar tendency with  $m = 0.9$  in Carbopol 901. The authors show that this apparent viscosity  $\mu^+$  can be predicted by the kinetic hardening since the Carbopol is not a perfect elastic solid below the yield stress. Kinetic hardening accounts for dynamical movement of the yield surface (in stress space), involving that the yield stress of the material evolves dynamically with time as the material is deformed.

Similarly, we have performed creep measurements below yielding, i.e., a shear stress is imposed and the shear rate is recorded (Fig. 4). Different time measurements (1200 s, 2000 s, 3600 s, 10 800 s) have been performed in order to investigate the time dependency of results below yielding. These creep times are the same order of typical times involved in our Rayleigh-Bénard experiments. A result of particular interest is the measurement of an apparent viscosity  $\mu^+ = \tau/\dot{\gamma}$  below the yield stress  $\tau_y$  (Figs. 4 and 5). As obtained in the literature, the apparent viscosity displays a constant value which varies with time as  $\mu^+ \sim t^m$  (Fig. 6), where  $m \approx 1$  within our measurement's resolution. This value is close to the ones obtained by Dimitriou *et al.*<sup>14</sup> ( $m = 0.9$ ), Coussot *et al.*,<sup>5</sup> and Caton and Baravian<sup>6</sup> ( $m = 1$ ). When the applied shear stress  $\tau_a$  is larger than  $\tau_y$ , the steady-state regime is reached and follows the HB law as shown in Figs. 4 and 5.

One can note that when the applied stress is such that  $\tau < \tau_r (< \tau_y)$ , a recent study<sup>15</sup> shows that residual stresses in the Carbopol gel can play a significant role and can lead to “anomalous” creep response, meaning that relaxing residual stresses tend to deform the gel in the opposite direction to that of preshear. In their experiments, Lidon

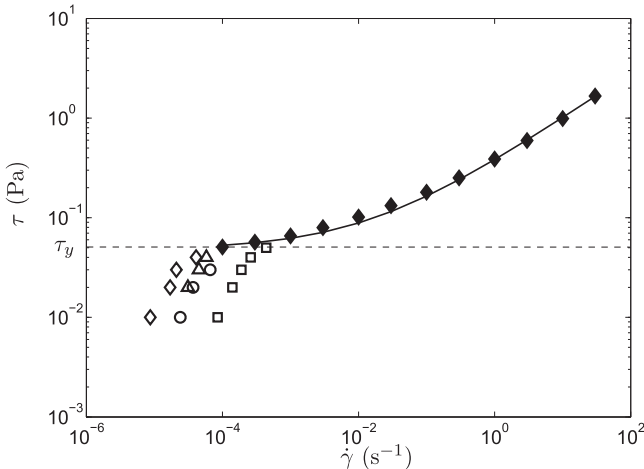


FIG. 4. Creep measurements for different time tests and one Carbopol gel ( $\tau_y = 0.05$  Pa)—◊: 10 800 s, △: 3600 s, ○: 2000 s, □: 1200 s, ♦: steady-state measurements for  $\tau_a > \tau_y$ , continuous line: the Herschel-Bulkley model.

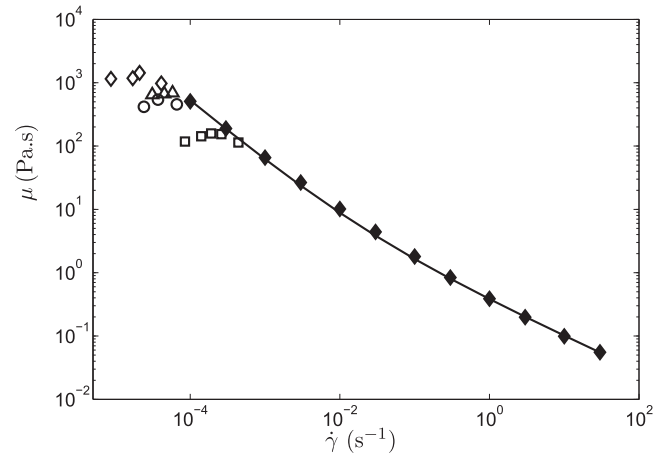


FIG. 5. Viscosity  $\mu$  as a function of shear rate obtained by creep measurements for different time tests and one Carbopol gel ( $\tau_y = 0.05$  Pa)—◊: 10 800 s, △: 3600 s, ○: 2000 s, □: 1200 s, ♦: steady-state measurements for  $\tau_a > \tau_y$ , continuous line: the Herschel-Bulkley model.

*et al.*<sup>15</sup> estimated the level of residual stresses around 20% of the yield stress. Residual stresses have already been observed by Piau<sup>4</sup> and Coussot *et al.*,<sup>5</sup> who showed that Carbopol gels can experience a significant level of stress relaxation. This phenomenon can have significant consequences as highlighted in the context of bubble rise,<sup>38</sup> for instance.

- (3) At the end of Andrade's creep regime, a minimal value of shear rate is observed,<sup>5,6,12</sup> then for larger time,  $\dot{\gamma}$  increases in a more or less abrupt way until the steady-state flow is reached. This regime corresponds to the total fluidization of the Carbopol gel. It is characterized by a total wall slip even with rough boundary conditions and by a transient shear banding which nucleates at the rotor and extends across the gap.<sup>11,12</sup> Full fluidization of the material is reached at the time  $t_f$  after which the velocity profiles across the gap remain homogeneous and steady. Divoux *et al.*<sup>11,12</sup> show that  $t_f \sim 272/\dot{\gamma}^{2.3}$  in their working system and also that  $t_f = D(\tau - \tau_y)^{\beta_1}$ , where  $D$  and  $\beta_1$  depend on the Carbopol concentration.

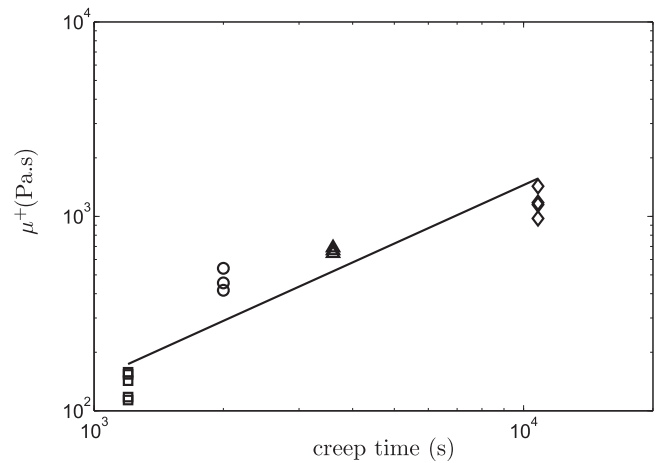


FIG. 6. Viscosity as a function of the creep time obtained by creep measurements for one Carbopol gel ( $\tau_y = 0.05$  Pa)—◊: 10 800 s, △: 3600 s, ○: 2000 s, □: 1200 s, continuous line: slope 1 ( $m = 1$ ).

### III. GELS' PERMEABILITY MEASUREMENTS

#### A. Experimental setup

The Carbopol gel sample of height  $e$  is contained in a cylindrical cell, closed at the upper and lower parts by two membranes made of a mixed cellulose ester (MF-Millipore, ref. GSWP04700). The size of the membrane pores is  $0.22\ \mu\text{m}$ , i.e., at least one order smaller than the microgel size (around  $2\text{-}20\ \mu\text{m}$ ). In addition, two millipore filters support the membranes and the porous medium. Similarly to the work of Ambari *et al.*,<sup>43</sup> who measured the permeability in deformable porous media such as gels, we use two vertical and parallel capillary tubes in order to generate the flow through the gel sample via an initial difference in height  $\Delta H_0$  leading to a pressure drop  $\Delta P$ . Here, the tubes are connected to the upper and lower parts of the cell. The whole system is full of solvent (water). The level of the capillary tube is measured with an accuracy of  $100\ \mu\text{m}$ .

At steady state, the permeability  $k$  is given by Darcy's law,

$$k = \frac{Q\mu e}{S\Delta P}, \quad (4)$$

where  $Q$  corresponds to the water flow rate through the porous medium (here Carbopol microgels),  $\mu$  is the viscosity of the solvent (water), and  $S$  is the cross-sectional area to flow. The flow rate  $Q$  is evaluated via the height variation  $h(t)$  of the meniscus in one capillary tube,  $Q = \frac{h(\delta t)\Sigma}{\delta t}$ , with  $\Sigma$  the diameter of the capillary and  $\delta t$  the measurement time. The pressure drop  $\Delta P$  is evaluated as follows:

$$\Delta P = \rho g (\Delta H_0 - 2h(t)). \quad (5)$$

One notices that measurements done without any gel in the cell show that the hydraulic resistance<sup>44</sup>  $R_h$  of the setup is two orders of magnitude smaller than the Carbopol gels' hydraulic resistance. In this way, the intrinsic resistance of the setup has been neglected in Eq. (5).

#### B. Permeability measurements

Two different fluids have been considered to flow through the Carbopol gels. The first solvent is distilled water (circles and squares in Fig. 7), and the second one is the liquid phase (triangles in Fig. 7) extracted directly from a Carbopol gel. This latter fluid has a similar physico-chemical composition to that of the Carbopol gels. The fluid phase has been extracted from a Carbopol gel by using a  $0.22\ \mu\text{m}$  filter cell under pressure. No significant difference between the two solvents was observed as shown in Fig. 7.

Mougin *et al.*<sup>38</sup> have shown that the trajectory of quasi-static bubbles in Carbopol gels presents a preferential path due to residual internal stresses in the gels. In the permeability measurements, the existence of such preferential paths for the solvent flow could modify significantly the  $k$  values. In this sense, we have verified that the flow is homogeneous in the whole volume of the setup by introducing a colored solvent in the gel. One observed that the colored water diffuses homogeneously in the whole sample. The independence of  $k$  values with  $\Delta H_0$  has also been verified by testing different values of initial height (2 cm and 12 cm). For larger  $\Delta H_0$  values

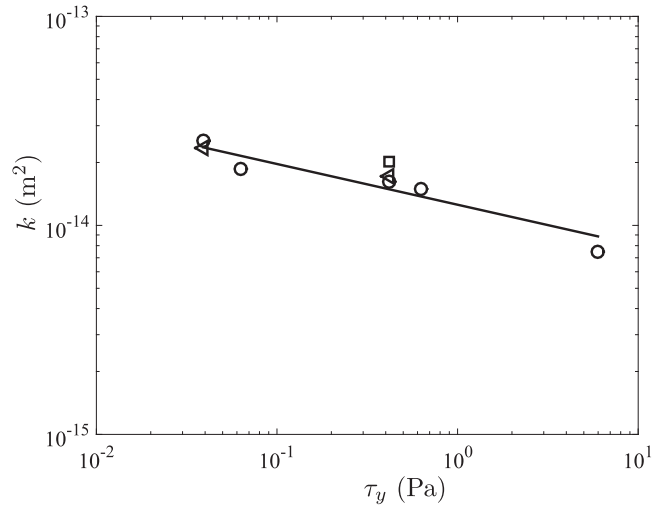


FIG. 7. Permeability as a function of the yield stress—○:  $\Delta H_0 = 2\text{ cm}$ , distilled water; □:  $\Delta H_0 = 12\text{ cm}$ , distilled water; △:  $\Delta H_0 = 2\text{ cm}$ , Carbopol liquid phase as the solvent; continuous line: slope  $-0.2$ .

such as  $\Delta H_0 = 60\text{ cm}$ , microgels deform, and one observes a large compacting of microgels. The compacting is such that one can observe an interface where the microgel concentration is very large. It traduces that our microgel suspension consists in a deformable medium when submitted to pressure. The initial pressure corresponding to  $\Delta H_0 = 60$  is close to 6000 Pa.

The gels' permeability as a function of the yield stress is displayed in Fig. 7. As expected, one observes that the permeability decreases with increasing values of  $\tau_y$  which is correlated with the increase in the microgel concentration. In the range of tested gel concentrations, one obtains  $k \propto \tau_y^{-0.2}$ . One can notice the relatively weak values of permeability since  $k = O(10^{-14})\text{m}^2$ . These values agree with the permeability values obtained in other gels such as polyacrylamide gels<sup>45-47</sup> and agarose gels.<sup>48</sup> These results confirm that the cross-linked regions (microgels) represent a non-draining or weak-draining core and that microgels are surrounded by a rather dilute freely draining zone as also observed in polyacrylamide gels.<sup>45-47</sup>

In their article, Ketz *et al.*<sup>2</sup> proposed a way to evaluate the permeability of the Carbopol gels by considering dimensional and structural arguments, leading to the following relationship:

$$k = \frac{\mu R^2}{G t_c}, \quad (6)$$

where  $\mu$  is the solvent viscosity,  $R$  is the microgel radius,  $G$  is the modulus of the microgel network, and  $t_c$  is the characteristic time for the volume equilibration after the gel network has been deformed which leads to changes in the microgel volume. Below the yield stress, one can evaluate from our measurements (see Fig. 1)  $G \approx G' = O(1)\text{ Pa}$  and  $t_c = O(10)\text{ s}$ . The solvent viscosity is that of water, i.e.,  $\mu = 10^{-3}\text{ Pa s}$ , and one can estimate a mean radius of the microgels<sup>4,7,13</sup>  $R = O(10^{-5})\text{ m}$ . By considering these values, one can obtain an estimation of the permeability  $k \approx 10^{-14}\text{ m}^2$  which agrees with our measurements.

#### IV. RAYLEIGH-BÉNARD CONVECTION

The Rayleigh-Bénard cavity is a circular cell of  $D = 179$  mm as the diameter and three different height values

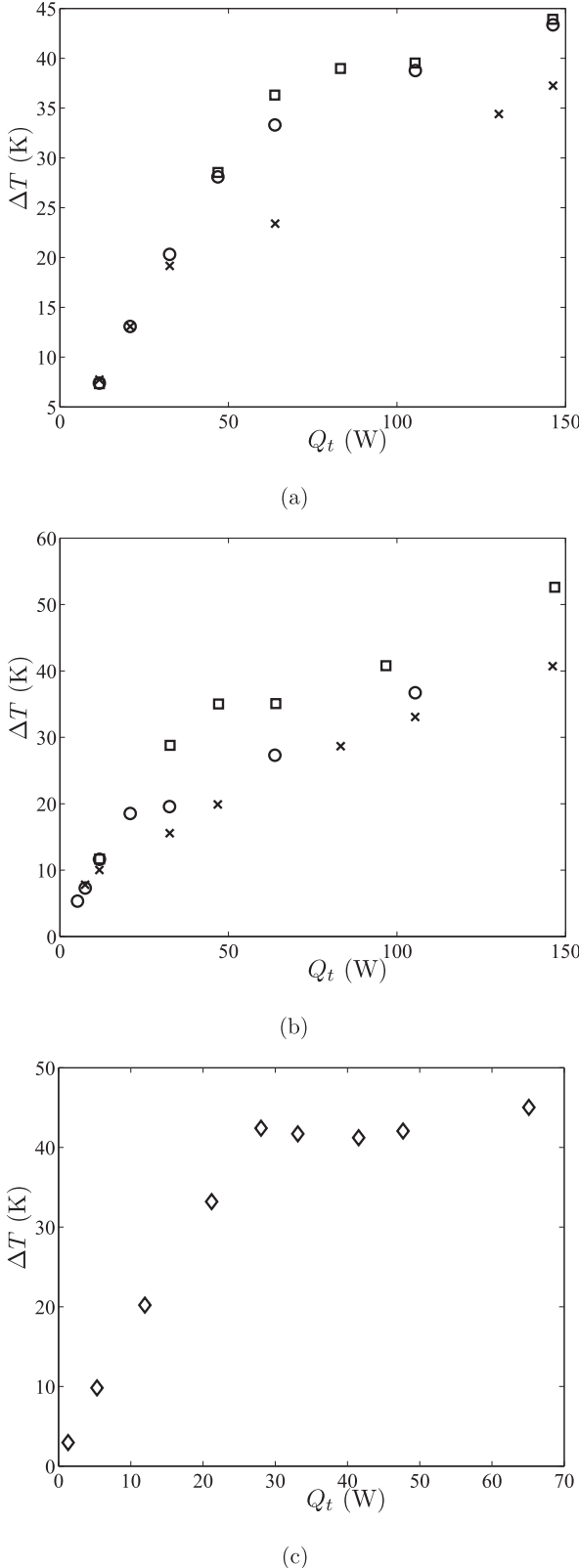


FIG. 8. Variations of  $\Delta T$  as a function of  $Q_t$  for different Carbopol gels ( $\diamond$ :  $\tau_y = 0.05$  Pa,  $\square$ :  $\tau_y = 0.02$  Pa,  $\circ$ :  $\tau_y = 0.008$  Pa,  $\times$ :  $\tau_y = 0.002$  Pa) and for (a)  $d = 10$  mm, (b)  $d = 17$  mm, and (c)  $d = 30$  mm.

$d = 10, 17$ , and  $30$  mm corresponding, respectively, to aspect ratio values  $\Gamma (=D/d)$  of  $18, 10$ , and  $6$ . The total heat flux  $Q_t$  of the bottom wall is controlled by means of an electrical heater plate, and the temperature upper wall is controlled via a (cold) water flow. The Polymethyl Methacrylate (PMMA) side walls of  $30$  mm thickness involve adiabatic conditions. Further technical details of the setup can be obtained from the work of Darbouli *et al.*<sup>24</sup> No-slip conditions at walls have been obtained by treating the cavity surfaces with a solution of polyethylenimine (PEI) in water.<sup>53</sup> This treatment is very useful since it allows us to obtain no-slip conditions on hydrophobic, smooth, and transparent walls such as glass (borosilicate) or PMMA walls, without modifying their transparency.<sup>53</sup> Four Carbopol gels ( $\tau_y = 0.002$  Pa,  $0.008$  Pa,  $0.02$  Pa, and  $0.05$  Pa) have been tested in the Rayleigh-Bénard setup. Temperature measurements are done at any time by thermocouples. The onset of convection is determined by using the Schmidt-Milverton principle<sup>54</sup> which considers that in the conductive regime,  $Q_t$  is proportional to the horizontal walls' temperature difference  $\Delta T = T_2 - T_1$ . These curve variations evolve significantly with the onset of convection. The convection tends to homogenize the temperature in the cavity, meaning that the variations of  $\Delta T$  vs.  $Q_t$  lead to a decrease in the curve slope as one can observe in Fig. 8 for different cavity heights  $d$ . One can notice that each value displayed in Fig. 8 has been obtained at steady state. At each change in  $Q_t$  values, we wait several hours up to  $10$  h in order to reach the steady state. In the conductive regime, one waits around  $2$  h to ensure that the linear profile of temperature is reached in the fluid layer. At the onset of convection and in the convective regime one waits  $6$ – $10$  h.

In order to highlight the governing parameter, values of  $\beta\Delta T_c/\tau_y$  are displayed as a function of  $d$  in Fig. 9. Similarly to the work of Darbouli *et al.*,<sup>24</sup> one obtains  $\beta\Delta T/\tau_y \propto d^{-1}$ , meaning that the governing dimensionless number is the (inverse) of the yield number as defined in Eq. (2). For all this set of experiments, one obtains

$$Y_c^{-1} = 80 \pm 15. \quad (7)$$

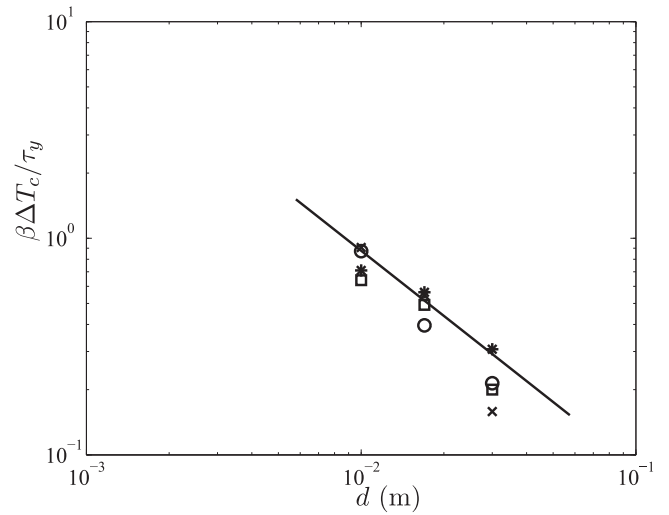


FIG. 9. Variation of  $\beta\Delta T_c/\tau_y$  as a function of  $d$  for Carbopol gels ( $\square$ :  $\tau_y = 0.02$  Pa,  $\circ$ :  $\tau_y = 0.008$  Pa,  $\times$ :  $\tau_y = 0.002$  Pa,  $*$ : results obtained by Darbouli *et al.*<sup>24</sup>)—continuous line: slope  $-1$ .

The physical origin of this number is discussed below considering the scenarios (i)-(iii).

## V. DISCUSSION AND CONCLUSION

- (i) The first proposed scenario has been well developed in the work of Darbouli *et al.*<sup>24</sup> in the slip case by considering an elasto-plastic material, i.e., a solid with an elastic response and then a plastic response when the stress (or strain) increases till  $\tau_y$ . In the elastic regime, the internal stress writes  $\sigma = G'\gamma$ . As shown in the SAOS measurements, when the flow occurs, the stress scale is such as  $G'\gamma_c = \tau_y$ . Based on SAOS measurements, a viscosity is introduced  $\mu^* = \frac{\sqrt{G'^2 + G''^2}}{\omega}$ , and a characteristic scale for the viscosity can be derived as  $\mu = \frac{\tau_y d^2}{\kappa}$ , where the diffusion time  $d^2/\kappa$  is the time scale. By replacing this scale in the Rayleigh number given by Eq. (1), one recovers the inverse of the yield number given by Eq. (2). In this particular case, the inverse of the yield number, i.e., the ratio between the buoyancy and the yield stress effects, is a generalized Rayleigh number  $Ra_g$ .
- (ii) Another possible scenario consists in considering the Rayleigh number for a viscous fluid  $Ra$  defined in Eq. (1) and determining a viscosity scale  $\mu$  obtained by creep rheometry close to the yield stress. By performing creep measurements, we have obtained a viscosity  $\mu^+$  which depends on the creep time such as  $\mu^+ = Bt^m$  with  $m \approx 1$ . If one considers the diffusion time  $d^2/\kappa$  as the time scale and  $m = 1$ , then one obtains

$$Ra = \frac{\rho g \beta \Delta T d^{3-2m}}{B \kappa^{m-1}} = \frac{\rho g \beta \Delta T d}{B}. \quad (8)$$

If  $m = 1$ , the dimension of  $B$  is the same as a stress. In creep measurements below the yield stress value,  $\tau_y$  appears as the upper bound for  $B$ . In this sense, one considers the yield stress as the scale for  $B$ , i.e.,  $B = \tau_y$  in Eq. (8) leading to the generalized Rayleigh number  $Ra_g = 1/Y$  as defined in Eq. (2).

- (iii) In this scenario, we consider the microstructure of the Carbopol gel as a matrix solid (percolated microgels) and a Newtonian fluid (water) all around. For this reason, we are interested in the Rayleigh-B  nard convection of Newtonian fluids in a porous medium. This configuration has been first investigated by Horton and Rogers<sup>49</sup> and Lapwood.<sup>50</sup> In their studies, the authors consider a layer of a porous medium confined by two horizontal walls where an adverse temperature gradient is imposed. It is assumed that the medium is homogeneous and isotropic, that the solid matrix is non-deformable, and that Darcy's law is valid. By considering these assumptions, the Horton-Rogers-Lapwood (HRL) problem leads to define the Rayleigh-Darcy number  $Ra_p$  which is the product of the Darcy number  $k/d^2$  and the Rayleigh number [Eq. (1)],

$$Ra_p = \frac{k \rho g \beta_l \Delta T d}{\kappa_l \mu_l}, \quad (9)$$

where the index  $l$  stands for the "liquid" phase. The linear stability analysis of this problem shows that the critical Rayleigh value obtained for solid porous media is 27.10 independently of the permeability  $k$  of the medium. This critical value is obtained when considering similar boundary conditions as those of our experiments, i.e., impermeable walls, isothermal and no-slip conditions on the upper wall, an imposed heat flux and no-slip conditions on the lower wall but considering an infinite layer of a porous medium.<sup>51,52</sup> It has been shown by Wang<sup>55</sup> that the critical Rayleigh-Darcy value can be modified depending on the aspect ratio of the cavity. Nevertheless, Wang<sup>55</sup> showed that in the range of  $\Gamma = 2$  to  $\Gamma = 6$ , the critical Rayleigh-Darcy value varies slightly (maximal value of 28.6) compared with the infinite layer case.

In the case of microgel suspensions, considered here as tenuous porous media, one has evaluated  $Ra_p$  at criticality with the values of  $k$  obtained previously (Sec. III B) and by considering water as the liquid phase all around the microgels. Results are displayed in Fig. 10, and they highlight a large difference with the HRL problem since  $Ra_p = O(10^{-4})$  in the case of our gels at criticality. Furthermore, results in our gels show that the critical  $Ra_p$  values depend on  $k$  and hence  $\tau_y$  as one can notice in Fig. 10. One would have expected an independence of  $Ra_p$  with  $k$  (and  $\tau_y$ ) because the microstructure of the gels remains quite similar in the range of the tested Carbopol concentrations (dispersion of fully swollen microgels). The dependency of  $Ra_p$  with  $k$  could imply that the Horton-Rogers-Lapwood problem is not appropriate to the Carbopol case. It leads to the conclusion that the analogy to porous media, at least the analogy to the HRL problem, fails. On the one hand, one could simply think that the analogy fails because the onset of convection is not only characterized by the motion of the solvent but by the motion of the bulk material. It means that the convection would be characterized by the movement of the individual gel particles

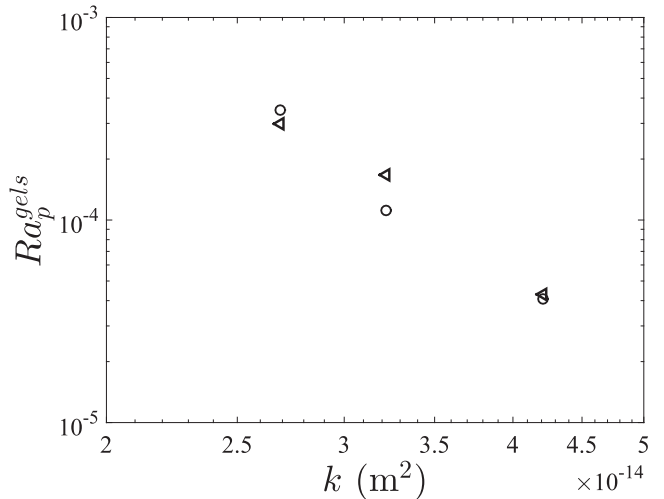


FIG. 10. Critical porous Rayleigh number in the case of Carbopol gels  $Ra_p^gels$  as a function of the permeability  $k$  (○:  $d = 17$  mm and ◇:  $d = 10$  mm).

as well as the motion of water, while only the fluid moves in the HRL problem. One could imagine another yield stress fluid, such as weakly aggregated suspensions or hard sphere suspensions above the yield stress concentration occurrence (about 50%) and below the random compact packing concentration (about 64%), in which the convection first occurs in the porous structure without any movement of the structural elements. This case would be in a better agreement with the HRL problem.

On the other hand, the comparison between the Rayleigh-Bénard convection in a porous medium made up of percolated microgels and the HRL problem might be audacious. Indeed, one knows that the microgel suspension is elastically deformable contrarily to the porous medium considered in the HRL problem. It means that our system should rather be compared with the Rayleigh-Bénard convection in deformable porous media. However, to our knowledge, the (heat) flow of Newtonian fluids in deformable porous media has been studied,<sup>56–61</sup> while the Rayleigh-Bénard problem in deformable porous media has never been addressed. In addition, focusing on the permeability measurement, a main assumption used in the HRL problem is that the Darcy law is valid. In the case of microgel suspensions, we could think that the measured permeability is not only the Darcy permeability given by Eq. (4). Since the microgels and the solution are ionized as highlighted by Borrega *et al.*,<sup>37</sup> further local effects, such as osmotic (and maybe electro-osmotic<sup>65</sup>) effects, can have a consequence on the flow conditions as highlighted by several studies<sup>62–64</sup> and thus on the permeability. The variation of the ionic concentrations during the flow can modify locally the osmotic pressure and can have a consequence on the mean velocity of the solvent flowing through the porous medium.<sup>63,64</sup> These different effects, i.e., the Darcy and the osmotic (and the electro-osmotic) effects, are additive when evaluating a mean velocity because each effect introduces an additional permeability. Finally, these complex phenomena could modify the onset of convection in our gels, when considering them as porous media, compared with the case of the RBC of the Newtonian fluid in a non-deformable solid porous medium such as the one considered in the HRL problem. It means that the Rayleigh-Darcy number defined in Eq. (9) would not be appropriate to the case of a suspension of microgels. Further investigations are required in order to determine the importance of the osmotic (and electro-osmotic) effects in the permeability measure in Carbopol gels as well as to consider the Rayleigh-Bénard problem in a weakly deformable porous medium including local osmotic and electro-osmotic effects.

As a conclusion, one can observe that the both approaches (i) and (ii) lead to recover the governing parameter of the RBC in Carbopol gels which is the (inverse) of the yield number  $Y$ . The first approach has already been proposed in the case of slip conditions at walls by Darbouli *et al.*,<sup>24</sup> and it has been confirmed in the light of our new results,

obtained in the case of no-slip conditions at walls. The second approach needed further investigations. By measuring the rheological properties of Carbopol gels, we have characterized the instantaneous viscosity  $\mu^+ \sim Bt^1$ . By replacing this viscosity in Eq. (1), we have shown that the yield number can be recovered as the governing parameter. It means that this approach can explain the origin of the onset of RBC in gels. In other words, the present study confirms that the solid-like to liquid-like transition has to be taken into account in order to understand the onset of motion (convection) in the Carbopol gels. It is of utmost importance to consider more realistic models as the inelastic Bingham or Herschel-Bulkley models to determine theoretical critical conditions. One thinks of an elastoviscoplastic model as the one proposed by Saramito,<sup>66,67</sup> for instance, or a more complex model which also introduces the viscosity  $\mu^+$  based on the kinematic hardening as proposed by Dimitriou *et al.*<sup>14,68</sup>

Finally, by considering the Carbopol microgel as a porous medium, approach (iii), for the first time, we have provided permeability values  $k = O(10^{-14}) \text{ m}^2$ , associated to a bulk pressure gradient (Darcy's law), in Carbopol gels. We have also determined a critical value of the Rayleigh-Darcy number in our gels  $Ra_p = O(10^{-4})$ . One gets that the critical Rayleigh-Darcy number depends on  $k$  which is surprising since the range of our gel concentrations leads to a similar microstructure. The comparison with the HRL problem fails in the Carbopol gels because the onset of convection could be characterized by the motion of the bulk material (not only in the fluid first) or also because the Carbopol gels represent a specific porous medium whose properties are far from that of the porous medium considered in the HRL problem. Considering a deformable porous medium including osmotic effects (maybe also electro-osmotic effects) should represent a more relevant comparison and a possible perspective to our work.

## ACKNOWLEDGMENTS

The work of the authors has been supported by the French National Agency of Research (ANR), grant called "ThiM" (ANR-10-BLAN-0925-01). The Laboratoire de Rhéologie et Procédés (LRP) is part of the LabEx Tec21 (Investissements d'Avenir—Grant No. ANR-11-LABX-0030) and the PolyNat Carnot Institut (Investissements d'Avenir—Grant No. ANR-11-CARN-030-01).

<sup>1</sup>A. Fernandez-Nieves, H. Wyss, J. Mattsson, and D. A. Weitz, *Microgel Suspensions: Fundamentals and Applications* (Wiley VCH, 2011).

<sup>2</sup>R. J. Ketz, R. K. Prud'homme, and W. W. Graessley, "Rheology of concentrated microgel solutions," *Rheol. Acta* **27**, 531–539 (1988).

<sup>3</sup>G. P. Roberts and H. A. Barnes, "New measurements of the flow curves for Carbopol dispersions without slip artefacts," *Rheol. Acta* **40**, 499–553 (2001).

<sup>4</sup>J.-M. Piau, "Carbopol gels: Elastoviscoplastic and slippery glasses made of individual swollen sponges. Meso- and macroscopic properties, constitutive equations and scaling laws," *J. Non-Newtonian Fluid Mech.* **144**, 1 (2007).

<sup>5</sup>P. Coussot, H. Tabuteau, X. Chateau, L. Tocquer, and G. Ovarlez, "Aging and solid or liquid behavior in pastes," *J. Rheol.* **50**(6), 975–994 (2006).

<sup>6</sup>F. Caton and C. Baravian, "Plastic behavior of some yield stress fluids: From creep to long-time yield," *Rheol. Acta* **47**, 601–607 (2008).

<sup>7</sup>F. K. Oppong, L. Rubatat, B. J. Frisken, A. E. Bailey, and J. R. de Bruyn, "Microrheology and structure of a yield-stress polymer gel," *Phys. Rev. E* **73**, 041405 (2006).

- <sup>8</sup>A. Ragouilliaux, G. Ovarlez, N. Shahidzadeh-Bonn, B. Herzhaft, T. Palermo, and P. Coussot, "Transition from a simple yield stress fluid to a thixotropic material," *Phys. Rev. E* **76**, 051408 (2007).
- <sup>9</sup>P. Moller, A. Fall, V. Chikkadi, D. Derkis, and D. Bonn, "An attempt to categorize yield stress fluid behaviour," *Philos. Trans. R. Soc., A* **367**(1909), 5139–5155 (2009).
- <sup>10</sup>P. Moller, A. Fall, and D. Bonn, "Origin of apparent viscosity in yield stress fluids below yielding," *Europhys. Lett.* **87**, 38004 (2009).
- <sup>11</sup>T. Divoux, D. Tamarii, C. Barentin, and S. Manneville, "Transient shear banding in a simple yield stress fluid," *Phys. Rev. Lett.* **104**, 208301 (2010).
- <sup>12</sup>T. Divoux, C. Barentin, and S. Manneville, "From stress-induced fluidization processes to Herschel-Bulkley behaviour in simple yield stress fluids," *Soft Matter* **7**, 8409–8418 (2011).
- <sup>13</sup>D. Lee, I. A. Gutowski, A. E. Bailey, L. Rubatat, J. R. de Bruyn, and B. J. Frisken, "Investigating the microstructure of a yield stress fluid by light scattering," *Phys. Rev. E* **83**, 031401 (2011).
- <sup>14</sup>C. Dimitriou, R. H. Ewoldt, and G. H. McKinley, "Describing and prescribing the constitutive response of yield stress fluids using large amplitude oscillatory shear stress (LAOSstress)," *J. Rheol.* **57**(27), 1–44 (2013).
- <sup>15</sup>P. Lidon, L. Villa, and S. Manneville, "Power-law creep and residual stresses in a Carbopol gel," *Rheol. Acta* **56**(3), 307–323 (2017).
- <sup>16</sup>N. Balmforth, I. A. Frigaard, and G. Ovarlez, "Yielding to stress: Recent developments in viscoplastic fluid mechanics," *Annu. Rev. Fluid Mech.* **46**, 121–146 (2014).
- <sup>17</sup>D. Bonn, M. M. Denn, L. Berthier, T. Divoux, and S. Manneville, "Yield stress materials in soft condensed matter," *Rev. Mod. Phys.* **89**(3), 035005 (2017).
- <sup>18</sup>S. Chandrasekhar, *Hydrodynamic and Hydromagnetic Stability* (Clarendon Press, Oxford, 1961).
- <sup>19</sup>E. L. Koschmieder, *B  nard Cells and Taylor Vortices* (Cambridge University Press, 1993).
- <sup>20</sup>E. Bodenschatz, W. Pesch, and G. Ahlers, *Annu. Rev. Fluid Mech.* **32**, 709–778 (2000).
- <sup>21</sup>J. Zhang, D. Vola, and I. A. Frigaard, "Yield stress effects on Rayleigh-B  nard convection," *J. Fluid Mech.* **566**, 389 (2006).
- <sup>22</sup>A. Vikhansky, "Thermal convection of a viscoplastic liquid with high Rayleigh and Bingham numbers," *Phys. Fluids* **21**, 103103 (2009).
- <sup>23</sup>N. J. Balmforth and A. Rust, "Weakly nonlinear viscoplastic convection," *J. Non-Newtonian Fluid Mech.* **158**, 36 (2008).
- <sup>24</sup>M. Darbouli, C. M  tivier, J. M. Piau, A. Magnin, and A. Adbelali, "Rayleigh-B  nard convection for viscoplastic fluids," *Phys. Fluids* **25**, 023101 (2013).
- <sup>25</sup>Z. Kebiche, C. Castelain, and T. Burgeleau, "Experimental investigation of the Rayleigh-B  nard convection in a yield stress fluid," *J. Non-Newtonian Fluid Mech.* **203**, 9–23 (2014).
- <sup>26</sup>M. Cloitre and R. T. Bonnecaze, "A review on wall slip in high solid dispersions," *Rheol. Acta* **56**, 283–305 (2017).
- <sup>27</sup>A. Davaille, B. Gueslin, A. Massmayer, and E. Di Giuseppe, "Thermal instabilities in a yield stress fluid: Existence and morphology," *J. Non-Newtonian Fluid Mech.* **193**, 144–153 (2013).
- <sup>28</sup>I. Karimfazli, I. A. Frigaard, and A. Wachs, "Thermal plumes in viscoplastic fluids: Flow onset and development," *J. Fluid Mech.* **787**, 474–507 (2015).
- <sup>29</sup>A. Massmayer, E. Di Giuseppe, A. Davaille, R. Tobias, and P. J. Tackley, "Numerical simulation of thermal plumes in a Herschel-Bulkley fluid," *J. Non-Newtonian Fluid Mech.* **195**, 32–45 (2013).
- <sup>30</sup>C. Li, A. Magnin, and C. M  tivier, "Natural convection in shear-thinning yield stress fluids in a square enclosure," *AICHE J.* **62**(4), 1347–1355 (2016).
- <sup>31</sup>P. R. Souza Mendes and E. S. S. Dutra, "Viscosity function for yield stress liquids," *Appl. Rheol.* **14**, 296–302 (2004).
- <sup>32</sup>I. A. Frigaard and C. Nouar, "On the usage of viscosity regularisation methods for viscoplastic flow computation," *J. Non-Newtonian Fluid Mech.* **127**(1), 1–26 (2005).
- <sup>33</sup>C. M  tivier and C. Nouar, "Stability of a Rayleigh-B  nard Poiseuille flow for yield stress fluids—comparison between Bingham and regularized models," *Int. J. Non-Linear Mech.* **46**, 1205–1212 (2011).
- <sup>34</sup>P. Cerisier, S. Rahal, J. Cordonnier, and G. Lebon, "Thermal influence of boundaries on the onset of Rayleigh-B  nard convection," *Int. J. Heat Transfer* **41**, 3309–3320 (1998).
- <sup>35</sup>G. Z. Gershuni, E. M. Zhukhovitskii, and I. G. Semakin, "On convective instability in a horizontal fluid layer separating walls of different conductivity," *Uchen. Zap. Perm. Univ.* **248**, 18–29 (1967).
- <sup>36</sup>G. Z. Gershuni and E. M. Zhukhovitskii, *Convective Stability of Incompressible Fluids* (Israel Programm for Scientific Translations, Jerusalem, 1976), p. 32.
- <sup>37</sup>R. Borrega, M. Cloitre, I. Betremieux, B. Ernst, and L. Leibler, "Concentration dependence of the low-shear viscosity of polyelectrolyte micro-networks: Form hard spheres to soft microgels," *Europhys. Lett.* **47**(6), 729–735 (1999).
- <sup>38</sup>N. Mougin, A. Magnin, and J.-M. Piau, "The significant influence of internal stresses on the dynamics of bubbles in a yield stress fluid," *J. Non-Newtonian Fluid Mech.* **171–172**, 42–55 (2012).
- <sup>39</sup>E. N. da C. Andrade, "On the viscous flow in metals and allied phenomena," *Proc. R. Soc. A* **84**(1), 1–12 (1910).
- <sup>40</sup>H. Nechad, A. Helmstetter, R. El Guerjouma, and D. Sornette, "Creep ruptures in heterogeneous materials," *Phys. Rev. Lett.* **94**, 045501 (2005).
- <sup>41</sup>M.-C. Miguel, A. Vespignai, M. Zaizer, and S. Zappert, "Dislocation jamming and Andrade creep," *Phys. Rev. Lett.* **89**(16), 165501 (2002).
- <sup>42</sup>A. J. Liu and S. R. Nagel, "Jamming is not just cool any more," *Nature* **396**, 21 (1998).
- <sup>43</sup>A. Ambari, C. Amiel, B. Gauthier-Manuel, and E. Guyon, "An experimental measurement of the permeability of deformable porous media," *Rev. Phys. Appl.* **21**, 53–58 (1986).
- <sup>44</sup>V. Lelievre, "Rh  ologie et filtration de dispersions aqueuses de nanoparticules d'hectorite en relation avec la structuration des d  p  ts," Ph.D. thesis, INPG, Grenoble, 2005.
- <sup>45</sup>N. Weiss and A. Silberberg, *Hydrogels for Medical and Related Applications*, ACS Symposium Series No. 31 (American Chemical Society, Washington, 1976), Chap. 5.
- <sup>46</sup>N. Weiss and A. Silberberg, "Inhomogeneity of Polyacrylamide gel structure from permeability and viscoelasticity," *Br. Polym. J.* **9**, 144–150 (1977).
- <sup>47</sup>C. A. Grattoni, H. H. Al-Sharji, C. Yang, A. H. Muggeridge, and R. W. Zimmerman, "Rheology and permeability of crosslinked polyacrylamide gel," *J. Colloid Interface Sci.* **240**, 601–607 (2001).
- <sup>48</sup>W. Y. Gu, H. Yao, C. Y. Huang, and H. S. Cheung, "New insight into deformation-dependent hydraulic permeability of gels and cartilage, and dynamic behavior of agarose gels in confined compression," *J. Biomech.* **36**, 593–298 (2003).
- <sup>49</sup>C. W. Horton and F. T. Rogers, "Convection currents in a porous medium," *J. Appl. Phys.* **16**, 367–370 (1945).
- <sup>50</sup>E. R. Lapwood, "Convection of a fluid in a porous medium," *Math. Proc. Cambridge Philos. Soc.* **44**, 508–521 (1948).
- <sup>51</sup>D. A. Nield, "Onset of thermohaline convection in a porous medium," *Water Resour. Res.* **11**, 553–560, doi:10.1029/wr004i003p00553 (1968).
- <sup>52</sup>D. A. Nield and A. Bejan, *Convection in Porous Media* (Springer-Verlag, New-York, 2006).
- <sup>53</sup>C. M  tivier, Y. Rharbi, A. Magnin, and A. Bou Abboud, "Stick-slip control of the Carbopol gels on transparent smooth walls," *Soft Matter* **8**, 7365 (2012).
- <sup>54</sup>R. J. Schmidt and S. W. Milverton, "On the instability of a fluid when heated from below," *Proc. R. Soc. A* **152** (877), 586–594 (1935).
- <sup>55</sup>C. Y. Wang, "Onset of natural convection in a fluid-saturated porous medium inside a cylindrical enclosure bottom heated by constant flux," *Int. Commun. Heat Mass Transfer* **25**, 593–598 (1998).
- <sup>56</sup>M. Biot, "General theory of three-dimensional consolidation," *J. Appl. Phys.* **12**, 155–164 (1941).
- <sup>57</sup>J. Ghaboussi and E. L. Wilson, "Flow of compressible fluid in porous elastic media," *Int. J. Numer. Methods Eng.* **5**, 419–442 (1973).
- <sup>58</sup>R. W. Lewis and B. A. Schrefler, *The Finite Element Method in the Deformation and Consolidation of Porous Media* (Wiley, New York, 1987).
- <sup>59</sup>E. Detournay and A. H.-D. Cheng, "Poroelastic response of a borehole in a non-hydrostatic stress field," *Int. J. Rock Mech. Min. Sci. Geomech. Abstr.* **25**(3), 171–182 (1988).
- <sup>60</sup>M. Spiegelman, "Flow in deformable porous media. Part 1. Simple analysis," *J. Fluid Mech.* **247**, 17–38 (1993).
- <sup>61</sup>M. Bai and J. C. Roegiers, "Fluid flow and heat flow in deformable fractured porous media," *Int. J. Eng. Sci.* **32**(10), 1615–1633 (1994).
- <sup>62</sup>W. Gu, W. Lai, and V. Mow, "A mixture theory for charged-hydrated soft tissues containing multi-electrolytes: Passive transport and swelling behaviors," *J. Biomech. Eng.* **120**, 169–180 (1998).
- <sup>63</sup>C. Moyne and M. A. Murad, "Electro-chemo-mechanical couplings in swelling clays derived from a micro/macro-homogenization procedure," *Int. J. Solids Struct.* **39**, 6159–6190 (2002).
- <sup>64</sup>T. Lemaire, "Couplages   lectro-chimio-hydro-m  caniques dans les milieux argileux," Ph.D. thesis, INPL, Nancy, France, 2004.

- <sup>65</sup>J. Boscus, “Transfert électro-osmotique en milieu poreux déformable—application au gel d’agar agar,” Ph.D. thesis, Université de Montpellier, 2005.
- <sup>66</sup>P. Saramito, “A new constitutive equation for elastoviscoplastic fluid flows,” *J. Non-Newtonian Fluid Mech.* **145**(1), 1–14 (2007).

- <sup>67</sup>P. Saramito, “A new elastoviscoplastic model based on the Herschel-Bulkley viscoplastic model,” *J. Non-Newtonian Fluid Mech.* **158**, 154–161 (2009).
- <sup>68</sup>C. Dimitriou and G. H. McKinley, “A comprehensive constitutive law for waxy crude oil: A thixotropic yield stress fluid,” *Soft Matter* **10**, 6619–6644 (2014).



## Natural convection in shear-thinning fluids: Experimental investigations by MRI



Mohamed Darbouli, Christel Métivier <sup>\*</sup>, Sébastien Leclerc, Chérif Nouar, Mondher Bouteera, Didier Stemmelen

Laboratoire d'Energétique et de Mécanique Théorique et Appliquée, UMR 7563 (Université de Lorraine, CNRS), France

### ARTICLE INFO

#### Article history:

Received 31 July 2015

Received in revised form 18 December 2015

Accepted 24 December 2015

#### Keywords:

Shear-thinning fluids  
Rayleigh–Bénard convection  
MRI  
NMR velocity mapping  
Non Boussinesq effects

### ABSTRACT

An experimental investigation of the Rayleigh–Bénard convection in shear-thinning fluids using MRI technics is presented. The experimental setup consists on a cylindrical cavity defined by a finite aspect ratio  $A = D/d = 6$ . Qualitative and quantitative results are provided. Flow structure is determined from velocity mapping for a Newtonian fluid, Glycerol and for shear-thinning fluids, Xanthan gum aqueous solutions with weight concentrations ranging from 0.1% to 0.2%. In the case of the Glycerol and the Xanthan solution at 0.1%, one recovers similar results in terms of criticality with  $Ra_c \approx 1800$  and patterns since the convection is characterized by rolls. When the Xanthan concentration is increased, the critical Rayleigh number is not modified, however the onset occurs with hexagonal pattern. Because the critical temperature differences increase with the concentrations due to an increase in viscosity, one can think that hexagonal patterns are due to variations of physical properties with temperature (non Oberbeck–Boussinesq effects). Similarities with some results obtained in the Newtonian case are highlighted. We have observed a transition from hexagonal patterns to rolls by increasing the Rayleigh number. This pattern transition is characterized by a discrepancy in the maximal velocity values. By using shear-thinning fluids, results show an increase in the intensity of convection compared with the Newtonian case.

© 2015 Elsevier Ltd. All rights reserved.

### 1. Introduction

The Rayleigh–Bénard instability is a buoyancy driven motion in a fluid layer confined between two horizontal walls separated by  $d$ . The Rayleigh–Bénard Convection (RBC) in Newtonian fluids has been extensively studied since more than a century, with pioneering studies led by Bénard [1] and Rayleigh [2]. Several reviews have been proposed in [4–6]. The fluid layer is initially at rest, a vertical temperature gradient is imposed by heating the lower wall. The transition from conduction to convection is governed by the Rayleigh number  $Ra = \frac{\rho g \beta \Delta T d^3}{\mu \kappa}$ , ratio between buoyancy effects and viscous and thermal diffusion effects, where  $\rho$  is the fluid density,  $g$  the gravitational acceleration,  $\beta$  the thermal volume expansion,  $\Delta T$  the temperature difference between walls,  $\mu$  the fluid viscosity and  $\kappa$  the thermal diffusivity. In the case of a Newtonian fluid with no-slip conditions at the walls, the critical Rayleigh number is  $Ra_c = 1708$  with a supercritical bifurcation and the convection is characterized by rolls patterns [3].

These last decades, a growing interest has emerged for non-Newtonian fluids, certainly due to wide fields of applications (e.g. oil, cosmetic, pharmaceutic, food stuffs industries). In particular, we focus our study on shear-thinning fluids for which the viscosity  $\mu$  decreases (non-linearly) with increasing shear rate  $\dot{\gamma}$ . First studies concerning the RBC in shear-thinning fluids were done by [7–9] who proposed, from experimental measurements, correlations between the Nusselt number  $Nu$  and the control parameters termed as the Rayleigh number  $Ra$ , the Prandtl number  $Pr$  and rheological parameters for a relatively large range of  $Ra$  values ( $10^3 < Ra < 10^6$ ). The rheological behavior of the fluids used in their experiments were fitted by the power law model. This model presents a singularity as the shear rate  $\dot{\gamma}$  tends to zero. Liang & Acrivos [10] were the first to study experimentally the onset of convection in shear-thinning fluids, where the onset of convection is determined by using the Schmidt–Milverton principle [11]. The fluids used in [10] are aqueous solutions of polyacrylamide, characterized by a Newtonian plateau at low  $\dot{\gamma}$  values. Due to this feature, the authors obtained a similar critical  $Ra$  number as in the Newtonian case. The main difference observed is that the heat transfer is larger in shear-thinning fluids than in Newtonian ones for increasing  $Ra$  values. This tendency has also been obtained in

\* Corresponding author.

E-mail address: [Christel.Metivier@univ-lorraine.fr](mailto:Christel.Metivier@univ-lorraine.fr) (C. Métivier).

numerical study [12] where authors consider power law and Ellis models. More recently theoretical studies [13–15] have considered the RBC in Carreau fluids in an infinite extent cavity. In these articles, weakly non linear stability analyses have been used and have shown that the increase in  $\alpha = \left[ \frac{d\mu^*}{d\Gamma^*} \right]_{\Gamma^*=0}$ , the degree of shear-thinning, with  $\Gamma^* = \dot{\gamma}_ij^*\dot{\gamma}_{ij}^*$  the second invariant of the shear rate tensor (here the star is used for dimensionless variables), leads to a transition from a supercritical bifurcation to a subcritical one. The critical value  $\alpha_c$  is obtained equal to  $24/(601\pi^4)$  for stress-free boundary conditions and  $\alpha_c \approx 2.15 \times 10^{-4}$  for no-slip conditions, meaning that for  $\alpha < \alpha_c$ , the bifurcation is supercritical while above  $\alpha_c$ , the bifurcation is subcritical. Bouteraa et al. [15] have also studied the stability of the convective patterns near the onset. They show that the only stable patterns are rolls in the supercritical bifurcation case. Finally, it is also shown that the degree of shear-thinning enhances the intensity of convection via the increase of heat transfer (Nusselt number  $Nu$ ) with the increase in  $\alpha$ .

Since Liang & Acrivos [10] in the 70's, there is no more experimental data. To our knowledge, the determination of the flow structure in the RBC for shear-thinning fluids have never been performed. In this respect, we propose to study the onset of convection as well as patterns in shear-thinning fluids using nuclear Magnetic Resonance Imaging (MRI) in order to obtain flow visualizations and velocity field. Very few studies on natural convection used MRI visualization technique [16,17] while it gives velocity maps for opaque fluids or highly scattering media such as porous media [18,19]. Concerning the RBC in shear-thinning fluids, as already indicated only few experimental results have been carried out in the past [7,8,10] but they have never given any indication on the convection patterns.

We propose to study the Rayleigh–Bénard convection in aqueous solutions of Xanthan gum which present a Newtonian plateau at low values of  $\dot{\gamma}$  and a shear-thinning behavior above a critical value  $\dot{\gamma}_c$ . These fluids are well described by a Carreau model. In this sense, a first objective of our paper is to compare experimental results with theoretical ones given by [15], in terms of critical Rayleigh number, patterns stability and variations of heat transfer via the intensity of convection with rheological parameters. Another objective is to provide original results in the general topic of thermal convection in non-Newtonian fluids.

The Section 2 of this paper details the fluids used in our experiments as well as their physical and rheological properties. The Rayleigh–Bénard setup is also presented and experimental protocols are explained. The Section 3 focuses on experimental results near onset and above criticality. Results are discussed all along this section. The paper closes with a brief summary.

## 2. Materials and methods

Different fluids have been implemented in our work. First, we have chosen a Newtonian fluid (Glycerol) in order to validate our setup. The physical properties other than viscosity of Glycerol respectively thermal capacity  $C_p$ , thermal expansion coefficient  $\beta$ , density  $\rho$  and conductivity  $\Lambda$  in the temperature range  $T = 0 – 50^\circ\text{C}$  are given by [22] based on data given by [21]:

$$C_{pg}(T) = 4186.6 * (54 + 0.15 * T) * 10^{-2} \quad [\text{J}/(\text{kg} \cdot ^\circ\text{C})] \quad (1)$$

$$\beta_g(T) = [47 + 0.2(T - 20)] * 10^{-5} \quad [1/\text{C}] \quad (2)$$

$$\rho_g = 1259 \quad [\text{kg}/\text{m}^3] \quad (3)$$

$$\Lambda_g = 0.28 \quad [\text{W}/(\text{m} \cdot ^\circ\text{C})] \quad (4)$$

In Eqs. (1)–(4), the index  $g$  is used to refer to Glycerol.

The shear-thinning fluids used in our experiments are aqueous solutions of Xanthan gum (Satiaxane CX 930, Cargill France). The Xanthan gum is a polysaccharide (five sugar residus) secreted by the bacterium *Xanthomonas campestris*. This polysaccharide is used in a wide range of applications such as cosmetic, oil, food industries but also in academic research [20]. The Xanthan gum is a polymer with a low ionic strength, soluble in water. Different concentrations of Xanthan gum in deionised water have been prepared: 0.1%, 0.15%, 0.18% and 0.2%. Solutions of Xanthan gum in water lead to transparent fluids and display a shear-thinning behavior [20] which increases with the concentration as indicated in the following paragraph. Thermo-physical properties of the Xanthan gum solutions have been determined by means of a calorimeter ( $\mu$  dsc3-SETARAM). Because thermo-physical properties of the Xanthan gum solutions vary little in the range of concentrations aforementioned, we have only measured these properties for the concentration 0.15%. Results obtained, in the range of temperature [20 °C, 60 °C], for the heat capacity  $C_p$  and for the thermal conductivity  $\Lambda$  are given as function of the temperature  $T(^{\circ}\text{C})$  in Table 1.

### 2.1. Rheological properties

The rheological properties of the Glycerol and the Xanthan gum solutions have been measured by using a TA Instrument DHR3 rheometer with a cone-plate geometry characterized by a 60 mm diameter and 1° angle. Flow curves have been obtained for several temperature values in order to characterize the viscosity thermodependence.

The Glycerol is a Newtonian fluid, i.e. the viscosity remains constant for isothermal conditions. By varying temperature, the Glycerol viscosity varies as displayed in Fig. 1. The thermodependency of the Glycerol viscosity is modeled by the following exponential law:

$$\mu(T) = \mu(T_{ref}) \exp(-K(T - T_{ref})) \quad (5)$$

with  $T_{ref}$  a reference temperature (here  $T_{ref} = 24^\circ\text{C}$ ) and  $K$  the thermodependent coefficient. The dashed line in Fig. 1 corresponds to this model (Eq. (5)) with  $K = 0.0174 \text{ } ^\circ\text{C}^{-1}$  and  $\mu(T_{ref}) = 0.31 \text{ Pa s}$ .

The Xanthan gum solutions are shear-thinning fluids, i.e. the viscosity decreases with increasing shear rate  $\dot{\gamma}$  (or shear stress  $\tau$ ). Flow curves are displayed in Fig. 2 for the different Xanthan concentrations. The Xanthan solutions are fitted by a Carreau model defined by:

$$\mu = \mu_\infty + (\mu_0 - \mu_\infty)[1 + (\lambda\dot{\gamma})^2]^{(n-1)/2} \quad (6)$$

where  $\mu_0$  and  $\mu_\infty$  set respectively for the viscosities at low and large shear rate,  $n < 1$  is the shear-thinning index and  $\lambda$  the characteristic time. Usually,  $\mu_\infty$  is negligible compared with  $\mu_0$  [24] which is the case for the Xanthan solutions used in our study as one can observe in Fig. 2. Then, the Carreau model writes:

$$\mu = \mu_0[1 + (\lambda\dot{\gamma})^2]^{(n-1)/2} \quad (7)$$

Values obtained for  $\mu_0$ ,  $n$  and  $\lambda$  are summarized in Table 2. These values are used in Fig. 2 in order to fit results (dashed lines). Furthermore, in order to compare our results with theoretical studies [13–15], the Table 2 displays the  $\alpha = \frac{1-n}{2} \frac{\lambda^2 K^2}{d^4}$  values for each

**Table 1**

Thermo-physical properties of Xanthan gum solution (0.15%) as a function of the temperature  $T(^{\circ}\text{C})$ .

Fluid	$C_p$ [ $\text{J}/(\text{kg} \cdot ^\circ\text{C})$ ]	$\Lambda$ [ $\text{W}/(\text{m} \cdot ^\circ\text{C})$ ]
Xanthan gum solution (0.15%)	$0.895T + 4225.2$	$0.0022T + 0.5153$

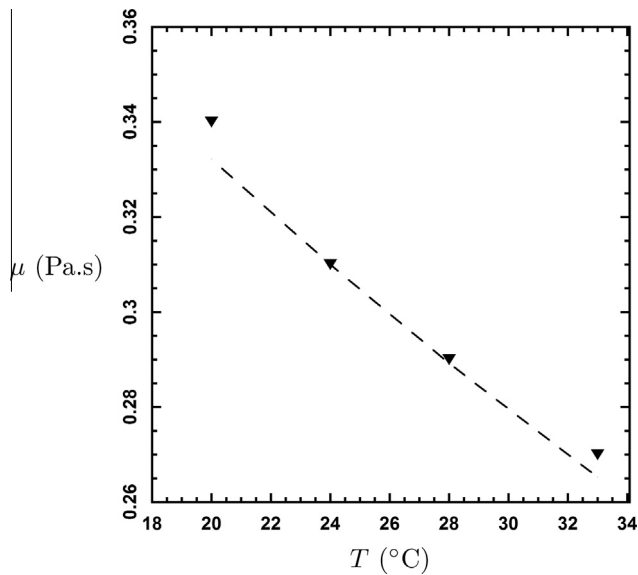


**Fig. 1.** Variations of the Glycerol viscosity with temperature. The dashed line corresponds to the exponential model (5). With  $K = 0.0173 \text{ }^{\circ}\text{C}^{-1}$  and  $T_{ref} = 24 \text{ }^{\circ}\text{C}$ .

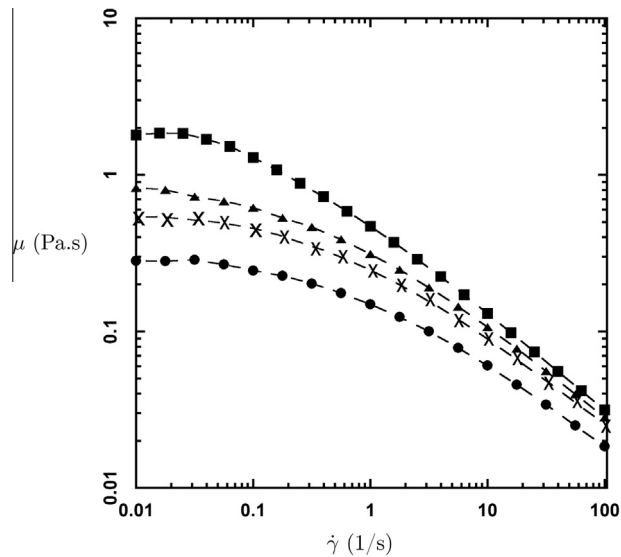


**Fig. 2.** Flow curves of the Xanthan gum solutions at  $T = 24 \text{ }^{\circ}\text{C}$ . The dashed lines correspond to the Carreau model given by Eq. (7). • : 0.1% Xanthan gum concentration, ×: Xanthan 0.15%, ▲ : Xanthan 0.18%, ■: 0.2%.

**Table 2**  
Carreau rheological parameters of the Xanthan solutions for the different concentrations.

C%	n	λ (s)	$\mu_0$ (Pa s)	α
0.1	0.59	4	0.27	$3.69 \cdot 10^{-7}$
0.15	0.50	4.2	0.51	$4.96 \cdot 10^{-7}$
0.18	0.46	5.4	0.85	$8.8 \cdot 10^{-7}$
0.2	0.44	11.4	1.77	$4.3 \cdot 10^{-6}$

Xanthan gum concentrations. In the light of these values, one can expect a supercritical bifurcation and rolls pattern close to the onset of convection according to [15].

The thermodependency of the Xanthan solutions have also been investigated, flow curves are displayed in Fig. 3 for the 0.15%

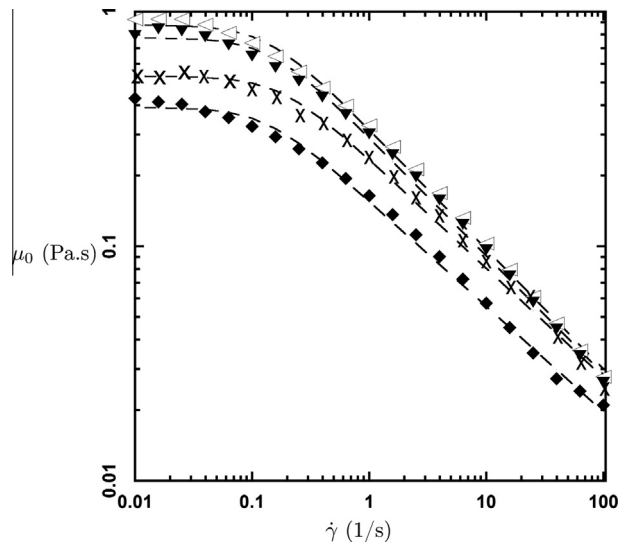


**Fig. 3.** Flow curves of the 0.15% Xanthan solution at different temperatures. ◇ :  $T = 10 \text{ }^{\circ}\text{C}$ , ▼ :  $T = 15 \text{ }^{\circ}\text{C}$ , × :  $T = 24 \text{ }^{\circ}\text{C}$ , ♦ :  $T = 30 \text{ }^{\circ}\text{C}$ . The dashed lines correspond to the Carreau model given by Eq. (7).

concentration. One observes that the viscosity variations with temperature are larger at low shear rate. Therefore, near the onset the thermodependency of viscosity is mainly governed by  $\mu_0$ . Similar tendencies are obtained for the other concentrations. The thermodependent viscosity is modeled by the exponential law given by Eq. (5) where  $\mu$  is replaced by  $\mu_0$ :

$$\mu_0(T) = \mu_0(T_{ref}) \exp(-K(T - T_{ref})) \quad (8)$$

where  $T_{ref} = 24 \text{ }^{\circ}\text{C}$  and  $K = 0.058 \text{ }^{\circ}\text{C}^{-1}, 0.048 \text{ }^{\circ}\text{C}^{-1}, 0.025 \text{ }^{\circ}\text{C}^{-1}$  and  $0.023 \text{ }^{\circ}\text{C}^{-1}$  respectively for 0.1%, 0.15%, 0.18% and 0.2% Xanthan concentrations. The  $K$  values aforementioned highlight a weak thermodependency of the Xanthan solutions, this would be discussed in the light of our results.

In the Rayleigh–Bénard situation, one usually defines the ratio  $r$  between viscosities at upper and lower walls defined by:

$$r = \frac{\mu(T_c)}{\mu(T_H)} = \frac{\mu_{max}}{\mu_{min}} \quad (9)$$

which indicates the degree of viscosity variations with temperature in the fluid layer,  $T_c$  (resp.  $T_H$ ) being the cold (resp. hot) temperature at the upper (resp. lower) wall. For instance, in the case of the concentration 0.18%, a temperature difference about  $\Delta T = 20 \text{ }^{\circ}\text{C}$  leads to  $r = 1.65$ , highlighting a weak viscosity dependence with temperature.

## 2.2. Rayleigh–Bénard setup

The fluid layer is confined in a cylindrical cell which is  $D = 120 \text{ mm}$  in diameter and  $d = 20 \text{ mm}$  thick providing an aspect ratio of  $A = D/d = 6$ . The aspect ratio value is limited by the MRI resonator which corresponds to a cylinder (horizontal axe) of 160 mm diameter as explained in the following paragraph. Furthermore, the depth  $d$  of the cavity has been chosen regarding the range of the fluids viscosity used. An objective of our study is to detect the onset of instability and to investigate the convective motion above criticality. Because the maximal difference temperature has to be moderate in our experiments ( $\Delta T < 45 \text{ }^{\circ}\text{C}$ ), the value  $d = 20 \text{ mm}$  was a good compromise.

All materials used in the setup have been chosen non-metallic to do not disturb the MRI measurements. The lateral walls are made of polymethyl methacrylate (PMMA) of 3 mm thick which

is an insulated thermoplastic material. The horizontal walls are made of sapphire characterized by a thermal conductivity  $\Lambda_s = 35 - 40 \text{ W m}^{-1} \text{ K}^{-1}$  (at 20 °C). The horizontal walls temperatures are imposed by using circulating water obtained via refrigeration units. The water bath temperatures are set constant to within  $\pm 0.01$  °C. Water temperatures are measured with thermocouples at the inlets and outlets as described in the Fig. 4 which displays a cross-section in the ( $O, x, z$ ) plane of the setup,  $O$  being the center of the fluid layer. One considers that the temperature of the upper and lower walls corresponds to the mean value between the respective water flow inlet and outlet. For relatively small values of  $\Delta T$  (less than 20 °C), the respective differences between the inlet and outlet of the water flows are in the order of 0.1 °C. With the aim of maintaining a constant temperature difference between the upper and lower walls, the water flows are in opposite direction. The insulation of the whole system is obtained by adding 5 mm thick thermoplastic foam. Heat losses are also limited by fixing the mean temperature of the boundary layer to  $T_m = 24$  °C which corresponds to the temperature in the resonator.

One can evaluate the thermal diffusion time ( $d^2/\kappa$ ) in the Xanthan gum solutions around 1 hour. In this sense, the temperature difference across the layer was held for about 2 hours, in the conductive regime. Close to the conductive-convective transition, the water bath temperatures were changed at equal rate in order to reach an additional difference temperature (step) of 0.5 °C. In this transition regime, each temperature step was maintained at least during 10 hours. When the temperature difference reaches about 3 times  $\Delta T_c$ , the minimal waiting time was 4 hours.

Finally, for all experiments, the upper and lower walls horizontality is reached within 0.035 rad (around 2°).

### 2.3. MRI technics and protocols

Magnetic Resonance Imaging experiments were carried out on a Bruker Avance Biospec 24/40 spectrometer (2.34T, proton resonance frequency : 100.3 MHz) equipped with a 200 mm inner diameter gradient coil and a 160 mm diameter quadrature resonator manufactured by Rapid Biomedical GmbH. Images are acquired using a flow encoding spin-echo protocol represented in Fig. 5, using the following parameters: repetition time (TR): 1000 ms, echo time (TE): 28 ms, field of view (FOV): 12 cm, matrix: 128 × 128 pixels, spatial resolution 938 × 938 μm. In order to encode velocity, gradient pulses of duration  $\delta = 4$  ms with a separation of  $\Delta = 12$  ms are used. In such images, the signal phase  $\phi$  of a pixel is given by the relation:

$$\phi = \gamma G \delta \Delta v \quad (10)$$

with  $\gamma$  the gyromagnetic ratio of the considered nucleus ( $26.75 \cdot 10^7 \text{ rad T}^{-1} \text{ s}^{-1}$  for  $^1\text{H}$ ),  $G$  the gradient pulses strength and  $v$  the component of the velocity vector in the direction of the applied gradient.

The phase resolution of the spectrometer has been evaluated to 0.02 rad according to previous works [23]. It leads to a velocity

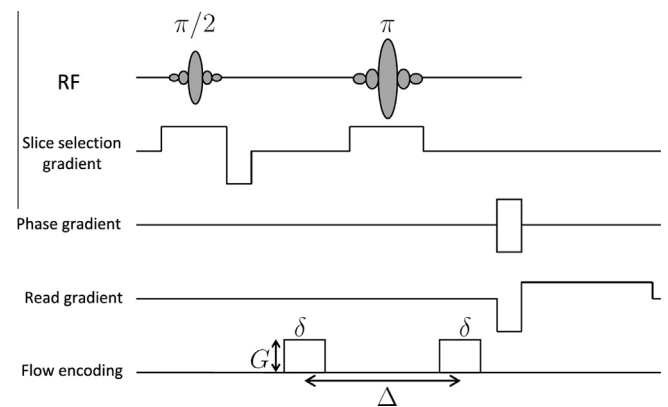


**Fig. 5.** Magnetic resonance imaging (MRI) pulse sequence used for acquiring velocity map. The flow encoding direction may be any of the three gradient directions (read, phase or slice).

value close to  $10^{-5}$  m/s. In this sense, we consider that the spectrometer resolution cannot allow us to detect the onset of motion when the velocity values are less than  $5 \cdot 10^{-5}$  m/s, i.e. 5 times the velocity resolution.

### 2.4. Image analysis

To obtain a velocity map, two experiments are performed with different gradient strengths of, respectively, 180 mT/m and 0 mT/m. The phases of the two resulting images are then subtracted on a pixel by pixel basis in order to remove unwanted contributions. The setup dimensions described in Section 2.2 have been defined and constrained by the spectrometer features, meaning the resonator size as well as the location of the maximal magnetic gradient intensity. Because the setup is quite large ( $D = 120$  mm), regions close to side walls lead to less accurate results or to gradient deviations. In order to remove these deviations, each velocity map have been subtracted to a reference map obtained in a fluid quiescent state at  $T_c = T_h = T_m = 24$  °C.

Finally, images were passed through a filter in order to smooth spatial variations caused by the random noise. The smoothing algorithm, proposed by Garcia [26], is based on a penalized least square method and discrete cosine transform.

## 3. Experimental results and discussion

### 3.1. Newtonian fluid

The setup has been validated by using a Newtonian fluid, i.e. the Glycerol characterized in the section above. Vertical velocity  $V_z$  results are displayed in the horizontal ( $O, x, y$ ) plane for increasing  $\Delta T$  (or  $Ra$ ) values in Fig. 6. In this figure, the axes are indicated in pixels, we recall that 128 pixels correspond to 12 cm. In Fig. 6(a), velocity values are in the same order of magnitude as the MRI resolution, implying that one considers a conductive regime (no motion occurs). The transition from the conductive to the convective regime is observed in Fig. 6(b), where  $\Delta T = 1.1$  °C leading to  $Ra = 1784$ . This value is in a very close agreement with the experimental results obtain in [27,28] who found  $Ra_c \approx 1800$  for  $A = 6$ . By considering the onset of axisymmetric convection in a cylindrical cavity of finite extent, Charlson and Sani [29] have shown theoretically that the critical  $Ra$  value depends on  $A$ . The expression is explicitly given in [30]:

$$Ra_c(A) = \frac{\pi^2 \zeta_0^2}{4A^2} Ra_c(\infty) + Ra_c(\infty) \quad (11)$$

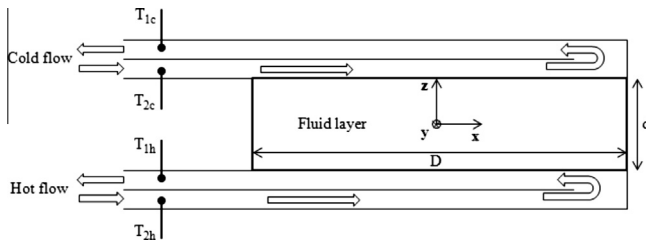


**Fig. 4.** Rayleigh-Bénard setup.

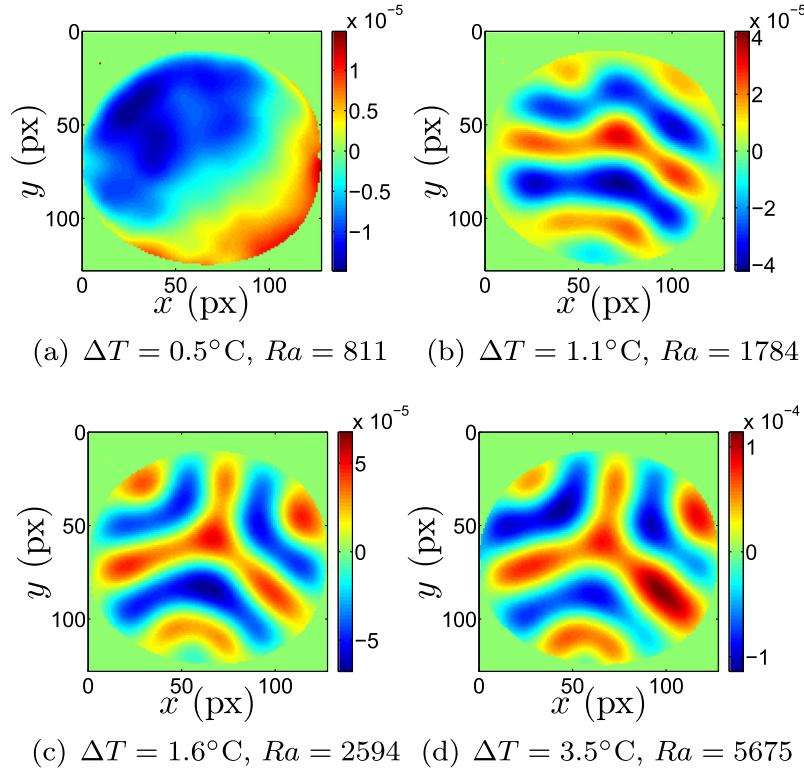


**Fig. 6.** Vertical velocity  $V_z$  (m/s) in the  $(O, x, y)$  plane with increasing  $Ra$  values for the Glycerol case.

with  $\zeta_0^2 = 0.148$  for rigid-rigid boundary conditions after [31] and  $Ra_c(\infty) = 1708$  is the critical Rayleigh number for  $A = \infty$ . In our case,  $A = 6$  leads to  $Ra_c(6) = 1725$ . This value can only give an indication in the sense that non-axisymmetric solutions are observed for low  $A$  values after [25].

Concerning the patterns, we find some parallel rolls close to the onset as displayed in Fig. 6. The wave number  $k = 2\pi d/\lambda$ , with  $\lambda$  the wave length, is evaluated to  $3.2 \pm 0.1$ . These results agree with the experimental results of [27,28]. Above criticality, the pattern observed consists of patches of fairly regular rolls with different orientations linked together by a line of disclinations [32].

Maximal values of velocity  $V_{zmax}$  are displayed as a function of  $Ra$  in Fig. 7. An axis corresponding to the dimensionless velocity  $V_z^*$ , defined by the ratio between  $V_z$  and the buoyancy velocity  $\sqrt{g\beta\Delta T_c d}$ , has also been added. In this Figure, a theoretical result (continuous line), obtained with a weakly non-linear stability analysis at the 7th order calculations for the perturbation mode (see [15] for the detailed method), has been plotted. One can observe that the velocity  $V_{zmax}$  increases with the increase of the Rayleigh number, i.e. the temperature differences  $\Delta T$ , in agreement with the theoretical variations. Differences with theory are larger for low values of  $Ra$  where experimental values are close to the measurements accuracy.

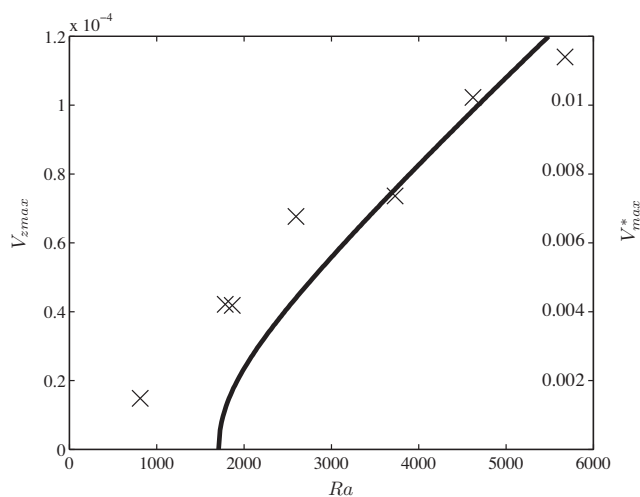


**Fig. 7.** Maximal velocity values  $V_{zmax}$  (m/s) and  $V_z^*$  as a function of the Rayleigh number for the Glycerol – Straight line corresponds to the theoretical result.

### 3.2. Non-Newtonian fluid – Xanthan gum

#### 3.2.1. Onset of convection

We now focus on the experimental Rayleigh–Bénard convection in a shear-thinning fluid, the Xanthan gum solutions. Results for the different concentrations used are displayed in Fig. 8 in terms of vertical velocity map in the horizontal mid-plane  $(O, x, y)$  of the cavity. The onset of convection is observed for all these concentrations around the Rayleigh value  $Ra_c = 1800 \pm 4\%$  which corresponds to the Newtonian value within our experiments accuracy. These results confirm a supercritical bifurcation which agrees with the theoretical prediction regarding the range of  $\alpha$  values as already discussed. However, one can notice that maximal velocity values below criticality is about 3 times the measurements resolution. While the maximal velocity values remain weak below  $Ra_c = 1800$ , one could think that one cell convective pattern have appeared for  $Ra < 1800$  by considering the Fig. 8. A convective motion could occur below criticality due to either a defect in the cavity horizontality or a horizontal temperature gradient in the upper and lower walls. Yet, as already discussed in paragraph 2.2, these defects remain very weak. It does not seem to perturb

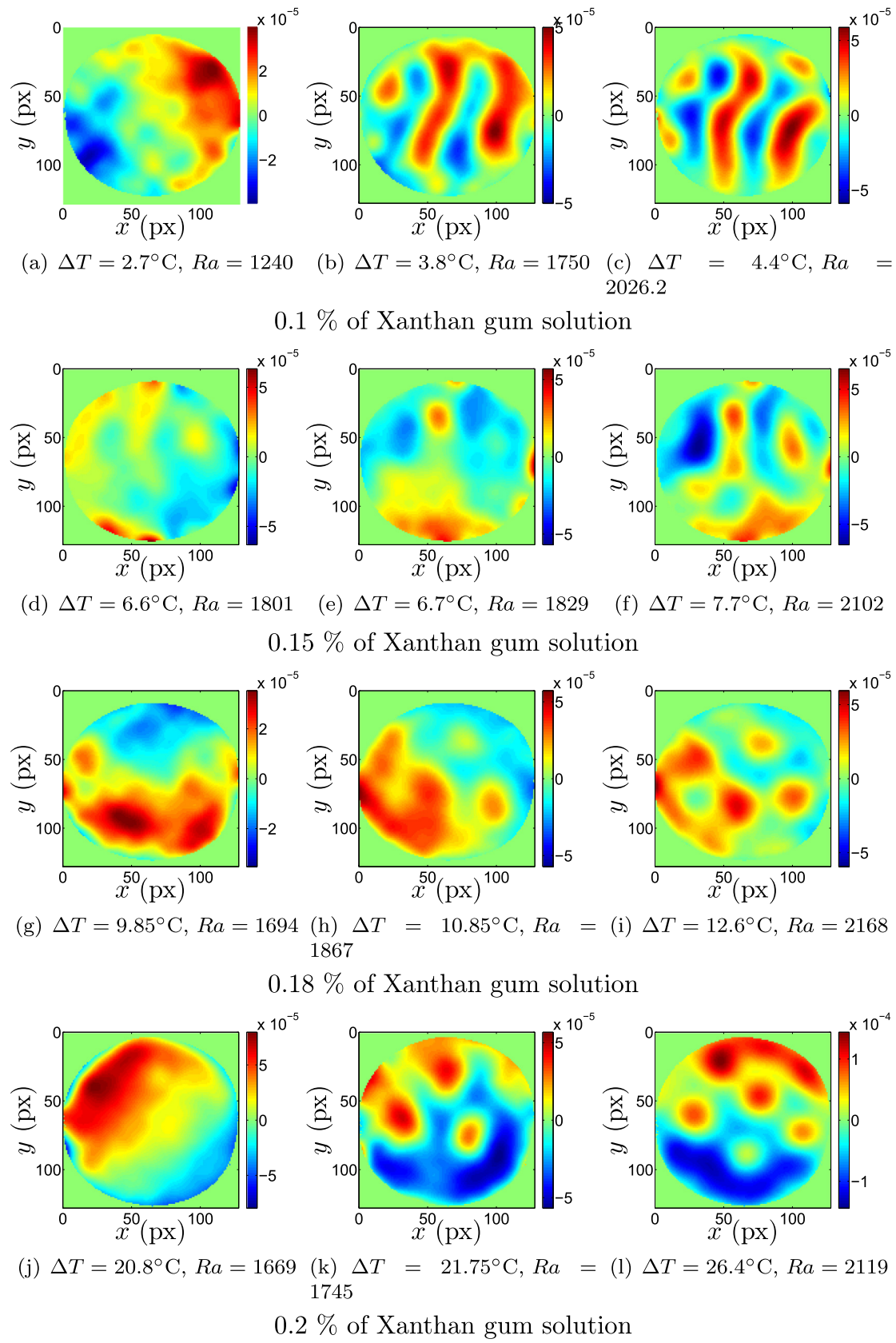


**Fig. 8.** Vertical velocity  $V_z$  (m/s) in the  $(0, x, y)$  plane at the onset of convection for the different Xanthan solutions. (a)–(b): 0.1%, (c)–(d): 0.15%, (e)–(f): 0.18% and (g)–(h): 0.2%.

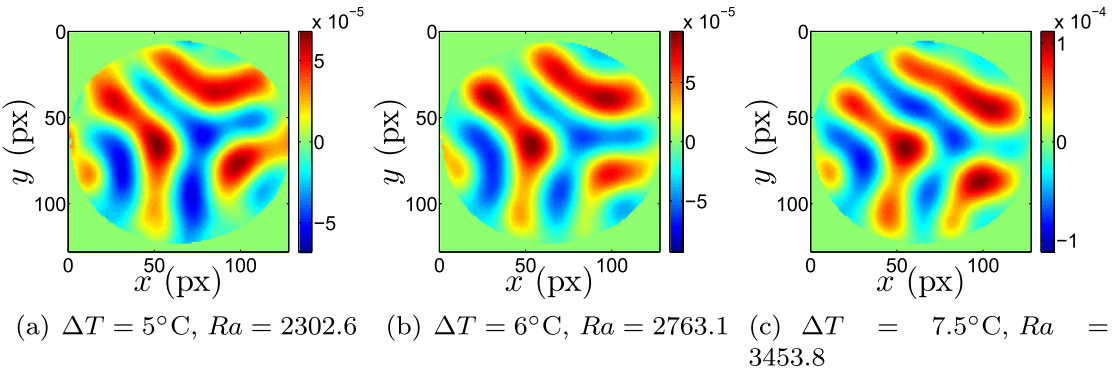


**Fig. 9.** Vertical velocity  $V_z$  (m/s) in the  $(0, x, y)$  plane with increasing  $Ra$  values for the Xanthan solution 0.1%.

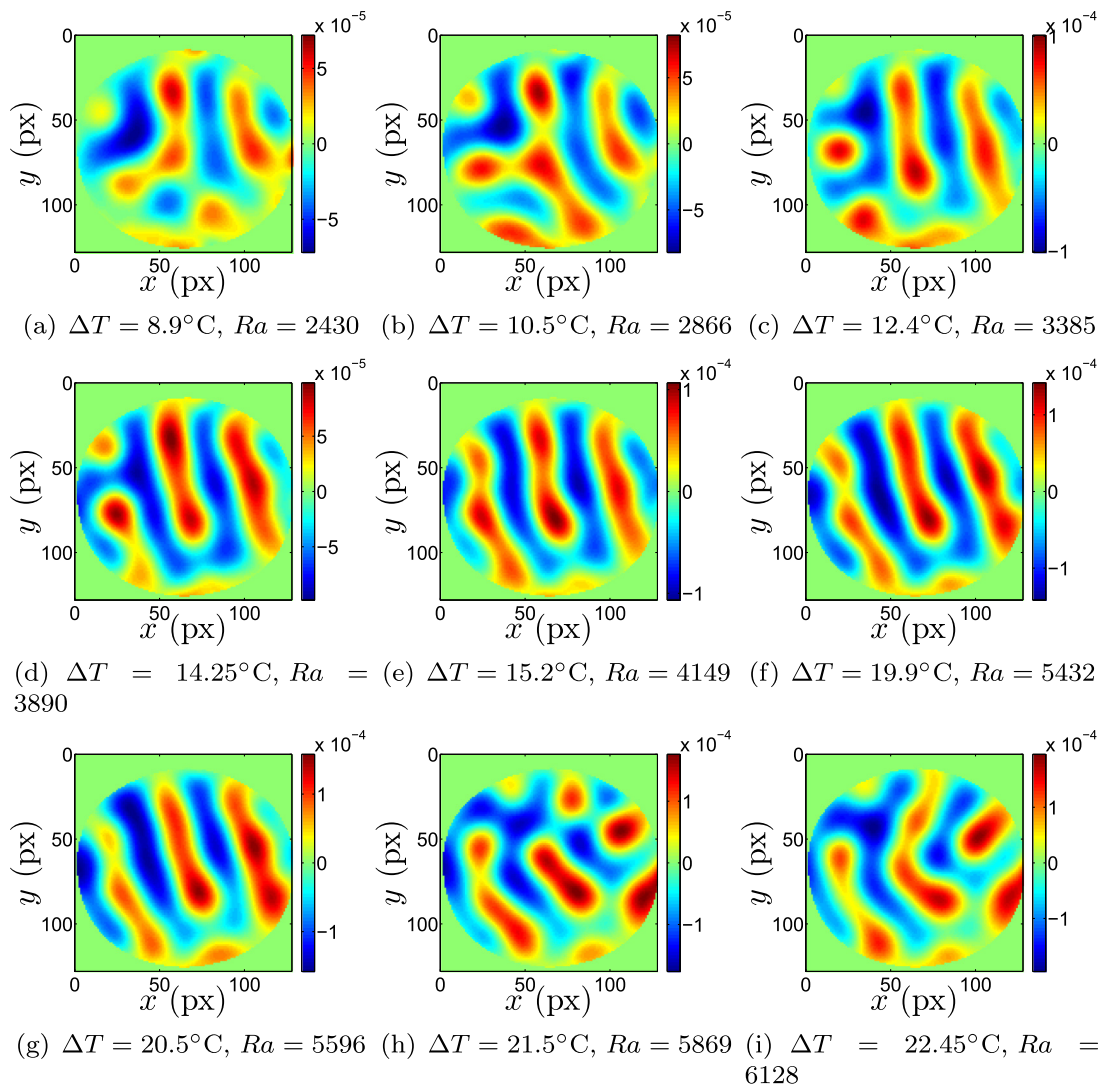


**Fig. 10.** Vertical velocity  $V_z$  (m/s) in the  $(0, x, y)$  plane with increasing  $Ra$  values for the Xanthan solution 0.15%.

the critical  $Ra$  value since one finds  $Ra_c \approx 1800$  for each fluid (Newtonian and non-Newtonian).

Concerning the patterns, one observes that close to the onset of convection, straight rolls characterized by a wave number of  $3 \pm 0.1$  appear for the lowest concentration used in this study, i.e. 0.1% of Xanthan gum (see Fig. 8(b)). When the Xanthan concentration is slightly increased, one observes convective cells (polygons) at the onset of convection. In the case of the concentration

0.15%, (imperfect) straight rolls are observed just above the criticality. However, the polygons remain stable above criticality for 0.18% and 0.2% Xanthan gum concentrations as shown in Fig. 8(i) and (l) for  $Ra \approx 2100$ . Our results disagree with those predicted by theory [15], since in the range of our  $\alpha$  values, only rolls are found stable at the onset of convection. The increase in concentration in our experiments increases the viscosity plateau  $\mu_0$ , hence increases also the critical  $\Delta T$  value needed to start the convection.

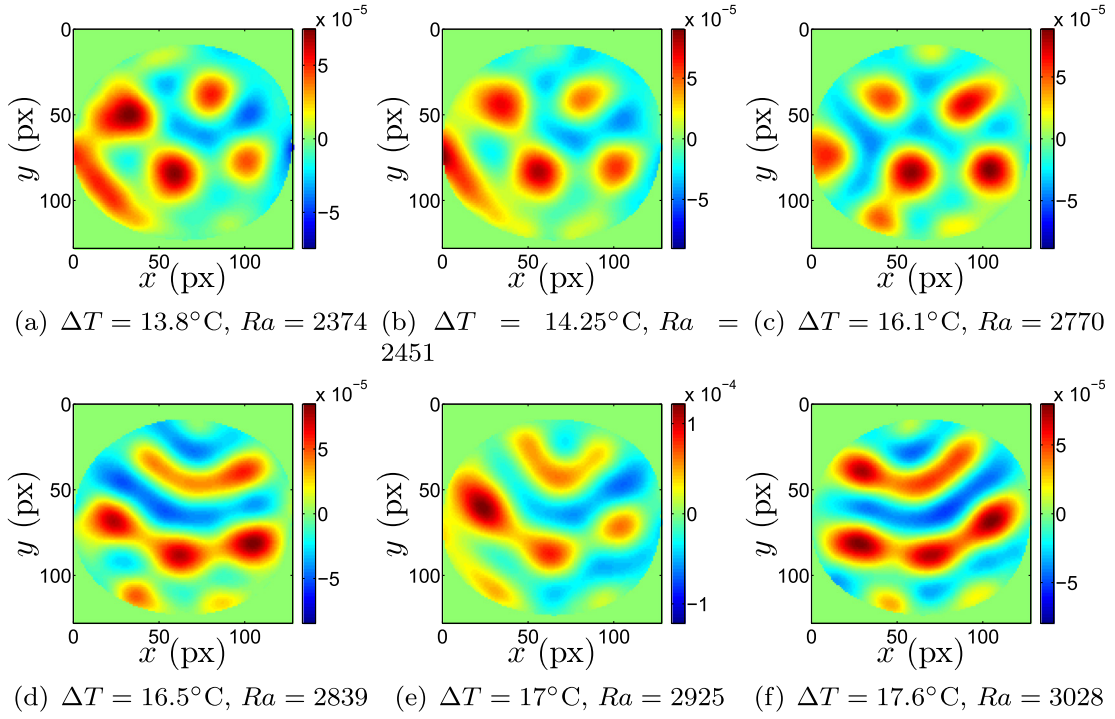


**Fig. 11.** Vertical velocity  $V_z$  (m/s) in the  $(0, x, y)$  plane with increasing  $Ra$  values for the Xanthan solution 0.18%.

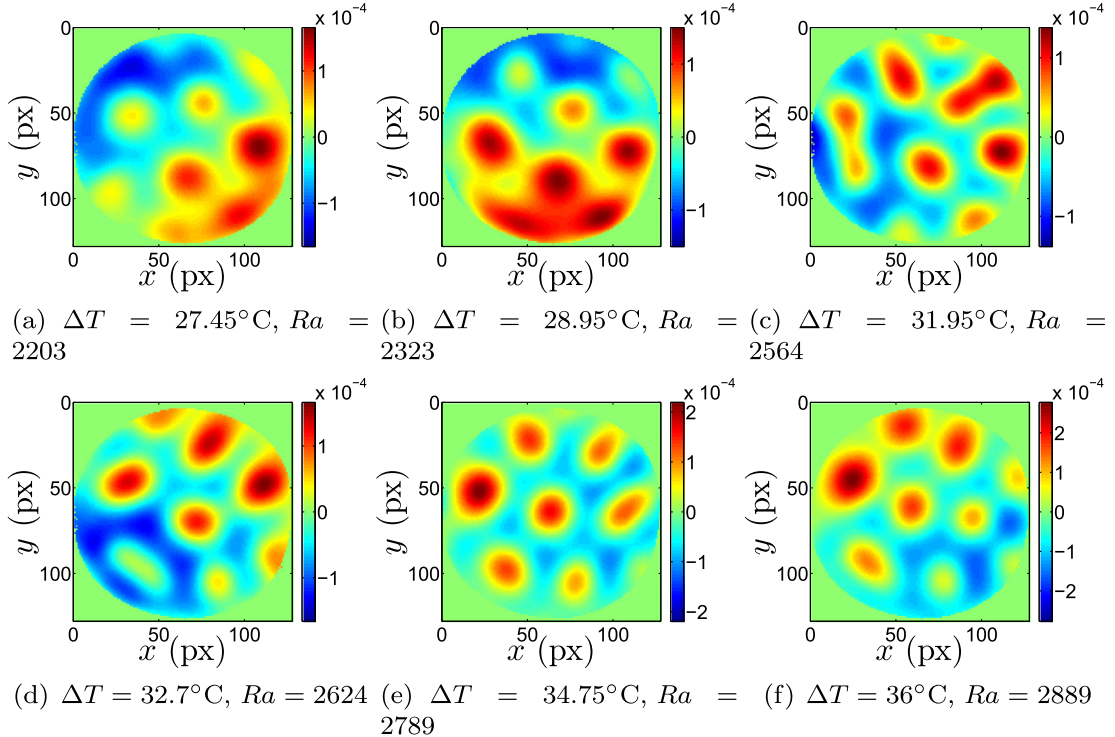


**Fig. 12.** Vertical velocity  $V_z$  (m/s) in the  $(0, x, y)$  plane with increasing  $Ra$  values for the Xanthan solution 0.2%.

In [15], the degree of viscosity variations  $r$  defined in Eq. (9) is fixed at 1. In our experiments, we can evaluate this parameter at criticality,  $r(Ra_c)$ , we find values around 1.3–1.4 for the largest concentrations and 1.25 for a concentration of 0.1%. In this range of  $r$  values, it does not seem that the viscosity thermodependency could involve convective cells as polygons, squares for instance according

to [22–35]. In these articles, it is shown that the rolls are stable for low values of  $r$ , i.e. for  $r \leq r_1$  with  $r_1 \approx 2$  in [34] and  $r_1 \approx 3$  in [35]. Above  $r_1$  squares are stable and the convection remains supercritical. At low  $Ra$  values, hexagons could also be the stable patterns for larger viscosity variations [36,37], yet it does not correspond to our experimental conditions.

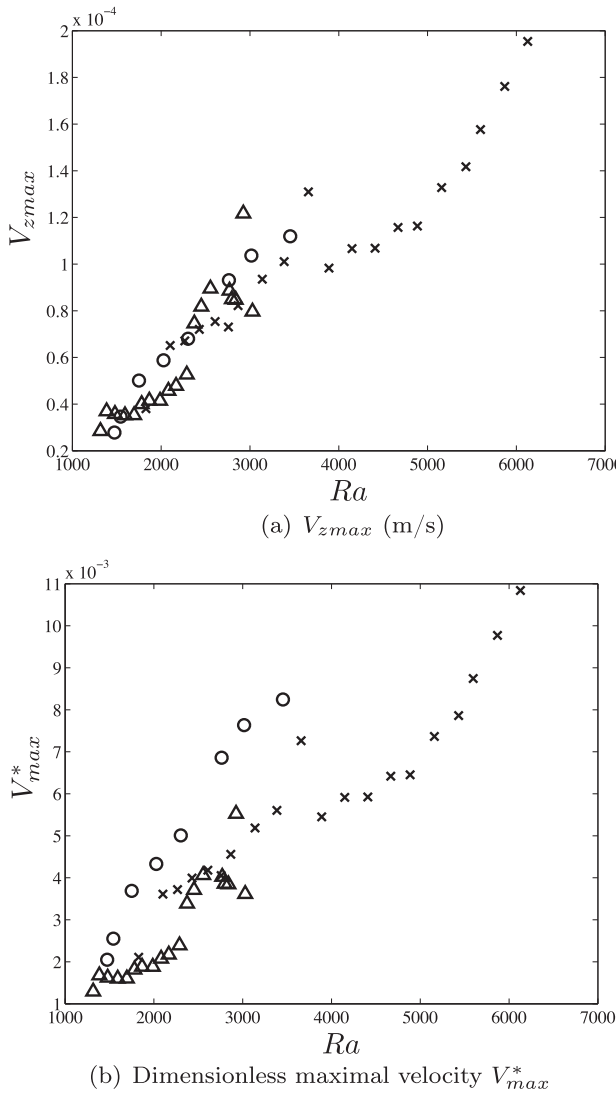


**Fig. 13.** Maximal velocity values (a)  $V_{zmax}$  (m/s), (b)  $V_{zmax}^*$  as a function of  $Ra$  for the Xanthan solutions:  $\circ$ : 0.1%,  $\times$ : 0.15%,  $\Delta$ : 0.18%.

Different parameters could cause the existence of polygons at the onset of convection, such as a large Prandtl values ( $O(10^3)$ ) combined with thermodependency and imperfect boundary conditions i.e. finite conductivity at walls [35,33], imperfect insulated lateral walls. We have checked each parameter. The use of sapphire as horizontal walls lead to a conductivity ratio between the wall and the fluid equal to  $\xi = \frac{\Lambda_w}{\Lambda_f} \approx 100$ . Regarding results given by [33–35], one finds that in our range of Prandtl values ( $Pr = O(10^3)$ ), the stable patterns are rolls. The influence of the lateral walls can be evaluated via the wall admittance defined by  $C = (D/2\Lambda_f)/(t_{lw}/\Lambda_{lw})$ , where  $t_{lw}$  stands for the lateral wall thickness and  $\Lambda_{lw}$  is the lateral wall conductivity. Our experimental setup leads to  $C \approx 80$  which is quite large (insulated lateral wall).

Finally, the polygons pattern remains stable for larger values of  $Ra$  when the Xanthan gum concentration increases. It also leads to an increase in  $\Delta T_c$  values. Concerning this point,  $\Delta T_c$  values can reach the order of  $10^\circ\text{C}$ , in the case of the 0.18 and 0.2% concentrations, corresponding to large values and inducing variations in values of thermo-physical parameters within 10% around that ones obtained at the horizontal walls temperature average. Thus, the comparison with theoretical results which use the Boussinesq approximation is no longer valid. Indeed, a theoretical study [38]

has shown that when all physical properties (e.g. density, conductivity, thermal heat capacity) depend with temperature, i.e. a non Oberbeck–Boussinesq (non-OB) convection case, a bistability of hexagonal and roll patterns occurs. In this study, the author has shown that when the thermodependency of properties is large enough to involve asymmetric conditions in the fluid layer, the convection starts via a subcritical bifurcation to hexagons from  $Ra \geq Ra_A$ . Busse [38] has shown that hexagons are the preferred patterns for  $Ra_A < Ra < Ra_B$ . By increasing the  $Ra$  values, a region of bistability is observed for  $Ra_R < Ra < Ra_B$ , meaning that both hexagons and rolls are stable. Finally, rolls are the preferred patterns for  $Ra > Ra_B$  (see Fig. 2 in [38]). These results have also been observed experimentally in [30–43]. It is possible that the polygons we observe are hexagons, however a better accuracy in our measurements is needed to confirm this point. Further experimental investigations led by [44] confirm that the polygons we have observed are hexagons. Similarly to Dubois et al. [41], we observe that the critical Rayleigh number is nearly similar to the one obtained in the Boussinesq case. In the range of our experiments accuracy, we do not observe any jump in the maximal vertical velocity (see Fig. 13) neither any hysteresis at the first threshold similarly to [41] but unlike in [42]. In this sense, if the hexagons bifurcation is subcritical as predicted by [38] for hexagons, then it is weak and not observable in the range of our experimental conditions.

### 3.2.2. Above criticality

In this paragraph, we present results when  $Ra$  values are increased above criticality. The patterns evolution is displayed for each Xanthan gum concentration in Figs. 9–12. Maximal velocity values  $V_{zmax}$  and  $V_{zmax}^*$ , obtained in the mid-plane ( $0, x, y$ ), are displayed as a function of  $Ra$  values in Fig. 13 for the different Xanthan gum concentrations except for 0.2% where technical problems reduced the accuracy of these measurements.

As previously, some differences in terms of pattern are observed by varying the Xanthan gum concentration. For low values of concentrations, i.e. 0.1% and 0.15%, it is found that rolls remain stable until  $Ra \approx 5600$  for 0.15%, even if one could notice some changes in the thermoconvective structures before this latter value. For instance, we could underline slight modifications around  $Ra = 3500$  (see Fig. 10(b) and (c) for the concentration 0.15%) and also around  $Ra = 5600$ –5800 (see Fig. 10(g) and (h) for the concentration 0.15%). These modifications in terms of structure can also be observed in Fig. 13 where there exists a discrepancy in  $V_{zmax}$  values around  $Ra \approx 3500$  in the case 0.15% (cross symbols) which corresponds to a change in the rolls patterns.

When the concentration is increased, one notices that hexagons could remain stable further above criticality until  $Ra \approx 2800$  for the concentration 0.18% and  $Ra \geq 2900$  for the concentration 0.2%. By considering hexagons pattern such as observed in Figs. 11(a)–(c), 12(c)–(f), in particular by considering the bounding cells (descending flow/blue regions), one could say that polygons might be hexagons. As already discussed, a better accuracy is needed to conclude. Concerning the secondary threshold from hexagons to rolls, in the 0.18% case, one observes that the change in pattern also involves a discrepancy in terms of velocity values  $V_{zmax}$  as displayed in Fig. 13 (open triangles in the case of 0.18%). Actually, one can observe a first discrepancy in  $V_{zmax}$  values around  $Ra \approx 2300$ . This first discrepancy is not correlated with a change in the structure but only with the increase in convective motion, see for comparison Figs. 8(i) and 11(a). The second discrepancy occurs around  $Ra \approx 2800$  where the pattern changes from hexagons to rolls. One notices that for  $2500 \leq Ra \leq 2800$ , the maximal velocity value in the mid-plane does not vary significantly ( $V_{zmax} \approx 8.6 \cdot 10^{-5}$  m/s), the large increase in  $V_{zmax}$  occurs at  $Ra = 2925$  for which

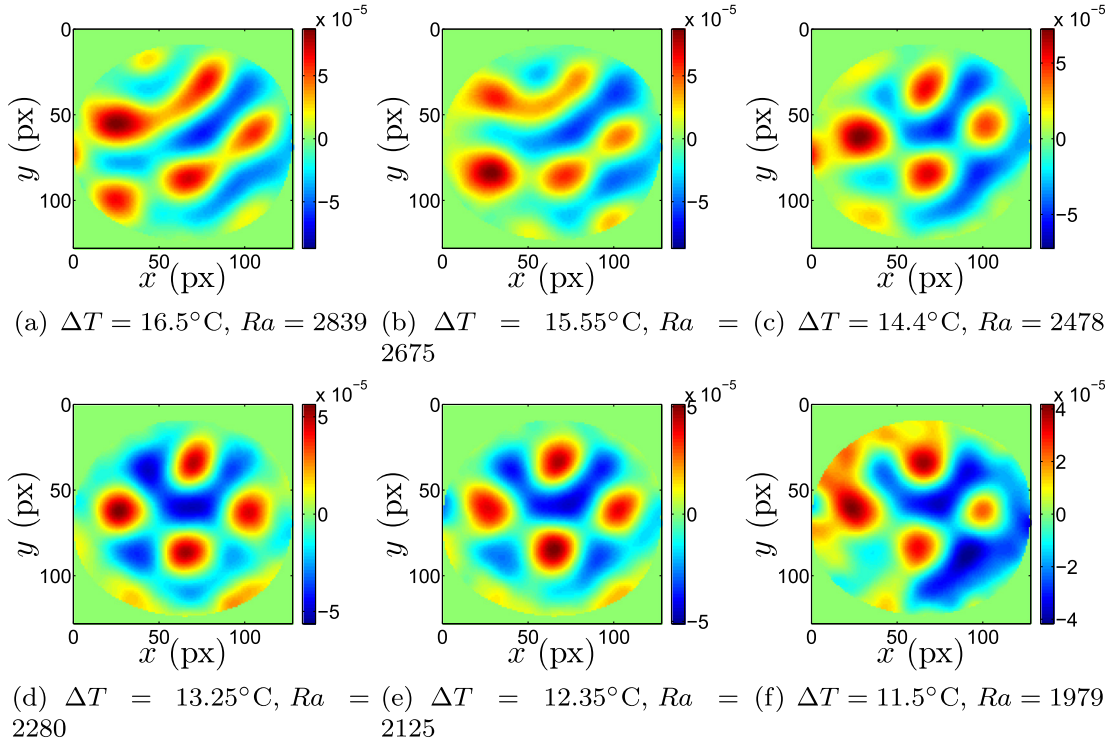


**Fig. 14.** Vertical velocity  $V_z$  (m/s) in the  $(0, x, y)$  plane with decreasing  $Ra$  values for the Xanthan solution 0.18%.

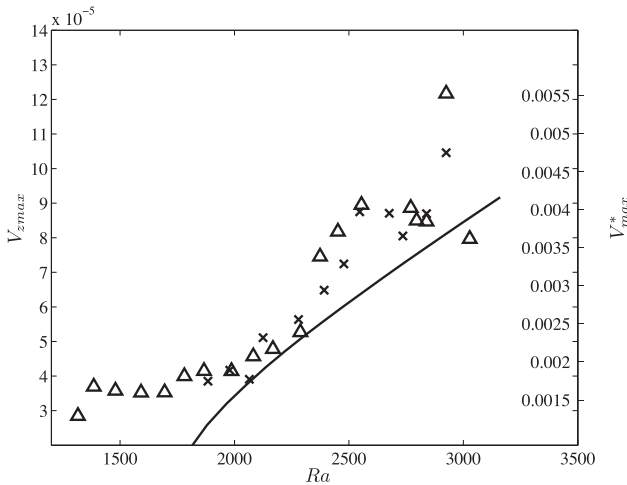


**Fig. 15.** Maximal velocity values  $V_{zmax}$  (m/s) and  $V'_max$  as a function of  $Ra$  for the 0.18% Xanthan solutions – Open triangles : increasing  $Ra$ , Full triangles : decreasing  $Ra$ , straight line: theoretical result.

$V_{zmax} \approx 1.2 \cdot 10^{-4}$  m/s. Then at  $Ra = 3028$ , the maximal velocity value decreases to  $V_{zmax} \approx 8 \cdot 10^{-5}$  m/s. The remarkable discrepancy in velocity values has also been observed in [41]. It is associated to the jump from the hexagonal patterns solution to the rolls solution in the range  $Ra_R < Ra < Ra_B$ . In our case, it means that for the Xanthan gum concentration of 0.18%, we obtain  $Ra_B \approx 3000$ . Increasing then decreasing  $Ra$  involves a hysteresis loop between hexagons and rolls in this latter  $Ra$  range values as predicted by [38] for hexagons and experimentally observed by e.g. [30,41,42]. In our experiments, this hysteresis is not such clear. When  $Ra$  is decreased, one can observe in Fig. 14 that rolls remain stable for smaller values of  $Ra$  compared with Fig. 11. However, it is possible that rolls and hexagons co-exist in the range  $2300 < Ra < 2800$ .

This observation is confirmed by considering Fig. 15 where  $V_{zmax}$  is displayed for increasing and decreasing  $Ra$ . The straight line corresponds to the weakly non linear solution for rolls. One can observe that experimental results are close when increasing and decreasing  $Ra$  and larger than expected results in the case of rolls only (theoretical curve). Finally when  $Ra < 2300$ , only hexagons exist, meaning that  $Ra_R \approx 2300$ . However, further resolution is required in order to determine more accurately this hysteresis loop if it exists effectively in non-Newtonian fluids.

Concerning the patterns, at  $Ra \approx 2300$ , one can highlight an azimuthal wave number  $m$  equal to 4. For hexagons, the wave number obtained for Xanthan concentrations of 0.18% and 0.2% (Figs. 11(a) and 12(a)) can be evaluated to  $k_h = 4\pi d/\sqrt{3}\lambda_h = 3.5 \pm 0.1$ , where  $\lambda_h$  corresponds to the separation of adjacent rising regions. This value is larger than 3.07 or 3.2 obtained for hexagons, respectively in [43,41] in the Newtonian case. One can notice that the increase in  $Ra$  increases the azimuthal wave number since for  $Ra \approx 2800$ ,  $m = 7$  (see Fig. 12(e)). The increase in  $m$  finally leads to a transition from hexagons to rolls pattern.

Finally, considering the maximal velocity variations with  $Ra$  when the concentrations vary, one notices that (i) the order of  $V_{zmax}$  values are larger than in the Newtonian case highlighting a more intense convection in the non-Newtonian case as shown in experimental [10] and theoretical [13–15] studies and (ii) the order of  $V_{zmax}$  values are the same in the range of tested Xanthan concentrations. In this sense, it seems that the intensity of convection is quite similar in this range of concentration as predicted by the theory [15]. It was not possible to evaluate more accurately the intensity of convection, in particular through heat flux measurements, since only non-metallic materials could be used in the MRI resonator.

### 3.2.3. Shear rate $\dot{\gamma}$ evaluation

Because the range of velocity values obtained is similar for all tested concentrations, we only focus on one concentration case, say 0.15%, in order to evaluate the main shear rate tensor

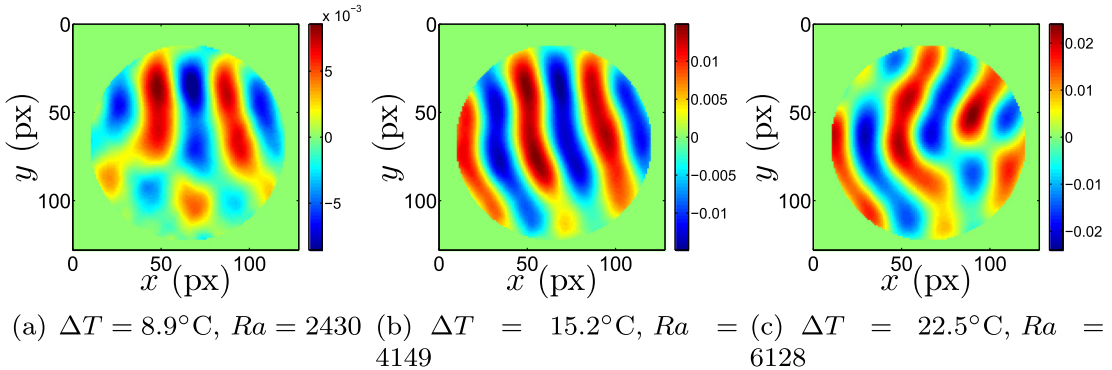


**Fig. 16.**  $\dot{\gamma}_{xz}$  ( $\text{s}^{-1}$ ) in the  $(0, x, y)$  plane with increasing  $Ra$  values for the 0.15% Xanthan solution.

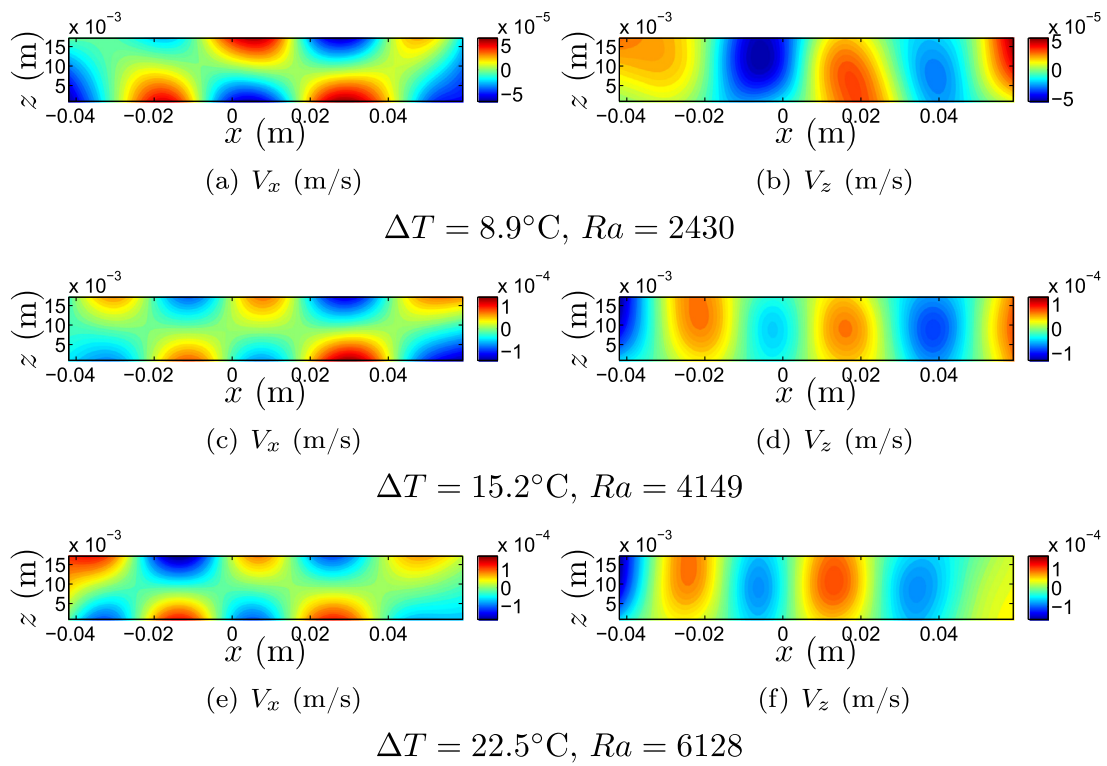


**Fig. 17.** Velocity maps in terms of horizontal velocity  $V_x$  (left) and vertical velocity  $V_z$  (right) in the  $(0, x, z)$  plane with increasing  $Ra$  values for the Xanthan solution 0.15%.

component. Due to the orientation of the rolls, the main component in the mid-plane  $(0, x, y)$  is the  $\dot{\gamma}_{xz}$  one which is represented in Fig. 16 for three values of  $Ra$ . The structure of  $\dot{\gamma}_{xz}$  values is obviously correlated with the pattern observed via the velocity maps. More important is the increase of the  $\dot{\gamma}_{xz}$  values from  $O(10^{-3}) \text{ s}^{-1}$  to  $O(10^{-2}) \text{ s}^{-1}$  by increasing  $Ra$  from 2000 to 6000 respectively. It has been shown by Coccia et al [45], Picot et al [46], Loulou et al [47], that the thermal conductivity can be a function of shear rate. Nevertheless, for the range of  $\dot{\gamma}$  values involved in our experiments, the modification of the thermal conductivity is weak (few percents) and could be neglected. One could have expected larger increase in shear-rate in this range of  $Ra$  values. However, one knows that larger shear-rate values are obtained close to walls. Figs. 17 and 18 display respectively velocity components ( $V_x$  and  $V_z$ ) in the vertical plane  $(0, x, z)$  and the main shear rate component  $\dot{\gamma}_{xz}$  in the same plane. Since  $\dot{\gamma}_{xz} \gg \dot{\gamma}_{zz}$ , the second invariant of the shear rate tensor is such as  $|\dot{\gamma}| \sim |\dot{\gamma}_{xz}|$ . It is worth noting that the shear rate has not been evaluated close to walls due to a lack of

accuracy in these regions. Considering Fig. 18 one finds similar  $\dot{\gamma}_{xz}$  values to that of obtained in the mid-plane. This is not surprising because we expect larger values close to walls. The shear-rate evaluation at walls  $|\dot{\gamma}_w|$  can be approximated by:

$$|\dot{\gamma}_w| \sim \frac{\Delta V_z}{\Delta x} \quad (12)$$

where  $\Delta x$  corresponds to the thickness where the measurements are inaccurate in the fluid close to walls. Typically, one obtains few pixels corresponding to  $\Delta x = 0.1 \text{ mm}$ . By considering no-slip conditions at walls, one finally obtains  $|\dot{\gamma}_w| = O(10^{-2}) \text{ s}^{-1}$  close to criticality and  $|\dot{\gamma}_w| = O(10^{-1}) \text{ s}^{-1}$  for  $Ra \gtrsim 2Ra_c$ . These values correspond to maximal  $|\dot{\gamma}|$  values in the flow. One can notice that close to criticality, the  $|\dot{\gamma}_w|$  value corresponds to the Newtonian plateau as displayed in Fig. 2. This is not surprising since we have not observed any subcritical bifurcation for this concentration which means that the increase in velocity and  $|\dot{\gamma}|$  values is continuous starting from a fluid at rest. When the  $Ra$  value is increased, around

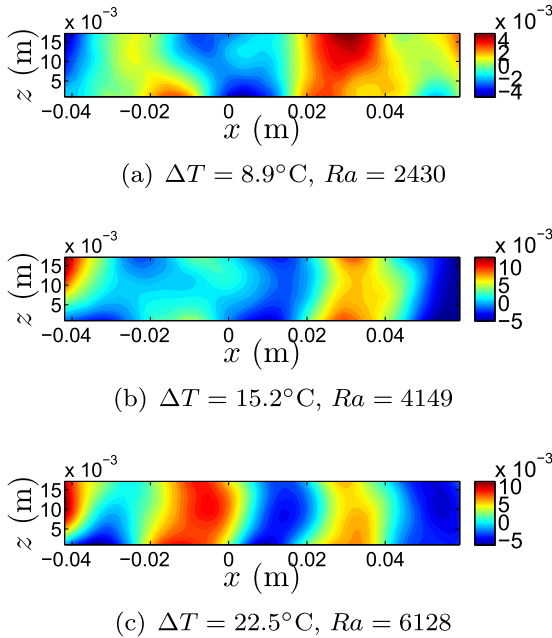


**Fig. 18.** Shear rate  $j_{xz}$  ( $\text{s}^{-1}$ ) component in the  $(0, x, z)$  plane with increasing  $Ra$  values for the Xanthan solution 0.15%.

$Ra \gtrsim 2Ra_c$ , one notices that the  $|\dot{\gamma}|$  values are such as the viscosity is no longer constant in the whole cavity since the fluid behaves as a shear-thinning fluid for  $|\dot{\gamma}| \geq 0.1 \text{ s}^{-1}$ . In this sense, close to criticality our results can be compared with that of the Newtonian fluids case (in the range of our tested fluids), while main differences should occur above criticality.

#### 4. Conclusion

An experimental investigation of the Rayleigh–Bénard convection in shear-thinning fluids is presented by using MRI technics. Flow structures are presented via velocity mapping for a Newtonian fluid, Glycerol and for shear-thinning fluids, Xanthan gum aqueous solutions with weight concentrations ranging from 0.1% to 0.2%.

In the case of the Glycerol and Xanthan solution at 0.1%, one recovers similar results in terms of criticality with  $Ra_c \approx 1800$  and patterns since the convection is characterized by rolls. When the Xanthan concentration is increased, the critical Rayleigh number is not modified, however the onset occurs with hexagonal pattern. These patterns are due to non Oberbeck–Boussinesq effects. Similarities with results obtained in the Newtonian case are highlighted. We have observed a transition from hexagonal patterns to rolls as predicted by [38] and observed by [41,43]. However, the subcritical transition from conduction to convection with hexagons as well as the hysteresis loop are not clearly observed in our study. In this sense, further theoretical and experimental investigations are needed to study the RBC in shear-thinning fluids when physical properties vary strongly with temperature.

Concerning the experimental technique, an ongoing work consists on obtaining both temperature and velocity mapping by using the MRI. The knowlegdege of temperature as well as temperature gradients and velocity are essential in natural convection studies. Furthermore, in future works the use of MRI could allow us to consider a large variety of industrial or natural fluids which are usually fluids where other velocity imaging methods are not usable since they could be opaque for instance.

#### Acknowledgments

The work of the authors has been supported by the French National Agency of Research (ANR), grant called “ThiM” and by the Fédération Jacques Villermoux.

#### References

- [1] H. Bénard, Etude expérimentale du mouvement des liquides propageant de la chaleur par convection. Régime permanent : tourbillons cellulaires, Comptes rendus de l'Académie des Sciences 130 (1900) 1004–1007.
- [2] L. Rayleigh, On convective currents in a horizontal layer of fluid when the higher temperature is on the under side, Phil. Mag. 32 (1916) 529–546.
- [3] A. Schlüter, D. Lortz, F. Busse, On the stability of steady finite amplitude convection, J. Fluid Mech. 23 (1965) 129.
- [4] A.V. Getling, Rayleigh–Bénard Convection: Structures and Dynamics, vol. 11, World Scientific, 1998.
- [5] E.L. Koschmieder, Bénard Cells and Taylor Vortices, Cambridge University Press, 1993.
- [6] E. Bodenschatz, W. Pesch, G. Ahlers, Recent developments in Rayleigh–Bénard convection, Annu. Rev. Fluid Mech. (2000).
- [7] S.T.C. Pierre, C. Tien, Experimental investigation of natural convection heat transfer in confined space for non-Newtonian fluid, Can. J. Chem. Eng. 41 (1963) 122–127.
- [8] H. Tsuei, C. Tien, Free convection heat transfer in a horizontal layer of non Newtonian fluid, Can. J. Chem. Eng. 51 (1973) 249–251.
- [9] C. Tien, H. Tsuei, Z. Sun, Thermal instability of a horizontal layer of non Newtonian fluid heated from below, Int. J. Heat Mass Transfer 12 (1969) 1173–1178.
- [10] S.F. Liang, A. Acrivos, Experiments on buoyancy-driven convection in non-Newtonian fluids, Rheol. Acta 9 (1970) 447–455.
- [11] R.J. Schmidt, S.W. Milverton, On the instability of a fluid when heated from below, Proc. R. Soc. London, Ser. A 152 (1935) 586–594.
- [12] H. Ozoe, W. Churchill, Hydrodynamic stability and natural convection in Ostwald de-Waele and Ellis fluids: the development of a numerical solution, AIChE J. 18 (6) (1972) 1196–1207.
- [13] N.J. Balmforth, A. Rust, Weakly nonlinear viscoplastic convection, J. Non-Newtonian Fluid Mech. 158 (2009) 36.
- [14] B. Albaalbaki, R.E. Khayat, Pattern selection in the thermal convection of non-Newtonian fluids, J. Fluid Mech. 668 (2011) 500.
- [15] M. Bouteraa, C. Nouar, E. Plaut, C. Métivier, A. Kalck, Weakly nonlinear analysis of Rayleigh–Bénard convection in shear-thinning fluids: nature of the bifurcation and pattern selection, J. Fluid Mech. 767 (2015) 696–734.
- [16] S.J. Gibbs, T.A. Carpentier, L.D. Hall, Magnetic resonance imaging of thermal convection, J. Magn. Reson., Ser. A 105 (1993) 209–214.
- [17] J. Weis, R. Kimmich, H.P. Müller, NMR imaging of thermal convection patterns, Magn. Reson. Imaging 14 (3) (1996) 319–327.
- [18] M.D. Shattuck, R.P. Behringer, G.A. Johnson, J.G. Georgiadis, Convection and flow in porous media. Part 1. Visualization by magnetic resonance imaging, J. Fluid Mech. 332 (1997) 215–245.
- [19] M. Weber, R. Kimmich, Rayleigh–Bénard percolation transition of thermal convection in porous media: computational fluid dynamics, NMR velocity mapping, NMR temperature mapping, Phys. Rev. E (2002) 056301.
- [20] K.W. Song, Y.S. Kim, G.S. Chang, Rheology of concentrated xanthan gum solutions: steady shear flow behavior, Fibers Polym. 7 (2) (2006) 129–138.
- [21] A.A. Newman, Glycerol, CRC Press, 1968.
- [22] K.C. Stengel, D.S. Oliver, J.R. Booker, Onset of convection in a variable-viscosity fluid, J. Fluid Mech. 120 (1982) 411–431.
- [23] W. Salameh, Imagerie par résonance magnétique nucléaire pour la vélocimétrie d'un écoulement en milieu poreux (Ph.D. thesis), Institut National Polytechnique de Lorraine, 2011.
- [24] R.B. Bird, R. Armstrong, O. Hassager, Dynamics of Polymeric Liquids, Wiley-Interscience, New York, 1987.
- [25] J.C. Buell, I. Catton, The effect of wall conduction on the stability of a fluid in a right circular cylinder heated from below, ASME J. Heat Transfer 105 (1983) 225.
- [26] D. Garcia, Robust smoothing of gridded data in one and higher dimensions with missing values, Comput. Stat. Data Anal. 54 (2010) 1167.
- [27] F. Hébert, R. Hufschmid, J. Scheel, G. Ahlers, Onset of Rayleigh–Bénard convection in cylindrical containers, Phys. Rev. E 81 (2010) 046318.
- [28] K. Stork, U. Müller, Convection in boxes: an experimental investigation in vertical cylinders and annuli, J. Fluid Mech. 71 (2) (1975) 231–240.
- [29] G.S. Charlson, R.L. Sani, Thermoconvective instability in a bounded cylindrical fluid layer, Int. J. Heat Mass Transfer 13 (1970) 1479.
- [30] E. Pampaloni, C. Perez-Garcia, L. Albavetti, S. Ciliberto, Transition from hexagons to rolls in convection in fluids under non-Boussinesq conditions, J. Fluid Mech. 234 (1992) 393–416.
- [31] J. Wesfreid, Y. Pomeau, M. Dubois, C. Normand, P. Bergé, Critical effects in Rayleigh–Bénard convection, J. Phys. Lett. 39 (1978) 725.
- [32] A. Pocheau, V. Croquette, Dislocation motion: a wavenumber selection mechanisms in Rayleigh–Bénard convection, J. Phys. 45 (1984) 35–48.
- [33] D.R. Jenkins, M.R.E. Proctor, The transition from roll to square-cell solutions in Rayleigh–Bénard convection, J. Fluid Mech. 139 (1984) 461–471.

- [34] F.H. Busse, H. Frick, Square-pattern convection in fluids with strongly temperature-dependent viscosity, *J. Fluid Mech.* 150 (1985) 451–465.
- [35] D.R. Jenkins, Rolls versus squares in thermal convection of fluids with temperature-dependent viscosity, *J. Fluid Mech.* 178 (1987) 491–506.
- [36] F.M. Richter, Experiments on the stability of convection rolls in fluids whose viscosity depends on temperature, *J. Fluid Mech.* 89 (1978) 553–560.
- [37] D.B. White, Planforms and onset of convection with temperature-dependent viscosity, *J. Fluid Mech.* 191 (1988) 247–286.
- [38] F.H. Busse, The stability of finite amplitude cellular convection and its relation to an extremum principle, *J. Fluid Mech.* 30 (4) (1967) 625–649.
- [39] C.Q. Hoard, C.R. Robertson, A. Acrivos, Experiments on the cellular structure in Bénard convection, *Int. J. Heat Mass Transfer* 13 (1970) 849–856.
- [40] E.F.C. Sommerscales, T.S. Dougherty, Observed flow patterns at the initiation of convection in a horizontal liquid layer heated from below, *J. Fluid Mech.* 42 (4) (1970) 755–768.
- [41] M. Dubois, P. Bergé, J. Wesfreid, Non-Boussinesq convective structures in water near 4 °C, *J. Phys.* 39 (1978) 1253–1257.
- [42] R.W. Walden, G. Ahlers, Non-Boussinesq and penetrative convection in cylindrical cell, *J. Fluid Mech.* 109 (1981) 89–114.
- [43] E. Bodenschatz, J.R. de Bruyn, G. Ahlers, D.S. Cannell, Transitions between patterns in thermal convection, *Phys. Rev. Lett.* 67 (22) (1991) 3078–3081.
- [44] M. Bouteraa Convection de Rayleigh–Bénard pour des fluides rhéofluidifiants. PhD thesis, Université de Lorraine, to be published, 2016.
- [45] A.A. Cocci, J.J.C. Picot, Rate of strain effect on thermal conductivity of polymer liquid, *Polymer Eng. Sci.* 13 (1973) 337.
- [46] J.J.C. Picot, G.I. Goobie, G.S. Mawhinney, Shear induced anisotropy in thermal conductivity of polyethylene melt, *Polymer Eng. Sci.* 22 (1982) 154.
- [47] T. Loulou, H. Peerhossaini, J.P. Bardon, Etude expérimentale de la conductivité thermique de fluides non-Newtoniens sous cisaillement application aux solutions de Carbopol 940, *Int. J. Heat Mass Transfer* 35 (10) (1992) 2557–2562.



## Rayleigh-Bénard convection for viscoplastic fluids

Mohamed Darbouli, Christel Métivier, Jean-Michel Piau, Albert Magnin,  
and Ahmed Abdelali

Laboratoire Rhéologie et Procédés, 1301 rue de la Piscine, Domaine Universitaire, BP 53,  
38041 Grenoble Cedex 9, France

(Received 7 May 2012; accepted 20 December 2012; published online 8 February 2013)

The influence of rheological and interfacial properties of yield stress fluids is investigated on the onset of the Rayleigh-Bénard convection. Different Carbopol® (B.F. Goodrich) gels are used in a circular cell for Rayleigh-Bénard experimental setup. The influence of the boundary conditions is also investigated by controlling either slip or no-slip conditions. The onset of thermoconvection is shown by measuring temperature differences and also by using shadowgraph flow visualization. Experimental results show that convection occurs in the range of our experiments. Considering Carbopol gels as elasto-plastic materials with a yield stress  $\tau_y$ , a generalized Rayleigh number is obtained:  $Ra_g = Y^{-1}$ , with  $Y$  the yield number, which represents the balance between the yield stress of the gel and the buoyancy effects. The results show that the Rayleigh number is proportional to  $d$ , the height of the setup, and that the control parameter is the yield number at the onset of convection. Critical values of  $Y^{-1}$  have been determined for slip conditions  $1/Y_c^S \approx 40$  as well as for no-slip conditions  $1/Y_c^{NS} \approx 80$ . It highlights that the change in surface conditions affect significantly the critical conditions. © 2013 American Institute of Physics.  
[<http://dx.doi.org/10.1063/1.4790521>]

### I. INTRODUCTION

Viscoplastic fluids are widely involved in industrial applications such as in, e.g., food processing, oil, chemical, and cosmetic industries. Numerous processes as well as natural settings involve thermal gradients. For instance, a key application in geophysics concerns the natural convection in the Earth's mantle.

The Rayleigh-Bénard configuration has been widely studied for Newtonian fluids and represents an archetype stability problem. The Rayleigh-Bénard configuration corresponds to a buoyancy driven source of instability (natural convection). For a pure viscous fluid heated from below, the instability occurs when buoyancy effects are larger than the viscous and the thermal diffusion effects, characterized by the Rayleigh number  $Ra$ . Detailed analyses of the Newtonian Rayleigh-Bénard problem can be found in Refs. 1 and 2.

In spite of its practical interest, only few studies<sup>3–5</sup> have considered the Rayleigh-Bénard convection in viscoplastic fluids. This is mainly due to the difficulty to deal with the two phases of the materials since viscoplastic fluids present a “solid-like” phase prior the yield stress  $\tau_y$  and a “viscous-like” phase afterward. The first analysis dealing with the onset of convection in an inelastic Bingham fluid has been performed by Zhang *et al.*<sup>3</sup> Because the base flow (conductive regime) is static, the viscosity as well as the stresses in the fluid are indeterminate, then the linear stability analysis based on normal modes approach cannot be developed and even the energy approach does not lead to the Euler-Lagrange equations. The authors<sup>3</sup> develop an energy approach and, by using functional inequalities, they show that the motionless state is always stable with respect to small perturbations. These results are completed and confirmed by direct numerical simulations using an Augmented Lagrangian Method<sup>3</sup> and Lattice-Boltzmann Method.<sup>4</sup> In these articles, it is shown that if perturbations are applied to the base state or if convection is initially imposed, the perturbations decay in finite time. Classical analyses being not applicable to the Bingham Rayleigh-Bénard

problem, approximations are done in Ref. 5 by assuming *a priori* a fully yielded fluid. Furthermore, the authors provide a qualitative Rayleigh-Bénard experiment with Carbopol gels. However, as the authors<sup>5</sup> say, the experiment conditions are not well controlled and results are not detailed. In a whole, the studies<sup>3–5</sup> conclude that the yield stress inhibits the (onset of) convection and that shear-thinning behavior can involve a subcritical bifurcation.<sup>5–7</sup> However, it is not clear to know if the inhibition of convection is due to the yield stress or due to the inelastic Bingham model, which describes a rigid solid-like to a fluid-like transition as an abrupt change in the material behavior. This is one among other questions we propose to investigate in this present article. More generally, we investigate, by experimental means, the influence of the rheological properties of viscoplastic fluids, the Carbopol gels, on the onset of thermoconvective instabilities.

Microgels suspensions such as Carbopol gels are known to slip on smooth surfaces,<sup>8,9</sup> which can have some consequences on the flow conditions. Considering the Newtonian fluids case, boundary conditions can significantly modify critical conditions since linear stability analysis leads to critical Rayleigh number  $Ra_c = 1708$  and  $Ra_c = 657$ , respectively, for rigid-rigid (i.e., no-slip) and free-free (i.e., perfect slip) conditions at walls.<sup>1</sup> In addition to this consideration, the wall slip involves an apparent motion of the gels below the bulk yield stress  $\tau_y$  and above a friction yield stress  $\tau_f$  such as  $\tau_f < \tau_y$ . The control of boundary conditions at wall-Carbopol interfaces is possible, since several techniques have been proposed these last decades. In this sense, and because it was not considered before, the effect of interfacial properties as well as the bulk ones are studied in this article.

The scientific context of the study is specified in Sec. II, in particular the difficulty to define a Rayleigh number when considering yield stress fluids is introduced. Then, the experimental setup is explained as well as the physical properties of the Carbopol gels are characterized in Sec. III. Experimental results are displayed in Sec. IV from the conductive regime to the onset of convection by increasing the temperature difference between the horizontal walls. For the first time, the criticality is clearly determined and the results are discussed for both slip and no-slip conditions at walls. Dominant effects are highlighted via the determination of the main control parameter. Finally, an outlook of this study is included in the concluding Sec. V.

## II. SCIENTIFIC CONTEXT

Considering viscous fluids, the Rayleigh-Bénard convection is governed by the ratio of the buoyancy effect to the thermal diffusion and viscous effects, namely the Rayleigh number defined by

$$Ra = \frac{\rho g \beta \Delta T d^3}{\mu \kappa} \quad (1)$$

with  $\rho$  the fluid density,  $g$  the acceleration due to gravity,  $\beta$  the thermal expansion coefficient,  $\Delta T$  the temperature difference between the lower and upper plates,  $d$  the distance between the plates,  $\mu$  the dynamic viscosity, and  $\kappa$  the thermal diffusivity. When considering a Newtonian fluid at a reference temperature, the choice of the viscosity scale is direct. However, it is not when considering non-Newtonian fluids, i.e., fluids for which viscosity varies with shear rates for instance. The choice of the characteristic viscosity is an important issue. Usually, when the viscosity value is defined at zero shear rates, this value is selected as the characteristic scale. One thinks for instance to the pseudoplastic fluids characterized by a Newtonian plateau at low values of shear rates. When considering viscoplastic fluids and in particular the inelastic Bingham (or Herschel-Bulkley) model, the apparent viscosity tends to infinity at low values of shear rates ( $\dot{\gamma} \rightarrow 0$ ) and is indeterminate, as well as the shear stress, below  $\tau_y$ . Based on the Von Mises criterion, the Bingham model writes

$$\underline{\tau} = \mu \dot{\underline{\gamma}} \quad \text{iff} \quad \tau > \tau_y, \quad (2)$$

$$\dot{\gamma} = 0 \quad \text{iff} \quad \tau \leq \tau_y \quad (3)$$

with  $\mu = K + \frac{\tau_y}{\dot{\gamma}}$  the effective viscosity,  $K$  the consistency (or plastic viscosity).  $\dot{\gamma}$  and  $\tau$  are the second invariants of the shear rates  $\dot{\underline{\gamma}}$  and deviatoric stress  $\underline{\tau}$  tensors, respectively.

In the steady conductive regime, the material is at rest and behaves as a rigid solid (Eq. (3)). In this regime, the momentum equation including the Boussinesq approximation is

$$\nabla \cdot \underline{\sigma} + \rho(1 - \beta(T - T_m))\mathbf{g} = \mathbf{0} \quad (4)$$

with  $\underline{\sigma}$  the stress tensor,  $T_m$  the average temperature between the upper and lower walls,  $T = -\frac{\Delta T}{d}z + T_m$  the temperature in the fluid obtained from the energy equation and  $z \in [-d/2, d/2]$  the vertical coordinate. Equation (4) allows to determine the stress tensor (except constant values at walls) and then the second invariant of its deviatoric part in order to evaluate the Von Mises criterion. In this sense, it is possible to determine regions in which the yield stress value is reached. However, a small perturbation of this system involves regions with either indeterminate stresses or infinite apparent viscosity leading to a linearly stable problem.<sup>3</sup>

This theoretical development disregards some physical or rheological behaviors of real viscoplastic fluids. In particular, physical gels are known to behave as elasto-viscoplastic materials with a dominant elastic behavior below the yield stress and a dominant viscous one above. A continuous material behavior is observed, in real gels, but the determination of a viscosity scale in the Rayleigh number remains a main difficulty.

In particular, Carbopol gels are concentrated and percolated suspensions of multi-micron size microgels, which can be schematically represented by elastic sponges.<sup>9</sup> The origin of the yield stress comes from the interparticle contacts of microgels; its intensity is dictated by the contact numbers. In this sense, Piau<sup>9</sup> has shown that the yield stress value is intimately correlated to the Carbopol concentration. From a macroscopic viewpoint, Carbopol gels are commonly described by the Herschel-Bulkley model given by Eq. (2) with an apparent viscosity  $\mu = (K\dot{\gamma}^{n-1} + \tau_y/\dot{\gamma})$  and  $n$  the shear-thinning index ( $n < 1$ ) above the yield stress. Similarly, to the Bingham model, the apparent viscosity given by this model tends to infinity when  $\dot{\gamma} \rightarrow 0$ , which remains a questionable result. A first source of investigation (i) would consist in determining a viscosity at low values of shear rates by creep measurements. Another approach (ii) is to consider the material as an elasto-(visco)plastic material below the yield stress. On the other hand, considering a microscopic viewpoint, the fluid at rest is represented by two phases system: the microgels and the solvent (water), i.e., a solid-like and viscous-like phases, respectively. It has been shown<sup>9,10</sup> that the Brownian diffusion of water is restricted to cavities due to the presence of Carbopol microgels, which correspond to obstacles. In this sense, (iii) the motion could first occur in the pools of solvent imposing then a stress on the microgels, which finally yields the whole material.

Considering these different aspects (i)–(iii), the question is no longer whether the onset of convection occurs in viscoplastic fluids but which mechanisms govern the onset of motion in the Rayleigh-Bénard configuration. More generally, this key issue concerns directly the viscoplastic fluids behavior close to the yield stress, i.e., the sol-gel transition. These aspects will be discussed in the light of our results (Sec. IV).

### III. EXPERIMENTAL METHODS

#### A. Rayleigh-Bénard experimental setup

The Rayleigh-Bénard setup is shown schematically in Fig. 1. It corresponds to a circular cell of diameter  $D = 0.179$  m and heights  $d = 0.01$  m,  $d = 0.017$  m, or  $d = 0.03$  m. These values of  $d$  lead to values of aspect ratio  $\Gamma = D/d$  such as  $6 \leq \Gamma \leq 17.9$ . In the Newtonian case and for this range of  $\Gamma$  values, the critical conditions are weakly dependent on  $\Gamma$ .<sup>11,12</sup> The bottom wall, a 6 mm thick CuZn<sub>5</sub> copper alloy plate is heated by an electrical heater plate, allowing to control the total heat input  $Q_r$ . The temperature-controlled upper wall, a 3 mm thick glass, is obtained by using a circulation from a water bath, with an accuracy in uniformity and stability less than 0.2 K. This system allows to obtain a constant upper wall temperature  $T_1$  during each experiment. All temperature measurements are done by means of thermocouples at any time, with a Keithley multimeter (Keithley 2700 Digital Multimeter). The horizontal walls temperature in the cavity are obtained by taking into account conduction in the bottom wall, defined by a thermal conductivity  $\lambda_c = 121$  W/(mK) as well as in

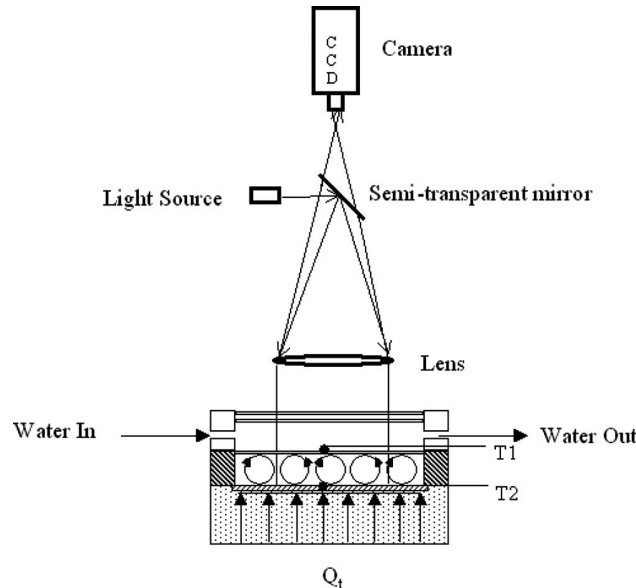


FIG. 1. Rayleigh-Bénard setup.

the upper one,  $\lambda_g = 1.2 \text{ W}/(\text{mK})$ , since the position of thermocouples does not lead directly to the boundary conditions.

The side walls are made of 30 mm thick and transparent Polymethyl methacrylate (PMMA) namely Plexiglas, which lead to adiabatic walls conditions.

The onset of convection is determined according to the Schmidt-Milverton principle.<sup>13</sup> The temperature difference  $\Delta T = T_2 - T_1$  between the upper and lower plates, respectively, is measured at steady state for each value of  $Q_t$  by using thermocouples. In the conductive regime,  $Q_t$  is proportional to  $\Delta T$ . Once the onset of the natural convection occurs, the heat transfer becomes active, and the slope of the curve  $\Delta T$  vs.  $Q_t$  decreases significantly, from this point, the critical temperature difference  $\Delta T_c$  is obtained. On the other hand, the observation of convection is realized by using shadowgraph technique, as represented in the upper part of the Fig. 1. The shadowgraph technique is an optical method, which consists in visualizing flows via the variations of the refractive index. For this purpose, the cell is lightened with a parallel light beam by means of a light source, a mirror, and a collimating lens. This lens converges the transmitted light at a Charge-Coupled Device (CCD)-camera infrared interferometer spectrometer (IRIS), used to record the shadowgraphs on video tape at a rate of 25 frames per second. The shadowgraph technique is described in Refs. 14 and 15.

## B. Material and rheological properties

The aqueous gels, Carbopol 940 are made from reticulated polyacrylic acid resins and manufactured by B.F. Goodrich. The polymer is dispersed in distilled water and neutralized with NaOH, since about  $pH = 7$ , the solution becomes a transparent gel exhibiting a yield stress.<sup>9</sup> The yield stress increases with the increase of polymer concentration. The structure of the gel corresponds to a dispersion of micro-gels in water. The arrangement of the micro-gels swollen with water varies with the polymer concentration. The polymer structure ranges from few microgels floating in water to a compact stack of homogeneous chemical composition, with variations in shape and degree of swelling. The density and thermal properties are essentially those of the solvent, i.e., pure water.

The bulk rheological properties of the Carbopol gels have been measured using a TA Instrument rheometer (AR-G2) with an angular resolution of  $10^{-8} \text{ rad}$  and a torque resolution of  $10^{-10} \text{ Nm}$ . The rheometer is used under controlled velocity (or shear rate) conditions. The controlled velocity is imposed on the upper cone tool. The cone-plate geometry is rendered rough by using a waterproof sandpaper to avoid the wall slip.<sup>8</sup>

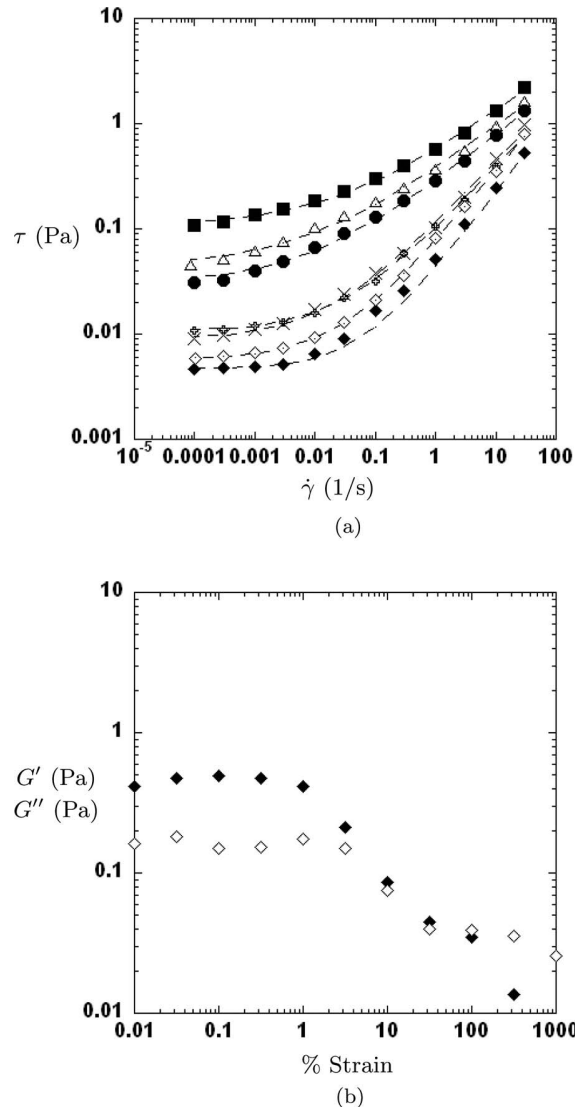


FIG. 2. Rheological properties of Carbopol gels at  $T = 293$  K. (a) Steady-state rheometry: Shear stress as a function of shear rate. (Black diamonds:  $\tau_y = 0.0047$  Pa, diamonds:  $\tau_y = 0.006$  Pa, plus:  $\tau_y = 0.01$  Pa, crosses:  $\tau_y = 0.009$  Pa, black circles:  $\tau_y = 0.031$  Pa, triangles:  $\tau_y = 0.045$  Pa, black squares:  $\tau_y = 0.104$  Pa, dashed lines: Herschel-Bulkley model). (b) Oscillatory rheometry: Variation of  $G'$  (black diamonds) and  $G''$  (white diamonds) as function of the strain for a Carbopol gel  $\tau_y = 0.006$  Pa, and a frequency  $f = 0.1$  Hz.

The rheological characterization shows the gels as elasto-viscoplastic materials.

Figure 2(a) displays the evolution of the shear stress as a function of shear rate in steady state, for the various gels used. For large shear rates values, the gels are shear-thinning. The yield stress  $\tau_y$  is determined at low shear rates, where the stress tends to a constant value. Viscoplastic behavior in stationary shear is commonly described by the Herschel-Bulkley model in the viscous-like region (Eq. (2)). For a unidirectional shear flow, the constitutive law can be read as follows:

$$\tau = \tau_y + K \dot{\gamma}^n \quad \text{iff} \quad \tau > \tau_y. \quad (5)$$

Table I summarizes the values of the model parameters for the gels, obtained from steady-state shear rheometry, namely,  $\tau_y$ ,  $K$ , and  $n$ . The properties determined previously are not sufficient to characterize entirely the Carbopol gels. The gel properties below the yield stress are determined by oscillatory rheometry. Figure 2(b) shows a typical variation of the elastic modulus  $G'$  and the loss

TABLE I. Identification of the gels coefficients and the values of yield stress obtained by both methods: Flow and oscillatory measurements at  $T = 293$  K.

$\tau_y$ (Pa)	$K(Pa.s^n)$	$n$	$G'$ (Pa)	$G''$ (Pa)	$\tau_c$ (Pa)
0.104	0.47	0.41	3.25	0.63	0.117
0.045	0.4	0.43	2.1	0.4	0.043
0.031	0.26	0.46	0.77	0.23	0.029
0.01	0.11	0.6			
0.009	0.093	0.62	0.5	0.15	0.0089
0.006	0.073	0.68	0.45	0.16	0.0067
0.0047	0.039	0.75			

modulus  $G''$  as a function of the strain. The measurements have been performed for a fixed value of frequency  $f = 0.1$  Hz. Similar tendencies are observed for the gels used. For low strain values, constant values of  $G'$  and  $G''$  define the linear viscoelastic domain, their values are reported in Table I. Then the moduli decrease for larger values of  $\gamma$  and they cross at a typical value  $\gamma_c$ . For the Carbopol gels used, one finds  $\gamma_c = 1$ . It has been shown that the stress  $\tau_c$  measured at  $\gamma_c$ , where  $G' = G''$ , i.e.,  $\tau_c = G'\gamma_c$ , is a good estimation of the yield stress  $\tau_y$ . This is confirmed in Table I since one finds  $\tau_y = \tau_c$  by using both methods.

Concerning the thermo-dependency of Carbopol gels, Forrest and Wilkinson<sup>16</sup> show that the yield stress does not depend on temperature since the yield stress is mainly due to the mechanical properties of contacting particles (microgels). It has been shown in Refs. 17–19 that the thermo-dependency of Carbopol is essentially due to the consistency  $K$  via an exponential variation  $K = K_0 \exp(-bT)$ , where  $b$  is a coefficient, which varies with the Carbopol concentration.

### C. Control of interface conditions

In the previous paragraphs, the rheological measurements have been performed by using rough surfaces, leading to no-slip conditions. These conditions permit to characterize the bulk properties of the Carbopol. However, the surfaces defining the boundaries in the Rayleigh-Bénard setup are non-wetting and smooth, i.e., the surfaces roughness is smaller than the microgels size. It is known that polymers can slip on smooth and non-wetting surfaces.<sup>8,20,21</sup>

In order to identify the interface properties and the wall slip, steady-state shear rheometry has been performed by remaining the rough cone (sandpaper) but replacing the lower plate by that ones used in the Rayleigh-Bénard cavity, i.e., the glass, PMMA, and copper alloy surfaces. The results are displayed in Fig. 3 and highlight the slip of the gel on these surfaces. The change in the curves and in the slip yield stress is due to the type of surface used.

Magnin and Piau<sup>8</sup> correlated the rheometric properties of Carbopol gels with direct observations of flow. The observations show that slip is located in a very thin layer close to the solid interface. When the gel is sheared between the rough surfaces, the flow is homogeneous throughout the bulk and the gel sticks at the interfaces. The gel is characterized by the yield stress  $\tau_y$ , which is a volume property. When the gel is sheared between a rough surface and a smooth surface under low stress, the flow is non-homogeneous. The gel sticks on the rough cone but slips on the smooth surface. Slip produces an apparent shear rate above a friction stress  $\tau_f$ , such as  $\tau_f < \tau_y$ . For larger shear rates values, and whatever the nature of the interface, the slip becomes negligible and the curves coincide with that one obtained with rough surfaces. In the absence of slip, Fig. 3 represents the homogeneous shear stress as a function of the shear rate applied to the bulk of the sample. In the presence of slip, Fig. 3 represents an average of the shear stress vs an apparent shear rate, which depends on the interfacial slip velocity at low stress values.

In order to control the surface conditions and to have similar conditions on all the cavity surfaces, 50  $\mu\text{m}$  thick sheets of PMMA have also been used in the Rayleigh-Bénard cavity by adding a sheet on the horizontal walls. In this case, the temperature at walls have been obtained taking into account the conduction due to these additional sheets ( $\lambda_p = 0.2$  W/(mK)).

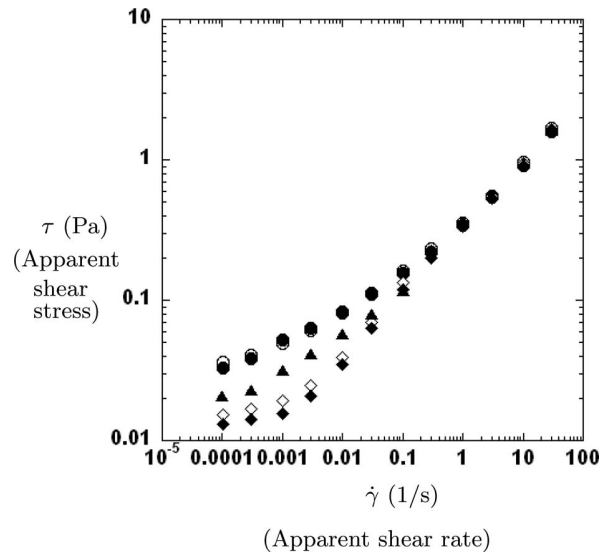


FIG. 3. Steady-state response of a Carbopol gel ( $\tau_y = 0.031$  Pa) when different lower surfaces are used at  $T = 293$  K. In the case of rough or treated surfaces (black circles: sandpaper, white circles: treated PMMA) the abscissa represents the shear rate and the ordinate axis the shear stress. In the case of smooth surfaces or non-treated surface (black diamonds: glass, black triangles: copper alloy, white diamonds: raw PMMA), the results represent an average of the shear stress vs an apparent shear rate.

The raw sheets involve slip conditions as represented by the decrease in  $\tau$  (white diamonds) in Fig. 3. No-slip conditions can be obtained by treating the PMMA surfaces as proposed by Métivier *et al.*<sup>22</sup> The treatment is a solution of polyethylenimine (PEI) in water with a concentration  $10^{-2}$  wt %. The PEI used is characterized by a molecular weight of  $M_w = 750\,000$  g mol<sup>-1</sup> and a number average molecular weight  $M_n = 60\,000$  g mol<sup>-1</sup>. No-slip conditions are obtained using these treated PMMA surfaces as shown by the flow curve (white circles) in Fig. 3 and as explained in Ref. 22.

#### IV. RESULTS AND DISCUSSION

The setup has been validated first with a Newtonian fluid, distilled water, defined by a viscosity  $\mu = 1.31 \times 10^{-3}$  Pa s, a density  $\rho = 999.7$  kg m<sup>-3</sup>, a thermal diffusivity  $\kappa = 1.46 \times 10^{-7}$  m<sup>2</sup>/s, and a thermal expansion coefficient  $\beta = 7.4 \times 10^{-5}$  K<sup>-1</sup> at  $T_m = 282$  K. In this experiment, the cell height is  $d = 0.01$  m. The transition between the conductive and convective regimes occurs for  $\Delta T_c = 0.47$  K, leading to a critical Rayleigh number  $Ra_c = 1787$ .

This last value is in good agreement with the theoretical value  $Ra_c = 1708$  given in Ref. 1, since the relative error is less than 5%.

Concerning the yield stress fluids, experiments have been led with  $d = 0.017$  m and  $d = 0.03$  m, the results are displayed in Figs. 4(a) and 4(b), respectively. As said before, each point in these figures corresponds to a steady state characterized by time-independent values of temperature at walls.

One can observe, in Fig. 4, two regimes: the conductive one with a linear behavior of  $\Delta T$  with respect to  $Q_t$ , then a convective regime. It means that convection occurs in yield stress fluids and that critical values  $\Delta T_c$  can be determined.

As expected, for a constant value of  $d$ ,  $\Delta T_c$  increases with increasing values of yield stress. All results have been obtained with surfaces of glass, PMMA, and copper alloy except for two set of results—circles with crosses and white circles—which have been obtained using raw and treated PMMA surfaces—respectively—for one gel defined by  $\tau_y = 0.031$  Pa. When no-slip surfaces are used, one observes that  $\Delta T_c$  is significantly increased. Indeed, the relative variation in  $\Delta T_c$  using slip and no-slip conditions is about 30%. This relative variation remains quasi-constant in the convective regime when  $Q_t$  is increased, in the range of our experiments.

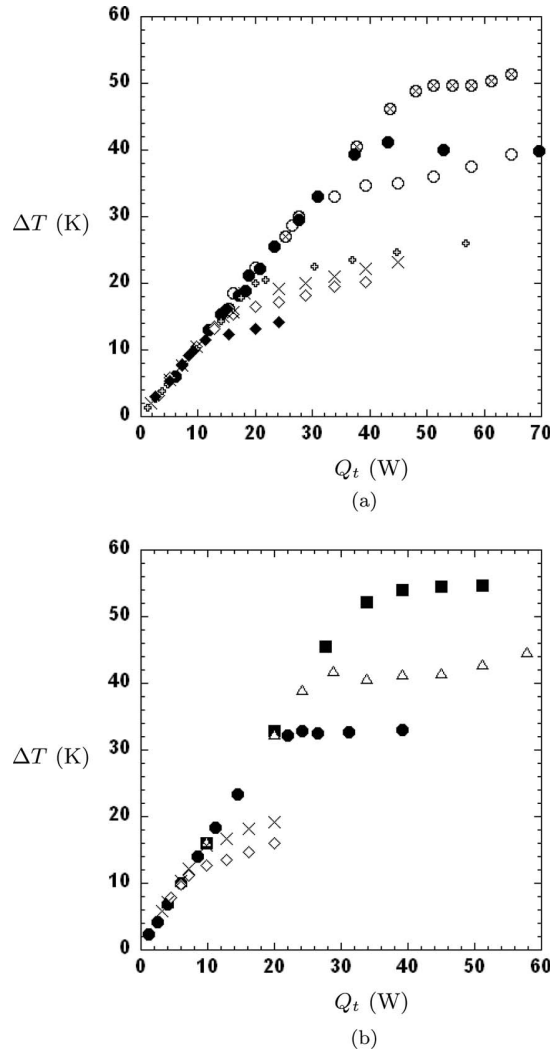


FIG. 4. Temperature difference  $\Delta T$  as a function of the total heat input  $Q_t$ , for different yield stress values of Carbopol gels. (Black diamonds:  $\tau_y = 0.0047$  Pa, diamonds:  $\tau_y = 0.006$  Pa, plus:  $\tau_y = 0.01$  Pa, crosses:  $\tau_y = 0.009$  Pa, black circles:  $\tau_y = 0.031$  Pa, triangles:  $\tau_y = 0.045$  Pa, black squares:  $\tau_y = 0.104$  Pa ; PMMA surfaces in the cavity-circles with crosses: treated PMMA and  $\tau_y = 0.031$  Pa, white circles: raw PMMA and  $\tau_y = 0.031$  Pa). (a)  $d = 0.017$  m; (b)  $d = 0.03$  m.

Further experiments have been led by increasing first  $Q_t$  from the conductive to the convective regime and by decreasing then  $Q_t$  in order to determine whether a hysteresis exists. Figures 5 and 6 show these results for different values of  $d$ ,  $\tau_y$ , and for two set of boundary conditions: slip (Figs. 5(a) and 5(b)) and no-slip (Fig. 6) ones. Close to the onset of convection, one observes few differences ( $\sim 0.5$  K) in  $\Delta T$  values when increasing and decreasing  $Q_t$  with slip conditions at walls. The differences are larger ( $\sim 2$  K) when using no-slip conditions at walls. This first set of results highlights a small hysteresis in values. In this way, a subcritical type of bifurcation could occur but its magnitude is weak and seems depend on the nature of the walls.

Considering the Rayleigh number given in Eq. (1), the difficulty with yield stress fluids is to determine a viscosity at zero or even at weak values of shear rates. As introduced previously, one could determine (i) a viscosity at constant shear rates by performing creep measurements. In this case, for a fixed gel, the Newtonian tendency could be recovered with:  $\beta \Delta T_c \propto d^{-3}$ .

However, in the Rayleigh-Bénard configuration, one can consider the buoyancy force as a transient source of perturbations. For this last reason and because the gels are elasto-viscous materials,

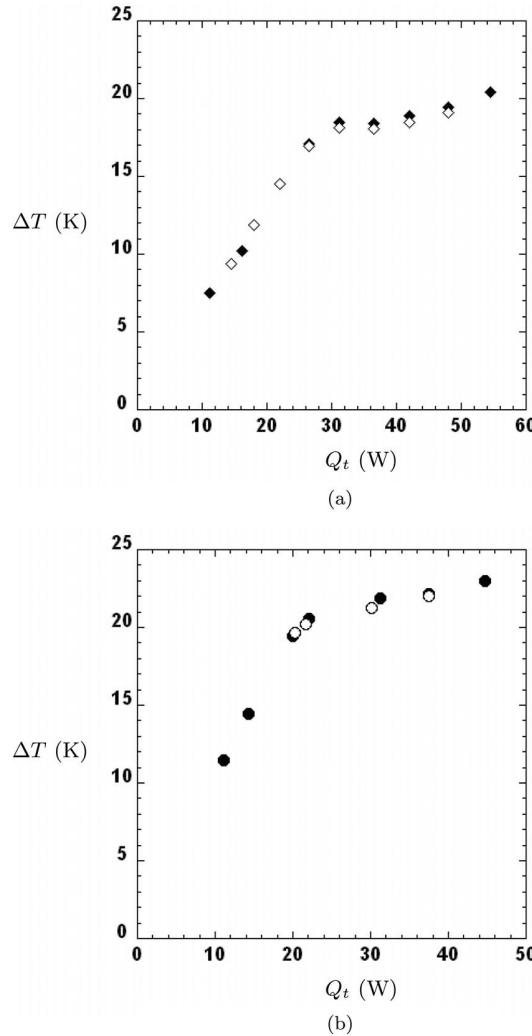


FIG. 5. Temperature difference  $\Delta T$  as a function of the total heat input  $Q_t$ , for different values of  $d$ ,  $\tau_y$ , and slip condition (untreated copper alloy, glass, and PMMA surfaces). The black (resp. white) symbols represent the results obtained by increasing (resp. decreasing)  $Q_t$ . (a)  $d = 0.01 \text{ m}$ ,  $\tau_y = 0.006 \text{ Pa}$ ; (b)  $d = 0.017 \text{ m}$ ,  $\tau_y = 0.01 \text{ Pa}$ .

one can introduce (ii) a viscosity  $\mu^*$  based on oscillatory rheometry measurements and defined by

$$\mu^* = \frac{|G^*|}{\omega} = \frac{\sqrt{G'^2 + G''^2}}{\omega}. \quad (6)$$

Considering  $\tau_y$  as a characteristic scale for  $G'$  and  $G''$  at the strain  $\gamma_c \sim 1$ , as explained in the Sec. III B, the Rayleigh number becomes

$$Ra = \frac{\rho g \beta \Delta T d}{\tau_y} \frac{d^2}{t_g \kappa} = Y^{-1} \frac{d^2}{t_g \kappa}, \quad (7)$$

where  $Y = \tau_y / (\rho g \beta \Delta T d)$  is the yield number representing the ratio of yield stress to buoyancy stresses and  $d^2/t_g \kappa$  represents a ratio of the thermal diffusion time  $t_d = d^2/\kappa$  to a gel characteristic time  $t_g$ , which will be discussed in the light of our results. Within this description, one can also consider the gels as elasto-plastic materials as highlighted by the dominant elastic response below the yield stress. Then, the Eq. (4) leads to the ratio  $\rho g \beta \Delta T d / \sigma$ , with  $\sigma = G' \gamma$  in the elastic solid

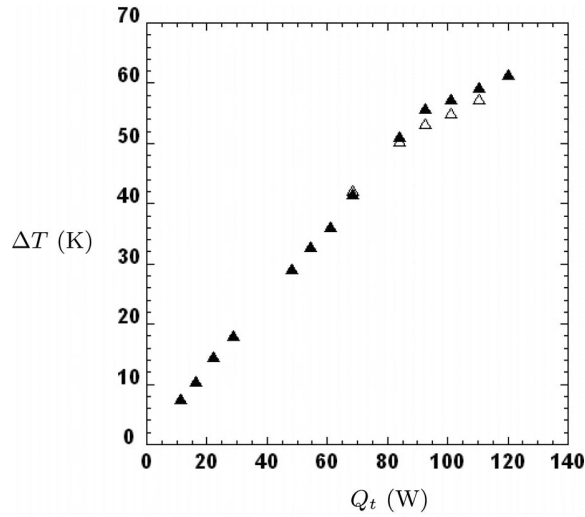


FIG. 6. Temperature difference  $\Delta T$  as a function of the total heat input  $Q_t$ , for the value of  $d = 0.01$  m,  $\tau_y = 0.031$  Pa, and no-slip conditions (treated PMMA surfaces at walls). The black (resp. white) symbols represent the results obtained by increasing (resp. decreasing)  $Q_t$ .

regime. Using the same scales for  $G'$  and  $\gamma$  as previously, a generalized Rayleigh number is obtained

$$Ra_g = \frac{\rho g \beta \Delta T d}{\tau_y} = Y^{-1}. \quad (8)$$

(iii) Finally, regarding the microstructure of Carbopol gels, one can consider the material as a porous medium, where the solid matrix consists in the swollen microgels and the fluid is the distilled water. In the Rayleigh-Bénard configuration, the buoyancy force, via the temperature difference, modifies the Brownian diffusion in water and the transition to the convective regime could be involved first by the flow of water through the solid matrix. The Rayleigh number in porous media is given by<sup>23</sup>

$$Ra_p = \frac{k \rho_w g \beta_w \Delta T d}{\kappa^* \mu_w}, \quad (9)$$

where the index  $w$  is used for water (the fluid),  $k$  is the permeability, and  $\kappa^* = \phi \kappa_w + (1 - \phi) \kappa_s$  is the equivalent thermal diffusivity,  $\kappa_s$  the solid one, and  $\phi$  the porosity. For the Newtonian case, critical values are given by  $Ra_{pc} = 4\pi^2$  and  $\alpha_c = \pi$  for no-slip and isotherm walls.<sup>23</sup> According to Eq. (9), one could expect that  $\beta \Delta T_c \propto d^{-1}$ . However, in Eq. (9), the permeability  $k$  remains a value to determine, which depends on the Carbopol microstructure. As a first approximation, if one considers that the microgels sizes distribution is closed to a mean value  $D_c$ , then the permeability can be given by the Kozeny-Carman relation

$$k = \frac{D_c^2 \phi^3}{36 A_0 (1 - \phi)^2}, \quad (10)$$

where  $A_0$  is a coefficient. Since the porosity is proportional to the Carbopol concentration, i.e.,  $1 - \phi \propto C$ , one can write

$$k \propto \frac{D_c^2 (1 - C)^3}{C^2}. \quad (11)$$

In dilute systems,  $C \ll 1$  and

$$k \propto \frac{D_c^2}{C^2}. \quad (12)$$

According to Piau,<sup>9</sup> the relation between  $\tau_y$  and  $C$  is given by  $\tau_y = (C/C_0 - 1)^3$  in the range of our gels concentrations, with  $C_0$  a minimal concentration value. It means that the permeability is

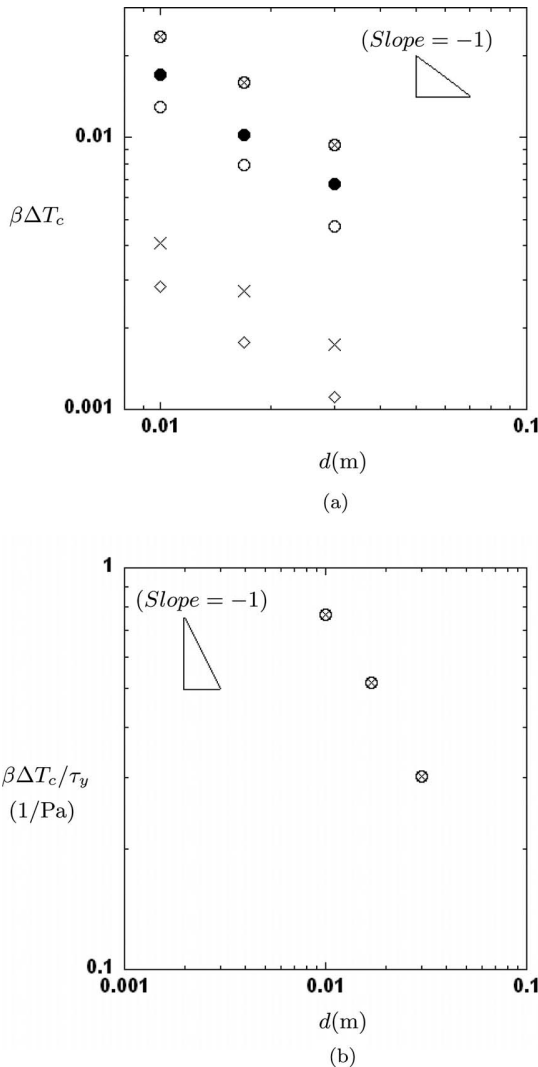


FIG. 7. (a) Variation of  $\beta\Delta T_c$  as a function of  $d$  for different Carbopol gels and surface conditions (white diamonds:  $\tau_y = 0.006 \text{ Pa}$ , slip surfaces (glass and copper alloy); crosses:  $\tau_y = 0.009 \text{ Pa}$ , slip surfaces (glass and copper alloy), black circles:  $\tau_y = 0.031 \text{ Pa}$ , slip surfaces (glass and copper alloy); white circles, white circles with crosses:  $\tau_y = 0.031 \text{ Pa}$  and, respectively, slip surfaces (raw PMMA), no-slip surfaces (treated PMMA)). (b) Variation of  $\beta\Delta T_c/\tau_y$  as a function of  $d$  for one Carbopol gel ( $\tau_y = 0.031 \text{ Pa}$ ) for the reference case: no-slip surfaces (treated PMMA).

not clearly correlated to  $\tau_y$  by using the Kozeny-Karman relation. However, this relation is not realistic for our gels and further investigations are needed to determine  $k$  with a better accuracy. It is important to underline that this approach can be considered in the conduction regime and at the very beginning of the onset of convection, i.e., while the microgels (matrix solid) are at rest. When the motion occurs, the whole material is yielded and behaves as a viscous-like material and the analogy to a porous medium lapses.

Figure 7(a) displays the variations of  $\beta\Delta T_c$  as a function of  $d$  for different Carbopol gels and different boundary conditions. For all the tested conditions, one obtains a variation close to  $\beta\Delta T_c \propto d^{-1}$  (within the error measurements). In the light of these results, the approach (i) can be excluded to describe the onset of convection in yield stress fluids. Considering Fig. 7(b), one can observe that the results are also close to  $\beta\Delta T_c/\tau_y \propto d^{-1}$ , implying that the Rayleigh number varies with  $d$  rather than  $d^3$  (pure viscous fluids) and also that the onset of convection is governed by  $Y$  in the range of our experiments. The approach (ii) is a good candidate since the (inverse of the) yield number

appears explicitly in the Rayleigh number (Eqs. (7) and (8)). However, in Eq. (7), the variation of  $Ra$  with  $d$  would imply that the ratio of times  $t_d/t_g$  does not depend on  $d$ , involving that  $t_g \propto d^2/D_s$ , with  $D_s$  a diffusion coefficient. At this stage, this diffusion coefficient is not clearly known. Considering the binary mixture of the Carbopol gels (suspension of microgels in water), one could think to a solute diffusivity for  $D_s$ . In this way, the times ratio should become a Lewis number defined by  $Le = \kappa/D_s$ . It has been shown theoretically by Martinez-Mardones *et al.*<sup>24</sup> that the thermal instability is different when considering either pure viscoelastic fluids (Maxwell fluids) or binary mixtures with viscoelastic properties.

However, the behaviour of yield stress fluids, such as Carbopol gels, is quite different from Maxwell fluids and in our case, the comparison with Martinez-Mardones *et al.*<sup>24</sup> is not direct. Furthermore, the physical identification of these dimensionless numbers, i.e.,  $Y^{-1}$  and  $Le^{-1}$  in the Rayleigh number is quite difficult. It seems preferable to consider the gels as elasto-plastic materials, i.e., a solid with an elastic and a plastic response by increasing the stress (or strain) within the material. The Rayleigh number is then defined by Eq. (8) and the control parameter is  $Y^{-1}$  as confirmed by our results; in other words, the onset of convection is mainly governed by the balance between the buoyancy and the yield stress effects. The inverse of the yield number reflects the stress balance in the material in the steady conductive regime; above a critical value, the system becomes unstable.

From a microscopic viewpoint, the approach (iii) considers the gels as binary mixtures, i.e., a solid and a fluid phases for which we assume the solid phase at rest in the conductive state. Within this approximation, the microgels are then considered as a porous medium and the control parameter given by Eq. (9) is found proportional to  $d$ . However, at this stage the permeability is unknown, in particular, the relationship between  $k$  and  $\tau_y$  is indeterminate. In this sense, further investigations are required in order to conclude about (iii).

In addition, one observes a difference in the set of results (circles) obtained with slip conditions and the results obtained with no-slip conditions Fig. 7(a). One finds that wall slip has a destabilizing effect since the values of  $\beta \Delta T_c/\tau_y$  are smaller than the values obtained in the no-slip case. This result is consistent with the Newtonian case since slip conditions destabilize the flow compared with no-slip conditions.<sup>1</sup> By using free-free conditions (perfect slip) criticality is characterized by  $Ra_c = 657$  and  $\alpha_c = \pi/\sqrt{2}$  in the Newtonian case. Similarly, a recent study<sup>25</sup> investigates the wall-slip effect on the Rayleigh-Bénard Poiseuille stability for viscoplastic fluids. The authors also show that the wall-slip destabilizes the flow and that critical conditions depend mainly on the friction factor at walls.

Figure 8 shows the evolution of the Nusselt number,  $Nu = Q_t/Q_{\text{conduction}}$  with  $Q_{\text{conduction}} = S\lambda \Delta T/d$ ,  $S$  the area of the lower plate and  $\lambda$  the thermal conductivity, as a function of  $1/Y$

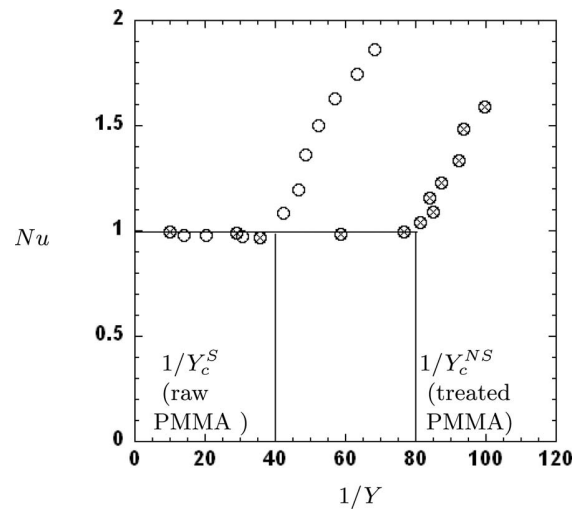


FIG. 8. Evolution of the Nusselt number  $Nu$  as a function of the inverse of the yield number  $1/Y$  for one Carbopol gel  $\tau_y = 0.031$  Pa,  $d = 0.017$  m (white circles with crosses: treated PMMA, white circles: raw PMMA).

given by Eq. (7) for a given Carbopol gel and controlled surfaces conditions. The control of surfaces conditions is obtained by using either raw PMMA (white circles) or treated PMMA (circles with crosses) for slip and no-slip conditions, respectively. In the conductive region and close to the onset of convection  $Nu = 1$ , the transition between conduction and convection is characterized by  $Nu \geq 1$ . The critical  $1/Y$  values are determined:  $1/Y_c^S \approx 40$  with slip conditions and  $1/Y_c^{NS} \approx 80$  with adherence conditions highlighting the destabilizing effect of wall slip as discussed previously. However, one observes that  $1/Y_c^S \times \tau_y/\tau_f \approx 1/Y_c^{NS}$ , meaning that rescaling  $1/Y_c^S$  with  $\tau_f$  leads to the critical value  $1/Y_c^{NS}$ . The yield stress value at interface,  $\tau_f$  has a main effect on the onset of instability, in the range of our experiments.

More generally, these results highlight that convection occurs in viscoplastic fluids and that steady states are obtained close to the threshold ( $Nu = O(1)$ ) in the conductive and convective regimes. These two points disagree with the theoretical and numerical predictions,<sup>3–5</sup> since the authors show that the yield stress inhibits the (onset of) convection. As discussed in Sec. II, the difference in results might be the consequence of the inelastic Bingham model used in these articles. The Bingham model, based on the Von-Mises criterion, is commonly used since it is the simplest one and since it accounts for two main features of viscoplastic fluids (yield stress and shear-thinning behavior). Numerous flow conditions in steady laminar fully developed or slowly varying flow regimes can be well described by using this type of models (inelastic Bingham or Herschel-Bulkley) but it is not adapted to the Rayleigh-Bénard configuration.

Figure 9 shows the evolution of the flow regimes for different  $Nu$  values via shadowgraph snapshots at the center of the setup. The reference picture, Fig. 9(a), is obtained in the conductive

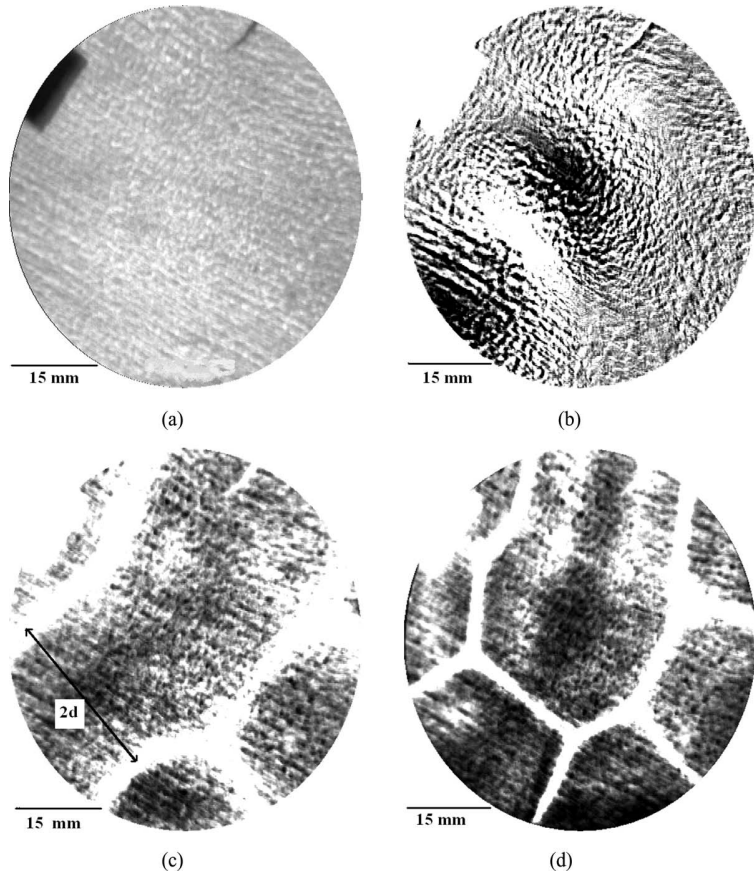


FIG. 9. Shadowgraph visualizations for one Carbopol ( $\tau_y = 0.031$  Pa) at different  $Nu$  values,  $d = 0.017$  m. (a)  $Nu = 0.98$ ,  $1/Y = 12$ ; (b)  $Nu = 1.12$ ,  $1/Y = 59$ ; (c)  $Nu = 1.39$ ,  $1/Y = 60$ ; (d)  $Nu = 1.84$ ,  $1/Y = 63$ .

regime since  $Nu \approx 1$ . This picture has been subtracted to the other ones (Figs. 9(b)–9(d)) in order to intensify contrasts. At the onset of convection  $Nu = 1.12$  (Fig. 9(b)), one can observe motion of fluid through the white and black regions, which characterize the convective cells. Larger values of  $Nu$  (Fig. 9(c)) permit to observe and identify the shape and size of the cells. The patterns observed consist on cells (Figs. 9(b) and 9(c)) at the onset of convection then seem to bifurcate to hexagonal rolls (Fig. 9(d)). The distance between two patterns at the onset of convection is close to  $2d$  (see Fig. 9(c)), leading to a wavenumber  $\alpha_c \approx 3$ . These results have been obtained by using the copper alloy wall (lower wall) and the glass wall (upper wall), i.e., with slip conditions. Critical results are not consistent to that one obtained in the Newtonian case.<sup>1,26,27</sup>

## V. CONCLUSION

For the determination of the onset of convection in viscoplastic fluids, the Schmidt-Milverton principle has been used by temperature measurements as well as the shadowgraph technique. The rheological and interfacial properties of the Carbopol gels have been determined by using steady rotational rheometry as well as oscillatory measurements. The gels are elasto-viscoplastic fluids, in particular below the yield stress  $\tau_y$ , the gels have viscoelastic properties. Interfacial properties have also been determined by using surface conditions involved in the Rayleigh-Bénard setup.

The onset of convection is observed in the range of our experiments, i.e., by varying the Carbopol gels, values of  $d$  and wall conditions. Experimental results show that  $\beta \Delta T_c / \tau_y \propto d^{-1}$ , highlighting the variation of  $Ra$  with  $d$  as well as the main influence of the yield number  $Y$ . Considering the Carbopol gels as elasto-plastic materials (approach (ii)), the (inverse of the) yield number appears explicitly as the governing parameter. Critical (inverse of the) yield numbers have been determined for slip conditions  $1/Y_c^S \approx 40$  and for no-slip conditions  $1/Y_c^{NS} \approx 80$ . These results highlight that interface conditions can affect criticality since the wall slip has a destabilizing effect ( $1/Y_c^S < 1/Y_c^{NS}$ ).

The differences found between our results and the theoretical predictions,<sup>3</sup> have been widely discussed in this article, they seem to be due to the treatment of the solid-viscous transition in the Bingham model. The prediction of the flow features close to the onset of convection is still a key issue. In this respect, considering a more realistic model in this transition constitutes one of our work perspectives.

Furthermore, experiments, which look in a more local detail the flow features of the onset of convection as well as the evolution of the thermoconvective perturbations, are currently under preparation by using Particle Image Velocimetre (PIV) flow visualization techniques.

## ACKNOWLEDGMENTS

This work was supported by the French National Research Agency (ANR), via the grant called “ThiM.”

- <sup>1</sup> S. Chandrasekhar, *Hydrodynamic and Hydromagnetic Stability* (Clarendon Press, Oxford, 1961).
- <sup>2</sup> E. L. Koschmieder, *Bénard Cells and Taylor Vortices* (Cambridge University Press, New York, 1993).
- <sup>3</sup> J. Zhang, D. Vola, and I. A. Frigaard, “Yield stress effects on Rayleigh-Bénard convection,” *J. Fluid Mech.* **566**, 389 (2006).
- <sup>4</sup> A. Vikhansky, “Thermal convection of a viscoplastic liquid with high Rayleigh and Bingham numbers,” *Phys. Fluids* **21**, 103103 (2009).
- <sup>5</sup> N. J. Balmforth and A. Rust, “Weakly nonlinear viscoplastic convection,” *J. Non-Newtonian Fluid Mech.* **158**, 36 (2009).
- <sup>6</sup> C. Métivier, C. Nouar, and J.-P. Bracher, “Weakly nonlinear dynamics of thermoconvective instability involving viscoplastic fluids,” *J. Fluid Mech.* **660**, 316 (2010).
- <sup>7</sup> B. Albaalbaki and R. E. Khayat, “Pattern selection in the thermal convection of non-Newtonian fluids,” *J. Fluid Mech.* **668**, 500 (2011).
- <sup>8</sup> A. Magnin and J. M. Piau, “Cone-and-plate rheometry of yield stress fluids. Study of an aqueous gel,” *J. Non-Newtonian Fluid Mech.* **56**, 221 (1990).
- <sup>9</sup> J. M. Piau, “Carbopol gels: Elastoviscoplastic and slippery glasses made of individual swollen sponges: Meso- and macroscopic properties, constitutive equations and scaling laws,” *J. Non-Newtonian Fluid Mech.* **144**, 1 (2007).
- <sup>10</sup> F. K. Oppong and J. R. de Bruyn, “Microrheology and jamming in a yield-stress fluid,” *Rheol. Acta* **50**, 317 (2011).
- <sup>11</sup> J. C. Buell and I. Catton, “The effect of wall conduction on the stability of a fluid in a right circular cylinder heated from below,” *ASME J. Heat Transfer* **105**, 255 (1983).

- <sup>12</sup>F. Hébert, R. Hufschmid, J. Scheel, and G. Ahlers, "Onset of Rayleigh-Bénard convection in cylindrical containers," *Phys. Rev. E* **81**, 046318 (2010).
- <sup>13</sup>R. J. Schmidt and S. W. Milverton, "On the instability of a fluid when heated from below," *Proc. R. Soc. London, Ser. A* **152**, 586 (1935).
- <sup>14</sup>W. Merzkirch, *Flow Visualisation* (Academic, New York, 1974).
- <sup>15</sup>W. Schöpf and J. C. Patterson, "Natural convection in a side-heated cavity: Visualization of the initial flow features," *J. Fluid Mech.* **295**, 357 (1995).
- <sup>16</sup>G. Forrest and W. L. Wilkinson, "Laminar heat transfer to temperature-dependent Bingham fluids in tubes," *Int. J. Heat Mass Transfer* **16**, 2377 (1973).
- <sup>17</sup>M. Naimi, R. Devienne, and M. Lebouché, "Etude dynamique et thermique de l'écoulement de Couette-Taylor-Poiseuille; cas d'un fluide présentant un seuil d'écoulement," *Int. J. Heat Mass Transfer* **33**(2), 381 (1990).
- <sup>18</sup>C. Nouar, R. Devienne, and M. Lebouché, "Convection thermique pour un fluide de Herschel-Bulkley dans la région d'entrée d'une conduite," *Int. J. Heat Mass Transfer* **37**(1), 1 (1994).
- <sup>19</sup>J. Peixinho, C. Desaubry, and M. Lebouché, "Heat transfer of non-Newtonian fluid (Carbopol aqueous solution) in transitional pipe flow," *Int. J. Heat Mass Transfer* **51**, 198 (2008).
- <sup>20</sup>H. A. Barnes, "A review of the slip (wall depletion) of polymer solutions, emulsions and particle suspensions in viscometers: Its cause, character, and cure," *J. Non-Newtonian Fluid Mech.* **36**, 85 (1995).
- <sup>21</sup>J. R. Seth, M. Cloitre, and R. T. Bonnecaze, "Influence of short-range forces on wall-slip in microgel pastes," *J. Rheol.* **52**, 1241 (2008).
- <sup>22</sup>C. Métivier, Y. Rharbi, A. Magnin, and A. Bou Abboud, "Stick-slip control of the Carbopol gels on transparent smooth walls," *Soft Matter* **8**, 7365 (2012).
- <sup>23</sup>D. A. Nield and A. Bejan, *Convection in Porous Media* (Springer-Verlag, New York, 1992).
- <sup>24</sup>J. Martinez-Mardones, R. Tiemann, and D. Walgraef, "Thermal convection thresholds in viscoelastic solutions," *J. Non-Newtonian Fluid Mech.* **93**, 1 (2000).
- <sup>25</sup>C. Métivier and A. Magnin, "The effect of wall slip on the stability of the Rayleigh-Bénard Poiseuille flow of viscoplastic fluids," *J. Non-Newtonian Fluid Mech.* **166**, 839 (2011).
- <sup>26</sup>A. Schlüter, D. Lortz, and F. Busse, "On the stability of steady finite amplitude convection," *J. Fluid Mech.* **23**, 129 (1965).
- <sup>27</sup>E. Bodenschatz, W. Pesch, and G. Ahlers, "Recent developments in Rayleigh-Bénard convection," *Annu. Rev. Fluid Mech.* **32**, 1 (2000).



Cite this: *Soft Matter*, 2012, **8**, 3365

[www.rsc.org/softmatter](http://www.rsc.org/softmatter)

## COMMUNICATION

# Stick-slip control of the Carbopol microgels on polymethyl methacrylate transparent smooth walls<sup>†</sup>

Métivier Christel,<sup>‡\*</sup> Rharbi Yahya, Magnin Albert and Bou Abboud Antoine

Received 26th January 2012, Accepted 11th June 2012

DOI: 10.1039/c2sm26244d

**Microgel suspensions such as Carbopol are commonly used as viscoplastic fluid models in fluid mechanics experiments. Polymethyl methacrylate (PMMA) walls are also frequently used in these experiments since they enable flow visualizations *via* their transparency properties. When sheared with smooth surfaces, the microgels slip on the surfaces and an apparent motion of the fluid occurs below the bulk yield stress  $\tau_y$ . This motion stops at a sliding yield stress  $\tau_s$ . The occurrence of this apparent slip below  $\tau_y$  can significantly modify the flow features. This article presents a PMMA treatment to inhibit the slip of the Carbopol microgels. The method is simple to perform, independent of the treatment conditions and stable over time.**

The control of the flow properties of complex fluids is central in order to optimize their processes and applications, since the stick or the slip of the fluid at walls can significantly affect the flow features; *e.g.*, the quality in the polymer extrusion processes<sup>1</sup> or the flow stability conditions<sup>2</sup> can depend highly on the shearing walls. It is therefore important, for both industrial applications and fundamental investigations, to understand and to control the wall slip. The wall slip occurs commonly in flows of concentrated dispersions,<sup>3</sup> such as microgel pastes. It occurs due to the displacement of the microgel particles on smooth substrates with no attractive interaction. The physics dictating the wall slip in microgel pastes can be described by elastohydrodynamical models.<sup>6–8</sup>

These materials display both a solid like behaviour at rest and a fluid like behaviour under large stresses. Wall slip occurs commonly below the bulk yield stress  $\tau_y$  when using relatively smooth surfaces. In this condition, an apparent motion occurs and a slip yield stress  $\tau_s$  is measured<sup>4,5</sup> below  $\tau_y$ . The simplest way to inhibit wall slip consists of modifying the surface roughness by sticking on sandpaper<sup>5</sup> or by using sandblasting or grooving surfaces.<sup>5,7</sup> However, these techniques modify the physical properties of the surface, such as *e.g.* thermodynamical or optical ones (transparency) due to the presence of sandpaper or due to diffuse reflection. Another way to control wall-

slip has emerged recently, it consists of chemically modifying the surfaces by incorporating attractive or repulsive interactions. Short-range interactions such as hydrophilic/hydrophobic or electrostatic forces have been obtained on surfaces.<sup>9–11</sup> It has been shown<sup>10,11</sup> that attractive interactions can suppress wall slip on smooth substrates, while repulsive interactions enhance the slip behaviour. The wetting properties have no significant effect on wall slip.<sup>6</sup> The control of wall slip by changing the surface chemistry remains scarcely explored and developed. There is still a need to develop simple surface treatment to inhibit the wall slip without affecting some functional substrate properties.

In this paper, we propose a simple treatment for polymethyl methacrylate (PMMA) substrates that inhibits wall slip in the case of microgel pastes.

Here, aqueous neutralized Carbopol 940 gels (Lubrizol) are used. They are reticulated polyacrylic acid resin ( $\text{COO}^- \text{H}^+$ ) particles. They are concentrated, percolated and disadhered suspensions of individual swollen microgels, characterized by a multi-micron size, with the behaviour of elastic sponges.<sup>8</sup> The gel preparation consists of mixing the polymer with double deionised water, leading to a low viscosity suspension at a concentration of 0.15 wt%. The suspension is neutralized dropwise with a 1 mol L<sup>-1</sup> sodium hydroxide solution (Aldrich) under mixing. A gel with a yield stress is built up when the groups ( $\text{COO}^- \text{H}^+$ ) are transformed into  $\text{COO}^- \text{H}^+ \text{Na}^+$ . Carbopol gels behave as elastoviscoplastic materials. Below the yield stress, the SAOS rheometry<sup>†</sup> indicates a dominant elastic modulus  $G$  for all oscillation frequency values; above  $\tau_y$ , the gel is described by the Herschel–Bulkley model.<sup>8</sup>

As explained by Magnin and Piau<sup>5</sup> and by Meeker *et al.*,<sup>7</sup> the presence of wall slip can be determined by steady-state rheological measurements. A TA Instrument ARG2 stress-controlled rheometer was used with a cone and plate geometry (49 mm diameter, angle 4°30'). To ensure adherence, the cone was covered with a waterproof sandpaper, characterized by an average roughness  $R_a = 120 \mu\text{m}$  larger than the microgel size. Different lower plates are used: (i) a plate with sandpaper, (ii) a raw PMMA and (iii) a treated PMMA substrate. The lower plates (ii) and (iii) are smooth substrates made of PMMA (Altuglas) with a roughness  $R_a < 0.1 \mu\text{m}$  smaller than the microgel size. The roughness was measured with a mechanical profilometer SM7 (Someco) which was homemade modified to yield a precision of 0.1  $\mu\text{m}$ .

The polymer used for treating the PMMA substrates is polyethylenimine PEI (Aldrich). PEI is formed of linear chains

Laboratoire de Rhéologie et Procédés – UMR 5520 (UJF, Grenoble-INP, CNRS), 1301 rue de la Piscine, BP 53 38041, Grenoble Cedex 9, France. E-mail: Christel.Metivier@univ-lorraine.fr

† Electronic supplementary information (ESI) available. See DOI: 10.1039/c2sm26244d

‡ Present address: LEMTA – UMR 7563, BP160, 54504 Nancy.

$\text{H}(\text{NHCH}_2\text{CH}_2)_n\text{NH}_2^+$  with an average molecular weight of  $M_w = 750\,000 \text{ g mol}^{-1}$  and a number average molecular weight of  $M_n = 60\,000 \text{ g mol}^{-1}$ .

Different concentrations of PEI in deionised water have been prepared ranging from  $10^{-8} \text{ wt\%}$  to  $2 \text{ wt\%}$ . The PMMA substrates are immersed into the polymer solution during a time  $t_t$ , varying from  $60 \text{ s}$  to  $24 \text{ h}$ . The substrates are then introduced into a container of double deionised water for  $6 \text{ hours}$  in order to remove the excess PEI. Finally, the substrates are dried and stored in a dry environment at room temperature. Light transmission in the PMMA substrates was analyzed using a Perkin Elmer UV/Vis spectrophotometer for wavelengths between  $300 \text{ nm}$  and  $700 \text{ nm}$ . The light transmission of the treated substrates ( $>90\%$ ) was found to be similar to the untreated ones within the precision of the spectrometer.

A first set of rheological measurements was obtained by covering the cone and plate geometries with sandpaper. With rough surfaces, the microgel particles are trapped in the substrate holes creating a sticking microgel layer which inhibits the displacement of particles on the surface and involves a homogeneous shear in the gel bulk. The results lead to a bulk yield stress values of  $\tau_y = 19 \text{ Pa}$  (Fig. 1). They have been fitted by the Herschel–Bulkley model (dashed lines) with  $\tau = (19 + 8.47\dot{\gamma}^{0.39})$  for  $\dot{\gamma} > \tau_y$ , where  $\tau$  is the shear stress and  $\dot{\gamma}$  is the shear rate.

When a rough cone and smooth plate are used, the gel is driven by the rough cone in rotation, but a slip velocity  $U_s$  is observed on the untreated PMMA plate. Slippage induces an apparent motion below  $\tau_y$  and above a slip yield stress  $\tau_s$  which depends on the tribological conditions at the gel–wall interface. When slip occurs, Fig. 1 displays a mean stress vs. an evaluation of the slip velocity  $U_s$ . At higher shear rates, the stress values exceed  $\tau_y$  and the gel flows in the bulk. The slip velocity becomes negligible compared with the cone and bulk velocities; the phenomena are then governed by the bulk behaviour.

By using direct visualizations, Magnin and Piau,<sup>5</sup> as well as Meeker *et al.*,<sup>6</sup> show that the slip is located in a very thin layer near the smooth wall and that the flow is homogeneous in the bulk. The results given in Seth *et al.*<sup>10</sup> show that wall slip of negatively charged particles occurs on several smooth substrates and with no particles–substrate interaction (uncharged substrate), *e.g.* PMMA, gold, silicon–silica substrates. The authors also show that wall slip is enhanced when the particles–substrate interactions are repulsive, and it is independent of the wetting substrate properties. In our case, the Carbopol microgels are composed of multi-micron size particles

which are negatively charged (COOH groups) and the untreated PMMA substrate is an uncharged surface with a  $\approx 100 \text{ nm}$  roughness. Because there is no particle–substrate interaction, and the substrate roughness is at least one order smaller than the particle size, there is no particles–substrate adherence and therefore the microgels slip.

The proposed treatment was tested for a  $2 \text{ wt\%}$  PEI concentration and a long treatment  $t_t = 24 \text{ h}$  in order to ensure an efficient paving of PEI onto the PMMA surface. Rheological measurements are displayed in Fig. 2 and show that the bulk properties of the Carbopol gels are obtained. The adherence has also been confirmed by using the same visualization technique as Magnin and Piau<sup>5</sup> (see ES†). It means that the proposed treatment inhibits the wall slip of Carbopol gels.

The influence of the PEI concentration on the wall slip was investigated by varying the treatment concentrations from  $10^{-8} \text{ wt\%}$  to  $2 \text{ wt\%}$ , fixing the time treatment at  $t_t = 24 \text{ h}$ .

As one can observe in Fig. 2, no-slip conditions are also obtained, meaning that the efficiency of the treatment does not depend on the PEI concentrations in the range of our experiments.

On the other hand, the influence of the time of treatment  $t_t$  has also been investigated by fixing the PEI concentration treatment to  $10^{-2} \text{ wt\%}$  and by varying  $t_t$  between  $60 \text{ s}$  and  $24 \text{ hours}$ . The results obtained are similar to those of Fig. 2, highlighting the independency of  $t_t$  on the interface conditions.

The adsorption of PEI on the PMMA has been explored for microchips for electrophoretic applications.<sup>12</sup> In this study, the authors presented experiments of adsorption of linear high molecular mass PEI ( $M_w = 750\,000 \text{ g mol}^{-1}$ ) on PMMA in the presence of borate buffer at  $\text{pH} = 11.5$ . They found that PEI adsorbs on PMMA surface by interaction of secondary amino groups with PMMA ester groups. In our experiments, by using low concentration PEI solutions ( $<2 \text{ wt\%}$ ) at neutral pH, wall slip is inhibited for all the conditions investigated here. The amino groups of PEI form complexes with the  $\text{COO}^-$  pending groups of the Carbopol leading to the attachment of particles on the substrate (Fig. 3). This leads to a stick layer of Carbopol microgels on the substrate with a thickness similar to the swollen particle size (a few  $\mu\text{m}$ ) which enables the inhibition of the slippage. At high PEI concentration and long treatment time, one expects the formation of a dense PEI brush on the substrate, which will adsorb a dense Carbopol layer. By reducing the PEI concentration and  $t_t$ , one would expect the reduction of the surface density

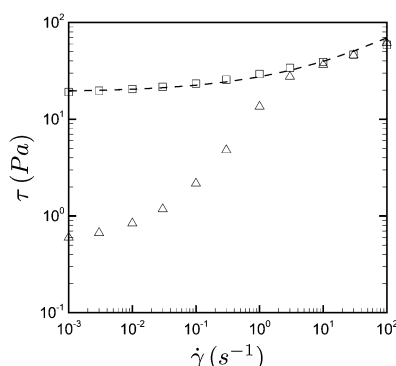


**Fig. 1** Shear stress measurements of Carbopol 940 gels.  $\square$ : rough surfaces,  $\triangle$ : smooth and untreated PMMA substrate, dashed lines: Herschel–Bulkley model.

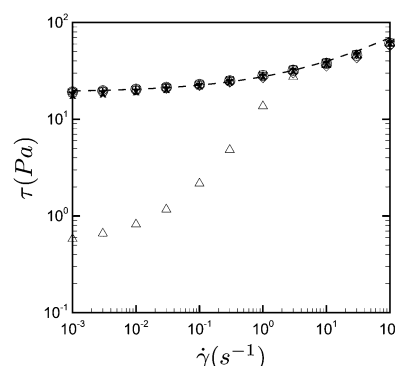


**Fig. 2** Shear stress measurements of Carbopol 940 gels on treated PMMA substrates (+: 2%, ×: 0.5%, □: 0.01%, ○:  $10^{-4}\%$ , ◇:  $10^{-6}\%$ , ▽:  $10^{-8}\%$ , △: not treated). Dashed line: Herschel–Bulkley model.

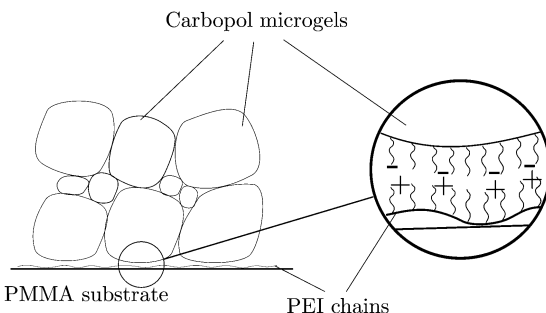


**Fig. 3** Schematic representing the attractive interactions between the PEI positive amino end chains and the Carbopol negative end chains.

of the PEI and a progressive enhancement of wall slip. Contrarily, wall slip was inhibited for all experimental conditions investigated. This result could infer that even sparse PEI distribution on the substrate is sufficient to inhibit wall slip. One possible explanation for this result could be the use of long PEI chains, enhancing the probability of attachment of Carbopol microgels on the substrate. The relationship between the surface distribution of PEI and the wall slip is an important question which is beyond the scope of this communication.

With the interactions between the PEI and the Carbopol being strong, it could involve a desorption of the PEI from the PMMA substrate and it could have some consequences on the surface conditions. In this sense, the time evolution of the treatment was also investigated. The tests consisted of treating PMMA substrates with a PEI solution of  $10^{-2}$  wt%. Substrates were immersed in a Carbopol solution and left for 42 days. During this period, several rheological measurements were conducted in order to follow the aging of the treated pieces through the surface conditions. As obtained previously, the rheological results led to flow curves which mean that polymer

treatment is stable over time. Finally the PEI-PMMA interactions are strong enough to lead to a stable adsorption of the PEI on the substrate over time, at least within a period of 42 days. Furthermore, the strong interactions induced between the PEI and the Carbopol are also stable over time and led to stick conditions in the range of our experiments.

As a conclusion, the proposed method is simple to perform, independent of the treatment conditions and stable over time. It enables inhibition of the wall slip of Carbopol microgels at the PMMA interface without affecting the physical properties of the PMMA, such as refractive index, roughness and thermodynamical coefficient. Finally, visualizations are rendered possible in flow experiments, with either stick or slip conditions.

## References

- 1 J.-M. Piau and J.-F. Agassant, *Rheology for Polymer Processing*, Elsevier, Amsterdam, 1996.
- 2 C. Métivier and A. Magnin, *J. Non-Newtonian Fluid Mech.*, 2011, **166**, 839–846.
- 3 H. A. Barnes, *J. Non-Newtonian Fluid Mech.*, 1995, **36**, 85–108.
- 4 G. V. Vinogradov, G. B. Froisheter and K. K. Trilisky, *Rheol. Acta*, 1975, **14**(9), 765.
- 5 A. Magnin and J. M. Piau, *J. Non-Newtonian Fluid Mech.*, 1990, **56**, 221–251.
- 6 S. P. Meeker, R. T. Bonnecaze and M. Cloitre, *Phys. Rev. Lett.*, 2004, **92**(19), 198302.
- 7 S. P. Meeker, R. T. Bonnecaze and M. Cloitre, *J. Rheol.*, 2004, **48**(6), 1295–1320.
- 8 J. M. Piau, *J. Non-Newtonian Fluid Mech.*, 2007, **144**, 1–29.
- 9 H. J. Walls, S. B. Caines, A. M. Sanchez and S. A. Khan, *J. Rheol.*, 2003, **47**(4), 847–867.
- 10 J. R. Seth, M. Cloitre and R. T. Bonnecaze, *J. Rheol.*, 2008, **52**(5), 1241–1268.
- 11 J. R. Seth, C. Locatelli-Champagne, F. Monti, R. T. Bonnecaze and M. Cloitre, *Soft Matter*, 2012, **8**(1), 140–148.
- 12 F. Kitagawa, K. Kubota, K. Sueyoshi and K. Otsuka, *Sci. Technol. Adv. Mater.*, 2006, **7**, 558–565.